

**THE UNIVERSITY OF MANCHESTER - APPROVED ELECTRONICALLY  
GENERATED THESIS/DISSERTATION COVER-PAGE**

Electronic identifier: 22621

Date of electronic submission:

The University of Manchester makes examined, Open Access electronic theses freely available for download and reading online via the University's Research Explorer <http://www.research.manchester.ac.uk>.

This print version of my thesis is a TRUE and ACCURATE REPRESENTATION of the electronic version submitted via the University of Manchester's eThesis submission system.

Blank page

# **DESIGN CONSIDERATIONS FOR**

## **LEO NANOSATELLITE**

## **PROPULSION TECHNOLOGIES**



The University of Manchester

A thesis submitted to the University of Manchester for the degree of

*Doctor of Philosophy*

in the Faculty of Science and Engineering

2017

by

Alejandro Macario Rojas

School of Mechanical, Aerospace, and Civil Engineering

Blank page

# Table of contents

<b>List of figures</b>	<b>7</b>
<b>List of tables</b>	<b>11</b>
<b>Nomenclature</b>	<b>13</b>
<b>Abstract</b>	<b>24</b>
<b>Declaration</b>	<b>26</b>
<b>Copyright</b>	<b>28</b>
<b>1 Introduction</b>	<b>33</b>
1.1 Problem Statement . . . . .	40
<b>2 Nanosatellites Overview</b>	<b>43</b>
2.1 Propulsion Systems for Nanosatellites . . . . .	44
2.2 ADCS in Nanosatellites . . . . .	56
2.2.1 Attitude Determination . . . . .	57
2.2.2 Attitude Stabilisation . . . . .	59
2.3 Typical Nanosatellite Mission Characteristics . . . . .	61
2.3.1 Nanosatellites Survivability to the Space Environment . . . .	66
2.3.2 Main Attitude and Orbital Perturbations in Nanosatellites . .	74
2.4 In-Orbit Power Resources . . . . .	80
2.4.1 Power Generation . . . . .	81

## Table of contents

---

2.4.2	Power Storage . . . . .	90
<b>3</b>	<b>Research aim and approach</b>	<b>93</b>
3.1	Research Aim . . . . .	93
3.2	Research Approach . . . . .	97
3.2.1	Orbit Propagator Verification . . . . .	101
<b>4</b>	<b>Solar Activity Forecast</b>	<b>109</b>
4.1	Solar Activity on Nanosatellites . . . . .	109
4.2	Observed Solar Activity . . . . .	115
4.3	Forecasting Solar Activity . . . . .	119
4.3.1	Categories of Solar Activity Forecasts . . . . .	120
4.4	The Proposed Forecast Approach . . . . .	122
4.5	The Mean Field Axisymmetric Dynamo Model . . . . .	124
4.5.1	Differential Rotation . . . . .	126
4.5.2	Meridional Circulation . . . . .	129
4.5.3	Flux Transport Dynamo Theory . . . . .	131
4.6	Solar Cycles Forecast . . . . .	141
4.6.1	Solar Polar Field Strength Reconstruction . . . . .	146
4.6.2	Solar Cycles Simulation and Forecast . . . . .	155
4.7	Chapter Conclusions and Further Work . . . . .	162
<b>5</b>	<b>Atmospheric Interaction with Nanosatellites from Observed Orbital Decay</b>	<b>165</b>
5.1	Background . . . . .	170
5.1.1	Gas-Surface Interactions . . . . .	170
5.1.2	Atomic Oxygen . . . . .	178
5.1.3	GSI Models . . . . .	179
5.1.4	Characteristic Cross-sectional Areas in CubeSats . . . . .	182
5.1.5	$C_D$ Estimations from TLE sets . . . . .	185

5.2	Simulation and Analysis . . . . .	189
5.2.1	Estimation of $\alpha_n$ from Fitted Drag Coefficients . . . . .	195
5.2.2	Analysis of Results . . . . .	196
5.3	Chapter Conclusions and Further Work . . . . .	204
<b>6</b>	<b>Spiral Coning Manoeuvre for In-Orbit Low Thrust Characterisation in Nanosatellites</b>	<b>209</b>
6.1	The Proposed Method . . . . .	210
6.1.1	Analytic Solutions . . . . .	216
6.1.2	Induced Error due to Temporal Mass Variation . . . . .	219
6.1.3	Rotation Stability and Energy Dissipation . . . . .	220
6.2	Application Example . . . . .	222
6.3	Chapter Conclusions and Further Work . . . . .	228
<b>7</b>	<b>Conclusions</b>	<b>229</b>
7.1	Conclusions of the Developed Methodologies . . . . .	230
7.2	Concluding Remarks . . . . .	236
<b>References</b>		<b>239</b>
<b>Appendix A: List of historic nanosatellite missions</b>		<b>257</b>
<b>Appendix B: Nanosatellite missions for 2017</b>		<b>267</b>
<b>Appendix C: Total Ionising Dose (TID)</b>		<b>271</b>
<b>Appendix D: Main orbit perturbations</b>		<b>287</b>
<b>Appendix E: Ideal photovoltaic solar cell efficiency</b>		<b>297</b>
<b>Appendix F: Propulsion systems in CubeSats</b>		<b>301</b>
<b>Appendix G: Fitted momentum accommodation coefficients</b>		<b>303</b>

## **Table of contents**

---

<b>Appendix H: Spiral coning algorithm example</b>	<b>311</b>
--	------------

Word count: 59 602

# List of figures

1.1	Nanosatellites timeline . . . . .	36
1.2	Propulsion system evaluation . . . . .	41
2.1	Nanosatellites launch history . . . . .	44
2.2	Electric propulsion system mass as function of specific impulse . . . . .	49
2.3	Varieties and operation characteristics of nanosatellite propulsion systems	51
2.4	Propulsion systems in CubeSats . . . . .	55
2.5	ADCS Scheme . . . . .	57
2.6	Resources for attitude determination in nanosatellites . . . . .	58
2.7	Attitude stabilisation approaches in nanosatellites . . . . .	60
2.8	Nanosatellite launch sites . . . . .	63
2.9	Nanosatellites perigee altitude-inclination space . . . . .	64
2.10	Whiskers growth in electronic components . . . . .	68
2.11	Earth's plasmasphere and LEO . . . . .	69
2.12	Dose at transmission surface of aluminium slab shield . . . . .	70
2.13	Concave and convex satellite geometries . . . . .	76
2.14	Surface-area-to-volume ratio plot . . . . .	77
2.15	Orbit perturbation accelerations . . . . .	77
2.16	Body torque perturbations . . . . .	79
2.17	Maximum ideal solar converter efficiency . . . . .	82
2.18	Best research multijunction vs nanosatellite solar cell energy conversion efficiencies . . . . .	85

## List of figures

---

2.19 Input power profile in a 3U CubeSat . . . . .	87
2.20 Estimation of $\beta$ for sunlight function . . . . .	89
2.21 Sunlight orbit percentage . . . . .	89
3.1 Solar activity and solar indices . . . . .	95
3.2 Orbit Propagator block diagram . . . . .	98
3.3 OP CAD model treatment example . . . . .	100
3.4 OP and SGP4 orbit propagations residuals . . . . .	102
3.5 OP sensitivity with respect to the initial state vector . . . . .	104
3.6 OP attitude propagation test . . . . .	107
4.1 Relationship between SSN and $\Delta v$ budget for station keeping manoeuvres in LEO . . . . .	110
4.2 SSN and rate of change of semi-major axis with time in nanosatellites	111
4.3 Cross-correlation between solar activity and nanosatellites orbit evolution	112
4.4 Orbit maintenance manoeuvres . . . . .	114
4.5 Observed magnetic butterfly diagram . . . . .	118
4.6 Observed solar polar field strength and SSN activity . . . . .	118
4.7 Performance of solar activity forecasts for the solar cycle 24 . . . . .	121
4.8 Sun density and temperature depth profile . . . . .	126
4.9 Solar longitudinal averaged isorotation contours and depth profiles for selected solar latitudes . . . . .	128
4.10 Meridional circulation profile . . . . .	131
4.11 Babcock-Leighton $\alpha$ profile . . . . .	135
4.12 Poloidal and toroidal diffusivity profiles . . . . .	137
4.13 Theoretical magnetic Sun . . . . .	139
4.14 3D Theoretical toroidal field evolution . . . . .	140
4.15 Probability density functions of emerging active regions and regular sunspot areas. . . . .	140
4.16 The average solar cycle . . . . .	143

4.17	The observed solar cycle 23 . . . . .	144
4.18	Calibrated average dynamo cycle . . . . .	145
4.19	Longitudinally averaged magnetic field diagram for the solar cycle 23.	147
4.20	NARX layer diagram . . . . .	150
4.21	NARX for polar field forecasting . . . . .	151
4.22	Start of the solar cycle 25 prediction . . . . .	152
4.23	Full solar polar fields series from the NARX reconstruction and forecasts.	154
4.24	Solar activity simulation results . . . . .	156
4.25	Solar maxima forward change percentage trends from the raw theoretical and observed SSN . . . . .	157
4.26	External solar activity studies . . . . .	159
4.27	Solar maxima forward change percentage trends from the corrected theoretical and observed SSN . . . . .	162
5.1	Atmospheric composition and flow characteristics . . . . .	172
5.2	Angular distributions of scattered particles . . . . .	175
5.3	Particle's interaction velocities with $\alpha$ . . . . .	177
5.4	Multiple reflections in concave geometries . . . . .	180
5.5	Projected cross-sectional area . . . . .	183
5.6	PMAC cross-sectional area profile . . . . .	186
5.7	Orbit evolution of the analysed CubeSat missions . . . . .	191
5.8	Identification of TLE outliers . . . . .	193
5.9	Fitting algorithm . . . . .	194
5.10	Sensitivity test of the principal $C_D$ term . . . . .	195
5.11	Fitting process summary chart . . . . .	197
5.12	Comparison of $C_D$ and $C_D^*$ . . . . .	201
5.13	Assembly of fitted drag coefficients . . . . .	202
5.14	Total and AO atmospheric concentrations . . . . .	203
6.1	Reference CubeSats . . . . .	210

## List of figures

---

6.2	Poinsot's construction . . . . .	214
6.3	Mass variation effect on the analytic angular frequency equation . . .	220
6.4	Effect of dissipative processes over the transversal angular velocities .	221
6.5	Spiral coning manoeuvre . . . . .	226
6.6	Example of body angular velocities response . . . . .	226
6.7	Estimations performance in a 1.5U CubeSat . . . . .	227
6.8	Estimations performance in a 3U CubeSat . . . . .	227
1	D: Earth oblateness . . . . .	288
2	D: Third-body perturbation elements . . . . .	289
3	D: Incident solar radiation . . . . .	293
4	D: Crosswind speed along GOCE orbit . . . . .	295
5	E: The hypothetical solar converter for calculating efficiency limit .	298
6	G: Reference cone geometry . . . . .	304
7	G: Cross-correlation map of $\sigma_t$ , AO, E, s, and $\phi_{ic}$ . . . . .	308
8	G: Fitted $\sigma_t$ for RAX-2 . . . . .	310

# List of tables

1.1	Typical classification of satellites by size . . . . .	33
3.1	Simulation parameters for OP verification . . . . .	106
4.1	Meridional circulation parameters . . . . .	130
4.2	Magnetic diffusivity parameters . . . . .	136
5.1	Best-fit parameters for a flat plate . . . . .	182
5.2	List of selected 3U CubeSats . . . . .	190
5.3	Fitting process success percentage . . . . .	198
5.4	Comparison of $\bar{C}_{DF}$ to external results . . . . .	200
5.5	Performance test results of the proposed $C_D(\rho)$ function . . . . .	207
6.1	Simulation parameters . . . . .	224
1	A: Historical nanosatellites missions . . . . .	257
2	B: Projected nanosatellite launches for 2017 . . . . .	267
3	C: Dose at transmission surface of aluminium slab shields . . . . .	271
4	D: Optical properties for surface materials . . . . .	293
5	F: Reported historical and planned CubeSat missions equipped with propulsion systems . . . . .	301

Blank page

# Nomenclature

## Roman Symbols

$\mathcal{T}_\odot$	Sunlight coefficient
$A$	Magnetic poloidal potential in Ch.4; Area in Ch.5; Substitution variable in Ch.6
$a$	Acceleration
$B$	Magnetic toroidal field
$C$	Correction vector in Ch.4; Coefficient in Ch.5; Substitution variable in Ch.6
$C_R$	Reflectivity
$D$	Substitution variable in Ch.6
$d$	Effective collision diameter
$d_m$	Effective moment arm in Ch.6
$E$	Electric power
$e$	Euler's number $\simeq 2.71828\dots$
$F$	Force in Ch.5; Substitution variable in Ch.6
$f$	Mathematical function
$g_0$	Standard gravity
$h$	Orbit angular momentum in Ch.2; Vector projection in Ch. 6

## Nomenclature

---

$I$	Body moment of inertia
$i$	Orbit inclination; Imaginary number in Ch.6
$I_{\odot}$	Solar irradiance
$I_{sp}$	Specific impulse
$J_2$	Second zonal harmonic
$K$	Body kinetic energy
$k_B$	Boltzmann constant
$Kn$	Knudsen number
$L$	Characteristic length in Ch.5; Angular momentum in Ch.6
$l$	Edge length
$M$	Rocket mass in Ch. 2; Body torque in Ch. 6
$m$	Mass
$n$	Normal vector
$P$	Power
$p$	Pressure
$q$	Flux quantity
$r$	Interior edges number in Ch. 2; Local radius in Ch.4
$R_{\odot}$	Solar radius
$R_p$	Penetration radius
$R_{SMA}$	Residual on SMA
$s$	Speed ratio

$T$	Thrust in Ch.2; Temperature in Ch.5
$t$	Time; Epoch time in Ch.5
$u$	Substitution variable in Ch.6; Number of building units in Ch. 2
$u_{et}$	Effective exhaust speed
$V$	Volume
$v$	Speed; Meridional circulation in Ch.4
$v_s$	Most probable thermal speed
$w$	Angular frequency in Ch.6
$x$	Interior vertex number in Ch. 2; Exogenous input series in Ch.4
$y$	Target series

### **Greek Symbols**

$\alpha$	Sun right ascension in Ch.2; Babcock-Leighton process in Ch.4; Energy accommodation coefficient in Ch.5; Body angular acceleration in Ch.6
$\beta$	Relative angle in Ch.2; Meridional circulation parameters in Ch.4; First fitting parameter in Ch.5
$\chi$	Mole fraction in Ch.5; The product $I_{sp}d_m$ in Ch.6
$\delta$	Sun declination in Ch.2; Third fitting parameter in Ch.5
$\varepsilon$	Meridional circulation parameter
$\eta$	Efficiency; Turbulent magnetic diffusivity in Ch.4
$\Gamma$	Meridional circulation parameter
$\gamma$	Meridional circulation parameters in Ch.4; Second fitting parameter in Ch.5

## Nomenclature

---

$\kappa$	Power supply specific mass
$\lambda_a$	Mean free path
$\nu$	Kinematic viscosity
$\Omega$	Solar longitudinal averaged rotation; Body transversal angular velocity in Ch.6
$\omega$	Body angular velocity
$\phi$	Azimuthal component
$\pi$	$\simeq 3.14159\dots$
$\psi$	Stream function
$\rho$	Mass density; Poinsot's vector in Ch.6
$\sigma$	Momentum accommodation coefficient
$\tau$	Tangential momentum
$\theta$	Sun colatitude
$\zeta$	Fourth fitting parameter

### Superscripts

$m$	Polytopic index
$N$	Total number of elements

### Subscripts

$-w$	Weighted average
$-F$	From fitted values
$\infty$	Freestream property
$a$	Ambient

$D$	Drag
$dyn$	Dynamic
$e$	At exit surface
$f$	Final condition
$ft$	Flux tube
$i$	Initial condition; Iteration number in Ch.5
$I - III$	Term number in equation
$ic$	Incident
$in$	Inward
$j$	Element number
$m$	Molecular
$N$	Observation number
$n$	Normal component
$p$	Projected
$R$	Re-radiated in Ch. 2
$r$	Relative
$ref$	Reference
$rf$	Reflected/Reemitted
$RZ$	Radiative zone
$SC$	Spacecraft
$SCZ$	Inside the convection zone

## Nomenclature

---

$srp$  Solar radiation pressure

$sta$  Static

$T$  Total

$t$  Tangential component

$w$  Surface property

$x$  Body axis

$y$  Body axis

$z$  Body axis

## Other Symbols

$\rightarrow$  Tensor

$\Omega$  Ascending node

$\bar{\cdot}$  Average value

$\hat{\cdot}$  Unit vector

$\text{erf}$  Gauss error function

$\Sigma$  Summation

$\square$  Solar cell

$\rightarrow$  Vector

$*$  Related to BSTAR drag term

## Acronyms / Abbreviations

$\nabla G$  Gravity-gradient stabilisation

$CLL$  Cercignani-Lampis-Lord

*H* Hydrogen

*He* Helium

*N*<sub>1</sub> Atomic Nitrogen

*N*<sub>2</sub> Molecular Nitrogen

*O*<sub>2</sub> Molecular Oxygen

*OP* Orbit Propagation

*R-SMA* Semi-major axis root-mean-square residual

3U 3 Units

ADS Attitude Determination System

AFSPCMAN Air Force Space Command Manual

AO Atomic Oxygen

BC Ballistic Coefficient

BLITS Ball Lens In The Space nanosatellite

CCAFS Cape Canaveral launch complex

CDH Command and Data Handling system

CDS CubeSat Design Specification

COTS Commercial off-the-shelf

CRN Carrington Rotation Number

CV Control Volume

DOF Degree Of Freedom

DSMC Direct Simulation Monte Carlo

## **Nomenclature**

---

ECI Earth-Centered Inertial reference frame

EGM Earth Gravitational Model

EP Electric Propulsion

EUV Extreme Ultraviolet

FRGUI Guiana space centre

GGM05G GRACE+GOCE Gravity Model

GNB Generic Nanosatellite Bus

GOCE The Gravity Field and Steady-State Ocean Circulation Explorer

GONG Global Oscillation Network Group

GSI Gas-Surface Interaction

HT HyperThermal flow approximation

ISO International Organisation for Standardisation

ISS The International Space Station

JB2006 Jacchia-Bowman 2006 thermospheric model

JB2008 Jacchia-Bowman 2008 thermospheric model

JSLC Jiuquan launch centre

KSCUT Uchinoura space centre

LEO Low-Earth Orbit

MEMS MicroElectroMechanical Systems

MHD MagnetoHydroDynamics

MHV Mojave space port

MRLLS Rocket Lab launch complex 1

NARX Nonlinear AutoRegressive network with eXogenous inputs

NN Artificial Neural Network

NOAA National Oceanic and Atmospheric Administration (USA)

NORAD North American Aerospace Defense Command

OP Special perturbation technique Orbit Propagator

PLMSC Plesetsk cosmodrome

PMAC Passive Magnetic Attitude Control

RoHS Restriction Of Hazardous Substances directive

RSW Satellite-Radial reference frame

SAVR Surface-Area-to-Volume Ratio

SC Schaaf and Chambre

SDSC Satish Dhawan space centre

SEB Single Event Burnout

SEE Single Event Effect

SEL Single Event Latch-up

SEU Single Event Upset

SGP4 Fourth Simplified General Perturbations Model

SILSO Sunspot Index and Long-term Solar Observations

SMA Semi-Major Axis

SORCE SOlar Radiation and Climate Experiment

## **Nomenclature**

---

SSN SunSpot Number; Space Surveillance Network in Ch.5

T Thermal flow approximation

TAISC Taiyuan launch centre

TASC Triangular Advanced Solar Cell

TEME True Equator, Mean Equinox

TID Total Ionising Dose

TLE Two-Line Element

TOD True equator Of the Date

TYMSC Baikonur cosmodrome

VBG Vandenberg launch complex

VOSTO Vostochny cosmodrome

WLPIS Wallops flight facility

WMM US/UK World Magnetic Model

WSO The Wilcox Solar Observatory

XTJ NeXt Triple Junction solar cell

## Abstract

**ABSTRACT OF THESIS** submitted by Alejandro Macario Rojas for the degree of Doctor of Philosophy at The University of Manchester, entitled "**Design Considerations for LEO Nanosatellite Propulsion Technologies**".

Submitted September 2017

In recent years the space industry has seen significant growth in numbers of sub 10kg satellite platforms now known more broadly in the industry as nanosatellites. Nanosatellites potential applicability is driven by flourishing technologies miniaturisation in the consumer electronics market and commercialisation of space. Currently nanosatellite mission operations are limited in both lifetime and manoeuvrability due to limitations in on board propulsion technologies. Further enhancement of mission operations relies on more effective integration of current reaction-mass-based propulsion technologies and further development of miniaturised propulsion systems. Paradoxically, the compact spacecraft size and mass that facilitate nanosatellite access to space is presently a drawback in terms of acceptable systems performance and propulsion systems capacity. Moreover characteristic power density and vulnerability to the space environment is already high in nanosatellites in contrast to major satellites, rendering the design, inclusion, and optimisation of propulsion technologies a challenging task.

This thesis focuses on techniques to support mission planning and characterisation of propulsion technologies for nanosatellites. Acknowledging the outweighing significance of solar activity modulating space environment perturbations and particularly atmospheric drag, a robust solar forecast method is proposed to support lifetime estimations. Complementing the pivotal framework information for propulsion system design and management, the vulnerability to atmospheric drag is assessed to identify the profile of the current vaguely defined drag coefficient of standard nanosatellites. Finally, addressing a crucial task on emerging propulsion technologies for nanosatellite systems, a method to improve low thrust characterisation via in-orbit manoeuvres using standard elementary attitude determination resources is devised.

The robust solar activity forecast is carried out using observed historic and reconstructed Sun's polar magnetic field, to define the initial state of an up-to-date solar magnetohydrodynamics computational model; the method successfully reproduces recent solar cycles activity, anticipating moderate-to-low activity during the next 25<sup>th</sup> cycle. The identification of the drag coefficient profile in standard nanosatellites is enabled by the statistical assessment of observed orbital decay through an iterative fitting process of propagated orbits; the profile is physically consistent and descriptive mostly in orbits below 350km during moderate-to-high solar activity. Finally, the devised thrust characterisation method exploits the regular geometry and mass distribution of standard nanosatellites to identify low thrust actuation via actuated body angular rotation rates in an intermediate axis spinner; precise computer simulations show that it is possible to improve low thrust estimations from weak and noisy sensor signals using the proposed method against typical methods using body angular acceleration.

Blank page

## **Declaration**

I hereby declare that except where specific reference is made to the work of others, the contents of this dissertation are original and have not been submitted in whole or in part for consideration for any other degree or qualification in this, or any other university. This dissertation is my own work and contains nothing which is the outcome of work done in collaboration with others, except as specified in the text and Acknowledgements.

Blank page

## **Copyright**

- i The author of this thesis (including any appendices and/or schedules to this thesis) owns certain copyright or related rights in it (the "Copyright") and s/he has given The University of Manchester certain rights to use such Copyright, including for administrative purposes.
- ii Copies of this thesis, either in full or in extracts and whether in hard or electronic copy, may be made only in accordance with the Copyright, Designs and Patents Act 1988 (as amended) and regulations issued under it or, where appropriate, in accordance with licensing agreements which the University has from time to time. This page must form part of any such copies made.
- iii The ownership of certain Copyright, patents, designs, trade marks and other intellectual property (the "Intellectual Property") and any reproductions of copyright works in the thesis, for example graphs and tables ("Reproductions"), which may be described in this thesis, may not be owned by the author and may be owned by third parties. Such Intellectual Property and Reproductions cannot and must not be made available for use without the prior written permission of the owner(s) of the relevant Intellectual Property and/or Reproductions.
- iv Further information on the conditions under which disclosure, publication and commercialisation of this thesis, the Copyright and any Intellectual Property and/or Reproductions described in it may take place is available in the University IP Policy (see <http://documents.manchester.ac.uk/DocuInfo.aspx?DocID=487>), in any relevant Thesis restriction declarations deposited in the University Library, The University Library's regulations (see <http://www.manchester.ac.uk/library/aboutus/regulations>) and in The University's policy on presentation of Theses.

Blank page

To my wife Hanna and my parents

Blank page

## **Acknowledgements**

I wish to express my heartfelt gratitude to my supervisor Dr Kate Smith for her deft guidance and patient support. Her feedback and invaluable suggestions have been essential in the development of this work.

I gratefully acknowledge my sponsor the Mexican Council for Science and Technology for supporting my studies. I would also like to sincerely thank the members of the MACE Space Research Group for their helpful criticism. I am indebted to the many fine teachers and professors who directly or indirectly have taught me along the years a powerful approach to scientific inference such that this work could ultimately be conceived.

I owe my greatest debt of gratitude to my wife Hanna for her unwavering love and support, and to my parents for their example and relentlessly devotion. Finally, I wish to thank my family and friends for their unconditional encouragement.

Blank page

# Chapter 1

## Introduction

Artificial satellites gather and transmit targeted information typically inaccessible by terrestrial means. Early satellite technology was greatly boosted by military demands such as navigation, battle field telecommunications, surveillance and espionage purposes. Gradually satellites began to serve civilian purposes retransmitting radio and television broadcasts, reporting global weather conditions, and ultimately interconnecting the world through the Internet. Yet, the most far-reaching asset of satellites for humankind is that they have vastly expanded our knowledge of the universe and assisted our understanding of nature.

Table 1.1 Typical classification of satellites by size [1, 2].

Class	Mass range*	Geocentric altitude †	Mission lifetime ‡
Standard	> 500	—	~ 15 §
Mini	100 – 500	1000 – 5000	4 – 7
Micro	10 – 100	500 – 2000	2 – 5
<b>Nano</b>	1 – 10	300 – 800	2 – 3
Pico	0.1 – 1	200 – 400	1 – 2
Femto	< 0.1	200 – 400	1

\* Unit in kg

† In km

‡ In Year

§ Average lifespan for a GEO satellite [3]

## **Introduction**

---

In the context of the artificial satellite categories presented in Table 1.1<sup>1</sup>, nanosatellites typify the limit of current technology and manufacturing capabilities to provide sufficient conventional space-mission functionality and performance. The nanosatellite category finds its niche in a wide variety of potential space applications mainly due to general mission cost reduction and the possibility of mission tasks fragmentation in nanosatellite constellations [5]. In principle traditionally large satellite missions could be replaced with several smaller satellites in formation flying as this concept allows greater mission flexibility and robustness; this topic is discussed by Sandau et al. [6] for Earth observation missions and by Hans [7] and Rhee et al. [8] on the future of space missions. However most nanosatellite precedents have served for specific technology demonstration, and as an affordable option to space access for small groups of developers [2, 9].

The CubeSat concept, originally conceived as an heuristic satellite platform for students in 1999 by Dr Puig-Suari and Prof. Bob Twiggs [10, 11], is based on a  $10 \times 10 \times 10\text{cm}$  cubic geometry and a mass of approximately  $1.33\text{kg}$  namely 1U. CubeSats are modular, this feature allows design flexibility to conduct timely cost-effective space operations that in turn have paved the way to the future profitability of nanosatellites. Current nanosatellite mission size is dominated by the 3U CubeSat standard which accounted for more than 50% in 2017, with a positive trend reaching 90% by 2019 [2]. CubeSats' proliferation and future domain amongst nanosatellites is mainly a result of components standardisation. Standardisation stresses on modular and scalable common features that inherently optimises the functionality of components and reduces the final geometric variability of missions. These in turn reduce the overall cost of manufacture, launch and operation, and eases fast mass production [9]. In this regard, the use of current Commercial Off-The-Shelf (COTS) components in CubeSats have endowed basic operational features such as semi-independent operation and telemetry capabilities. In contrast to the traditional CubeSat technology demonstration mission,

---

<sup>1</sup>Satellite customary classification. Homan [4] argues that a more descriptive classification should use functional capabilities too, redefining the mass range for nanosatellites as  $5 - 50\text{kg}$ .

---

more specialised on-board systems have enabled basic scientific missions wherein active attitude control systems play a fundamental role.

According to the 2017 Nano/Microsatellite Market Forecast [2], nanosatellites market potential is high with an annual growth expectancy of 10%. Although the projection was more favourable, launch delays and limited launch vehicle availability impacted the rate in 2016. Starting from 2017, new dedicated small satellite launchers will support the increasing demand allowing for improved growth forecasts in the near future. The overall viability of nanosatellites is further fostered by numerous launch systems and reducing target launch prices. Some examples include the NanoRacks [12] since 2014 and deployed from the International Space Station (ISS) at US\$60000/kg, Virgin Galactic's Launcher One [13] starting in 2017 at US\$33000/kg, and the Intrepid-1 [14] in 2019 at US\$14000/kg.

Chiefly motivated by reduced development time and low launch cost in comparison to traditional larger satellite categories [15], nanosatellite missions have been increasing in complexity and applicability over the years as new technology development sectors become interested in the versatility of this satellite category. These appealing characteristics of nanosatellites are the outcome of decades of refinement and optimisation of major satellite technologies subsequently adapted and effectively miniaturised, in conjunction with the accelerated miniaturisation of consumer electronics seen in recent years. The adoption of mature technology concepts from major satellite platforms is feasible due to the common fundamental physical laws governing any satellite's dynamics [16] and space features. It is thus common to find examples of inherited technologies cascading from larger satellite platforms to smaller platforms as they reach the required scalability and reliability level for the new smaller platform. An example of such gradual implementation of mature space technologies is the attitude gravitational-gradient stabilisation, which was firstly implemented on the 4000kg Gemini 11 mission (1966) and then inherited to several missions such as the 200kg Fast On-Orbit Recording of Transient Events FORTE (1997), and recently on the 4kg Firefly CubeSat mission (2013). Whilst some technologies find direct transfer to small platforms as in the previ-

## Introduction

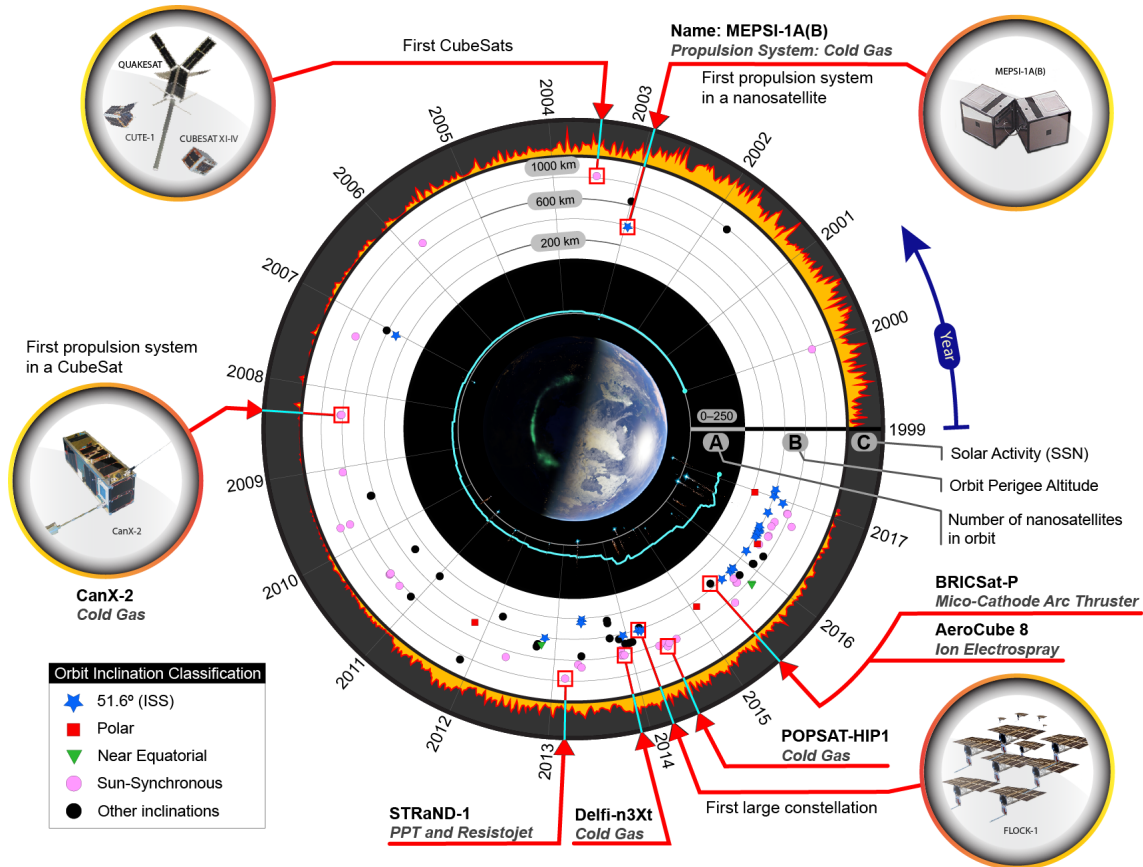


Fig. 1.1 Recent nanosatellites timeline. Illustration compiled with orbital data from 363 nanosatellites. A detailed list of data source missions is reported in Appendix A.

ous example, others present remarkable technical challenges particularly if specialised components miniaturisation and requalification to scale is required. A quintessential case of the intricacies of technology miniaturisation is the propulsion system, which was absent in early instances of nanosatellites [4, 17] and is presently in the process of development and integration. In general, the development of propulsion systems for nanosatellites have centred on providing the CubeSat standard with this service for active fine throttleable attitude control in an early attempt to embed the system for future full range of propulsion applications.

Fig. 1.1 shows the timeline of reported nanosatellite missions to date as well as milestones towards the inclusion of propulsion systems. Initial trades of miniaturised propulsion systems for nanosatellites use inherited cold/warm gas monopropellant technologies, for example the VACCO Micro-Propulsion System [18] (MiPS) on-board

---

of MEPSI-1 A and B and the NANOsatellite Propulsion System (NANOPS) [19] on CanX-2, and more recently the Rocketdyne MPS-130 [20] employing customisable green propellants. These cold/warm gas propulsion systems have the potential to expand the range of mission capabilities by enabling responsive attitude control, station keeping, and de-orbiting capabilities with low power requirements. However, actual typical mass and volume efficiencies of these systems represent a penalty in payload mass fraction. In fact, the potential growth of the nanosatellite platform has been partially deterred by its reduced payload capacity [2]. In a similar way, the utilisation of highly efficient electric propulsion (EP) technologies with high specific impulses ( $I_{sp}$ ), are normally tempered with high power supply mass [21] and power conditioning complexity [22] for the typical nanosatellite mission. Nonetheless technical advancements in on-board power generation and storage as well as in micro electronics have opportunely assisted the refinement and optimisation of adequate scale-down EP technologies. A survey of the current main developers of commercial propulsion systems for nanosatellites shows that high thrust-to-mass ratio propulsion systems [23–26] (e.g. cold gas, hydrazine, chemical) are in the main constrained to the upper mass range of nanosatellites due to system size requirements. In contrast, the low thrust-to-mass ratio EP systems [27–30] (e.g. electrospray, RF ion, pulsed plasma) show higher system size adaptability. Thus, in terms of potential payload mass fraction allowance and propulsion system efficiency, EP systems are appearing to become the prospective standard propulsion systems for nanosatellites as indicated by the current products offering.

In order to illustrate the scenario of EP in nanosatellites, it is worthwhile to discuss the following two CubeSat-based examples. One of the primary objectives of the STRaND-1 mission was to test a pulsed plasma propulsion system (PPT), the first EP on a nanosatellite [31]. Laboratory tests of the PPT module established an average performance of  $0.6 \mu\text{N W}^{-1}$ . Unfortunately, STRaND-1 stopped communications apparently after being affected by a geomagnetic storm [32]. Apart from the relevance of the mission for nanosatellites technological advancement, the mission failure highlights a crucial current general deficiency in radiation shielding in nanosatellites. Commonplace

## Introduction

---

radiation effects in nanosatellites are customarily mitigated with functional redundancies, radiation-hardened electronics if accessible, and paramountly operation in Low Earth Orbits (LEO). Besides the appealing potential of nanosatellites in LEO for Earth observation and the relative radiation protection of low LEO, these orbits are greatly penalised by atmospheric drag prompting rapid orbital decay. For these reasons, one of the main objectives of propulsion systems on nanosatellites is that of extending mission lifespan by offsetting atmospheric drag. The more recent EP system demonstrated on the AeroCube 8, the Scalable ion Electrospray Propulsion System [33](S-iEPS), reported a laboratory performance of  $49.3 \mu\text{N W}^{-1}$  setting a new milestone in nanosatellites development. Overall, nanosatellite compatible EP technologies encompass electrostatic and electromagnetic thruster concepts such as Electrospray (Colloid [34] and Field Emission Electric Propulsion FEEP [35]) and Pulsed Plasma Thrusters (PPT) [36] respectively.

Low thrust levels in the order of few tens of micro-Newton are typical amongst EP propulsion concepts. Even though current laboratory apparatuses are able to resolve low thrust levels as for example the nano-Newton Thrust Stand (nNTS) [37], in-orbit operations are fundamental to the integral characterisation of emerging EP systems [38] because outer space represents a irreproducible operational environment. In-orbit satellite operational features ( e.g. eclipse thermal excursions, residual dipole, etc.) and low thrust levels in conjunction with the irreproducible space environment interaction (e.g. spacecraft charging, thermospheric species surface absorption, electric plume interaction, etc.) place a unique and challenging set of conditions for effective propulsion system characterisation.

Attitude determination technologies for nanosatellites are currently able to resolve to some extent low thrust levels for in-orbit thrust characterisation via attitude manoeuvres [31, 39] and proximity operations [40]. Typical examples of attitude determination technologies are star trackers, Earth sensors, Sun sensors, and gyroscopes. A relevant example of EP characterisation on nanosatellites is the AeroCube 8 [41], wherein bespoke specialised attitude sensors are used to resolve low thrust actuation. Although some attitude sensing and determination technologies are readily available from commercial

---

providers [42] and may provide acceptable attitude determination during thrust characterisation in standard nanosatellite missions, the total cost in terms of spacecraft outlay, volume, and power consumption for most of these technologies exceeds the resources of the average nanosatellite mission. For this reason it is common to find chiefly accessible Commercial Off-The-Shelf (COTS) elements (non radiation-hardened) such as MicroElectroMechanical Systems (MEMS) constituting the basic inertial measurement unit in standard nanosatellites.

Successful characterisation of propulsion systems in nanosatellites ensure its efficacious application in orbital manoeuvring and maintenance, and attitude control. A handy example of practical implementation of EP on-board of a satellite comes from the ESA's Gravity field and steady-state Ocean Circulation Explorer (GOCE [43]), in circular orbit at 260km from March 2009 to October 2013. Empirical evidence of the operation of EP in GOCE, highlights the importance of spacecraft-atmosphere interaction and the existing relationship to the propulsion control scheme and its optimisation. In GOCE, exceptionally low and almost constant solar activity, illustrated in the outermost ring in Fig. 1.1, reduced the intensity of atmospheric gas-surface interactions. The resulting diminished atmospheric drag led to propellant saving that in turn permitted the extension of the mission for more than two years, doubling the original mission lifetime of 20 months [44]. In terms of atmospheric gas-surface interaction, it is important to bear in mind that surface-area-to-volume ratio is higher as objects scale down because surface area decreases at a slower rate than volume. This fact is fundamental when analysing extensive properties of a surface interaction because it greatly defines its intensity. Hence dynamic interaction of atmospheric species with exposed surfaces is of critical importance for the optimisation of nanosatellite propulsion systems.

Recapitulating the previously discussed panorama, some aspects emerge as key factors for the development and utilisation of propulsion systems in nanosatellites. Firstly, it is fundamental to develop effective in-orbit propulsion characterisation methods for EP on standard nanosatellite missions; primarily enabling adequate in-orbit low thrust characterisation by employing COTS technologies, being that nanosatellite mission

trends are based on COTS attitude sensors due to their general accessibility. Secondly, atmospheric interaction with nanosatellite surfaces has a pivotal role in orbit lifespan definition, which in turn defines the required characteristics of an atmospheric drag-dealing propulsion system; thirdly, aiming at the maximum optimisation of on-board propulsion resources it is fundamental to improve space weather forecast methods due to the remarkable vulnerability of nanosatellites in LEO to atmospheric drag.

### 1.1 Problem Statement

Propulsion technologies for nanosatellite systems aim at active orbit and attitude dynamics control for enhanced missions performance and operational return. From the engineering point of view, propulsion technology design and selection processes are chiefly based on safety regulations compliance, mission requirements, technological readiness, and technical know-how. The propulsion system (PS) of the specific mission is critically dependent on mission characteristics such as target operational lifetime, propulsion function, available power resources, and mass fraction profile. Typically propulsion system development is a tailored process, however component standardisation in nanosatellites is encouraging the development of commercial modular systems capable of fulfilling varied mission characteristics. The availability of such commercial systems is gradually enabling the incorporation of propulsion capabilities on-board a higher number of nanosatellite missions. In tailored as in commercial PS, the ultimate system performance in achieving mission goals is dictated by the PS-nanosatellite integration and mission characteristics. The diagram in Fig. 1.2 illustrates the aforementioned dependencies.

Based on the supporting evidence briefly discussed in this chapter, this thesis sets out to obtain convenient analytic tools to enhance *propulsion system service* for the standard nanosatellite. To attain this objective, the investigation will look into the development of comprehensive methodologies to express key factors influencing propulsion system operation in nanosatellites analytically. The investigation is assisted by high

resolution numerical models and observed data, which in conjunction provide iterative feedback for models validation and opportune identification of relevant phenomena. The development of analytic tools targeting improved in-orbit PS characterisation and atmospheric perturbation definition, will assist the enhancement of PS service in standard nanosatellites; this implies on-board resources optimisation, benefiting the payload mass fraction allowance and profitability upgrade of nanosatellites. Specifically, analytic models for standard nanosatellite-atmosphere interaction, forecasts of solar activity as a proxy for atmospheric state definition, and attitude dynamics under low thrust actuation are proposed. These investigation objectives are elemental constituents of propulsion technologies service evaluation as shown by the Mission Characteristics and PS-Nanosatellite Characteristics blocks in Fig. 1.2. The choice and interlinkage of the topics in the thesis are detailed in chapter 3, after the nanosatellites overview presented in the following chapter 2.

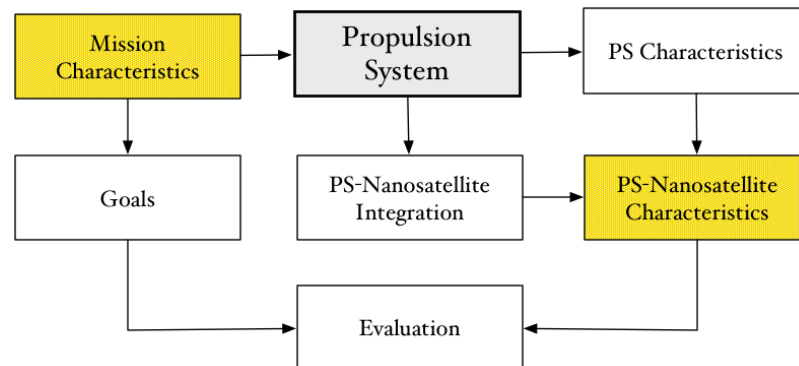


Fig. 1.2 Propulsion system evaluation

Blank page

# Chapter 2

## Nanosatellites Overview

Since the launch of the first CubeSats in 2003, accelerated growth of nanosatellite missions has been greatly sustained by the advent of the CubeSat platform as shown in Fig. 2.1. For 2017 the number of projected nanosatellite missions exceeded 280 of which 98% are CubeSats<sup>1</sup>, gradually prompting new launch opportunities and diversifying mission objectives. The roadmap to the incorporation of propulsion systems on nanosatellites is demarcated by identifiable factors intrinsic to this category of satellite. Apart from the miniaturisation design challenges to overcome for the particular nanosatellite mission, the launch method and orbit and space environment characteristics are of general interest.

This chapter presents a survey of the present panorama for the development and application of propulsion technologies for nanosatellite systems. Acknowledging the preponderant role of the CubeSat platform on the actual development of the nanosatellite category, the analysis is centred on CubeSats. However, analyses can be extrapolated to the Generic Nanosatellite Bus (GNB) platform [45] since its standardised quality allows for general similar assumptions. This chapter is subdivided into three main sections emphasising typical characteristics of nanosatellite missions and extrinsic factors leading the development of onboard propulsion systems. Section one presents a synopsis of propulsion system alternatives for nanosatellites, and the techniques

---

<sup>1</sup>Detailed lists of historical and projected nanosatellite missions are presented in the Appendixes A and B

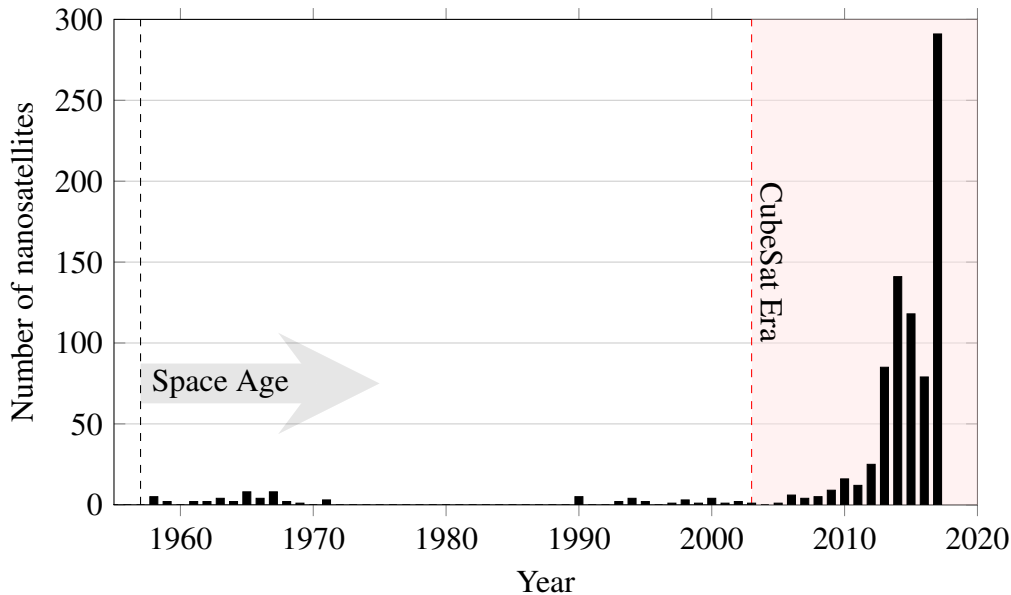


Fig. 2.1 Nanosatellites launch history. Plot compiled with data from DePasquale and Charania [9], Doncaster et al. [2], Krebs [46], eoPortal Directory [47], and from Kulu [48] for the year 2017.

used in their attributes definition. Section two discusses the impact of available orbit insertion opportunities on characteristic nanosatellite Earth orbit features, nanosatellites survivability challenges, and orbital perturbations dominating mission operations. Section three discusses the plausible solar input power to endow mission operativeness in characteristic Earth orbits.

## 2.1 Propulsion Systems for Nanosatellites

Propulsion can be defined as the action of changing the motion of a body through the operation of a locomoting force. In satellites, this force can be directly generated using environment resources, e.g. solar sails, or ejecting onboard stored propellant, e.g. gas thruster. Ongoing research on solar sails and its application on nanosatellites [49] (e.g. NanoSail-D, LightSail, InflateSail) will help to explore compelling future mission objectives such as propellantless deorbit (< 700km), non-Keplerian Earth orbits, and interplanetary transfers. At present, however, propellant-based propulsion systems are widely used due to their high technological maturity, versatility and level

of autonomy at all satellite sizes. Therefore, this investigation is focused on propellant-based propulsion systems because the aim is to provide comprehensive analyses as discussed in Chapter 1.

In nanosatellites, propulsion systems aim to provide the ability of attitude and orbit manoeuvrability. Propulsion system performance requirements are in general preconditioned in nanosatellites chiefly due to the current state of development of miniaturised technologies, ancillary key components (e.g. valves, power processing units), and concerns related to the launch method as discussed in Section 2.3. In order to assist subsequent discussions about the quality and performance of propulsion technologies on nanosatellites, it is convenient to revisit some fundamental concepts of rocket propulsion. The following descriptions use the Navier-Stokes equations [50] in an inertial reference system moving at the instantaneous rocket velocity.

Firstly, the integral form of the mass conservation equation can be used to describe the mass rate of change within the control volume ( $CV$ ) and the transport of mass (propellant) across an exit surface ( $A_e$ ) with velocity  $\vec{u}$ . Assuming that all other existing control surface boundaries are impermeable, the mass conservation can be modelled through Eq. (2.1).

$$\frac{\partial}{\partial t} \int_{CV} \rho \, dV + \int_{A_e} \rho \vec{u} \cdot \hat{n} \, dA = 0 \quad (2.1)$$

A handy approximation in 1D of Eq. (2.1), is given by Eq. (2.2). It describes the mass balance of the hypothetical propellant flow rate ( $\dot{m}$ ) and the instantaneous rate of change of the rocket mass ( $M$ ).

$$\frac{dM}{dt} + \dot{m} = 0 \quad (2.2)$$

The conservation of momentum on the  $CV$  in a free rocket, i.e. no external forces acting on  $CV$ , yield Eq. (2.3) that describes the force balance on the free rocket. The total force in this case is given by the momentum and pressure<sup>2</sup> thrust provided by the exhausted

---

<sup>2</sup>Caused by the relative propellant  $p$  and ambient  $p_a$  pressure

propellant.

$$\frac{\partial}{\partial t} \int_{CV} \rho \vec{v} \, dV - \left[ \int_{Ae} \rho \vec{u} (\vec{u} \cdot \hat{n}) \, dA + \int_{Ae} (p - p_a) \hat{n} \, dA \right] = 0 \quad (2.3)$$

In 1D approximation, Eq. (2.3) is simplified to Eq. (2.4) describing the instantaneous propellant mass flow rate moving at the effective exhaust speed  $u_{et}$ , which in turn produce thrust on the rocket.

$$\frac{d}{dt} (Mv) = \dot{m}u_{et} \quad \Big| \quad u_{et} = u_e + \frac{(p_e - p_a)A_e}{\dot{m}} \quad (2.4)$$

Eq. (2.4) can be conveniently written as in Eq. (2.5). It is important to notice that the equations described so far, are valid for infinitesimal time intervals. This characteristic acquires relevance when these mathematical concepts are applied to practical phenomena. For example, one important observable effect of the exhaust stream is the change in speed it causes on the rocket ( $\Delta v$ ). Substituting Eq. (2.2) in Eq. (2.5) and solving for the rocket change in velocity yields Eq. (2.6).

$$M \frac{dv}{dt} = T = \dot{m}u_{et} \quad (2.5)$$

Eq. (2.6) can be solved if the effective exhaust velocity dependency on  $M$  is known, or if  $u_{et}$  is constant in such case reducing to the simplest form so called Tsiolkowsky equation.

$$\Delta v = - \int_{M_i}^{M_f} u_{et} \frac{dM}{M} \xrightarrow{\frac{du_{et}}{dM}=0} u_{et} \ln \frac{M_i}{M_f} \quad (2.6)$$

The effective exhaust velocity is a function of the commonly observable quantities  $T$  and  $\dot{m}$ . Moreover, from the instant relationship of  $u_{et}$ ,  $T$ , and  $\dot{m}$  in Eq. (2.5),  $u_{et}$  can be expressed as the ratio of impulse and propellant mass as shown by Eq. (2.7).

$$u_{et} = \frac{T}{\dot{m}} \frac{dt}{dt} \quad (2.7)$$

This new form in Eq. (2.7) provides the means of a practical use of the theory discussed so far because the  $u_{et}$  value can be averaged over a period of time  $t$  as shown in Eq. (2.8). If  $T$  and  $\dot{m}$  can be assumed as constants over the analysed time, then it is possible to take the equality in Eq. (2.9) as true.

$$\bar{u}_{et} = \frac{\int_0^t T dt}{\int_0^{t_p} \dot{m} dt} \quad (2.8)$$

$$\bar{u}_{et} = u_{et} \quad (2.9)$$

Another important parameter is the specific impulse. The specific impulse ( $I_{sp}$ ) is universally employed to technically specify propellant usage efficiency of a rocket. The instantaneous specific impulse in Eq. (2.10) [21] is the ratio of the impulse and the propellant weight.

$$I_{sp} = \frac{T dt}{g_0 \dot{m} dt} \quad (2.10)$$

As with the effective exhaust velocity, an average equation is of more practical value. Using Eq. (2.11) to show the explicit dependance of  $I_{sp}$  on  $M$ , viz.  $I_{sp}$  is just an artefact of Eq. (2.6), an adequate equation to estimate the average specific impulse due to mass consumption is given by Eq. (2.12)

$$I_{sp} = \frac{T}{g_0 \dot{m}} \frac{dM}{M} \frac{M}{dM} \quad (2.11)$$

$$\bar{I}_{sp} = \frac{\int_{M_i}^{M_f} \frac{T}{g_0 \dot{m}} \frac{dM}{M}}{\int_{M_i}^{M_f} \frac{dM}{M}} \quad (2.12)$$

If  $T$  and  $\dot{m}$  are constant, then the average and instantaneous  $I_{sp}$  can be assumed equivalent as in Eq. (2.13)

$$\bar{I}_{sp} = I_{sp} = \frac{T}{g_0 \dot{m}} \quad (2.13)$$

## Nanosatellites Overview

---

The foregoing definitions describe the rocket dynamics caused by expelled propellant. The movement of propellant can be originated by pressure differences, as explicitly shown in Eq. (2.4), or implicitly by other sources of energy. However the momentum component usually dominates the total thrust, i.e.  $u_{et} \approx u_e$  in Eq. (2.4), whose energy may come from different sources. Historically, the propellant energy source in space applications comes from chemical reactions, or thermal or electrical interactions. With the exception of systems dependent on electrical energy for propellant acceleration, the source of energy is an essential feature of the propellant. This means that a rocket is only required to guide the natural processes taking place to effectively transform that energy into kinetic energy. In principle this implies a reduced number of basic rocket elements to produce useful thrust. On the other hand, rockets using electric energy require extra components for electric power storage and administration.

The mass of the electric power supply in electric rockets,  $m_{\frac{1}{2}}$ , is typically assumed as proportional to the required power for propulsion  $P$ . The constant of proportionality in this case is the power supply specific mass  $\kappa$ .

$$m_{\frac{1}{2}} = \kappa P \quad (2.14)$$

The power required for electric propulsion is related to the conversion efficiency of the rocket, namely *thrust efficiency*, in the following way. Assuming that the combustion and exhaust thermal power are negligible in an adiabatic free rocket, the exhaust mechanical power is given by Eq. (2.15)<sup>3</sup>

$$P_e = \frac{1}{2} \int_{Ae} (\rho \vec{u} \cdot \hat{n}) (\vec{u} \cdot \vec{u}) dA \quad (2.15)$$

Which can be further simplified in 1D to Eq. (2.16)

$$P_e = \frac{\dot{m} u_e^2}{2} = \frac{T u_e}{2} \quad (2.16)$$

---

<sup>3</sup>From the RHS second term in Eq.2.13 in [50].

The thrust efficiency ( $\eta$ ) is then given by Eq. (2.17)[51]. Note that the thrust efficiency is a proportional strong function of  $u_e$ .

$$\eta = \frac{P_e}{P} = \frac{\dot{m}u_e^2}{2P} = \frac{Tu_e}{2P} \quad (2.17)$$

By solving Eq. (2.17) for  $P$  and substituting in Eq. (2.14) it is clear that the power supply scales with the square of  $u_e$ .

$$m_{\zeta} = \frac{\kappa \dot{m} u_e^2}{2\eta} \quad (2.18)$$

Finally, the electric propulsion system mass in Eq. (2.19) is given by the power supply mass from Eq. (2.18), and the propellant mass from Eq. (2.10).

$$m_{EPS} = \frac{\kappa g_0 T I_{sp}}{2\eta} + \frac{Tt}{g_0 I_{sp}} \quad (2.19)$$

The plot of Eq. (2.19) for variable  $I_{sp}$  in Fig. 2.2, shows that there exists an optimum value to reduce the overall mass of the electric propulsion system. Additionally, the optimum operation point highlights the importance of  $\kappa$  and  $\eta$  as design factors. In practice,

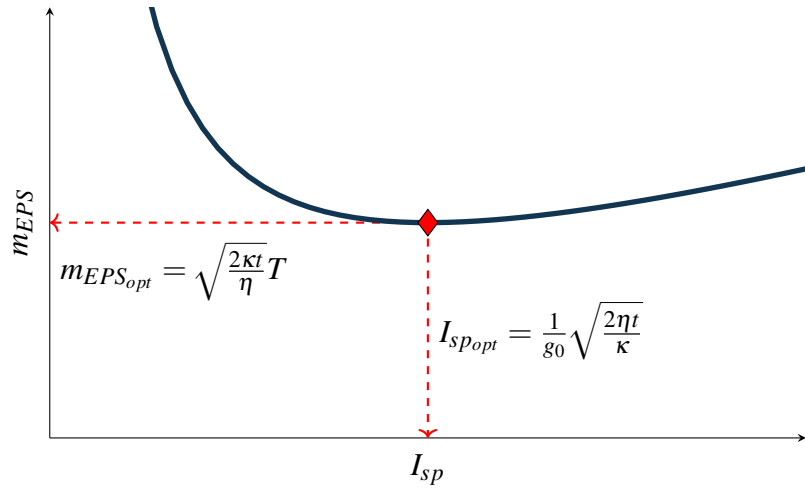


Fig. 2.2 Electric propulsion system mass as function of specific impulse. The minimum mass point for electric propulsion systems Eq. (2.19) is identified in the plot.

the rocket parameters described above are customarily used to report characteristics of thrusters and propulsion systems. Because onboard resources optimisation is a critical

goal in nanosatellites design, the values of  $I_{sp}$  and  $\kappa$  acquire special relevance. Fig. 2.3 summarises the state-of-the-art of the lower limit of miniaturised propulsion systems for nanosatellites. Several aspects of current technologies and level of miniaturisation can be observed from the figure. The value of  $I_{sp}$  is the first parameter of attention in this discussion. High values of  $I_{sp}$  imply an equivalent propellant mass optimisation for a particular thruster design as discussed above. An appropriate classification for discussion is to divide the systems in Fig. 2.3 into two groups according to  $I_{sp}$  and the energy source of the systems. The first group encompasses solely electric propulsion systems due to their large diversity. In this group the power supply mass penalty, Eq. (2.19), is of immediate attention. Although it is difficult to identify the value of  $\kappa$  from available information for the reported systems, it is possible to have a rough estimation of  $\eta$  using the values of thrust, specific impulse, and power demand from Fig. 2.3. It is important to recall that Eq. (2.17) is valid to estimate the thrust efficiency, not the thruster efficiency, however it can still serve as reference for the following discussion.

The electrothermal branch in the figure encompasses the resistojet, the simplest form of electric propulsion. This type of propulsion relies on gas dynamics thermally energised by electricity. The thruster efficiency of the commercial resistojet [27] in the figure is estimated to nearly one percent for the primary built-in thruster. Conversely to this electrothermal system, the commercial colloid system [55] thruster efficiency in the electrostatic branch in the figure, is estimated at about forty five percent. This is the best efficiency observed amongst the surveyed systems and arguably the best in the current market for nanosatellites. High efficiency levels in colloid propulsion systems can be partially explained by unnecessary propellant ionisation required by other electric propulsion concepts, and therefore less effective input power requirement. Further, some system designs may expel positive and negative ions avoiding the use of power consuming neutralisers. Colloid propulsion systems are modular and adequately scalable to fit most nanosatellite mission sizes.

## 2.1 Propulsion Systems for Nanosatellites

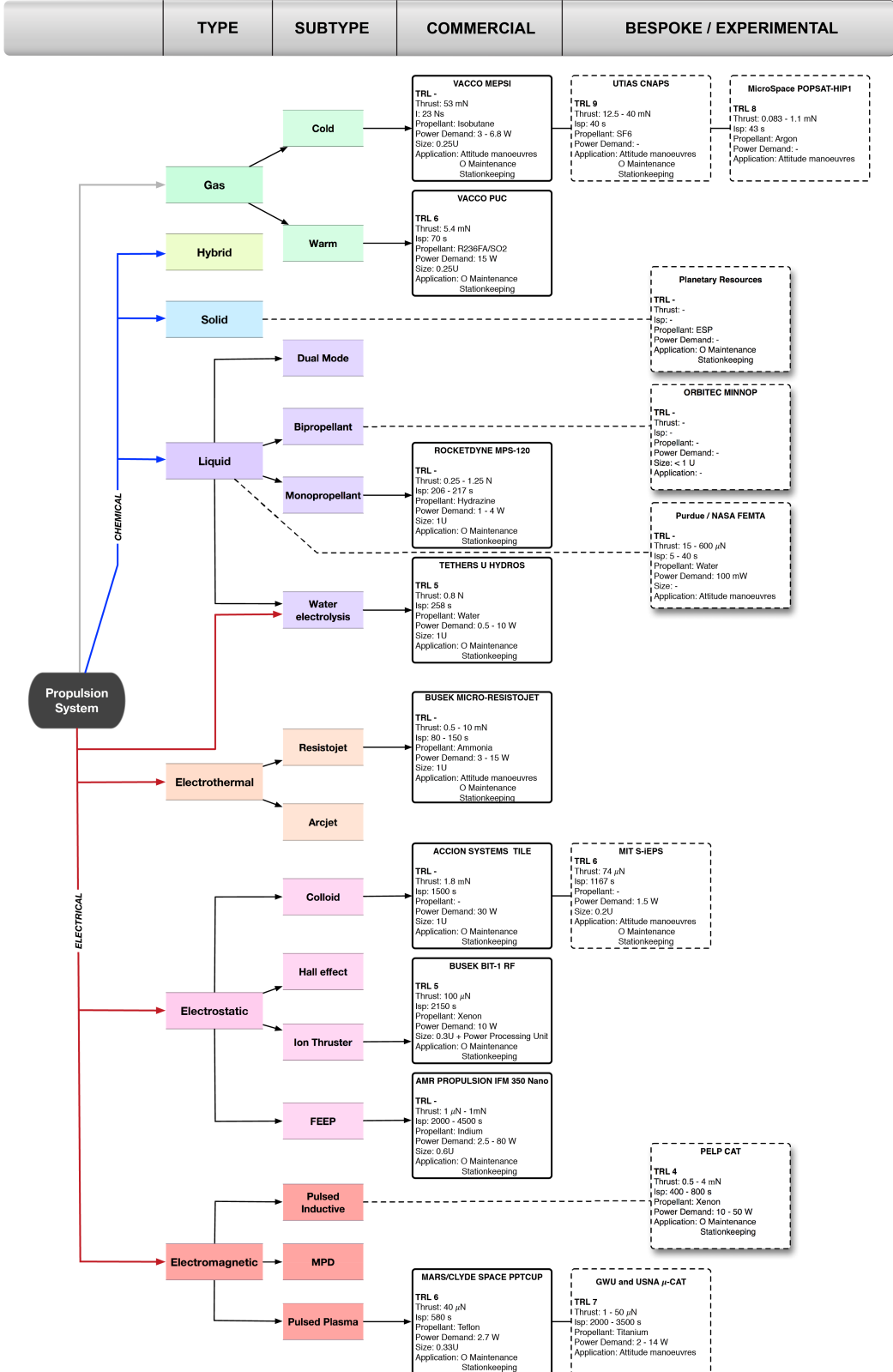


Fig. 2.3 Varieties and operation characteristics of nanosatellite propulsion systems. The selected examples of commercial devices represent the current lower limit of miniaturisation of each type. Shadowed dashed boxes are examples of prototypes, using the systems classification reported by Larson and Wertz [52], and commercial device data from [23, 26, 27, 36, 53–55]. Refer to Appendix F for experimental systems details.

## Nanosatellites Overview

---

The ion thruster in Fig. 2.3, reports higher  $I_{sp}$  than the colloid and resistojet examples. The reported power demand corresponds only to the thruster in this case, which enables a better estimation of the thrust efficiency computed to nearly ten percent. This type of thruster technology has to ionise the propellant to subsequently accelerate it electrostatically, and finally neutralise the resulting ion beam. Although the current ion thruster for nanosatellites is less thrust efficient and less power supply mass efficient than its counterpart in major satellites, its main attractor is that it can use a wide variety of propellants including the solid-storable and highly dense iodine suitable for nanosatellites [27].

The last example of commercial electrostatic propulsion systems in Fig. 2.3, is based on a Field Emission Electric Propulsion (FEEP) thruster. It shows the best maximum attainable propellant efficiency ( $I_{sp} = 4500$  [53]) amongst current commercial systems for nanosatellites. The estimated thruster efficiency is of nearly thirty percent. Another important characteristic of this system, is that it allows a wide dynamic thrust range. However, specifically for propellants based on metals, the thruster plume may deposit electrically conductive material on the surfaces that require special satellite design attention.

The final example of commercial electric propulsion system for nanosatellites in Fig. 2.3 is based on Pulsed Plasma Thrusters. The estimated thruster efficiency is of nearly four percent. PPT has long been used in satellites being the first form of electric propulsion in space. PPT technology in nanosatellites uses ablation of a solid propellant via high voltage discharges. The ablated material plus the high energy of the discharge generates plasma, which establishes a current sheet and a self-generated magnetic field that accelerates the plasma through the Lorentz force. PPT systems are easily scalable, controllable, and require few elements for operation.

In the second group, chemical and thermal propulsion system technologies with extensive flight heritage, are related to the highest thrust levels amongst all the surveyed systems. Interestingly, the theoretical simplicity of these systems is complicated by technological and physical limitations at the required system scale of nanosatellites,

specially in the elements associated to flow control. In addition, propellant energetic and toxicity limitations may further restrict the adequacy of these systems as discussed in Section 2.3. Therefore non-toxic propellants, commonly termed green propellants, are used in nanosatellites although these are generally less energetic than traditional propellants. In spite of these possible drawbacks, this second group of systems is characterised by higher thrust levels than those attainable by the first group.

Recapping the suitability of current commercial propulsion systems to nanosatellites, PPT systems are easily adaptable to the general mission mainly due to their scalability and general simplicity whereas considerable technological advancements place current colloid thruster technology as the most far-reaching system for nanosatellite application. In general, high  $I_{sp}$  in EP implies suitability for long duration propellant-efficient orbit manoeuvres such as atmospheric drag offsetting, whereas low thrust in EP implies adequacy in fine attitude manoeuvres such as target pointing. Chemical and thermal systems on the other hand can enable high impulse manoeuvres at relatively low input system power demand, appealing characteristics for short propulsion lifetime operations like in end of mission deorbit or rapid attitude control manoeuvres such as post-deployment detumbling.

It is necessary to recognise that the reported parameters of the propulsion systems discussed above regard to real devices characterised under laboratory conditions and that most of them have not been flight validated. In actual thruster characterisation, the values of the propellant mass flow rate and input power are commonly well known and controlled. In contrast, the thrust magnitude has to be estimated. Adequate thrust characterisation is fundamental in the development, improvement, and optimization of propulsion technologies, however it is far from being a trivial task. In general, there exists a wide variety of space propulsion technologies developed to meet specific application requirements [56]. The selection of the propulsion system technology is often dictated by the delivered thrust level and working performance under the objective mission and environmental conditions. Thus, a method to correlate thrust level and input parameters, to identify performance dependency on external factors with sufficient

precision, is required for optimal employment of any kind of propulsion system. Thrust characterisation is an arduous task that commonly involves the identification of the thrust vector, beam or jet divergence, plume structure, transient and steady-state responses, vibration modes, thermal ranges, electrostatic charging, ambient effects, and supply dependencies amongst other factors. The role of relevant parameters involved in the thruster performance can be estimated by using direct thrust measurements or by assessing features associated to the thrust. However, whenever possible, direct thrust measurement is universally preferred [57, 58]. Various characterisation methods have been devised in line with the thrust level of the systems. Whilst some aspects of high levels of thrust are easily measured, low thrust features are often barely noticeable even for high accuracy state-of-the-art measuring apparatuses. Thrust characterisation under laboratory conditions is commonly carried out using static test rigs, pendulum balances, torsion balances, and time-of-flight mass spectrometry [59–61]. Additionally propulsion system characterisation tests for in-space operation are generally performed in vacuum environment adding complexity to the tests design, qualification, and implementation.

Reduced dynamic noise generation and fine throttle control capability in the range of mN to  $\mu$ N [60, 62] are frequently considered to be of paramount importance in satellite propulsion system requirements. These considerations clearly reduce the margin of possible laboratory test conditions to a few constringent scenarios. In some cases, higher vacuum level requirements as well as propellant reactivity concerns add to the complexity of the characterisation [62]. For propulsion systems in the order of  $\mu$ N, the characterisation can be particularly difficult because factors such as the weight of the thruster, stiffness of the feed and supply elements, ambient noise, thermal deformation, electrostatic and electromagnetic forces, and vacuum pump vibrations, are generally of higher magnitude than the thrust level itself overwhelming its action [57, 62, 63]. Another relevant aspect of these sort of laboratory tests is that in the absence of a dominant damping medium, primarily air, the start-up transient responses are long lasting. Despite all the above, current gauging technologies are able to resolve thrust values of few tens of nN for specific thruster characteristics [37].

Recalling the simplifications and assumptions used in the derivation of the standard formulae, e.g. free rocket and 1D reduction, it might be argued that these still hold under laboratory conditions providing an adequate analytic framework for the evaluation of the average thruster operation. However, important aspects of the ultimate operational environment (outer space) for satellite propulsion systems, have not been successfully reproduced in laboratory conditions. During the derivation of the standard formulae, specially in the conservation of momentum Eq. (2.3), neglected factors such as system rotation, aerodynamic and viscous forces (atmospheric drag) may be pivotal in outer space operation. Additionally, the characteristic progressive or regressive thrust profile of some chemical and thermal thrusters may add uncertainties to the extended validity of the laboratory characterisation specifically in weak thruster actuation with respect to other occurring perturbations. This makes supplementing laboratory data with in-orbit characterisation specially for low-thrust systems appropriate [64].

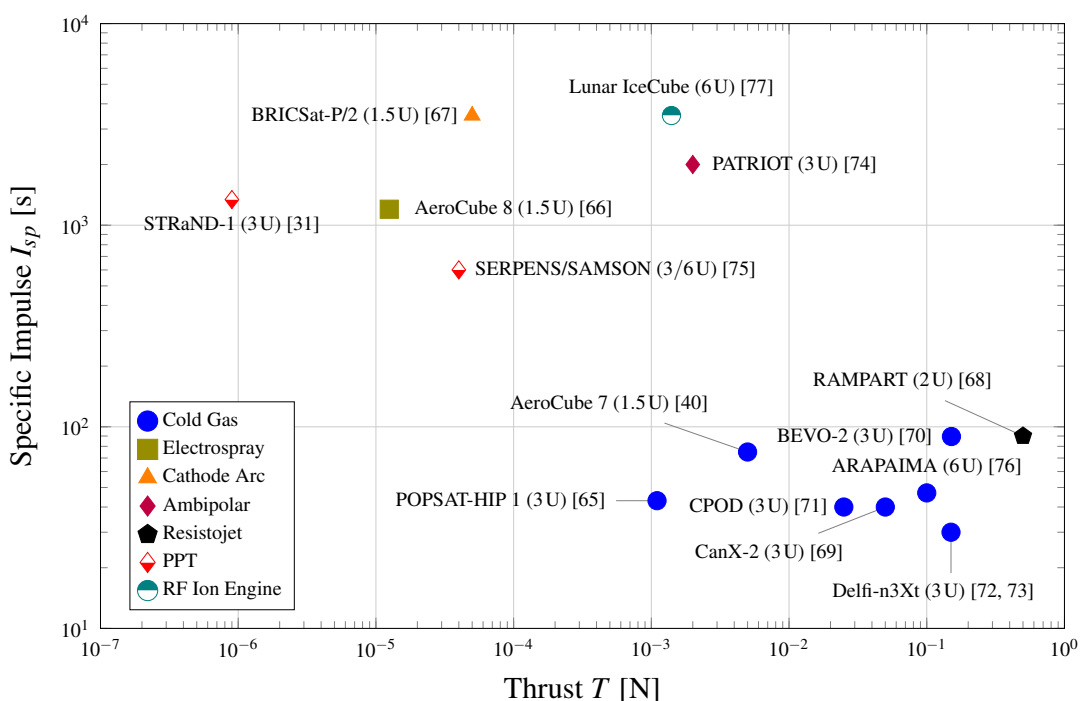


Fig. 2.4 Log-log plot of reported propulsion systems in CubeSats for various size factors (inside the parentheses) thus far. The value of  $I_{sp}$  is proportional to the efficiency of propellant mass consumption in the production of thrust for a given propulsion system. Propulsion systems details are reported in Appendix F.

In-orbit propulsion systems characterisation in nanosatellites has been mainly implemented and planned in CubeSats representing the current frontier of propulsion miniaturisation in space applications. The capabilities of the miniaturised propulsion systems range from tenths of N to few  $\mu\text{N}$  as illustrated in Fig. 2.4 for various CubeSats missions. Current attitude determination technologies for CubeSats allow in-orbit thrust characterisation in most operational ranges mostly through attitude changes like target pointing, tumbling-detumbling, and bang-bang manoeuvres [39, 64, 72]. Available sensing technologies may include Sun sensors, Earth horizon sensors, MEMS accelerometers, MEMS gyroscopes, magnetometers, star trackers, or even synergic attitude determination in formation flying [40], yet thrust levels in the order of few  $\mu\text{N}$  require sensor technologies not fully compatible in terms of size and power requirements to the average CubeSat mission.

Propulsion system in-orbit characterisation and operation relies completely upon onboard sensors and actuators constituting the Attitude Determination and Control System (ADCS). The ADCS in standard nanosatellites is constituted mostly by combinations of components that altogether endow propulsion systems with various levels of test and applicability potential. The following section 2.2 presents a survey of the ADCSs reported in historic nanosatellite missions to identify the characteristics of current systems.

## 2.2 ADCS in Nanosatellites

The knowledge and management of nanosatellite orientation is fundamental for propulsion system operation. The essential characteristics of the ADCS are a function of the existing environment disturbances acting upon the spacecraft, and the required quality of orientation measurements to fulfil specific mission goals. The ADCS functionality typically consists in measuring the spacecraft attitude to perform closed-loop controlled attitude corrections through the action of actuators as shown in the scheme in Fig. 2.5. Attitude closed-loop control involves tailored control laws to meet objectives of the

specific mission. In this regard and in the framework of this thesis, a simplistic and generic open loop system is preferred (in Chapter 6), i.e. controlled thrust level and firing time.

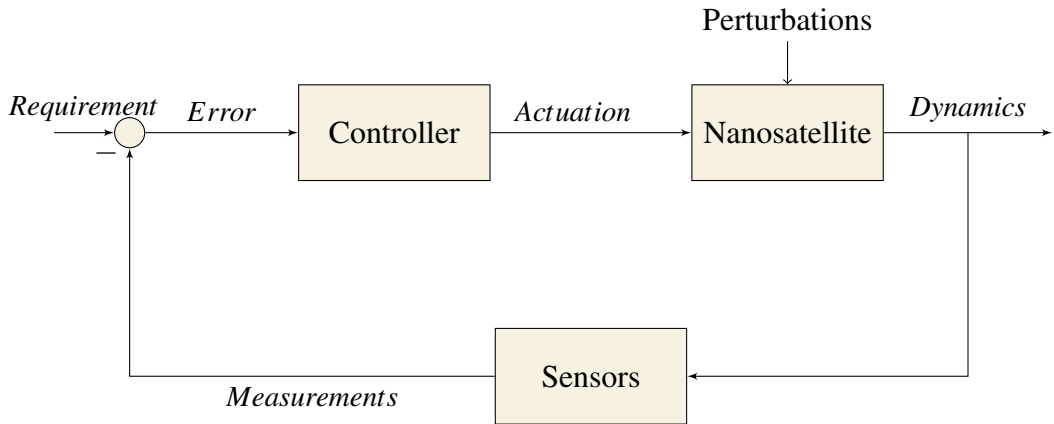


Fig. 2.5 ADCS Scheme for typical closed-loop attitude control [78].

### 2.2.1 Attitude Determination

In terms of propulsion system operation in nanosatellites, acceptable attitude determination is of central importance for system characterisation through in-orbit attitude manoeuvres such as detumbling, target pointing (Sun, Nadir, etc.), and controlled spin. A survey of available attitude determination approaches in nanosatellites from randomly selected historical nanosatellite missions is shown Fig. 2.6. For the sake of homogeneity, the selected nanosatellites are approximated to standard CubeSat form factors (when necessary) and sensors with similar characteristics are grouped into eight representative classifications. Fine and coarse sensors measuring the Sun vector (2-axis) may include specialised or COTS elements. Some missions like the surveyed Colony-1 and GeneSat-1, use the solar panels power input for coarse solar vector estimations. The second group includes missions using the stars as reference frame (2-axis). This group encompasses high-end missions like the RAVAN, MinXSS, Aalto-1, STARE, AeroCube 7-OCSD, CADRE, and SENSE. The third group uses the Earth shape as reference (2-axis) mostly in the form of horizon sensors (in configurations of COTS IR pyroelectric sensors).

## Nanosatellites Overview

---

This group include missions like the DICE, Drag-free CubeSat, GOMX-3, AeroCube-3, AeroCube-4, CUTE-1.7+APD-2, and AeroCube 7-OCSD. The Earth's magnetic field is amply used for 3-axis attitude determination in all nanosatellite size factors as shown in the fourth group in Fig. 2.6. In this case, magnetometers mostly in the form of COTS elements, provide local magnetic field measurements that are compared to onboard reference Earth magnetic field models, e.g. the International Geomagnetic Reference Field (IGRF) or the World Magnetic Model (WMM), to estimate spacecraft attitude. Although the space environment produces fluctuations in the Earth's magnetic field, which increase with altitude, available models capture most of its characteristics in low LEO enabling reliable coarse estimations within short time arcs. Nanosatellites have

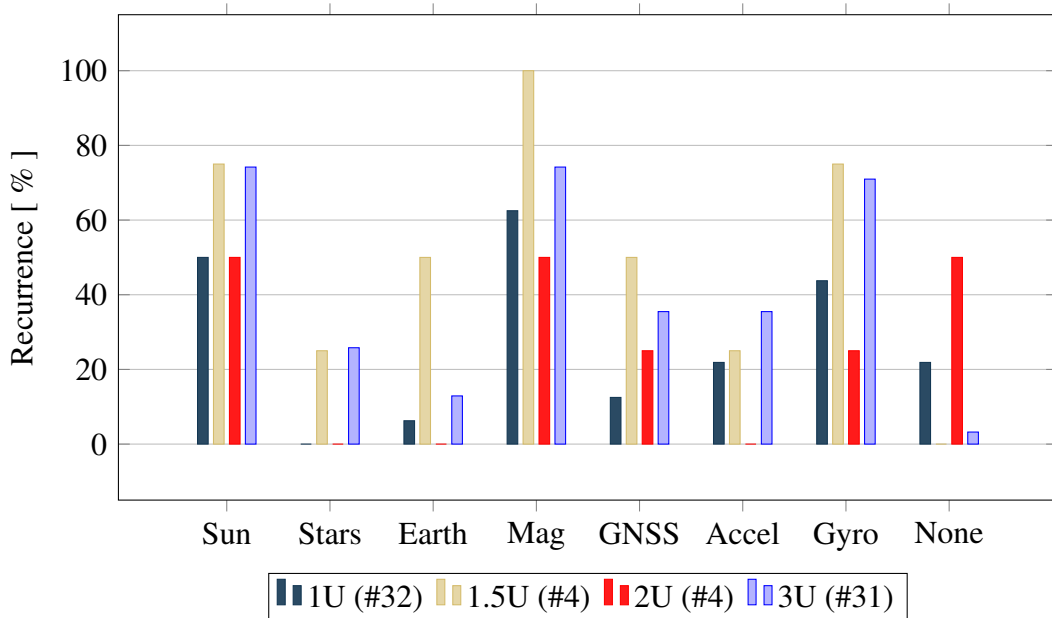


Fig. 2.6 Resources for attitude determination from a sample of 71 historical nanosatellite missions selected upon data availability under the CubeSat standard only. The surveyed number of each size factor is reported in parentheses.

greatly benefitted from the development, optimisation, and miniaturisation of Global Navigation Satellite System (GNSS) receivers from the electronics consumer market. COTS GNSS receivers assist enhanced attitude estimations by providing superior spatial identification to complement star map and Earth magnetic models. Although in some cases the nanosatellite location continues to be estimated by onboard orbit propa-

gations, the use of GNSS receivers is gradually implemented in all nanosatellite sizes. In a similar way to GNSS technologies, MicroElectroMechanical Systems (MEMS) are in constant improvement to meet the electronics consumer market demand. The basic Inertial Measurement Unit (IMU) in standard nanosatellites is composed of COTS MEMS accelerometers and gyroscopes providing a simple and low-cost solution for attitude variation identification. However, intrinsic fluctuations within the fundamental device operation gradually add measurement errors, namely bias or drift instability, which need correction. Eventual device calibration, i.e. zeroing, normally suffice to mitigate this fact. In spite of this, MEMS gyroscopes provide the current best short-term reference for 3-axis attitude determination in nanosatellites. In practice each group shown in Fig. 2.6 may contribute to form an integral estimation of spacecraft attitude. Raw data from a variety of different sensors can be combined, e.g. using Kalman filtering, to furnish improved attitude estimations.

### **2.2.2 Attitude Stabilisation**

Current miniaturised propulsion systems for nanosatellites consist of a single fixed thruster or a fixed array of thrust units due to the complexity and reliability concerns of miniaturised mechanisms for thrust vector control. Differential throttling is thus common amongst nanosatellites implementing propulsion system concepts for attitude control. Depending on the characteristics and requirements of the nanosatellite such as size, available power, mass distribution, manoeuvring time, etc., there exists other attitude stabilisation resources that in conjunction to propulsion systems may extend the manoeuvring capabilities. For example, EP systems aiming orbit operations would require assistance from other attitude stabilisation methods to achieve adequate thrust vectoring.

In Fig. 2.7 is presented a survey of common attitude stabilisation methods and technologies used in nanosatellites. Analogous to the selection criteria and classification discussed in the previous subsection, the groups represented in this case are magnetic

## Nanosatellites Overview

---

torquers (MTQ), reaction wheels (RW), momentum wheels (MW), Passive Magnetic Attitude Control (PMAC), Gravity gradient stabilisation ( $\nabla G$ ), aerodynamic control (ADyn), and spin stabilisation.

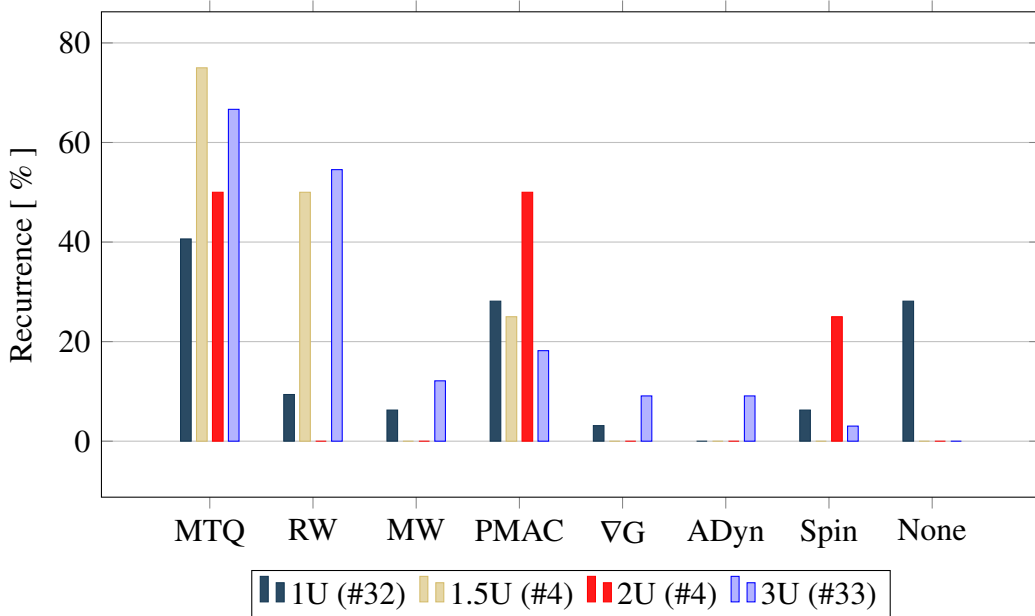


Fig. 2.7 Resources for attitude stabilisation from a sample of 73 historical nanosatellite missions selected upon data availability under the CubeSat standard only. The surveyed number of each size factor is reported in parentheses.

A magnetic torquer is a solenoid used to generate a dipole moment. The controlled dipole establish a restoring torque that aligns itself to the local external magnetic field. The strong Earth magnetic field in low LEO facilitate coarse attitude control using magnetic torquers in a simple and reliable way. In the next group, reaction and momentum wheels create body torques by varying the angular momentum vector of a fixed assembly of spinning masses. The survey shows that most systems employ three spinning masses aligned to the three body axis to provide three axis control such as in Aalto-1, AeroCube 7-OCSD, and CADRE, or four kinematically redundant systems (pyramid formation) such as in SwampSat, Prometheus CubeSat, SENSE, in conjunction to magnetic torquers for momentum damping (saturation).

PMAC consists of a permanent magnet and, in most cases, an hysteretic material to damp body kinetic energy. This simple and compact attitude control system provides

coarse alignment to the local magnetic field, which is preferred by small form factors as shown in Fig. 2.7. Although PMAC system is commonly used alone, it can be combined with other stabilisation methods to enhance its operation as in the UKube-1 wherein magnetic torquers were added (Active Magnetic Attitude Control).

In gravity gradient stabilisation, the Earth gravity field establishes coarse restoring torques on the nanosatellite according to its moments of inertia distribution. Gravity gradient stabilisation is used alone in missions such as UniCubeSat-GG, Firefly, and Aalto-1 in its deorbit electrostatic plasma brake, or in combination with a reaction wheel in Ho'oponopono and ExoCube for yaw stabilisation. PMAC and  $\nabla G$  stabilisation systems are discussed in more detail in Chapter 5. In the next group in Fig. 2.7, control surfaces are used in the low LEO missions Colony-1 (300 km) and MicroMAS (400 km), the so-called Space Dart configuration, where aerodynamic torques furnish coarse velocity-vector pointing. A similar approach is proposed in the ZACUBE-2 CubeSat (planned at 600 km). Finally, spin stabilisation is used in CXBN and OPUSat for Sun pointing, in both cases magnetic torquers are used for activation.

The ADCS in nanosatellites offers crucial capabilities for propulsion systems operation. The characteristics of the ADCS are in turn strongly dependent to space environment as discussed in the following section.

## **2.3 Typical Nanosatellite Mission Characteristics**

Distinctive features of the average nanosatellite mission such as launch time, orbit parameters and manufacture materials have been notably regulated by available launch opportunities. This marked dependency is a consequence of the high cost of a dedicated mission using traditional launch vehicles designed for larger payloads. In this way, most nanosatellite mission launches are carried out as secondary payloads wherein the primary payload assigns most of the orbital characteristics. A clear effect of launch opportunity dependency on historical nanosatellite missions is observed during the year 2016 in Fig. 2.1 where launch delays impacted the total number of deployed

## Nanosatellites Overview

---

nanosatellite missions [2]. The backlog of nanosatellite launches in 2016 and postponed to 2017 explains part of the unprecedented number of projected missions for the year 2017.

Launch primary payload requirements have restricted nanosatellite missions to major launch sites as shown in Fig. 2.8. However the future viability of traditional launch methods for the growing nanosatellite demand is questionable. The major challenge in this respect is to provide sufficient future launch opportunities at affordable prices. The concept of specialised launch vehicles for nanosatellite missions is highly desirable because it allows tailored space access, enabling more flexibility for onboard experimental components and systems such as propulsion elements otherwise banned or highly restricted as secondary payloads. In addition, current range safety costs, launch site facilities, personnel, mission assurance and other miscellaneous costs can be further reduced using specialised launch methods. Ongoing efforts to tackle current deficiencies are mainly focused on the development of specialised launchers. Some examples are the JAXA's SS-52-4 nanosatellite launcher launched from KSCUT in Fig. 2.8, the Rocket Lab's Electron from the recently opened and apposite for nanosatellites MRLLS, the Virgin Galactic's LauncherOne from MHV, and the Generation Orbit Launch Services' GOLauncher-2 from Cecil Field Airport, Florida. The latest two examples, being air-launched, are instances of cost reduction strategies by cutting range safety expenses.

From the analysis of historical nanosatellites orbital data in Fig. 2.9, in the form of Two-Line Element sets in this example, identifiable aspects emerge amongst missions. The majority of missions appear agglomerated around Sun-synchronous orbits ranging 450 – 650 km in altitude and around the track of the ISS. The cluster within the ISS track shown in Fig. 2.9 comprise predominantly nanosatellite constellations like the Flock-1b, Lemur-2, and varied missions under the QB50 initiative. Nanosatellite missions in the ISS cluster use the CubeSat platform and are deployed from the NanoRacks CubeSat Deployer onboard of the ISS and from the ISS resupply Cygnus vehicles, all in launch rideshare category. This method provides recurrent launch opportunities for the particular set of orbital parameters shown in Fig. 2.9. The other major group of nanosatellite

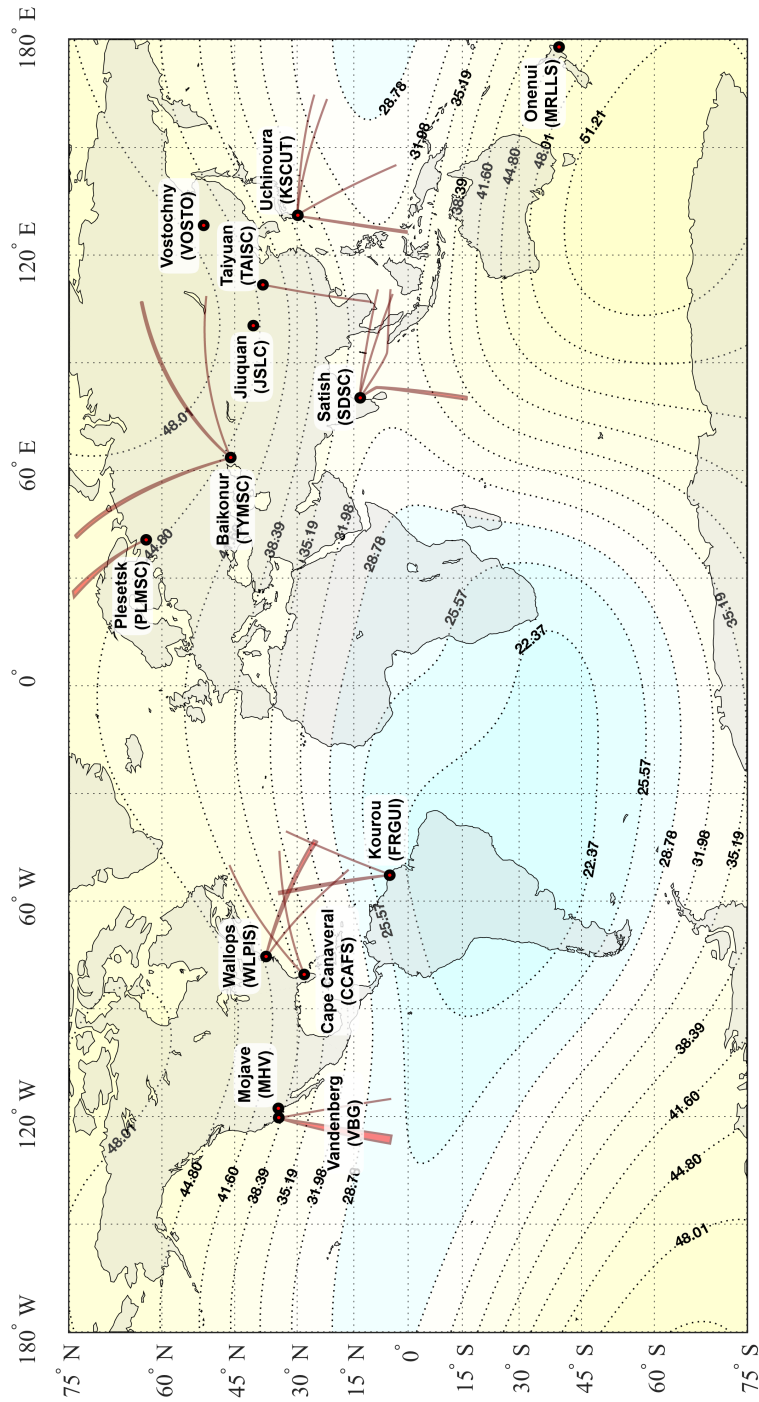


Fig. 2.8 World map of the launch sites associated to historical nanosatellite missions. Red lines represent typical launch azimuths and manoeuvres defining the final orbit inclination. Contour levels show the Earth's magnetic total intensity, in  $\mu\text{T}$  at 400 km, related to important parameters of the orbital space environment.

## Nanosatellites Overview

---

missions have used sparse sun-synchronous launch opportunities as secondary payloads. A spectrum of orbit parameters is normally achievable for nanosatellites under the secondary payload category using the services of specialised companies [79]. A detailed discussion on launch opportunities for nanosatellites systems is presented by Crisp et al. [80].

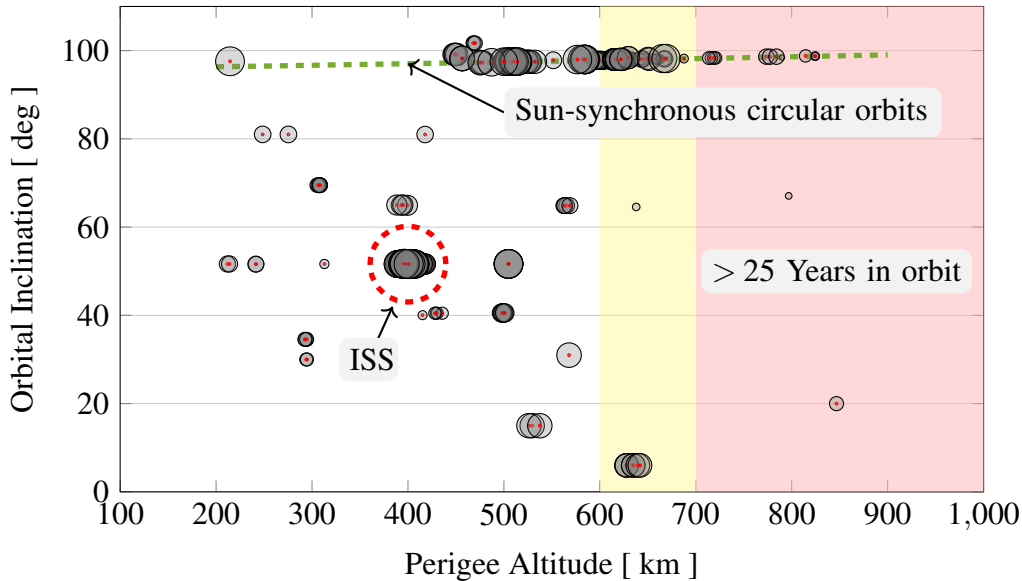


Fig. 2.9 Distribution in the perigee altitude-inclination space of reported nanosatellites and their expected orbit lifespan. For illustration purpose only, circle sizes represent deploy dates ordered from the oldest (smaller circle) to the latest (larger circle) mission. Image prepared with data from historical nanosatellite missions reported in Appendix A, and orbit lifespan ranges from de Selding [81].

A relevant aspect of historical nanosatellite orbits shown in Fig. 2.9 is that orbit altitudes above  $\sim 600\text{ km}$ , assuming circular orbits<sup>4</sup>, have expected orbit lifespans of more than 25 years [82, 83]. According to the standard for the disposal of satellites operating in or crossing Low Earth Orbit, ISO 16164:2015 [84], post-mission disposal is required by means of controlled manoeuvring or by complete natural orbit decay within the following 25 years after the end of the mission. The nonexistent propulsion capability on nanosatellites inevitably places most missions above  $\sim 600\text{ km}$  in altitude in violation of the international disposal guidelines. Further discussion about this topic

<sup>4</sup>The circular orbit assumption is reasonably applicable to the historical nanosatellite missions in view of the overall average eccentricity of 0.0045.

is presented by de Selding [81], Kato et al. [82] and Meador-Anz [83]. Compliance to the international disposal guidelines ISO 16164:2015 defines key aspects for the general nanosatellite mission in relation to onboard propulsion systems. Firstly, orbits above  $\sim 600$  km require active deorbit systems and secondly, adequate assessment of orbital decay is required to ensure natural reentry within the allowed time margin as function of the onboard propulsive means.

Although launch options are under diversification as previously discussed, propulsion systems on nanosatellites inherently set potential hazards that require additional attention and qualification when launched as secondary payloads. In this respect, several nanosatellite dispensers have been developed and used for secondary payloads. Some examples include the ISIS Payload Orbital Dispenser (ISIPOD), JAXA-Picosatellite Orbital Deployer (J-POD), Single Picosatellite Launcher (SPL), and the Poly-Picosatellite Orbital Deployer (P-POD). At the present time the P-POD [85] is the most widely used dispenser, for this reason the following discussion is centred on the P-POD CubeSat Design Specification [86] (CDS) and associated propulsion system design requirements. According to the current CDS revision 13, requirement 3.1.3, "No pyrotechnics shall be permitted", implying combustion restrictions which is particularly relevant for chemical propulsion systems. Requirement 3.1.4 explicitly sets rules for propulsion systems and redirects to the more general Air Force Space Command Manual 91 – 710 Volume 3 [87] (AFSPCMAN). Requirement 3.1.5 states that "Propulsion systems shall have at least 3 inhibits to activation", this may represent an important design restriction for propulsion systems with mechanical parts such as valves. Requirement 3.1.6 "Total stored chemical energy will not exceed 100 Watt-Hours" may set restrictions on general chemical reactions for propulsion. Requirement 3.1.7 "CubeSat hazardous materials shall conform to AFSPCMAN 91 – 710, Volume 3", is a novelty of the current version since hazardous materials were banned in earlier revisions. Requirement 3.1.10 "... it is advised to limit magnetic field outside the CubeSat static envelope to 0.5 Gauss above Earth's magnetic field" may represent an important restriction for some electromagnetic

EP concepts. Overall, the current CDS is less restrictive than earlier versions in favour of the already challenging development of propulsions systems for nanosatellites.

The launch and orbital characteristics of nanosatellite missions discussed in this section, define important aspects of their design, useful life, mission objectives, space environment, and orbital perturbations, that in turn establish basic attitude determination and propulsion system requirements. For example, consider a NanoRacks deployment at 400km. In this case, the nanosatellite's ground track would sweep out latitudes encompassing  $51.6^{\circ}\text{S} - 51.6^{\circ}\text{N}$ . Fig. 2.8 illustrates the Earth's magnetic total intensity at vernal equinox 2017 using the World Magnetic Model [88] at 400km. Magnetic intensity reduction in the south Atlantic region evince high energetic protons and electrons constituting the Earth nearest part of a complex plasma system bow shock [89], resulting from the interaction for the Earth's magnetic field and the solar wind known as Van Allen radiation belts. The enhanced radiation dose within this region could result in faulty electronics operation, attitude sensors malfunction, and in the worst case systems permanent failure. The following subsection discuss in more detail typical mission characteristics and the role of the space environment in the development of propulsion systems in nanosatellites.

### 2.3.1 Nanosatellites Survivability to the Space Environment

Propulsion technology demonstration and development missions are fundamental to achieve the level of sophistication and proficiency needed for *functional* nanosatellite missions. In the context of this thesis work, the term "functional mission" refers to the capability to guarantee sufficient and effective survivability to the harsh space environment aiming the reliable fulfilment of mission objectives. Commercialisation of space has been the main driver of the envisaged applicability and technological advancement of nanosatellites on the quest for functionality. As with nanosatellite launchers, commercial manufacturers are gradually diversifying space qualified products to nanosatellite platforms expanding the potential of missions. However, migration of

## **2.3 Typical Nanosatellite Mission Characteristics**

---

components is far from completed. Whilst some elements find direct or almost direct transfer to the nanosatellite scale such as solar cells [90] and some common electronics [91], many others are difficult to miniaturise or adapt. Examples of integration difficulty are found in conventional radiation mitigation and thermal control schemes used in larger satellites, e.g. metallic electronics housing, MultiLayer Insulation (MLI), and heat pipes.

In regard to the electronic components available for general design, space qualified components are in general more expensive, less power efficient, and less advanced than COTS. This may represent a major challenge to the development of functional nanosatellite missions because, despite the advantageous economical cost, increased mission capabilities demand higher power consumption. Additionally, small satellite size implicitly increases the power density of the satellite calling for additional design considerations, e.g. power system margins and capability. Foreseeable consequences of the present underdeveloped technology options for nanosatellites is that all missions to date have had to rely on COTS electronics at some operational level in the hope of tolerable performance degradation in space. Thusly, it is common to find COTS in nanosatellites' Attitude Determination Systems (ADS), and in Command and Data Handling systems (CDH) fundamental for the development and operation of propulsion systems.

The use of COTS electronics in space applications implies the exercise of extreme caution to meet launch requirements and ensure sufficient mission survivability. For instance, according to a survey reported by Swartwout [92] encompassing CubeSats launched in 2000 – 2012, inadequate thermal design, inattention to COTS electronics, and radiation issues are common sources of failure amongst missions. Some basic considerations are COTS plastic package outgassing level [86] (in space vacuum), epoxy encapsulates' hygroscopic and absorptive susceptibility [93] (moist absorption), thermal cycle response (low thermal capacitance in nanosatellites imply rapid thermal response), and sufficient component vent to withstand extreme pressure gradients. An interesting example of the last point are the holes drilled to COTS pyroelectric sensors

## Nanosatellites Overview

---

for the Earth nadir sensor in the PSSCT-2 nanosatellite [94]. COTS compliance to the Restriction of Hazardous Substances Directive [95] (RoHS) specifically on the restriction of lead use in electronics bring additional concerns. Soldering and plated terminals in RoHS components use pure tin or other tin-based alloys prone to tin whisker growing<sup>5</sup>. Tin whiskers are spontaneous conductive crystalline structures with growth rate of  $0.03 - 9 \text{ mm/year}$  responsible for various satellite failures by short circuits [96], internal debris contamination, and conductive plasma generation owing to vaporisation.

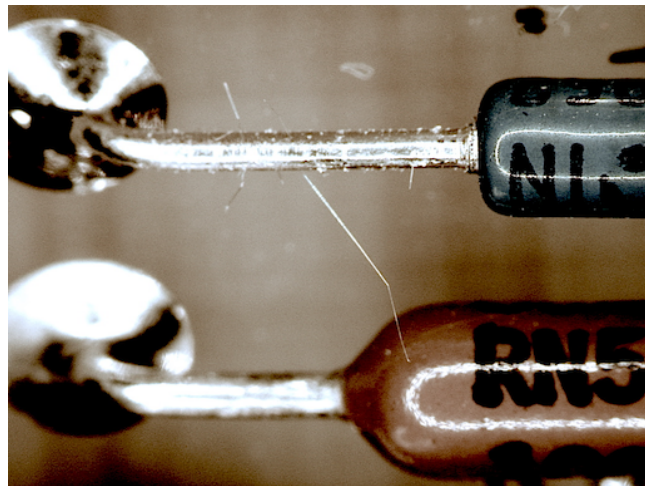


Fig. 2.10 Whiskers growth in tin-plated diodes. Some COTS components incorporate materials prone to whisker growth, which may produce eventual short circuit leading to electronics malfunctioning or fatal failure in satellites. Image courtesy of T. Riccio/STPNOc [96].

Space environment largely controls dominant factors affecting the performance of COTS in space. As previously introduced in Section 2.3, space poses a highly radioactive environment which effects on any space systems cannot be neglected. Space environment in low Earth orbits is dominated by the presence of plasma confined by the Earth's magnetosphere extending from  $\sim 90 \text{ km}$  to  $30 - 50 \times 10^3 \text{ km}$  depending on geomagnetic conditions. The plasma structure within this region is called the plasmasphere [97], shown in Fig. 2.11, and is mostly constituted by low-energy high-density plasma ( $< 100 \text{ eV}$  and  $> 1 \text{ cm}^{-3}$  respectively), and to a lesser extent by

<sup>5</sup>Although tin whiskers are common in electronic components, other metals and alloys may produce them like silver, zinc, etc.

high-energy (typically 0.1 – 10 MeV) low-density plasma. The plasmasphere can be idealised as a highly dynamic toroidal shape centred and corotating about the Earth’s magnetic equator with 1 – 3 high-energy plasma circuits at separated altitudes, the Van Allen radiation belts. The cross-sectional area of the Van Allen radiation belts resemble a crescent shape aligned to the Earth’s magnetic equator.

In the case of the inner belt, its domain may encompass altitudes as low as 200km, in the South Atlantic Anomaly region introduced in Fig. 2.8, to approximately 1000km. During geomagnetic storms the plasmasphere shrinks compressing, and sometimes merging, the radiation belts bringing additional high energetic plasma to LEO orbits.

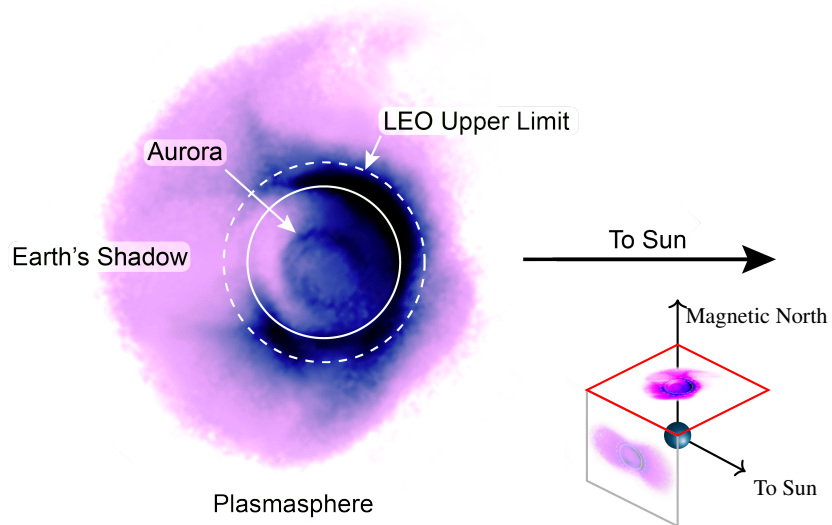


Fig. 2.11 Earth’s plasmasphere and orbits below 2000km (LEO). The main figure shows the plasmasphere structure as seen from the Earth’s magnetic north wherein darker colours show higher plasma density, and the solid circle represents the Earth’s contour. Illustration composed with data from the NASA’s Imager for Magnetopause-to-Aurora Global Explorer (IMAGE) extreme ultraviolet instrument [98] (detail and top view), and from the CNSA’s Chang’E-3 Lander Extreme Ultra-Violet Camera [99] (side view).

In orbiting satellites, high energetic particles and photons degrade most exposed materials via kinetic energy deposition, including the semiconductors constituting vital electronic components. The total absorbed dose resulted from this impingement, is the sum of the resulting ionisation, atomic displacement and excitation on the exposed material. The consequences to the mission of such degradation greatly depend on the

level and criticalness of the affected component. In general, the effect of radiation exposition in electronics is technically classified in two broad categories: the Total Ionising Dose (TID) and Single Event Effects (SEE), viz. Single Event Upset (SEU), Single Event Latch-Up (SEL), and Single Event Burnout (SEB). The TID is the amount of energy deposited by radiation that in the case at hand, the semiconductor-based device is able to absorb before failure. On the other hand, the SEEs are produced by eventual extreme exposure to radiation that may cause single bit flip in digital electronics and output noise in analog components; potentially destructive rise of localised currents that temporarily disable the affected electronic component; and triggering of currents and heat leading to permanent damage. SEEs are temporal random phenomena spatially correlated to the south Atlantic anomaly in low LEO from trapped subatomic particles in the Earth's magnetic field, and at high latitudes mostly originated by cosmic rays and solar activity. Detailed information on radiation assessment, effects and design margins is presented by ECSS [100].

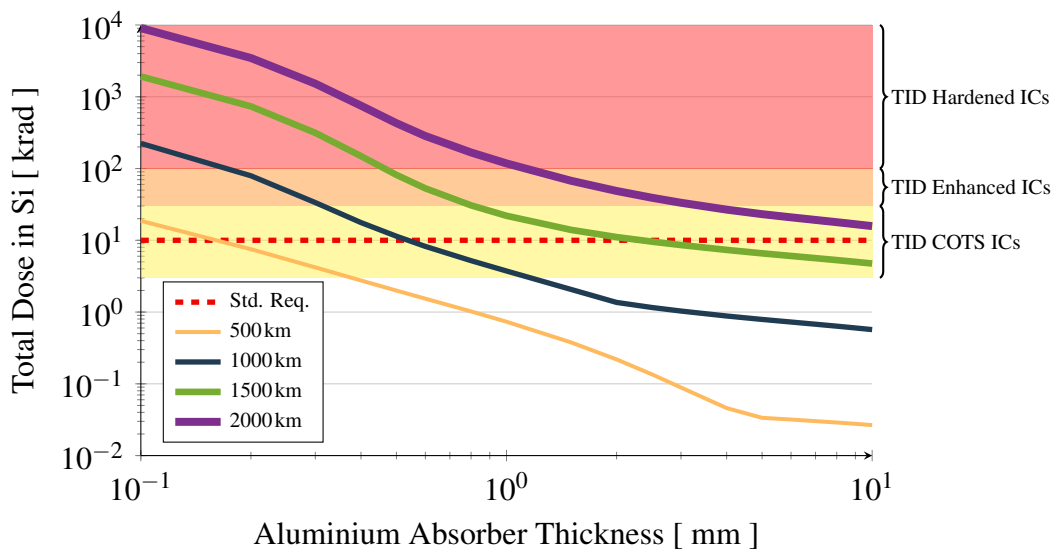


Fig. 2.12 Log-log plot of the worst-case dose at transmission surface of Aluminium slab shields at various altitudes. The dashed line shows the dosage requirement for small scale satellites [101] according to the standard ISO2002. A detailed breakdown of radiation source contributors is presented in the Appendix C.

Fig. 2.12 illustrates the dose at transmission surface of aluminium slab shield<sup>6</sup>, dose-depth method typically used to quantify effects of spot built-in shielding [100]. The figure shows the expected maximum value of total radiation dose for each orbital altitude, i.e. for all orbital inclinations at an specific altitude. From Fig. 2.12, it is evident that radiation cumulative effects can be easily addressed with fortuitous shielding, e.g. spacecraft external structure, due to the read trivial absorber thickness for COTS Integrated Circuits (ICs) within the spacecraft at LEO [103]. In this way, built-in shielding at LEO is chiefly critical for survivability extension and SEEs mitigation. Specialised commercial options are available for COTS components shielding, for example the Tethers Unlimited Versatile Structural Radiation Shielding (VSRS) [104] and the Maxwell Technologies RAD-PACK [103]. However, shielding against SEEs is ineffective in most cases. SEEs are better mitigated with cautious hardware design [101] and with software-based radiation protection [105] instead. SEEs are common in nanosatellites and have been reported as sources of anomalous operation, e.g. SELs in CSSWE and HORYU-2, and catastrophic failures in the CUTE-1.7+APD and possibly in the STARS-II [106]. Dedicated nanosatellite missions to the study of space radiation and induced degradation of COTS electronics, e.g. AAUSAT 2 and ROUSTA, are key to the development of future functional missions. In summary COTS electronics endurance to the space radiation stems from many factors like quality of raw materials, manufacturing processes, internal circuitry design, temperature tolerance, self shielding amongst components, collective arrangement of electronics and other fortuitous spacecraft shielding, orbit characteristics, and solar activity. Thusly, radiation tolerance assessment of COTS electronics and the selection of adequate mitigation methods is an essential task for nanosatellite designers.

Another important effect of space-plasma immersion in LEO environment is spacecraft charging, which may occur on external and internal surfaces. Spacecraft charging phenomena in space, thoroughly discussed by Lai [107], is a critical issue for nanosat-

---

<sup>6</sup>Data from the ESA's Space Environment Information System [102] using the AE-8/AP-8 Radiation Belt Models and the SHIELDOSE-2 dose model.

## Nanosatellites Overview

---

lite missions mainly due to electronics low current and low voltage operational values. In the plasmasphere electrons and ions naturally differ in flux magnitude from mass inertia contrast. In this way lighter electrons have distinctive higher flux than ions. Under this condition, a plasma-immersed static surface rapidly collects more electrons than ions establishing a negative charge with respect to the surrounding plasma potential conventionally defined as zero. Once the system plasma-surface reaches equilibrium through electrostatic interactions, i.e. the surface capacitance is filled up, a Debye sheath is formed and the application of the Kirchhoff's circuit law to the system is enabled, i.e. the sum of input and output currents to the node (surface) are equal. Hence, in the occasion of outflow of photoelectrons emitted when surfaces are impacted by UV and EUV radiation, back-scattered electrons, and secondary and reflected electrons, serve to reduce the accumulation of negative charge on the surface. Conversely, charges leaving the surface may be steered back to the surface in the presence of magnetic fields (Lorentz force law), adding to further negative surface charging [108]; if the magnetic field fluctuates relative to the surface, additional electric fields are induced on the surface (Faraday's induction law). The equilibrium of input and output currents in the surface is sustained by the surface potential that adjusts itself accordingly.

In LEO and within the low energy plasmasphere, i.e. note that high orbit inclinations may lay outside the plasmasphere, an object's orbital speed is higher than the low thermal speed of ions due to the characteristic low plasma energy. Leading surfaces collect ions along the object's motion whilst shielded surfaces are able to collect electrons solely. The resulting uneven charged geometry can reach equilibrium by the local migration of the abundant charges available due to the high plasma density in LEO as discussed above. However, charge migration may not be sufficient to establish equilibrium if the shielded area overwhelms the object's capability of collecting ions. In this case of substantial surface potential differences, high-current surges may appear. In satellites, the conditions for soft surface charging auto-regulation are difficult to meet because of the mixed use of electrically conducting and electrically insulating materials. Spacecraft local charging, known as differential charging, is affected by

the characteristics of the surfaces' materials leading to potentially dangerous surface electrostatic discharges.

In satellites traveling in regions outside the low-energy plasmasphere or within the Van Allen radiation belts, in near LEO at aurora latitudes about  $60^{\circ} - 70^{\circ}$ , surfaces are charged to the energetic level of the impinging particles because of the scarce presence of high density plasma and therefore the regulating mechanism described above. High energy particles precipitating in aurorae events can easily charge spacecraft surfaces to the order of kilovolts whilst high energy electrons ( $> 10\text{ keV}$ ) can penetrate deeper in surfaces and even internal components depending on the existing shielding characteristics, contributing to internal spacecraft charging. Deep charging deposits on internal dielectric materials where electric fields buildup, and if not adequately discharged, the electric field eventually reaches the breakdown strength of the material causing internal electric arcing.

In nanosatellites, space environment shielding may be difficult to achieve and deep charging can easily become a problem. Additionally, high inclination orbits have been historically used in nanosatellite missions placing them in potential risk as discussed above, adding to the already low working survivability of the mission. However, no mission failure in nanosatellites has been explicitly attributed to spacecraft charging to date. Instead, spacecraft charging effects in nanosatellites extend from telecommunication interference, environment magnetic and electric fields shielding in science and attitude sensors, electronics noise generation through induced electromagnetic fields, and anomalous invasive currents on circuits.

An important concern with respect to spacecraft charging in nanosatellites is the possible set of consequences derived from the operation of EP. The assessment of EP in major satellites and its influence on spacecraft charging [109] has shown that the emitted particles and plume plasma can interact with the spacecraft and alter the surrounding ambient plasma. The nature and magnitude of such interaction is established by specific thruster properties and configuration of the spacecraft. EP operating at large satellite scales typically reduce the spacecraft potential, with respect to the ambient plasma,

to few volts, acting effectively as a plasma contactor. However, these EP systems are characterised by low levels of backflow currents from the plume to the spacecraft surfaces. On the other hand, low power and thrust levels in nanosatellite propulsion systems could change the level of backflow currents and therefore spacecraft charging. It can be hypothesised that the resulting electric fields may be of significant importance for emerging micro-thrust EP systems. Unforeseen electric fields could substantially interact with the exhaust particles sensibly affecting the thrust vector, plume, and efficiency of thrusters. The analysis of the possible interaction and consequences of EP actuation on nanosatellites surface charging is therefore limited to specific characteristic mission features. Specialised software such as SPIS [110] and NASCAP-2K [111] are valuable tools for the required tailored analysis of specific missions assessment of spacecraft charging.

Acceptable systems survivability to the space environment is a basic requirement for propulsion systems operation in nanosatellites. In a similar way, the basic operational propulsion profile is determined by external perturbing forces acting on the nanosatellites. The next subsection discusses this topic.

### 2.3.2 Main Attitude and Orbital Perturbations in Nanosatellites

One of the primary objectives of nanosatellite propulsion systems is to provide sufficient autonomy capabilities to tackle the effects of orbit and attitude dynamics environment perturbations. There exists an ample source of motion perturbation forces naturally acting on orbiting objects in space. When considering the effects of perturbations, it is important to distinguish between conservative and non-conservative forces. For conservative systems the total kinetic and potential energy remains constant over time. On the other hand, non-conservative systems interchange energy through different mechanisms such as friction or thrust action. Regarding the major natural acting forces over satellites, central body and third-body ones are conservative whilst atmospheric drag, radiation pressure, and thrust are non-conservative. Of special interest for the

purpose of this thesis work are the effects of environment perturbations caused by non-conservative forces because they prompt orbital decay and attitude dynamics concerns to the general nanosatellite mission. A review of main orbit perturbations and analytical models used along this work is presented in Appendix D.

The acceleration magnitude of the non-conservative Solar Radiation Pressure (SRP) and atmospheric drag perturbations are functions of area as observed in the simplified equations<sup>7</sup> Eq. (2.20) and Eq. (2.21) respectively. In other words, the magnitude of these fundamental perturbations depend on the ratio of the extensive properties area and volume. The areas, called cross-sectional areas in these simplified equations, are abstractions of complex spacecraft surface area interactions.

$$a_{srp} = \frac{A_{sp}}{V_{sc}} \left( \frac{1}{\rho_{sc}} p_{srp} C_R \right) \quad (2.20)$$

$$a_{drag} = \frac{A_{dcs}}{V_{sc}} \left( \frac{1}{2\rho_{sc}} C_D \rho v_{rel}^2 \right) \quad (2.21)$$

In the context of this thesis, the discrimination between convex and concave nanosatellite geometries is important because these display different reflection properties impacting the representativeness of cross-sectional areas; this subject is further discussed in Chapter 5. A convex nanosatellite geometry can be identified if a drawn line passing through the satellite's geometry crosses the external surfaces only two times as shown in the Fig. 2.13, otherwise it is defined as concave. Acknowledging that convex spacecraft geometries are difficult to obtain because small dents (inward curves) are present most of the time, the above definition applies to large spacecraft surface elements like deployable panels.

To illustrate the implications of the Surface-Area-to-Volume Ratio (*SAVR*) in Eq. (2.20) and Eq. (2.21) consider the following assumptions. The Eq. (2.22) derived from the Pick's theorem [112] for the *SAVR*, is applicable to structures built with cubic blocks. In the *SAVR* equation,  $l$  is the edge length,  $u$  is the number of building

---

<sup>7</sup>Note that the spacecraft mass is shown as the product of volume  $V_{sc}$  and density  $\rho_{sc}$  for the purpose of the explanation.

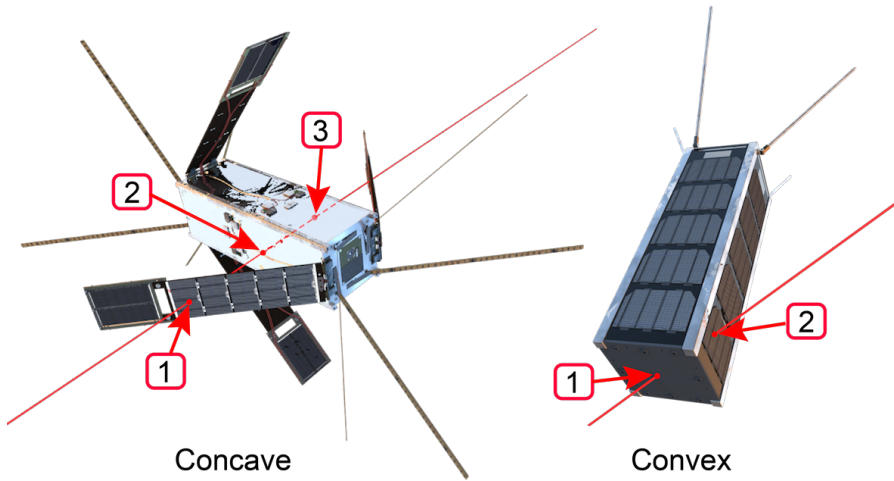


Fig. 2.13 Identification of concave and convex nanosatellite geometries. In convex geometries an imaginary straight line passing through the nanosatellite body, crosses the external surfaces only two times.

units,  $r$  is the interior edges number, and  $x$  is the interior vertex number. Thus, in a linear polycube configuration like in a 3U CubeSat, variables in Eq. (2.22) are given by  $l = 0.1 \text{ m}$ ,  $u = 3$ ,  $r = 0$ , and  $x = 0$ . In other example, a big solid cube (no notches) composed by 8U, the values would be  $l = 0.1 \text{ m}$ ,  $u = 8$ ,  $r = 6$  (e.i. 2 1U edges running from front to back, top to bottom, and left to right), and  $x = 1$ .

$$SAVR = \left( \frac{2}{l} \right) \left( \frac{2u - r + x + 1}{u} \right) \quad (2.22)$$

A plot of  $SAVR$  for linear polycube configurations of CubeSats is presented in Fig. 2.14. From the values of  $SAVR$  in the figure it can be inferred that solar radiation pressure and atmospheric drag perturbations would be incremented just by the reduction of satellite size assuming all other variables constant. Despite the fact of actual interactions complexity and that not all surface area is subject to even interaction, this is an important conclusion because it highlights unique characteristics of nanosatellites that may require the redefinition of standard criteria inherited from major satellite analyses.

The break down of commonplace orbit perturbation accelerations in Fig. 2.15 shows the preponderant role of atmospheric drag over the SRP for orbits below  $\sim 600 \text{ km}$ . The

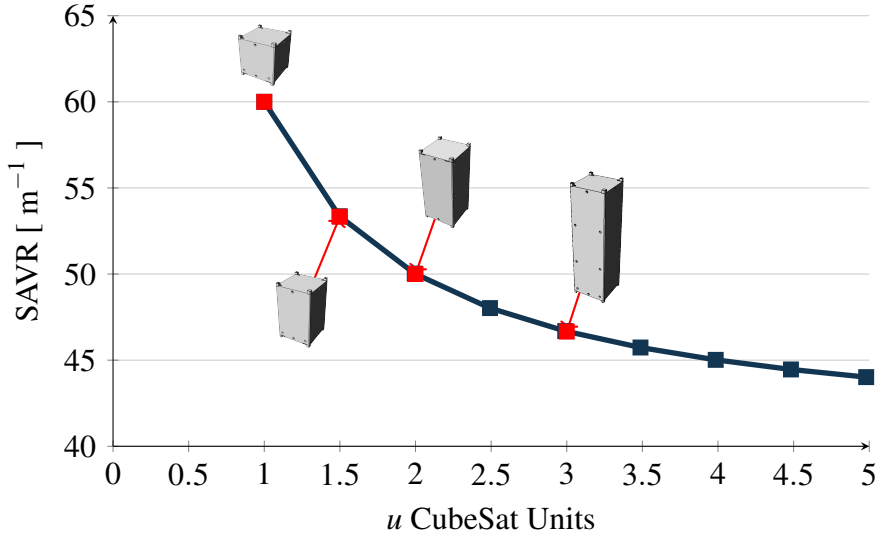


Fig. 2.14 Surface-area-to-volume ratio plot from Equation (2.22) with  $l = 0.1\text{ m}$ ,  $r = 0$  and  $x = 0$ . These settings correspond to a collection of 1U CubeSats meeting at an entire face only.

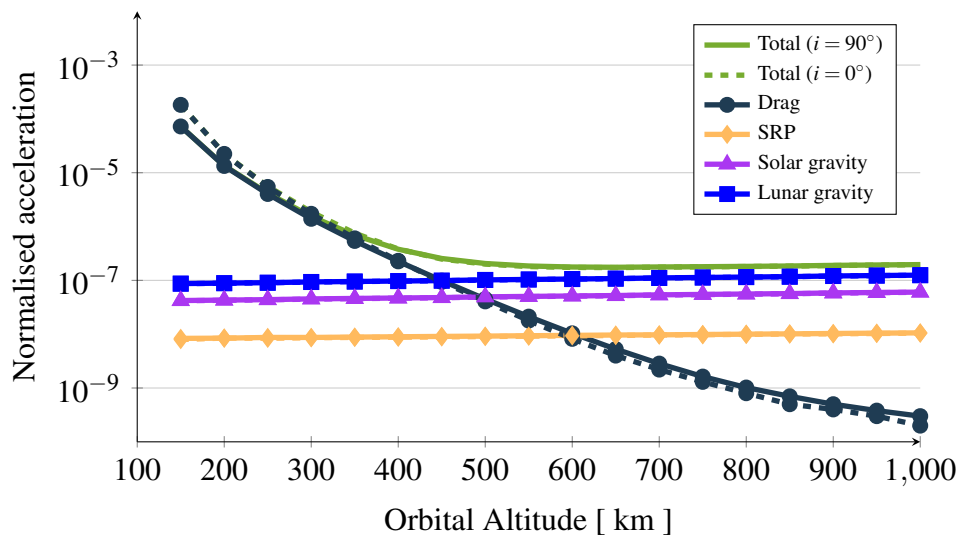


Fig. 2.15 Log-lin plot of the accelerations for the main natural sources of orbital perturbation normalised to the gravitational acceleration value. The reported values are averages for each case and condition, obtained with the numerical orbital propagator presented in Chapter 3, for a standard 3U CubeSat. Solid lines report perturbation values from a polar orbit and dashed lines report those of an equatorial orbit (most dashed and solid lines overlap in the figure).

## Nanosatellites Overview

---

acknowledged importance of this orbital altitude range and SAVR on nanosatellites, call for special attention on the analysis of atmospheric drag attributes.

Atmospheric drag progressively reduces orbital velocity at rates primarily dictated by the fluctuating atmospheric density,  $\rho$ . Mass density and chemistry temporal-spatial variations in rarefied atmospheric conditions can be abrupt and markedly dependent on solar activity. Significant advancements in the atmospheric dynamics understanding [113, 114], assist the development of high accuracy atmospheric models [115, 116] that in turn improve their ability to effectively reproduce density changes. Amongst the variables in Eq. (2.21), the drag coefficient  $C_D$  is the less tightly defined quantity. Typically the barely understood atmosphere-spacecraft actual interaction have restrained the adoption of  $C_D$  values within a plausible, and sometimes arbitrary, constants range. In this respect the atmospheric highly reactive atomic oxygen, a common dominant species in LEO, is known to be a key parameter of  $C_D$ . However, to date, sparse in situ measurements of atomic oxygen have been taken from nanosatellites to identify the actual interaction with exposed materials surfaces and resulting implications on  $C_D$  values. Varied in situ atomic oxygen measurements from dedicated nanosatellite missions, like the VZLUsat 1 (QB50 CZ02) [117] using the Flux-Φ-Probe EXperiment (FIPEx), could provide important information prompting the advancement of models for  $C_D$  estimation. With regard to the remaining factors in Eq. (2.21), the spacecraft mass, orbital state vector, and attitude dynamics, are commonly known and predictable to some extent. In fact, the crux of the overall assessment of orbital perturbations on satellites is focused on the significance of its sources and the ability to predict them.

These arguments spot two major sources of uncertainty in atmospheric drag estimation on nanosatellites: the drag coefficient, and the atmospheric density for forecast. As the atmospheric model forecast ability is essentially enabled with the in advance knowledge of solar activity, the foregoing statement implies that the driving source of uncertainty comes from the Sun. The relevance of satisfactory estimation of these values is fundamental for the primary orbit operations of propulsion systems in functional nanosatellite missions.

The assessment of the collective effect of perturbing body torques is elementary for in-orbit operations such as pointing control. Pointing control is an immediate requirement for functional nanosatellite missions because of the technical complexity of mechanical systems miniaturisation for directing critical onboard hardware. Nonetheless, suitable attitude sensing and control components for precise steering have been historically unavailable for most nanosatellite missions due to size and power constraints. Hence most missions rely on coarse pointing at best [118]. This panorama is rapidly changing with the commercialisation of space and the increasing demand of operational missions, e.g. for Earth observation. A major breakthrough in attitude

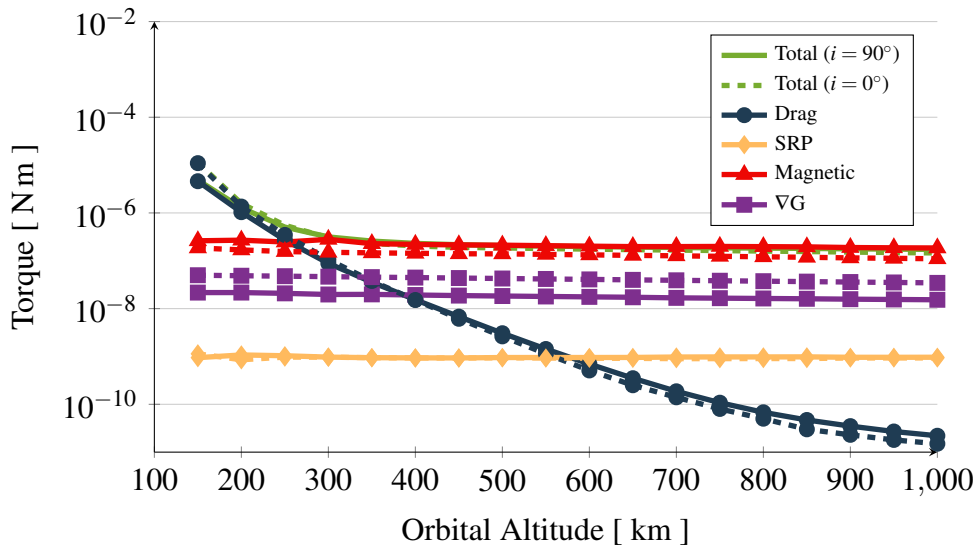


Fig. 2.16 Log-lin plot of the external body torques for the main sources of orbital perturbation. Assuming a standard 3U CubeSat with upper range residual dipole [119] of  $0.01 \text{ Am}^2$ , and coincident centre of geometry and mass. The reported values are averages for each case and condition, obtained with the numerical orbital propagator presented in Chapter 3. Solid lines report torque values from a polar orbit and dashed lines report those of an equatorial orbit.

control in nanosatellites is the incorporation of propulsion systems capable to provide remarkable manoeuvrability. The minimum degree of manoeuvrability depend on the magnitude of the perturbing body torques that the system has to overcome to control attitude dynamics. Body torques owing to natural occurring perturbations in space environment for a 3U CubeSat are shown in Fig. 2.16. As observed from the figure, typical body torque magnitudes are heavily reliant on specific spacecraft design. In the

presented case, magnetic perturbations dominate attitude dynamics at orbit altitudes above  $\sim 250\text{km}$ , according to the residual dipole corresponding to the upper range commonly found on CubeSats [119]. However, the magnetic dipole generated by the operation of EP can easily surpass this reference upper level if not carefully neutralised.

Typical mission characteristics define important aspects of functional nanosatellites design as discussed in this subsection. Further, propulsion systems power demand adds to the already increased power density in nanosatellites. This points out to another crucial design parameter, the input power requirement to fulfil subsystems operation.

## 2.4 In-Orbit Power Resources

Electric power is the basis of active<sup>8</sup> nanosatellites functionality. The power system in satellites are divided in three main subsystems [121]: generation, storage, and management. The attributes of the power system are chiefly allocated by the mission average and peak power requirements as well as orbit characteristics, i.e. eclipses duration. Altogether, the system is expected to provide sufficient power resources to operate all fundamental components including propulsion systems onboard of nanosatellites. The energy budget design is an arduous task unique amongst missions, which is a function of onboard physical resources, orbit characteristics, and overall systems efficiencies.

Nanosatellite designers rely on COTS technologies available in the consumers market for power system design. This fact eases the identification and classification of power subsystem components that for many reasons have been historically preferred for nanosatellite designers. With the exception of power management that greatly depend on specific mission requirements, power subsystems in nanosatellites show distinguishable characteristics which are discussed below.

---

<sup>8</sup>The Ball Lens In The Space [120] (BLITS and BLITS-M) nanosatellites are examples of passive concepts.

### **2.4.1 Power Generation**

In general, there are few options for power generation in spacecraft that are further reduced in nanosatellites due to inexistent miniaturisation, exorbitant costs, high operational complexity, or reliability matters. Power generation technologies in satellites can be classified in three main groups:

- Photovoltaic solar cells: convert solar radiation into electrical energy
- Static power sources: convert temperature differences or emitted electrons to electrical energy i.e. the Radioisotope Thermoelectric Generator
- Dynamic power sources: convert heat into electrical energy via a thermodynamic power cycle i.e. Stirling cycle

Examples of these power generation technologies have been flight-validated in major satellites but, with the exception of solar cells, are unavailable for nanosatellites. Fortunately, photovoltaic solar cell technology is ideal for most low power missions due to its maturity, reliability, and continuous development occurring in a very active consumers market. Other concepts remain as technology demonstrations, which with additional development could add to the options for particular nanosatellite mission requirements. Two relevant examples of emerging concepts for nanosatellites are the bio-fuel cell technology, and the electrodynamic tether concept. In the bio-fuel cell technology an enzyme catalysed bioreactor produces electric power. This technology could be used, for example, to cover some energetic requirements during long eclipse periods. The first prototype of bio-fuel cell technology for nanosatellites was projected<sup>9</sup> for the BillikenSat-II CubeSat. The prototype was developed by Boeing and the Saint Louis University and intended to use flat beer as fuel [123]. In the tether concept *for electric power generation* [124], conductive tethers harvest environment electrons transforming some orbital kinetic energy to electricity with the use of the dynamic interaction with the Earth's magnetic field (Faraday's law of induction). Although this concept penalises

---

<sup>9</sup>The status of the program is unknown [122]

on attitude dynamics freedom and orbital kinetic energy enhancing re-entry, it can produce several hundred volts per kilometre of tether.

Photovoltaic solar cell technologies remain the most practical option for nanosatellites to date. Hence, it is indispensable to identify the capabilities of photovoltaic solar cell technologies by virtue of their importance to sustain propulsion system operations.

**Photovoltaic solar cell** conversion efficiency is determined by many factors in practice. Solar radiation angle of incidence, cell temperature gradients, and fundamental technology are some of them. The ideal efficiency attainable by a photovoltaic solar cell can be identified in thermodynamic arguments. Albeit unachievable, it is worthwhile to introduce the ideal efficiency concept as it sets a reference framework for technology performance assessment. Fig. 2.17 shows the ideal solar converter efficiency  $\eta_{\square}$  with respect to the re-radiated temperature  $T_R$  and ambient temperature  $T_A$  variations. A detailed derivation of the function plotted in Fig. 2.17 is presented in Appendix E.

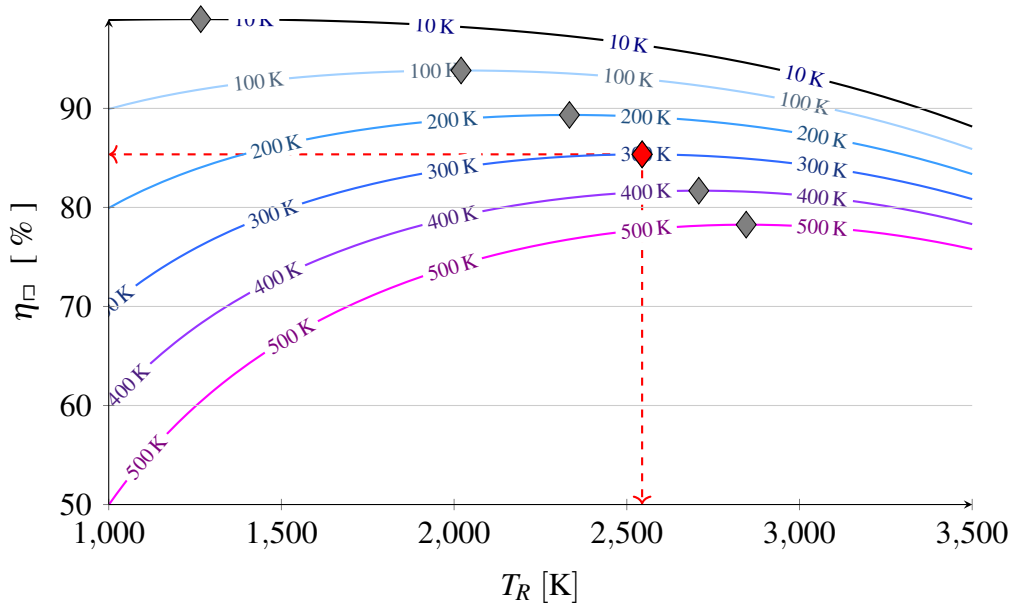


Fig. 2.17 Maximum ideal solar converter efficiency. The plot shows the relationship amongst the re-radiated temperature  $T_R$  and ambient temperature  $T_A$  (contour lines), assuming null irreversibilities associated to the generation process. See Appendix E for more details.

It is estimated that in an ideal solar converter near standard temperature, the maximum attainable efficiency is approximately 85% as indicated in Fig. 2.17. In a real solar converter, namely photovoltaic solar cell, the existence of thermodynamic irreversibilities reduce the conversion efficiency. Irreversibilities are produced by intrinsic material properties (e.g. glass transparency), radiation transmission (e.g. diffuse light has higher entropy), and other processes involved in the conversion. Limitations established by semiconductor material such as the energy required to transport an electron to the conduction band, inherently narrows the useful wavelengths available from the incident electromagnetic spectrum for an specific semiconductor. This implies that different types of semiconductors would filter distinct spectrum ranges opening the possibility of a multi-semiconductor converter. In theory, an infinite number of ideal tandem-stacked monochromatic converters could reach maximum ideal efficiency. In practice, it is estimated that the real limiting maximum efficiency (at  $T_A = 300\text{K}$ ) for single, double, and triple junction<sup>10</sup> cells is 40.8%, 63.8%, and 63.8% respectively [125].

In a brief overview of photovoltaic solar cell technologies, these are categorised in three common groups so called generations. The first generation is widely used accounting for 86% of terrestrial applications due to its reliability and good performance. The first generation is based in single layer p-n junction single-crystal silicon wafers with  $\eta_{\square}$  ranging from 15 to 20%. Second generation cells are usually named thin-film solar cells because are manufactured by epitaxial deposition of semiconductors, commonly produced with amorphous silicon, polycrystalline silicon, microcrystalline silicon, cadmium telluride, and copper indium selenide. Typical performance of second generation cells range 10 – 15%, and for specialised applications can reach 28%. For example the second generation triple junction BTJ EMCORE Photovoltaic cell, InGaP/InGaAs/Ge, has an  $\eta_{\square}$  of 28.5% [126]. Third generation solar cells, mainly in the form of multi-junction modules, make use of organic materials or polymers to photo-generate charge carriers. Due to the nature of its constituents, the third generation does not use the

---

<sup>10</sup>Different junctions of semiconductors are stacked using crystalline deposition on crystalline substrates in the so-called epitaxial process.

## Nanosatellites Overview

---

common p-n junction, namely diode, to separate carriers. Current best research third generation cells can achieve  $\eta_{\square}$  values of nearly 45%. The distinction of a fourth generation was proposed by Silva in 2013 [127]. This new generation combines low costs and production flexibility of organic conduction polymers alongside the stability of novel materials such as  $TiO_x$ ,  $MoO_3$ ,  $V_2O_5$ ,  $ZnO$ , Carbon nanotubes, Graphene, and metal nanoparticles. In essence, fourth generation cells allow the manufacture of reduced-size multispectral layers with improved lifetime stability and better conversion efficiency than the reported for the third generation ones.

In space applications, photovoltaic solar cells have been a constant in spacecraft design since the first solar-powered satellite, the Vanguard I in 1958. This pioneering satellite used six first generation Silicon (Si) and Gallium Arsenide (GaAs) solar cells with  $\eta_{\square}$  of 14% [128]. In subsequent years, increasing mission complexity and onboard higher power demand chiefly in telecommunications satellites, prompted the development of CdS on CuS<sub>2</sub> heterojunction cells, in a trade-off between light weight and low conversion efficiency (7%). The general panorama of photovoltaic solar cells efficiency for space applications has improved along the years up to a current average maximum value of 30%. These efficiency ranges encompasses nanosatellites because solar cells can be easily adapted to satellite's size and shape.

Multi-junction GaAs on germanium substrate solar cells are commonly used in the space industry. For instance, Spectrolab [129] offers different options with flight-tested technologies based on GaInP<sub>2</sub>/GaAs/Ge with conversion efficiencies up to 29.5% reported for the NeXt Triple Junction (XTJ) Solar cell. A Spectrolab product of particular relevance for nanosatellite platforms is the Triangular Advanced Solar Cell (TASC) with  $\eta_{\square}$  of 27%. Although the TASC was originally designed for terrestrial applications, it has been used in nanosatellites to fit irregular geometries (e.g. KySat-1) and small sizes (e.g. KickSat). In another example, AZUR SPACE [90] offers advanced triple junction InGaP/GaAs/Ge solar cells with the best current performance in the market, i.e. 30% reported in its 3G30C advanced solar cell. Fig. 2.18 illustrates the reported best research multi-junction cell efficiency and the current efficiency of commonplace

cells for space applications. From Fig. 2.18, the reported cell conversion efficiencies

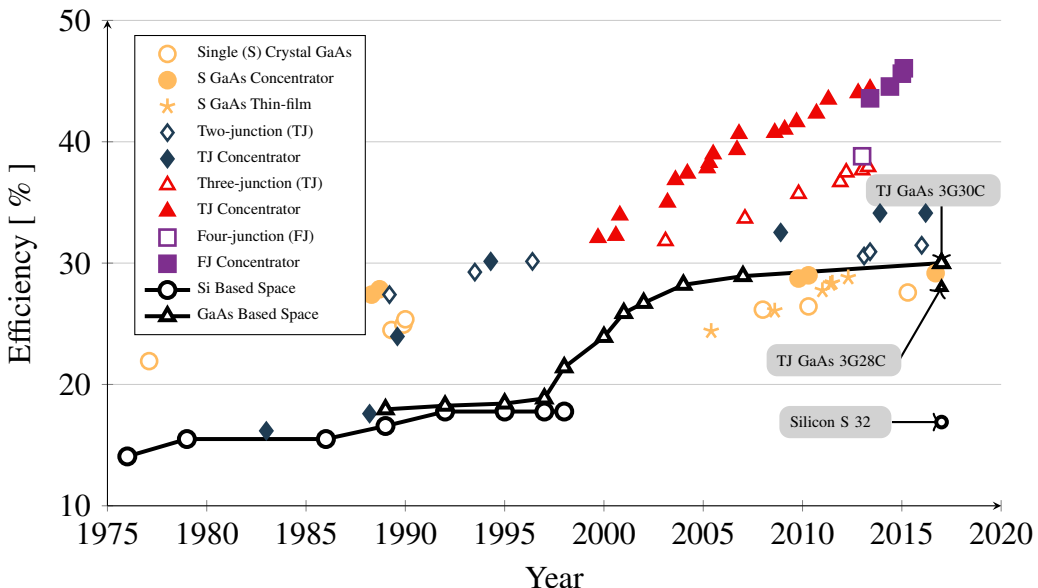


Fig. 2.18 Best research multijunction vs nanosatellite solar cell energy conversion efficiencies. Examples of current nanosatellite cells are labeled in the plot. Data from the National Renewable Laboratory - Photovoltaic research [130] and AZUR SPACE [90].

for space applications are evidently lower than those for cutting edge cells. Selection of space qualified technologies and materials is restrained by their adequacy to endure the harsh space environment conditions such as high-energy radiation, thermal cycling, electrostatic discharge damage, materials outgassing, micrometeoroids, chemical reactions, propulsion system plume impingement, etc. Ionising radiation eventually reduces transmittance in cover glasses by a complex mechanism where exited electrons are trapped by impurities present in the glass forming stable compounds that darkens the material. Another effect of ionising radiation is the displacement of silicon atoms from their lattice. With time, the generated vacancies form stable defects lowering efficiency. Ongoing research is focused on developing new glass materials with improved radiation endurance and wider spectral transmittance to enable more efficient multi-junction units. A research study on temperature and radiation effects in space-qualified GaAs-based and Si-based solar cells at 80 – 300 K [131], show that conversion degradation is almost independent on temperature for GaAs and strongly dependent on temperature for Si.

## Nanosatellites Overview

---

However, distinctive low thermal capacitance in nanosatellites could raise long term issues about the cyclical thermal loading resulting from orbit eclipse-daylight conditions. For example, thermo-mechanical fatigue in the solar cells can form micro cracks reducing power conversion efficiency. Even though for the current short lifespan technology demonstration nanosatellite mission, solar cell degradation does not represent a big concern, it would require special attention for functional nanosatellite missions with broader lifespans and characteristic high power densities (e.g. for EP operation).

The inexorable solar cell degradation is a very important factor for power system design. In nanosatellite platforms, modest efficiency variations could impact the overall mission plot due to the high aforementioned power densities. This in turn has repercussions on the required solar cell area and characteristics of the power storage subsystem. Solar cell degradation prompts the definition of the terms Beginning-Of-Life BOL and End-Of-Life EOL to describe extreme limits of cell performance. Reported BOL and EOL values are usually referenced to standard laboratory conditions, i.e.  $T_A = 28^\circ\text{C}$ , solar irradiance spectrum in space (AM0), and solar flux equal to  $135 \text{ mW/cm}^2$ . Clearly, BOL values correspond to the best product performance, and EOL to the worst performance scenario. Thus, EOL values are used in the power system design process. A common rule of thumb is to scale down the EOL solar panel efficiency by 60 – 96% depending on power design margins of the mission.

The input power generated by solar cells onboard of a satellite depend on cell parameters, orbit and attitude characteristics, and solar influence. Fig. 2.19 presents an example of input power profile for a tumbling CubeSat about 3 axis wherein the effect of satellite dynamics on the bare harvested power is clearly visible. The factors in the input power equation (2.23) are the solar cell effective area  $A_{\square}$ , cell conversion efficiency  $\eta_{\square}$ , sunlight coefficient  $\mathcal{T}_{\odot}$  (i.e. 0 – 1 from eclipse to sunlight), solar irradiance  $I_{\odot}$ , and solar radiation angle of incidence with respect to the cell surface  $\phi_{inc}$ .

$$E_{in} = \underbrace{A_{\square} \eta_{\square}}_{Cell} \underbrace{\mathcal{T}_{\odot}}_{Orbit} \underbrace{I_{\odot}}_{Sun} \underbrace{\cos \phi_{inc}}_{Attitude} \quad (2.23)$$

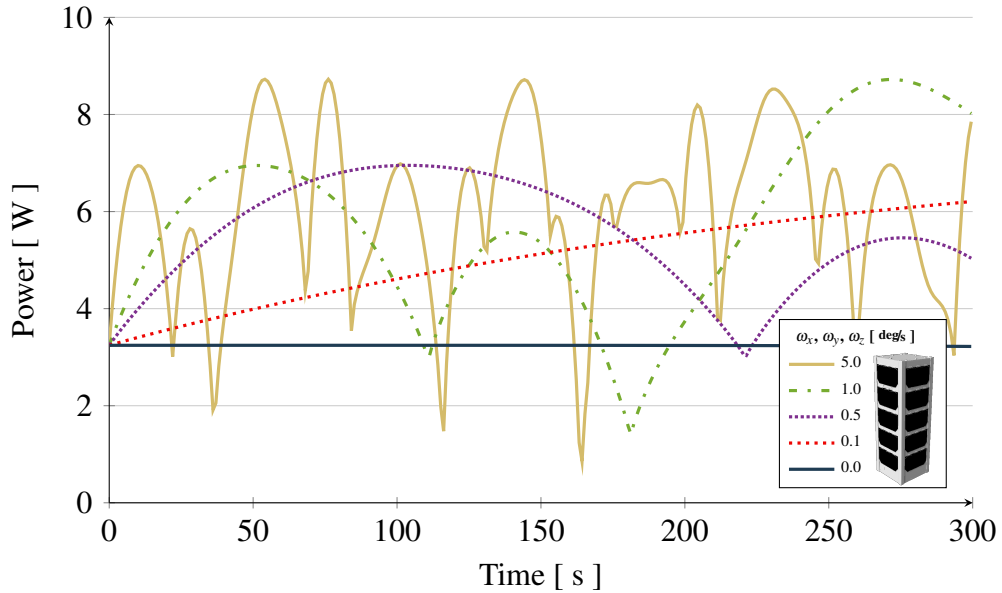


Fig. 2.19 Example of input power profile in a 3U CubeSat during sunlight for various body angular velocities. Simulation results for 15 solar cells with 30% conversion efficiency, distributed on three lateral surfaces of a standard 3U CubeSat.

Regarding the solar cell parameters, these are normally well defined for short periods of time. The orbit trajectory defines the time the satellite remains in sunlight ( $\mathcal{T}_{\odot}$ ) per orbit having a direct effect on the amount of produced power. Earth's orbital eccentricity causes  $I_{\odot}$  variations of approximately  $\sim \pm 3.4\%$  on the average total solar irradiance of  $1361 \text{ W/m}^2$ ; observed trends are presented in Appendix D. The value of  $\phi_{inc}$  is the less tightly defined factor, specially in the typical tumbling or coarsely controlled nanosatellites.

The value of  $\mathcal{T}_{\odot}$  is a function of the orbit parameters and solar vector. For circular orbits, a reasonable assumption for average nanosatellite missions<sup>4</sup>, the state of the orbit-sun vectors system can be easily assessed using the relative angle  $\beta$  between the orbital angular momentum vector direction  $\hat{h}$  and the solar vector direction. In this proposed approach, Equation (2.24) defines the solar position unit vector as function of the Sun declination  $\delta$  and right ascension  $\alpha$  in Earth-Centered-Inertial (ECI) reference frame, whereas the unit vector  $\hat{h}$  can be expressed in terms of orbit inclination  $i$  and

orbit right ascension of the ascending node  $\Omega$  as shown in Equation (2.25).

$$\hat{r}_\odot = \begin{bmatrix} \cos \alpha \cos \delta & \sin \alpha \cos \delta & \sin \delta \end{bmatrix}^T \quad (2.24)$$

Equation (2.25) is obtained with the transformation from perifocal frame to the ECI reference frame of the unit vector normal to the plane of the orbit, i.e. parallel to the orbital angular momentum vector.

$$\hat{h} = \begin{bmatrix} -\sin i \sin \Omega & \sin i \cos \Omega & -\cos i \end{bmatrix}^T \quad (2.25)$$

Finally, the angle  $\beta$  is obtained from the dot product of  $\hat{h}$  and  $\hat{r}_\odot$  shown in Equation (2.26). Note that the sign of  $\hat{h}$  is established by whether the orbit is prograde or retrograde, however the value of  $\beta$  should be considered absolute.

$$\cos \beta = \cos i \sin \delta - \cos \delta \sin i \sin (\alpha - \Omega) \quad (2.26)$$

Fig. 2.20 illustrates an example of the relative angle  $\beta$ ,  $45^\circ$  in this case, between an orbit ( $i = 45^\circ$  and  $\Omega = 90^\circ$ ) and the Sun vector at vernal equinox ( $\delta = 0^\circ$  and  $\alpha = 0^\circ$ ) projected on the celestial sphere. The parameters used in the computation of  $\beta$  relate the solar vector to the orbit orientation. The final step to estimate  $\mathcal{T}_\odot$  is to introduce the effect of orbit altitude to its value. The gradual atmospheric dimming effect on orbits transiting from sunlight to eclipse condition and effects of Earth oblateness adds to the complexity of an analytic solution in this case. A way to overcome this difficulty and obtain a simple method to estimate  $E_{in}$ , is through the comparison of precomputed values of  $\mathcal{T}_\odot$  as function of  $\beta$  from high accuracy numeric orbit propagations. Fig. 2.21 shows the plots of the average sunlight orbit percentage, i.e.  $\mathcal{T}_\odot$  as a percentage of orbit period, for the possible range of  $\beta$  values and orbit altitudes of interest.

After the description of the method and continuing with the preceding example, the analysed inclined orbit would be in sunlight from  $\sim 60\%$  up to  $\sim 75\%$  per orbit for the possible range of altitudes reported in the Fig. 2.21. It is necessary to bear in

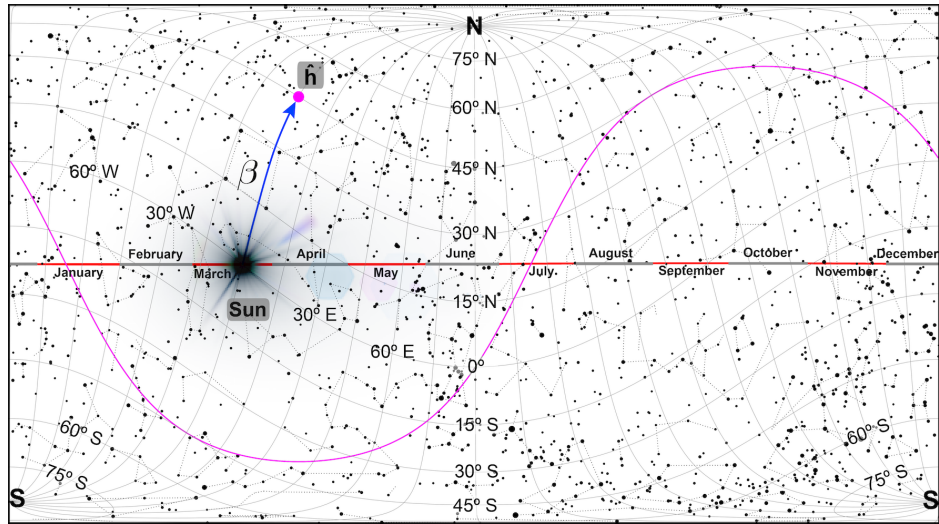


Fig. 2.20 Relative angle  $\beta$  between the orbital angular momentum vector direction  $\hat{h}$  and the solar vector direction. In this example the undulating thick curve represents an inclined circular orbit, at  $45^\circ$  with right ascension of the ascending node of  $90^\circ$ , projected on the celestial sphere. The solar vector, moving horizontally from left to right along the year, is positioned at the vernal equinox in this example. The corresponding value of  $\beta$  is  $45^\circ$ .

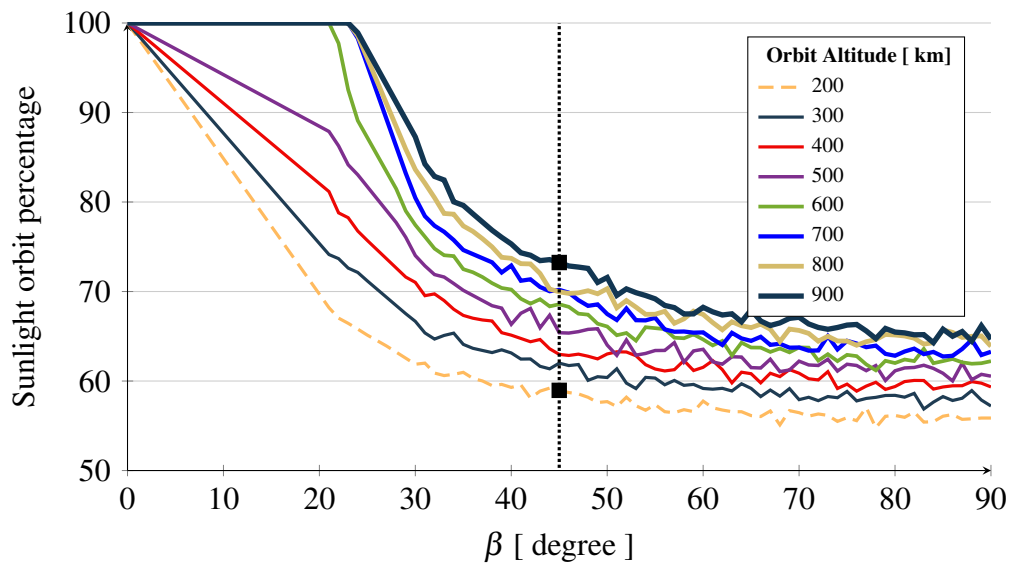


Fig. 2.21 Sunlight orbit percentage. Extreme condition values correspond to circular polar orbits ( $\beta = 0^\circ$ ), and circular equatorial orbits ( $\beta = 90^\circ$ ). Note that higher orbital altitude yields to an increased  $\beta$  margin for 100% sunlight, e.g.  $\beta = 0 - 20^\circ$  at 600 km. The angle of aperture of this tolerance cone results from the effect of the play between orbit size and Earth's shadow avoidance. In continuation to the example at hand, the vertical dashed line marks a range of sunlight orbit percentages for various orbit sizes for  $\beta = 45^\circ$ .

mind that  $\beta$  is a remarkably dynamic variable as it varies with the Sun position and orbit nodal precession. With the exception of sun-synchronous orbits, where orbit nodal precession and  $\Omega$  are tuned, estimations using this simple method remain valid only for short periods of time depending on the Sun-orbit system variation.

### 2.4.2 Power Storage

Current nanosatellites use rechargeable batteries, so called secondary batteries, in a trade-off between onboard resources and mission objectives as most nanosatellites are capable of generating power using photovoltaic solar cells. Rechargeable batteries are used to sustain and support operations during peak power requirements or eclipse periods. Conversely to the power generation subsystem, which is chiefly limited by surface availability using solar cells and therefore relatively distinctive in standard nanosatellites, power storage subsystem is contained and carefully protected within the nanosatellite specially against extreme temperature exposure. Hence, specific nanosatellite mission energy budget requirements tightly define most of its characteristics.

Power storage subsystems in nanosatellites are based on COTS technologies originally developed for the personal electronic devices market, which is in constant and accelerated innovation. In this respect, the quest for better, reliable, light weight, and powerful personal electronic devices stimulates the development of miniaturised and high energy density batteries. Fortunately, these characteristics are ideal for nanosatellites. Suitable rechargeable battery options for nanosatellite formats [24, 28, 132, 133], show the common selection of Lithium-ion and Lithium polymer technologies. This preference is based on characteristic element size and specific energy values for these technologies. For instance NiCd or NiH<sub>2</sub> rechargeable batteries are excluded for the use in nanosatellites mainly because are large and heavy even though these options offer around 120 times more life cycles. On the other hand, in terms of specific energy, Li-Ion and Li-Polymer typical values range from 135 Wh/kg to 160 Wh/kg versus 25 – 35 Wh/kg for NiCd or NiH<sub>2</sub> [122].

The concepts and current state-of-the-art in nanosatellites discussed in this chapter, enable the identification of key factors for the advancement of propulsion technologies for nanosatellite systems. Chapter 3 presents the research aim and approach of this thesis.

Blank page

# **Chapter 3**

## **Research aim and approach**

The objective of this thesis investigation is the development of generic inclusive tools for the characterisation and optimisation of propulsion systems in nanosatellites. The investigation topics are chosen by the their practicality and general relevance to typical propulsion systems in commonplace nanosatellite missions. Particular aspects of propulsion technologies susceptible to improvement such as specific design concerns, unusual spacecraft configurations and hardware, etc., are out of the scope of this investigation. The chosen topics from the research aim delimitation, render appropriate the development of suitable computational tools for concepts assessment. This chapter presents the investigation hypotheses and developed research computational tools.

### **3.1 Research Aim**

The inclusion of propulsion systems in nanosatellites represents a major breakthrough to their development and extended applicability. Miniaturisation of relevant technologies in conjunction with the development of suitable propulsive concepts for nanosatellites are leading to specific technologies that will enable functional and profitable missions. Overall systems miniaturisation in nanosatellites, and the platform size itself, establish concomitant challenges to overcome to permit optimal propulsion systems operation.

## **Research aim and approach**

---

Historical nanosatellite missions are limited to low LEO orbits due to several factors as discussed in Chapter 2. Although broad specialised nanosatellite mission concepts are possible, e.g the Garatéa-L lunar mission, low LEO orbits are commercially valuable chiefly for Earth observation, as advertised by the numerous Spire Global Lemur and Planet Labs Flock missions. This observation identifies common circumstances of the general application of propulsion systems in nanosatellites. Specifically the predominant effect of atmospheric drag on low LEO orbits evolution, puts forward the need for more detailed analysis of atmospheric interaction with nanosatellites. The outcome of such analysis would improve the design and optimisation of propulsion systems for drag offsetting, or prompt timely orbit re-entry in compliance to international disposal guidelines.

Current atmospheric density models are able to capture most major spatial and temporal variations by employing solar and geomagnetic indices from observations. Fig. 3.1 shows the record of solar indices inputs of the Jacchia-Bowman thermospheric density model 2008 and the corresponding interval of the sunspot number record. From the figure it is observed that sunspot activity is highly correlated to the input solar indices of the density model. On the other hand geomagnetic index fluctuation is correlated to a lesser extent to solar activity, viz. the correlation coefficient of the Disturbance Storm Time (DST) index record and the SSN record is 0.20. Yet solar activity largely dominates most aspects of atmospheric density variation with only slight interference of geomagnetic characteristics. The above implies that atmospheric density models encompass time intervals in which indices values are known. This condition inevitably limits the use of atmospheric density models to assess historical orbital data. However, it is still possible to use atmospheric density models in analyses applied to future conditions if the solar and geomagnetic conditions are expected to be similar to past documented data. This is an acceptable approach by taking into consideration that uncertainty is expected from a solar activity forecast.

Short-term atmospheric density forecasts are of reduced value in the design and optimisation of propulsion systems intended to offset its effects yielding longer lifespan.

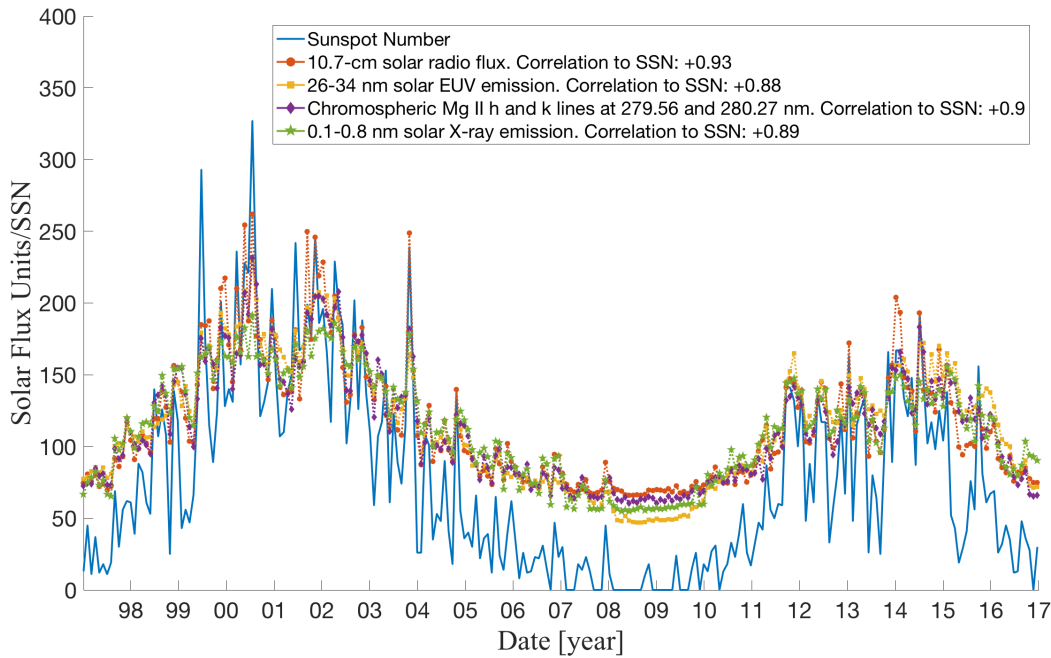


Fig. 3.1 Sunspot number and solar radiation wavelengths responsible of major Earth atmosphere variations. These solar radiation wavelengths and a geomagnetic index are used as input indices in the Jacchia-Bowman thermospheric density model 2008 [134]. Sunspot activity is highly correlated to the solar indices input, which largely dominates most aspects of atmospheric density variation.

However, long-term atmospheric density forecasts are prone to high levels of uncertainty. The case of the GOCE satellite [43] discussed in Chapter 1, is a clear example of the tight dependency of propulsion system sizing to long-term atmospheric density forecast validity. Overall reduced resources in nanosatellites step up the importance of satisfactory atmospheric density forecasts.

Another aspect of relevance of atmospheric drag on low LEO orbits, is the way the atmosphere interacts with the spacecraft. The interaction may be unique according to atmospheric composition, surfaces' characteristics, and environment conditions. Fortunately, the standardised characteristics of nanosatellites may serve as an asset to identify common interaction profiles. Note however that atmospheric composition estimation is limited, as in atmospheric density estimations, to outdated analysis or forecasted data from the mission design point of view. Consequently useful atmospheric

## **Research aim and approach**

---

density and atmospheric composition estimations for propulsion system design and optimisation, point out to adequate and reliable forecasted data.

With respect to onboard technology, low thrust propulsion systems are intrinsic to nanosatellites as discussed in Chapter 2. Low thrust related to high propellant mass efficiency, as in EP systems, is valuable in long term orbit manoeuvres such as atmospheric drag offsetting discussed above. Supplementary attitude manoeuvres are possible with low thrust actuation, such as fine pointing capability for Earth observation, wherein adequate thruster characterisation is fundamental to ensure satisfactory operation. Amongst the parameters in thruster characterisation, the thrust vector profile is preferably determined through the physical reaction it produces. Whilst thrust vector transients phenomena are mainly dictated by the specific thruster technology attributes and operation conditions, out of the scope of the investigations presented herein, the determination of distinctive thrust levels is of general interest and therefore suitable for investigation in the framework of this thesis project.

Motivated by the aforementioned aspects, this thesis sets out to address general key factors for the advancement of propulsion technologies for nanosatellite systems. Ordered by importance for propulsion systems, the hypotheses presented in this thesis are:

- *Solar activity forecast reliability can be improved by assembling historical sparse accumulated knowledge about solar attributes because it allows the refinement of current solar physics models*
- *Observed orbital decay assessment in standard nanosatellites furnish valuable information about distinctive drag-entailing phenomena because atmospheric interaction is led by geometric and material features intrinsic to nanosatellites*
- *Low thrust levels are effectively characterised using COTS sensors through the analysis of induced low frequency responses because long term changes are more easily identifiable by non-specialised low resolution sensors*

The first hypothesis looks into the forecast of solar activity since it is a proxy for meaningful orbital perturbations chiefly atmospheric drag in LEO orbits. The second hypothesis looks into the geometrical properties of standard nanosatellites to identify characteristic drag coefficients. The final hypothesis in this thesis looks into the inertial properties of standard nanosatellites to overcome common attitude determination deficiencies using COTS sensors precluding satisfactory in-orbit low thrust characterisation. A point worth remembering is that this comparison is valid with respect to specialised attitude determination equipment as discussed in subsection 2.2.1, e.g. the Modular Gravitational Reference Sensor [135], since general-use space qualified components are typically less advanced and less power efficient than COTS (subsection 2.3.1).

## 3.2 Research Approach

By virtue of the characteristics of the hypotheses set forth, numerical simulations provide the sole means for testing. Bespoke algorithms are developed to this aim, including updated precise mathematical models to reproduce main features of interest with sufficient detail to carry out the analyses. The block diagram in Fig. 3.2 presents the generic features of the devised Orbit Propagator (OP), wherein the blocks related to specific test are marked accordingly.

The selection of an adequate programming language for scientific computing is based on project priorities and factual reasons. Opinions on this topic are abundant as discussed by Maclaren [136]. In this thesis the OP algorithm is implemented in MATLAB<sup>®</sup> due to its accessibility and suitability during the development of the investigations. The main motivation in selecting MATLAB is the reduced time required for project *development* due to the numerous built-in routines. From the runtime standpoint, there may be inherently quicker low-level programming languages such as FORTRAN or C++, however great variability exists in this respect according to

## Research aim and approach

---

performance tests [137]. As performance is not as critical as development time in the investigations presented herein, the use of MATLAB is rationally justified.

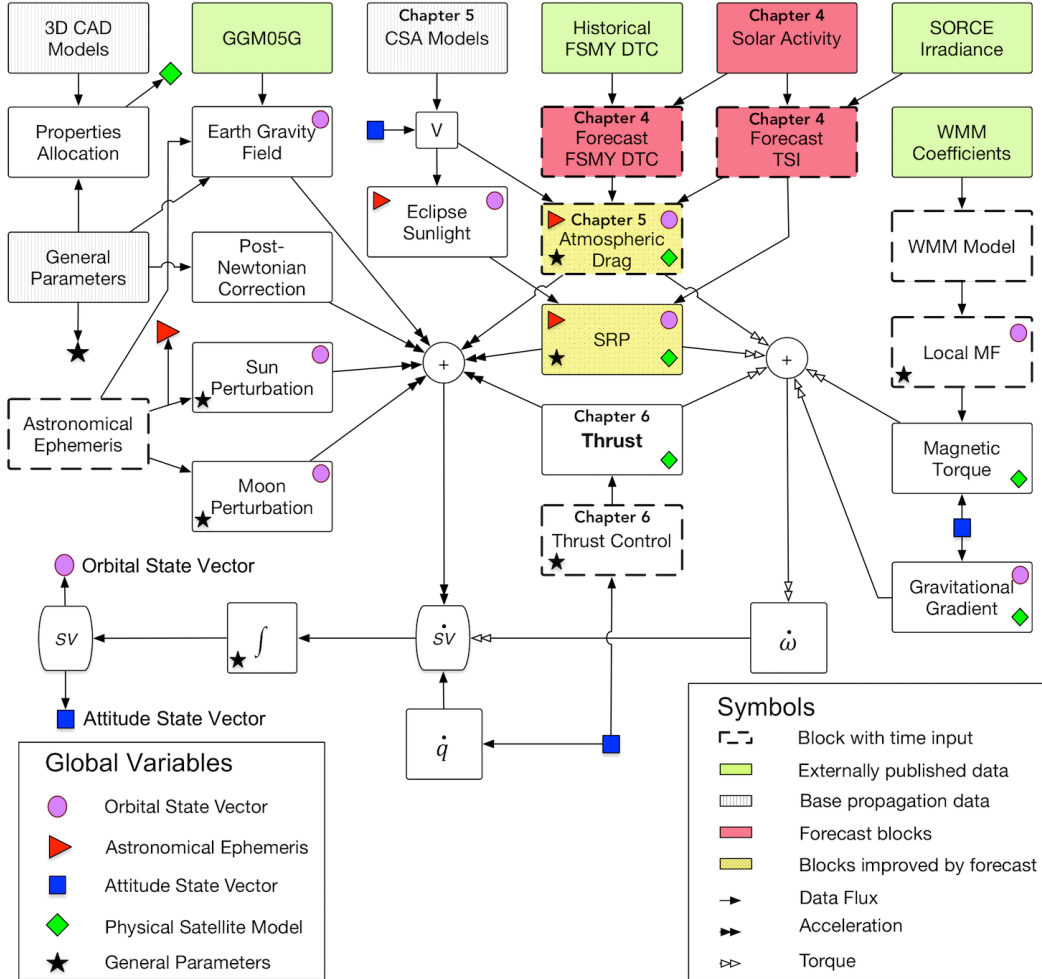


Fig. 3.2 Orbit Propagator generic block diagram. Blocks related to the main investigation topics presented in the following chapters are marked accordingly. Blocks concerning Chapter 4 are labeled *Forecast* as the outcome of that investigation aims to replace the current short-term forecast algorithm implemented with an autoregressive time series model (AR [138]). Blocks related to external databases e.g. indices and coefficients, are highlighted in light green colour.

The OP implements the numerical integration of the Cowell's formulation in Earth-Centred Inertial (ECI) reference frame [139]. Firstly, the main orbit perturbations (discussed in Chapter 2) estimated by the OP model include the Earth's gravity field using the GRACE+GOCE Gravity Model [140] (GGM05G). The GGM05G model incorporates GRACE and GOCE accelerometer and gradiometer data represented in the published model spherical harmonics. This publicly available data is used by the OP's

algorithm to estimate the gravity field for a maximum degree and order of 240. The selection of the GGM05G model was motivated by its updated characteristics amongst other models, by the time the Earth Gravity Field block algorithms in the OP were developed (2015). A comprehensive database of recent global gravity field models is available at the International Centre for Global Earth Models [141] website.

The atmospheric drag is estimated using atmospheric data supplied by the Jacchia-Bowman Thermospheric density model 2008 (JB2008). The selection of the JB2008 follows the recommendation of the ECSS [142] regarding the use of JB2006 for atmospheric density calculations above 120km, the CIRA Working Group [143] ratification of JB2008 for preferred use above that orbital altitude, and the JB2008 performance tests reported by Vaughan [144]. The JB2008 code and related indices embedded in the OP are publicly available from the Space Environment Technologies [134] website. Due to OP data interface adequacy and cross-platform considerations, e.g. executable files (.exe files) portability limitations, dedicated JB2008 code translation from its native FORTAN to MATLAB was carried out.

The OP Solar Radiation Pressure (SRP) estimation uses empirical solar irradiance data from the SOlar Radiation and Climate Experiment SORCE [145] and conical eclipse condition formulae from Neta and Vallado [146]. Third-body perturbations algorithm use high-precision ephemeris with formulae from Reda [147]. Magnetic torque estimations use the Wold Magnetic Model (WMM). Similarly to the gravity field model, the WMM uses spherical harmonics (degree and order 12) publicly available from the BGS and NCEI [88] website. The WMM code is in the public domain and an implementation is included in the MATLAB Aerospace Toolbox. In this case an optimised version of the existing code for iterative application, viz. for OP ODE solution, is developed for the incorporation to the OP.

Amongst the bespoke algorithms making up the OP, satellite attitude dynamics handling is of major relevance for the investigations presented in Chapter 5 and Chapter 6. In this respect, body torques are estimated on 3D CAD satellite models. An example of OP CAD model treatment is shown in Fig. 3.3 for a given instantaneous perturbing

## Research aim and approach

---

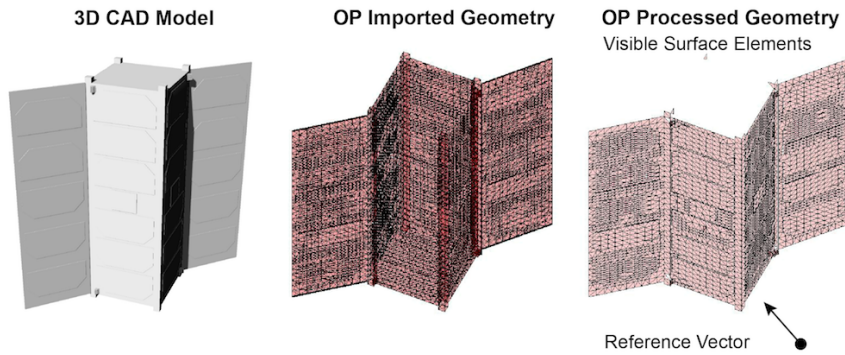


Fig. 3.3 OP 3D CAD model treatment example. The satellite model is processed from left to right in the figure.

reference vector, e.g. SRP. In this application, the algorithm processes the 3D CAD model in order to identify relative visible surface elements for computation; this dynamic process enables detailed self-shadowing identification. In terms of computational burden, attitude estimation involving 3D CAD processing is by far the most demanding process in the OP. Attitude propagation may represent up to 90% of the computing time depending on the characteristics of the current ODE dynamic model solution. Another source of major computational burden variation in the OP is the number of gravity model spherical harmonics ( $sh$ ) used for propagation, which follow a near square rule viz.  $ctime \propto sh^{1.94}$ .

Solar activity forecast is linked to the main non-conservative disturbing forces in the OP model, i.e. the atmospheric drag and solar radiation pressure. In Chapter 4 a solar activity forecast approach for space environment estimation is proposed. The atmospheric drag and the Cross-Sectional Area (CSA) models blocks are used in Chapter 5 to estimate drag-entailing phenomena. Finally Chapter 6 describes the implementation of the thrust blocks to propose a method for in-orbit low thrust characterisation. Altogether, these topics tackle the key general matters aiming towards the development and improvement of propulsion systems in nanosatellites.

### **3.2.1 Orbit Propagator Verification**

The OP programming is an arduous task involving iterative code revisits to improve execution time and agreement between estimated and existing data. The programming language choice made necessary the translation and adaptation of existing external models to suit the OP format. The most relevant example of this kind is the JB2008 model, which was formerly available only in FORTRAN language requiring full translation into MATLAB language followed by exhaustive self verification. In general, exhaustive verification is applied to every piece of code conforming the OP from the spacecraft 3D CAD model design and import, properties and materials allocation, up to the required accuracy of the OP integrator.

The OP algorithm resulted from the judicious selection of mathematical models and careful programming implies some degree of precision that requires quantification. For the sake of OP verification, observed orbital data of the Ball Lens In The Space (BLITS) nanosatellite is used in this discussion. The BLITS nanosatellite launched in September 2009, is a spherical glass reflector of 17 cm in diameter and mass of 7.53 kg designed for precise satellite laser ranging. The basic geometry and negligible attitude dynamics impact on orbit estimations, at least before its collision with space debris in January 2013, makes BLITS mission ideal for OP verification. Orbital data in the form of TLE sets is used for this purpose, though TLEs resolution and exactness are reduced they represent the only resource of orbital data used in this thesis, specifically in Chapter 5. For the purpose of the investigations herein, verification of the OP to ensure required estimations quality is sufficient. However, it is necessary to emphasise that OP *validation* requires highly accurate and precise orbit ephemeris stating a clear difference between the validation and verification concepts.

Orbit propagations from the customary Simplified General Perturbations 4 (SGP4), which is based in Kozai's theory and uses TLE set data natively, offers an adequate benchmark for OP verification. Fig. 3.4 presents the residuals in satellite-radial reference frame (RSW) of 1000 TLE sets (before the year 2013) propagated for time arcs

## Research aim and approach

---

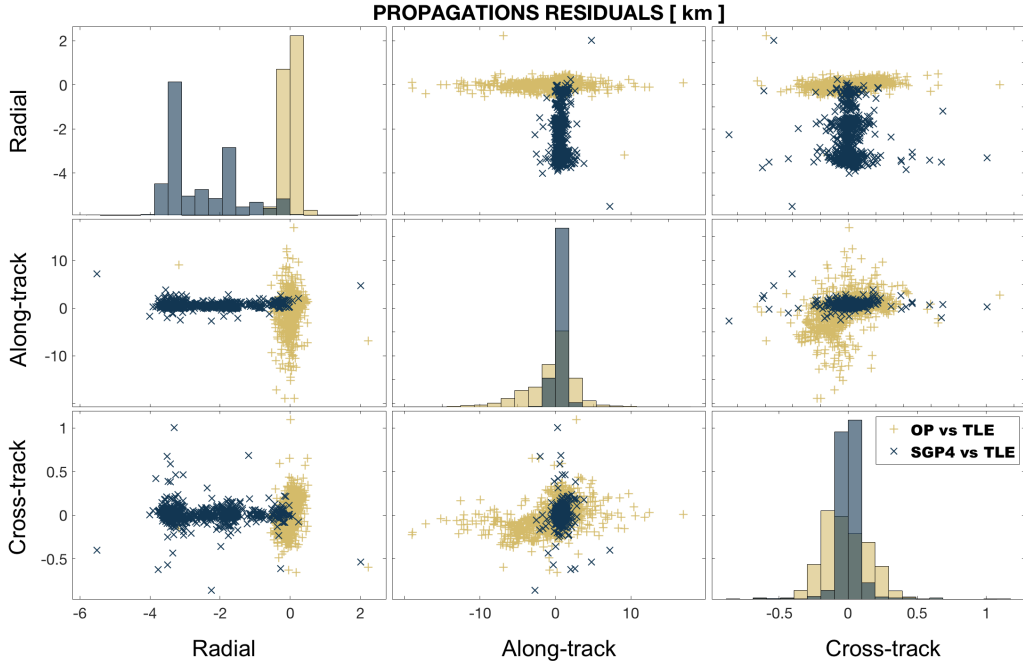


Fig. 3.4 Propagations residuals in satellite-radial reference frame from OP and SGP4 orbit propagations with respect to TLE data. Test on BLITS nanosatellite orbital data.

corresponding to the time gap between a TLE set to next successive set, e.g. 0.57 Julian days in average. Residuals from TLE-SGP4-TLE show reduced variability along-track and cross-track in comparison to TLE-OP-TLE propagations. Conversely residuals in the radial direction, related to orbital decay, from TLE-OP-TLE propagations are better contained. The reduced consistency observed in the OP residuals in comparison to the SGP4 residuals is clearly foreseeable as a consequence of the additional TLE data transformations needed to interphase to the OP. In general terms the TLE data is transformed from its original form involving Kozai mean values to Keplerian orbital elements, and from the True Equator Mean Equinox TEME [148, 139] coordinate system to the True equator Of the Date TOD reference system. These transformations inherently add slight errors resulting primarily from numeric computation rounding. At this point it is important to recognise that the OP estimated data, although presumably highly precise, is a function of the quality of the initial orbital state used in the propagation. The major advantage of the OP is that it provides opportune discrimination of orbit perturbations, unattainable by the SGP4. In summary, the magnitude of the residuals presented in

Fig. 3.4 roughly verify the OP and evince initial state conversion concerns requiring additional attention.

In order to look into more detail at the OP sensitivity to the initial state vector, it is prudent to evaluate the significance of orbital velocity variation. In this analysis the BLITS nanosatellite state vector in ECI derived from the first reported TLE set is used. Each velocity component is modified individually and propagated for one Julian day. The overall range of velocity variation encompasses  $\pm[0.001 - 100]$  metres per second. The propagation of the residuals with respect to the unmodified initial state vector are shown in Fig. 3.5. From the figure it is observed that the along-track residual component is subject to large variation in all  $\Delta v_{ECI}$  components. Variation of  $\sim 0.1$  metre per second, or  $\sim 0.0001$  kilometres per second in the TLE format and OP model scale, prompts along-track residuals from 10 kilometres to nearly 90 kilometres. This observation provides a qualitative explanation to the magnitude of the along-track residuals variability in the TLE-OP-TLE plot in Fig. 3.4.

The identified sensitivity of orbit propagations to the initial orbital state vector forewarns about the possible implications of interfacing TLE data. In this regard, the investigation presented in Chapter 5 employs observed orbital data from TLE sets as fundamental constituent for analysis of atmospheric drag. However, the formulated robust approach expound in that chapter is attentive to orbit propagation sensitivity issues. It is found that orbits below 500 km are less likely to suffer major repercussions although the general rate of successful identification of useful data is inevitably reduced in all instances analysed in that chapter. Considering that the major source of uncertainty is extrinsic to the OP itself (it is caused by quality of the interfaced data), and the consistency of the successfully identified data, the mitigating approach employed in Chapter 5 is deemed as opportune.

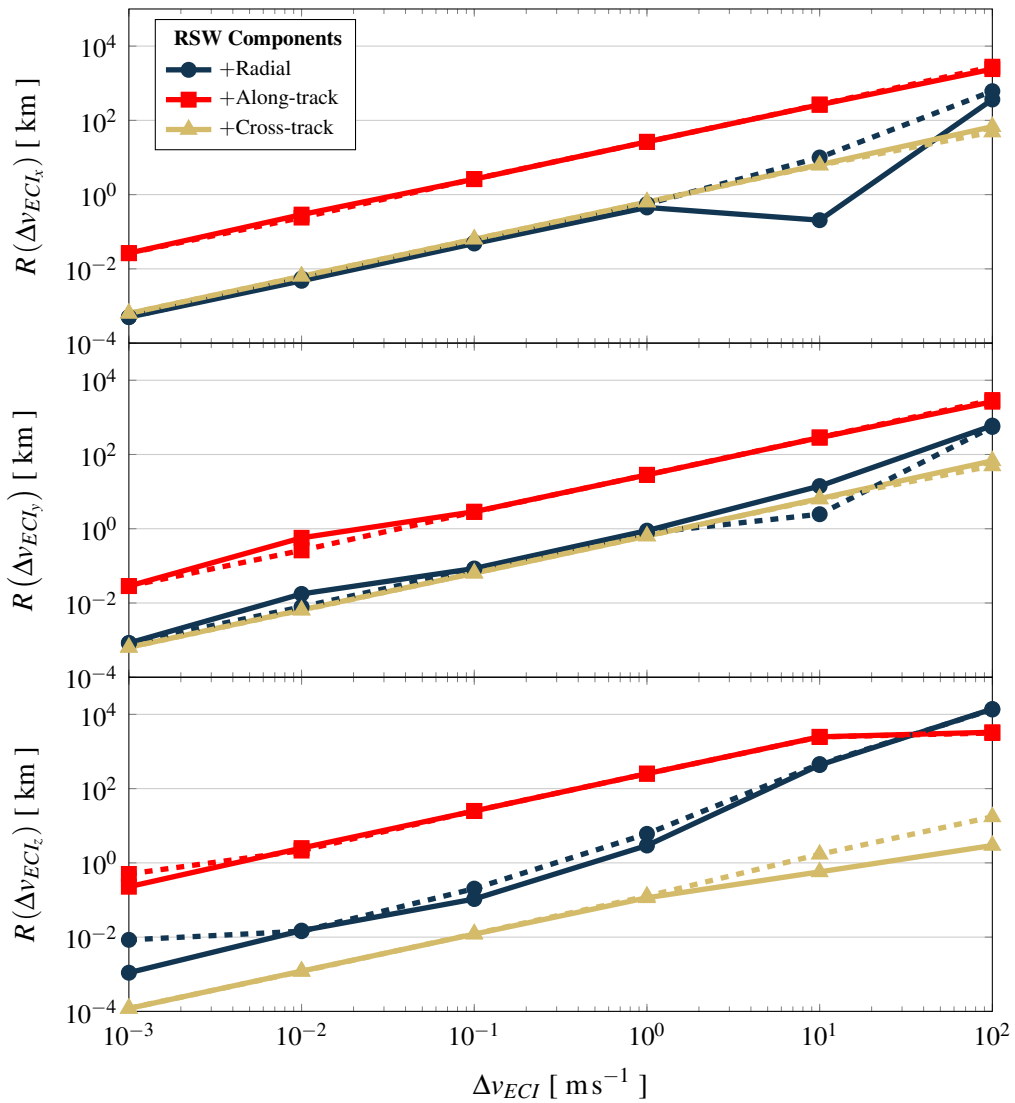


Fig. 3.5 OP sensitivity with respect to the initial state vector. Test on BLITS nanosatellite orbital data. Dashed lines show the residuals of decrements in each RSW component.

### Attitude Propagation Verification

Attitude propagation relies on the estimated precision of the perturbing forces and their interaction with the nanosatellite model. As a method of verification of the OP attitude propagation, the propagator's ability to emulate magnetic lock of a Passive Magnetic Attitude Control system on a 3U CubeSat is evaluated. Magnetic lock is assumed in this test when the permanent dipole vector follows stably the local Earth magnetic field vector and that it does not deviate from the latter by more than  $30^\circ$ . This method of verification is chosen because it tests the maximum capabilities and complexity endowed to the OP, viz. all environment perturbations interacting with the nanosatellite model. Additionally, the magnetic lock reference value is chosen from the reported design requirement simulations for the 3U CubeSat Delfi-C<sup>3</sup> [149]. A selection of main simulation parameters is presented in Table 3.1. The Magnetic Torque block in Fig. 3.2 comprises the residual dipole (byproduct of onboard electric operation), a permanent dipole along the  $z$  axis providing restoring torque to match the local Earth magnetic field, and two transversal hysteresis rods in the  $x - y$  plane to dissipate body kinetic energy.

Fig. 3.6 shows the simulation results for the magnetic angle, body kinetic energy, body angular velocities, and input electric power as a proxy of the cyclic space conditions along the orbit. The simulation starts at near antiparallel magnetic vectors to reproduce extreme magnetic interaction conditions. Successful emulation of magnetic lock is by no means a fortuitous event. It requires the gradual stabilisation of the spacecraft dynamics along the fluctuating space environment, reaching quasi-equilibrium (if exists) about the varying local Earth magnetic field. For the parameters in Table 3.1, magnetic lock is achieved after 450 min in the simulation. Body energy dissipation through the hysteresis rods gradually damps out the drastic initial restoring torque from the magnetic system alignment. The body angular velocity plot shows progressive reduction on the three axes, with maximum amplitude in  $\omega_z$  in concordance to the nanosatellite's reduced moment of inertia on that axis.

## Research aim and approach

---

Table 3.1 Main simulation parameters

Variable	Value	Remarks
<b>Keplerian orbital elements</b>		
Geometric altitude	500	km
Eccentricity	0	—
Inclination	90	°
Longitude of the ascending node	0	°
Argument of periapsis	0	°
True anomaly	90	°
<b>Nanosatellite*</b>		
Mass	3	kg
$I_x$	0.0281	$\text{kg m}^2$
$I_y$	0.0281	$\text{kg m}^2$
$I_z$	0.0050	$\text{kg m}^2$
$\omega_{x_0}$	0.0	°/s
$\omega_{y_0}$	0.0	°/s
$\omega_{z_0}$	0.0	°/s
<b>Magnetic circuit</b>		
Residual dipole	0.01	$\text{Am}^2$
Permanent dipole flux density	1.28	T
Coercive force $H_c$	1.59 †	A/m
Remanence $B_r$	0.35 †	T
Saturation induction $B_s$	0.73 †	T
<b>Miscellaneous</b>		
Propagation time	500	min
Simulated date and time	2003/03/21 12 : 00 : 00	Near to vernal equinox
Gravity model	GGM05G	10 <sup>th</sup> Degree and order
Thermospheric density model	JB2008	—
Solar irradiance data	SORCE	—

\* 3U CubeSat

† Magnetic hysteresis material HyMu80

The OP general simulation capability is used in Chapter 5 and Chapter 6. Supplementary models are used to forecast solar activity that because of their specific nature, Chapter 4 is devoted to their description.

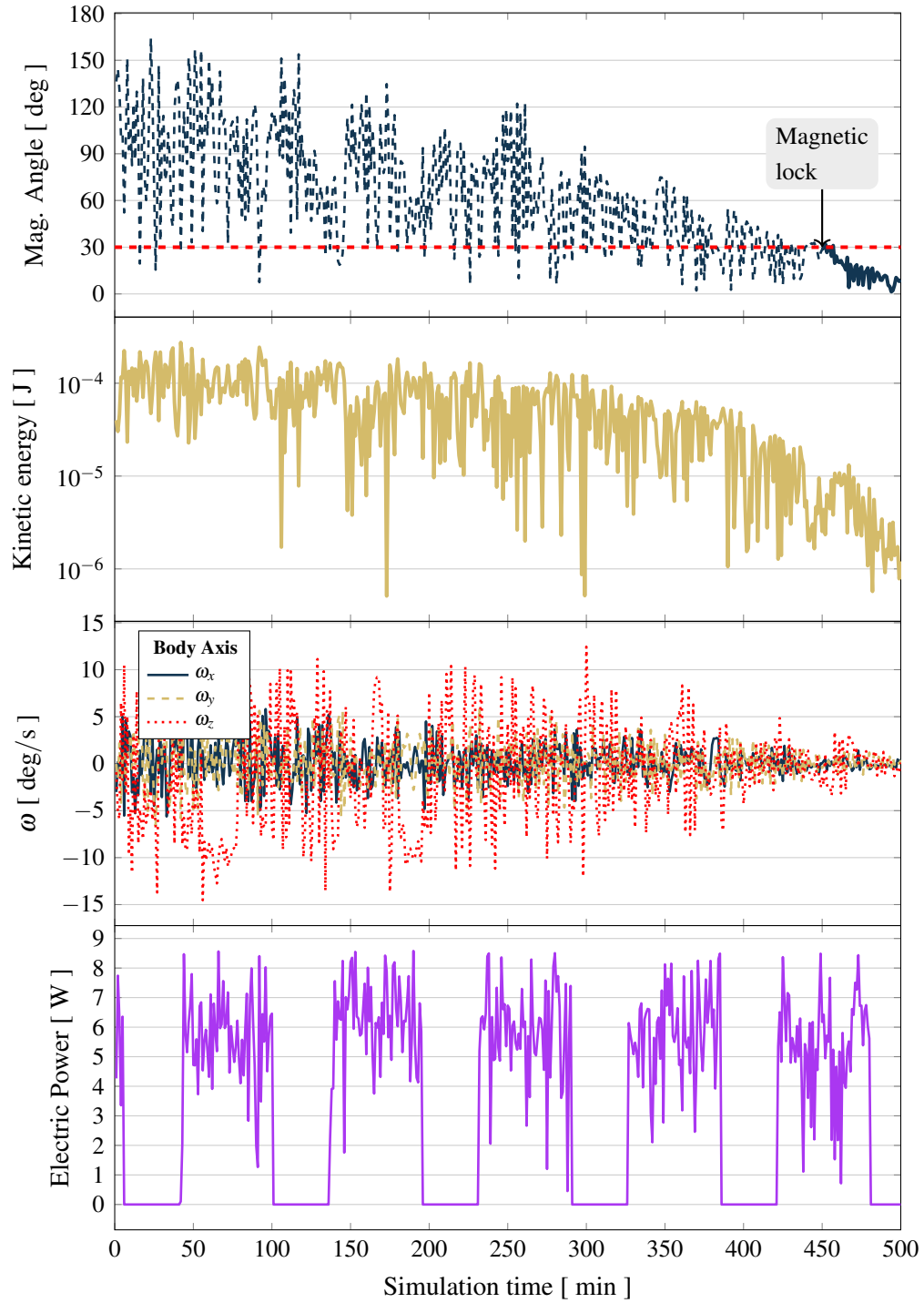


Fig. 3.6 OP attitude propagation test. The test aims to simulate a Passive Magnetic Attitude Control system on a tumbling 3U CubeSat. After gradual body kinetic energy dissipation by a pair of hysteresis rods in conjunction with a magnetic restoring torque, magnetic lock is achieved in the simulated 450 min.

Blank page

# Chapter 4

## Solar Activity Forecast

Solar activity is related to every aspect in the life of an orbiting spacecraft at some level. The effect of solar activity variation on satellites in LEO is mostly observed indirectly through the interaction of solar radiation with the Earth's magnetic field and atmosphere<sup>1</sup>. Despite the interaction path, solar activity is the main driving force raising concern about spacecraft survivability and orbit decay progression. Since the ability to predict orbit decay and external body perturbations is fundamental for the design and operation of propulsion systems in nanosatellites, this chapter focuses on the analysis of solar activity to develop an enhanced forecast method based on observation records and updated theories regarding solar physics.

### 4.1 Solar Activity on Nanosatellites

The effect of solar activity fluctuations is easily observable in LEO in naturally decaying orbits, as a result of induced atmospheric density variation. Fig. 4.1 shows the monthly  $\Delta v$  budget required for station keeping manoeuvres in a standard 3U CubeSat according to the observed monthly SunSpot Number (SSN) average. The predominant perturbing contribution of atmospheric drag on low LEO renders solar activity fluctuations important, mostly in orbits lingering within the atmospheric bulge. For example in low EO is

---

<sup>1</sup>Atmospheric interaction with nanosatellites is discussed in Chapter 5

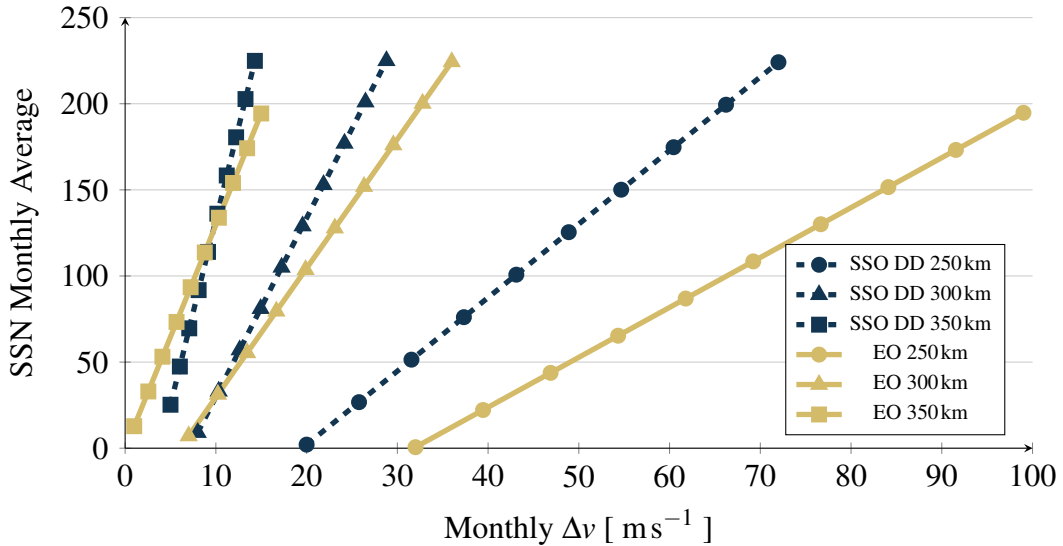
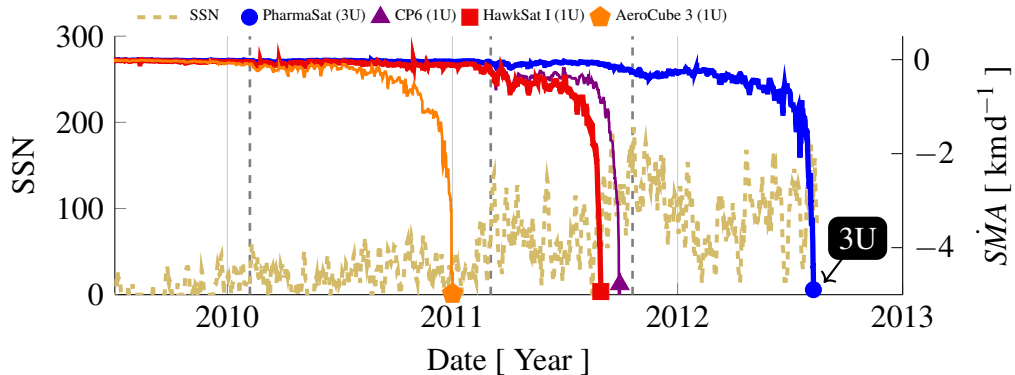


Fig. 4.1 Relationship between SSN and  $\Delta v$  budget for station keeping manoeuvres in LEO. Curves obtained from OP simulations on a standard 3U CubeSat in Sun-Synchronous Dawn-Dusk Orbit (SSO DD) and Equatorial Orbit (EO) respectively near vernal equinox. During the orbit raising manoeuvres, continuous thrusting parallel to the local horizontal is applied to recover orbit altitude.

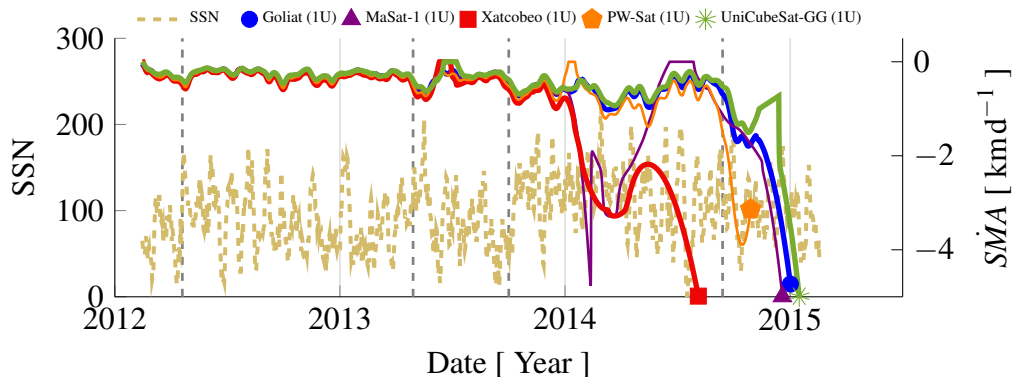
observed a higher  $\Delta v$  requirement per SSN increment because the atmospheric bulge is centred on the equator during equinox time. In another example, Fig. 4.2 presents three groups of nanosatellite missions along their observed natural orbital decay and contemporaneous observed solar activity, represented by the orbit Semi-Major Axis decay velocity (*SMA*) from TLE sets data [150] and reported daily SSN [151] respectively. The nanosatellites in the figure cover varied orbit characteristics and solar activity scenarios, in all cases periods of rapid decay on the SMA curves are easily identified by visual inspection. These localised abnormal gradient points, some of them marked with vertical dashed lines in the plots, coincide with peaks or sudden increase in SSN.

A relevant aspect identifiable from orbit decay in Fig. 4.2, is the higher vulnerability of small nanosatellite size factors (1U vs. 3U) to solar activity, presumably due to comparative reduced ballistic coefficients (*BC*), viz. *BC* may be chiefly proportional to spacecraft mass in these cases. With the aim of establishing a quantitative indicator of the relationship between SSN and orbits decay evolution, the analysis of a larger group of nanosatellite missions is carried out and summarised in Fig. 4.3. The figure shows the cross-correlation results between solar activity and orbit decay variation from

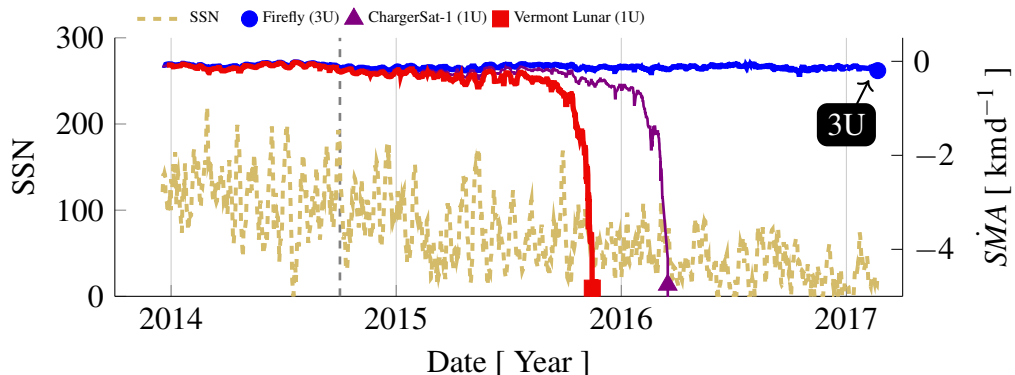
363 nanosatellites, emphasising immediate solar activity echo on orbital decay (zero lag). In this case the orbit node line acceleration is presented because it showed the best performance for this analysis amongst the Keplerian orbit elements.



(a) Group 1. Near-circular orbits (perigee altitudes  $\sim 428$  km and apogee altitudes  $\sim 466$  km) at inclination  $40.49^\circ$ .



(b) Group 2. Elliptic orbits (perigee altitudes  $\sim 300$  km and apogee altitudes  $\sim 990 - 1101$  km) at inclination  $69.49^\circ$ .



(c) Group 3. Near-circular orbits (perigee altitudes  $\sim 440$  km and apogee altitudes  $\sim 450$  km) at inclination  $40.54^\circ$ .

Fig. 4.2 SSN and rate of change of semi-major axis with time ( $SMA$ ) in nanosatellites. The vertical dashed lines mark points of abnormal orbit decay. Note the higher vulnerability to solar activity in 1U CubeSats in comparison to 3U CubeSats as marked in a) and c) plots.

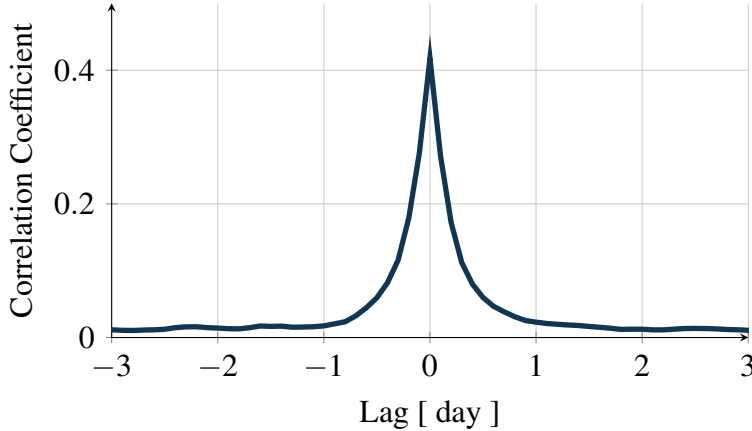


Fig. 4.3 Cross-correlation between solar activity and nanosatellites orbit evolution. The curve shows the average similarity between the second derivative of observed SSN with respect to time and the observed orbit node line acceleration ( $\ddot{\Omega}$ ) from 363 nanosatellites, for shifted (lagged)  $\ddot{\Omega}$ . It is noted the marked correlation at zero delay between the two signals, which indicates the rapid perturbing effect of solar activity fluctuations over nanosatellites orbits.

It can be inferred that the main implication of solar activity on propulsion systems operation, is related to propellant mass consumption. This is shown in the example presented in Fig. 4.4 wherein space environment conditions are reproduced for maximum and minimum solar activity on a nanosatellite in circular inclined orbit. In this example, the OP designed for this thesis is employed to propagate 60 days of orbit evolution of a standard 5 kg 3U CubeSat for controlled propulsion actuation and natural orbital drift. The reported nominal thrust and specific impulse values of the commercial MARS/CLYDE Space PPTCUP [36] are used in the simulation. The objective of the propulsion system actuation in the example is to keep the orbit altitude at 400 km, with a maximum orbit decay margin of 13 km. For the sake of simplicity, the thrust vector is antiparallel to the instant orbit velocity vector for orbit rising during sunlight operations. The resulting difference between the analytic precession of the node line<sup>2</sup> and numeric propagations ( $\Delta\Omega$ ) is plotted in the figure. It is observed from Fig. 4.4a that in the case of natural orbit drift,  $\Delta\Omega$  grows with time in a non-linear trend (primarily due

---

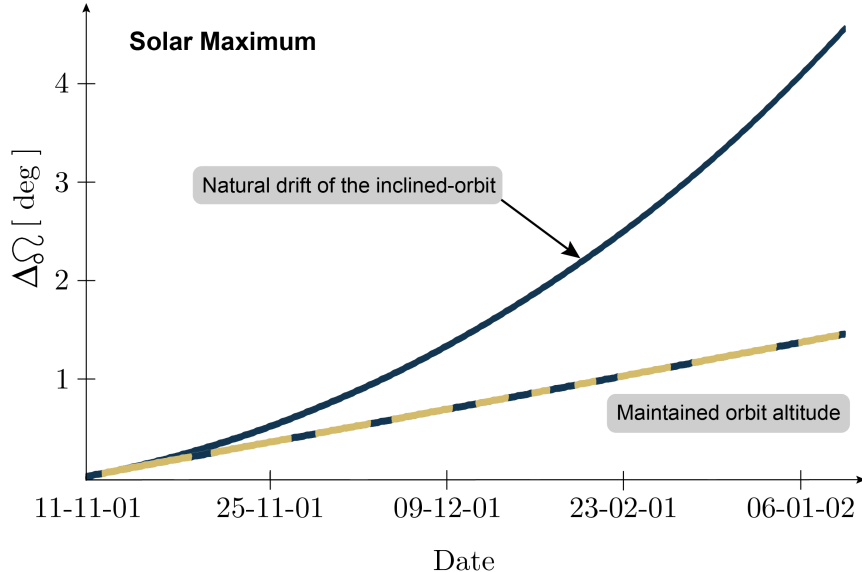
<sup>2</sup>The analytic equation [152] can be written as  $\dot{\Omega} = \Omega_0 - \left[ \frac{3}{2} \frac{\sqrt{\mu_{\oplus}} J_2 R_{\oplus}^2}{(1-e_0^2)^2 a_0^{7/2}} \right] \cos i_0 \quad t$ , with  $t$  as the propagation time vector.

to SMA decrease) whereas in an orbit kept at constant altitude  $\Delta\Omega$  growth is linear due to small contributions of minor zonal harmonics neglected by the analytic formula. Acknowledging this, the propulsion managed orbits in the example must show a near linear growth. The estimated propellant mass consumption under the aforementioned circumstances are 1.438 g and 15.648 g, during minimum and maximum solar activity respectively. This represents approximately ten times more propellant consumption during solar maximum.

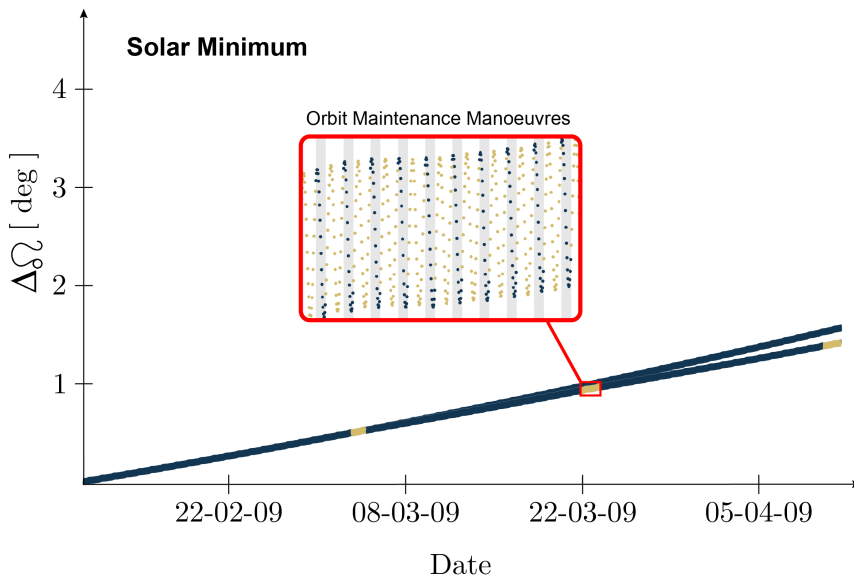
This example highlights the importance of adequate solar activity forecasts on propulsion system design for orbit maintenance. In a similar way, nanosatellites in drag-dominated orbits may exhibit specific levels of attitude perturbation caused by solar activity fluctuations via atmospheric and solar radiation interactions with exposed spacecraft surfaces. Altogether functional propulsion system actuation in nanosatellites has to ensure adequate manoeuvrability with utmost limited resources stressing on solar activity forecast accuracy. The benefits and requirements of such a forecast are manifold as these are established by specific mission characteristics, e.g. Orbit and propulsion system efficiency. However, a benchmark for a nanosatellite operational life of more than three years [4] may be easily compromised by unanticipated high solar activity (Fig. 4.1) and premature fuel exhaustion. Bearing the three years mission lifetime benchmark in mind and acknowledging the cyclic nature of solar activity, adequate forecast of the solar cycle rising phase (spanning for  $\sim 5$  years and discussed later in this chapter) is of utmost importance as this is normally steeper than the declining phase. In general terms, forecasting the solar cycle rising phase and maximum are of interest in this investigation because these have a potentially greater great impact on propulsion system design margins due to fixed prelaunch satellite fuelling than other solar cycle parameters.

In the following section 4.2 key observed features of solar activity are discussed. These observations disclose underlying processes and trends that sustain current solar activity forecast methods presented in section 4.3. On the basis of current forecast method assets, it is proposed a robust forecast method in section 4.4 followed by the

theoretical background in section 4.5. Finally, section 4.6 assesses the proposed method along the solar activity of 13 solar cycles and forecasts the next solar cycle 25.



(a) Orbit altitude maintenance limits  $\Delta\Omega$  to a linear relationship with time.



(b) Orbit maintenance manoeuvres, plotted in light colour, are performed during sunlight only.

Fig. 4.4 Orbit altitude maintenance manoeuvres in a 400km circular orbit inclined at  $51.64^\circ$ , for 60 days propagation and 13km orbit decay tolerance. The plots show the precession of the node line difference between the second degree harmonic analytic solution (at  $t_0$ ) and numeric simulations for a perturbed orbit. During solar maximum the simulated propulsion system, thrust  $40\mu\text{N}$  and  $I_{sp} = 580\text{s}$ , consumes  $15.648\text{ g}$  of propellant. During solar minimum the propellant consumption is reduced to  $1.438\text{ g}$ .

## 4.2 Observed Solar Activity

The earliest solar activity indicator observed by astronomers were the dark areas known as sunspots that appear on the photosphere, the outer shell of the Sun. Although the first plausible record of this phenomenon was reported around 800 BC in China [153], it was sparsely reported around the world [154] until the first decade of 1600 when Thomas Harriot, Galileo Galilei, and others, provided the first detailed drawings of sunspots [155]. The record of sunspot count has improved and continued since then, which is regularly updated and published by the NOAA [156] and SILSO [151].

The sunspot number varies almost periodically, in a seemingly complex nested compound of periodic phenomena in which quasi-periodicity of an 11 year cycle is easily identifiable. This cyclical behaviour was firstly identified by Christian Horrebow in the 1770s followed by Samuel H. Schwabe in the 1840s [157], and became known as the Schwabe cycle. Amplitude modulation of the Schwabe cycle occurs over a long-term cycle of 60 – 120 years, termed the Gleissberg cycle [157], resulting in periods of grand minima of solar activity, e.g. Oort (centre at year 1040), Wolf (1305), Spörer (1470), Maunder (1680), Dalton (1844), and Gleissberg (1910) grand minima periods [158]. It is argued the existence of other super-secular cycles such as the Vries/Suess cycle of 205 – 210 years and even a cycle of 2000 – 2400 years suggested by the reconstruction of several millennia of radionuclides history produced in Earth by cosmic ray particles [159]; cosmic radiation is able to penetrate deeper into the atmosphere as the geomagnetic field is weakened by high solar activity, viz. radionuclides concentration and solar activity are anti-correlated.

Observations carried out by Richard Carrington [160] during 1853 – 1861 showed that the sunspots appear and disappear at mid latitude belts in both solar hemispheres at the beginning of the solar cycle, gradually drifting to the solar equator with the progress of the cycle. The latitudinal drift of sunspots is characterised by the reduction in sunspots number and size as times goes on during the cycle. After sporadic faint sunspots reach near-equator latitudes, new midlatitude sunspots appear marking the beginning of a

new cycle. This latitudinal variation of sunspots during the solar cycle is known as Spörer law, named after Gustav Spörer who refined observations made by Carrington. Edward Maunder plotted these observations in a diagram of historical sunspots latitude of appearance along latitudinal drift, i.e. solar latitude versus time. This representation known as the butterfly diagram, shows a characteristic nearly symmetric distribution pattern of sunspot activity in both solar hemispheres. The butterfly diagram has been regularly compiled and published [161] since 1874, representing the largest record of historic hemispheric solar activity.

An important discovery made by Pieter Zeeman announced in 1896 [162], provided a critical basis to the development of modern solar physics theory. Zeeman reported a magneto-optical discovery from laboratory experiments, that light spectral lines create multiplets<sup>3</sup> that are a function of an applied external magnetic field. In other words, the light frequency produced by atomic electrons is split into two distinct wavelengths by the applied magnetic field in which the wavelength difference increases with the magnitude of applied magnetic field in a predictable way. The resulting pair of spectral lines are polarised inversely due to the opposite atomic electrons spin. George E. Hale observed the Zeeman effect in 1908 [163] within the instruments sensitivity of that time in spectroheliograms, identifying strong magnetic fields in sunspots of above 1000 G that is four orders of magnitude higher than Earth's magnetic field. This finding resulted in the explanation of sunspots as regions originated by high magnetic flux density piercing the solar photosphere that in turn inhibit plasma heat transport from few days to weeks in a region otherwise characterised by turbulent convection and regular luminosity.

Further contributions were made by Hale after the evaluation of a full solar cycle. It was observed that sunspots appear in pairs of opposite polarities (dipoles) wherein the leading spots, that is the spots leading the direction of the solar rotation<sup>4</sup>, have the same polarity in the same hemisphere and have opposite polarity in the other hemisphere

---

<sup>3</sup>Closely spaced spectral lines.

<sup>4</sup>Solar rotation is commonly measured in Carrington Rotation Number (CRN) equivalent to a synodic rotation period of 27.2753 days.

during a given solar cycle. In the following solar cycle the leading spot polarities are reversed in the hemispheres establishing a 22 year cycle<sup>5</sup> known as Hale polarity law and Hale cycle respectively. Another critical contribution was made by Alfred Joy, who observed that dipoles appear on average at various tilt levels with respect to the solar equator. In addition, Joy noticed that the average inclination of sunspots increases at higher latitudes. This statistically observable phenomena is known as Joy's law.

With the development of more sensitive instruments and the development of the magnetograph by Horace W. Babcock in 1955 [164], it was possible to observe the weak magnetic field in other regions of the Sun [165]. A representation of these observations summarising important aspects of the solar cycle is the magnetic butterfly diagram shown in Fig. 4.5. The areas of sunspot activity, typically below 30° latitude, are recognisable as well as the average weak diffuse polar magnetic field. Trails of unipolar field of opposite polarity in each hemisphere and in poleward migration are also recognisable. The unipolar fields are apparently transported by *meridional circulation* flows from the regions of sunspot activity [166] to the poles where these gradually accumulate building up distinguishable polar fields of maximum strength near the end of the SSN cycles, i.e. sunspots activity is phase shifted with respect to the polar field strength. This is shown in the plot of the average field strengths polewards of 55° reported by WSO [167] and the SSN in Fig. 4.6, where the polar magnetic field delay with respect to SSN can be identified at 1500 days (4.1 years) via cross-correlation analysis. This topic is discussed in more detail in subsection 4.6.1.

A major progress in the development of solar physics theory came from the detection of resonant oscillations on the photosphere [168, 169]. The observed spectrum of oscillations have been identified as waves chiefly generated by turbulent processes taking place in the Sun interior. The waves propagate beneath and on the Sun's surface, originating interference patterns from the interaction with internal plasma structures. Helioseismology studies these resonant oscillations, distinguishable on the solar surface, to infer internal solar hydrodynamic phenomena. Helioseismology

---

<sup>5</sup>The sign-alternating polarity cycle takes two Schwabe cycles.

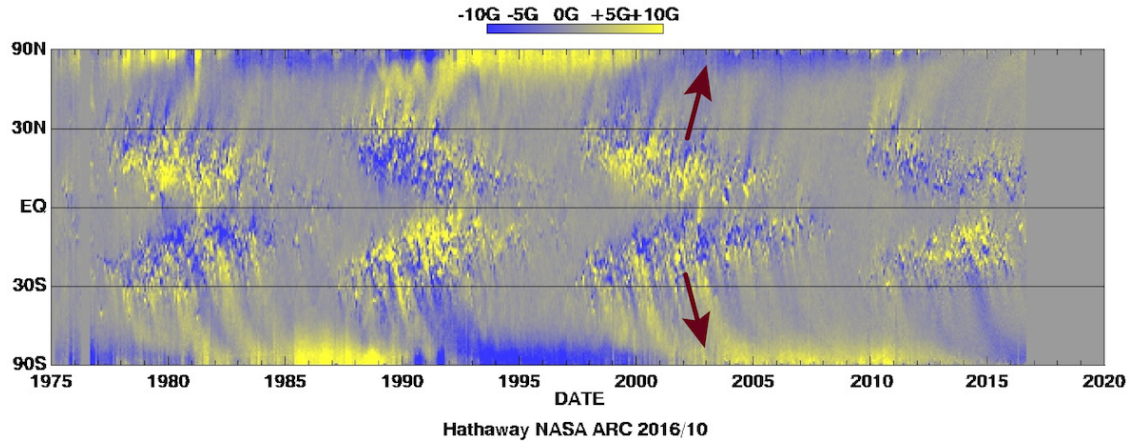


Fig. 4.5 Observed magnetic butterfly diagram from average weak diffuse magnetic field [161]. The arrows show the observed trail of unipolar poleward drift on the solar cycle 23. The same poleward drift is observed in all other solar cycles with alternating polarities according to the Hale cycle.

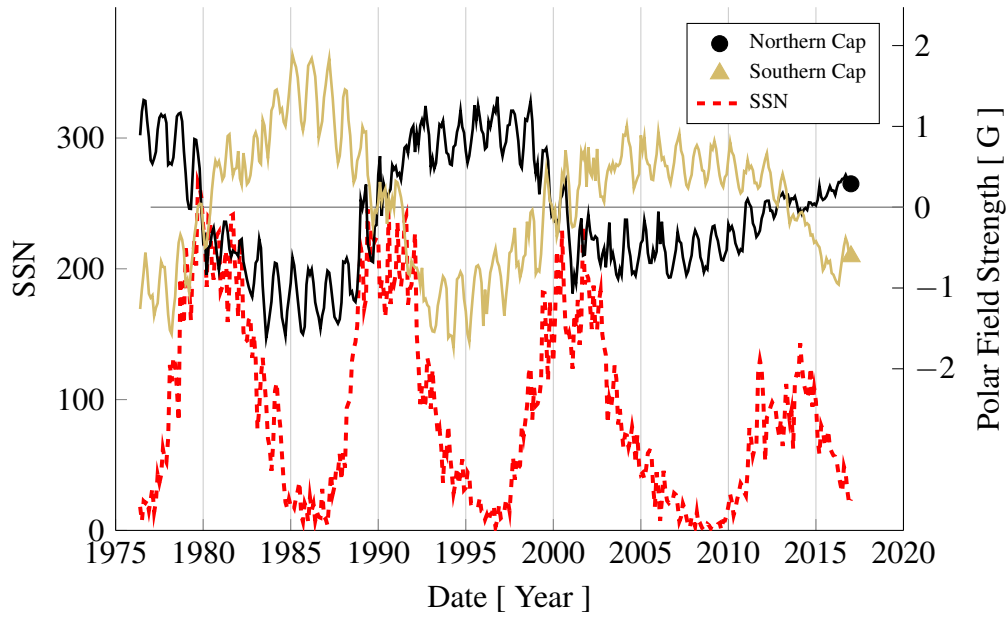


Fig. 4.6 Observed solar polar field strength and SSN activity. Complementary to Fig. 4.5, this plot shows a portion of the SSN record and the polar field strengths, which are related by the unipolar patches drift from solar activity latitudes to the poles.

has contributed to important discoveries and the advancement of a comprehensive consistent theoretical model to explain observational phenomena. Amongst these important discoveries, helioseismology has provided a mapping of the *internal rotation* of the Sun through the assessment of the frequency oscillation split established by rotation, and the discovery of the tachocline, a region of concentrated differential rotation [170] located at approximately 70% of the solar radius. Manifold solar activity phenomena are generated by complex interactions of plasma flows under the influence of gravitational and magnetic forces. Macroscopic plasma flows in the solar interior can be acceptably theorised using magnetohydrodynamics (MHD) as shown by various authors [171], capturing effectively conspicuous observed phenomenology such as the Schwabe cycle although many aspects remain unexplained.

The aforementioned observations have encouraged the development of various methods for solar activity forecast. As MHD-based models seek the deduction of solar activity, other methods rely on the apparent predictability and precursor likeliness of some observable features of solar activity. Section 4.3 presents a review of solar activity forecast approaches, to identify the pros and cons of the existing methods on their reliability, viability, and application access for the aim of this chapter.

## 4.3 Forecasting Solar Activity

The SSN is the most common proxy investigated for solar activity forecasting, preference encouraged by the large availability of data and analysis accessibility. A range of more representative proxies of solar activity have gradually become available, such as the solar electromagnetic spectrum (common wavelengths of interest are shown in Fig. 3.1 in Chapter 3), and hemispheric solar magnetic field maps. In this respect, hemispheric magnetic field information is highly valuable for solar forecasting because it offers a synoptic outline of solar activity; ultimately sunspots are just a byproduct of large scale magnetic field interactions. Unfortunately, the solar magnetic record only

extends back to the last four solar cycles (Fig. 4.5), in contrast to the SSN record covers 24 solar cycles.

Typical forecasting approaches focus on the *statistical* understanding of historical data to predict future values, chiefly using time series techniques. Forecasts based on time series statistical analysis assume observed solar activity as the output of a system statistically determined by past data. Physics-based methods on the other hand are based on conservation equations and assimilative methods to incorporate observational data into computational models with the aim of deducing future solar activity. Various levels of prediction reliability and time validity are achievable with these methods entailing the classification categories discussed below. For the sake of performance comparison of categories of solar activity forecasts, the following descriptions use the survey reported by Pesnell [172] for the solar cycle 24, against the observed smoothed monthly maximum of 80 sunspots during that cycle [173, 174]<sup>6</sup>.

### 4.3.1 Categories of Solar Activity Forecasts

Two popular categories of forecasts are defined according to the analysed span of the data record. Climatological prediction methods take all data, or most of it, whereas recent climatological forecasts use recent past data only. In both cases short-term reliable prediction is possible during specific phases of the solar cycle [175], however long-term forecasts generally show wide divergence. Solar cycle 24 was incorrectly predicted by recent climatology (RC) forecasts overestimating a maximum of 143 sunspots on average from four studies compared to the recorded smoothed maximum of 80 [173] as shown in Fig. 4.7. Conversely, climatology forecasts (C) provided a loose approximation (within the forecasts dispersion) of 105 on average from eighteen studies. The precursor category of forecasts employs recorded time series to predict future values by using leading indicators. Geomagnetic activity and solar polar magnetic field are the most commonly used leading indicators, although the number of spotless days

---

<sup>6</sup>Solar maximum of cycle 24 was reached during April 2014, with 81.8 13-month smoothed sunspot number [174]

may be of use. Precursor analysis is fostered by the idea that new cycle solar activity is explained by a precursor quantity observed during the previous solar cycle. In general, precursor methods are more accurate and reliable than purely statistical methods for the estimation of solar cycles amplitude. For example the group of solar polar magnetic precursor forecasts, SP in Fig. 4.7, made the best average prediction of 88 sunspots from three studies. Conversely, geomagnetic precursor forecasts (GP) failed to forecast the observed value with 127 sunspots on average from sixteen studies surveyed. Another

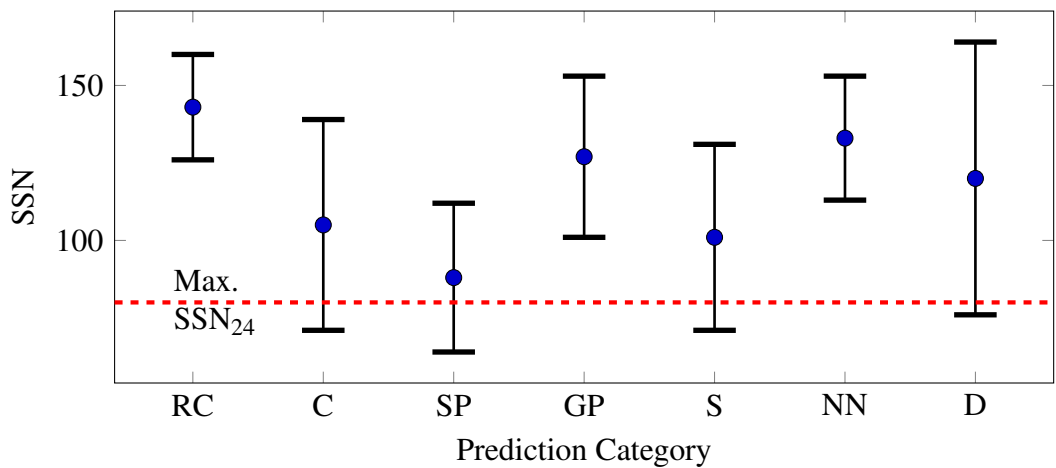


Fig. 4.7 Performance of solar activity forecasts for the solar cycle 24. Plot prepared with data from Pesnell [172]. Prediction category abbreviations are Recent Climatology (RC), Climatology (C), Solar polar magnetic Precursor (SP), Geomagnetic Precursor (GP), Spectral (S), Neural network (NN), and Dynamo model (D) forecasts respectively. The dashed line shows the observed smoothed monthly maximum for the solar cycle 24 [173, 174].

forecast classification comprises the spectral analysis of periodic or quasi-periodic phenomena, e.g. SSN cycle, planet conjunction periods, solar system's barycentre acceleration, etc. Spectral analysis is commonly carried out using autoregressive-moving-average models, Fourier analysis, chaos theory, or wavelet analysis. Spectral resemblance amongst historical solar cycle features support forecasts such as solar cycle amplitude and timing of solar minimum, however the dispersion of such predictions are similar to those of climatology methods. Most spectral-based forecasts (S) anticipated solar activity below the historic SSN average for the solar cycle 24, with 101 sunspots

on average from eighteen studies and in loose agreement to the observed maximum as shown in Fig. 4.7.

With the enhancement of computer processing capabilities, new solar activity forecasting methods have become available requiring new classifications. Forecast methods employing highly versatile computational artificial neural networks, use non-linear statistical methods to train a designed network of adaptable processing elements to determine the relationship between reference and target solar time series. The ability of neural networks to handle complex data relationships may be adequately used in conjunction with other methods to upgrade forecast reliability. However, neural networks involve heuristic algorithms that in conjunction with quasi-periodicity and low predictability level of SSN may lead to low forecast reproducibility. Neural network (NN) predictions of the maximum sunspot number for the solar cycle 24 failed to anticipate the observed value, forecasting 133 sunspots on average from three studies.

The final classification comprises dynamo model forecasts (D). The potential of predictions made with dynamo models is based on the inclusive consolidation of data by means of physics conservation equations, and modern accelerated computer processing capability. Thus, the potential of dynamo models for solar activity forecasting resides in the gradual and *consistent explanation* of observed phenomena. However, as the current understanding of solar physics and available synoptic data for models calibration are fairly limited, forecasts using dynamo models may be contradictory if key obscurely defined parameters are varied. Dynamo model forecasts loosely predicted the solar cycle 24 maximum with 120 sunspots on average from four studies.

## 4.4 The Proposed Forecast Approach

All forecast categories present characteristic assets that can be used to consolidate a superior forecast methodology. Climatology estimations can be reliable and relatively accurate within short time spans, neural networks can handle complex variable relationships, spectral analysis can provide useful information of long-term variations, solar

polar magnetic precursor forecasts can lead to acceptable predictions, and dynamo models can capitalise on cohesive phenomenological representations of established and theorised solar parameters. In this regard, dynamo models are fundamental tools for solid steps towards future reliable solar activity forecasts [172]. However, with the current state of the knowledge on solar parameterisations, some remain poorly constrained resulting in reduced predictive capability of dynamo models. Recognising the central role of the dynamo models for the development of robust forecasts methods, the efforts presented in this chapter are concentrated on strengthening key common features through extended testing scenarios.

Solar dynamo models used for forecasts are related by MHD theory, nonetheless parameterisations are varied. In general, the aim is to first calibrate the dynamo model to reproduce the main temporal-spatial characteristics from solar observations, and subsequently extrapolate solar activity. The identification of plausible combinations of parameters yielding acceptable reproduction of observed activity is an arduous endeavour that does not necessarily guarantee forecast reliability. The main deficiency in this respect, is the narrow record of detailed solar activity to test abundant solar activity scenarios. Attempts to overcome this limitation use the periods of SSN cycles to calibrate tailored dynamo models by varying the meridional flow speed, as shown by Dikpati [176] and Karak [177], or by fitting simplified dynamo equations to the observed SSN as shown by Kitiashvili and Kosovichev [178]. However, the approach presented by Jiang et al. [179] using observed photospheric magnetic fields data as a leading indicator, properly anticipated the magnitude of the solar cycle 24 and satisfactorily reproduced the three precedent cycles.

The proposed solar activity forecast approach is centred on the dynamo model forecast, to reproduce mean large-scale solar activity features. The preferred solar activity leading indicator is the solar polar magnetic field strength in a similar approach to Jiang et al. [179]. To enrich the calibration process helioseismic data is employed, and the short record of past solar polar magnetic field strength is extended by means of neural network reconstruction. The following section 4.5 describes relevant solar features

and dynamo model theory, as well as characteristic model assumptions and caveats. In addition, descriptions of supporting observational phenomena are introduced.

## 4.5 The Mean Field Axisymmetric Dynamo Model

The application of dynamo models aiming to reproduce aspects of solar activity is based upon the most updated understanding about observed and inferred phenomena. Despite the utmost efforts to assemble self-consistent models in detailed agreement to reality, the highly complex underlying mechanisms and voids in solar physics knowledge have to date prevented theorists from doing so. Current wisdom points at varied nonlinear three-dimensional processes converging on observed phenomena, whose large-scale overall evolution is remarkably systematic; this allows, under specific circumstances discussed below, the axisymmetrisation of leading phenomena.

The interaction of magnetic field structures with the greatly dynamic solar plasma is the origin of all known aspects of solar activity. The most popular proxies of solar magnetic activity are sunspots as discussed in section 4.2. The analysis of methodical observation of sunspots provides important details of the magnetic field such as its strength and direction. Intriguingly, sunspots drift faster than the neighbouring surface plasma. Furthermore, in bipolar sunspot groups (leader-follower) the leader spot, which is normally at lower latitude, drifts faster than the follower sunspot. These observations suggest that the strong magnetic field beneath the visible surface rotates with a differential morphology function of solar longitude, latitude, and depth [180].

With the development of magnetohydrodynamics (MHD) theory [181], it was possible to establish a solid framework to explain large-scale features of solar activity such as sunspot drift and solar cycle periodicity. MHD theory is formulated with the combination of the Navier-Stokes and Maxwell equations, applicable to the Sun under the assumption of non-relativistic plasma in macroscopic electric charge balance. That is, the solar plasma is treated as a slow moving<sup>7</sup> highly conductive continuum

---

<sup>7</sup>In this case the plasma flow speed is considerably lower than the speed of light

fluid dominated by gravitational and magnetic forces. As plasma in this condition maintains its global neutral charge whilst transmitting efficiently electric currents, the movement of internal charges produce no electric fields inducing magnetic fields only. The fundamental induction equation in Eq. (4.1) from MHD theory furnishes important details of the solar plasma's macroscopic characteristics. In contrast to laboratory plasmas, in astrophysical systems the induction term depending on the relative velocity  $\vec{v}$  of a fluid with respect to the magnetic field  $\vec{B}$ , is much greater than the diffusion term where  $\eta$  is the diffusion coefficient. This condition has an important effect on the behaviour of solar magnetic fields because it implies that a plasma element moving along a magnetic gradient would experience an induced eddy current; induced element currents establish an overall fluidic magnet interacting with the external magnetic gradient that in turn generates magnetic drag. In this way the spatial evolution of the magnetic field is governed by plasma movements which is called magnetic freezing [182].

$$\frac{\partial \vec{B}}{\partial t} = \underbrace{\vec{\nabla} \times (\vec{v} \times \vec{B})}_{\text{Induction}} + \underbrace{\eta \nabla^2 \vec{B}}_{\text{Diffusion}} \quad (4.1)$$

Magnetic freezing identifies plasma flow as a central ingredient in the evolution of solar activity making necessary its evaluation. To this aim, it is convenient to introduce some important concepts about the solar interior. The Sun is constituted almost entirely by hydrogen 91.2%, helium 8.7%, and other 65 heavier elements<sup>8</sup>. In the central region encompassing one-fourth of the solar radius as show in Fig. 4.8, atoms are ionised by gravitational potential energy (inward force) and nuclear energy (outward pressure) generating a highly dense plasma assumed in thermal and hydrostatic equilibrium. The energy generated within this core is transported to outer layers by photons. Leaked photons are absorbed and re-radiated in a random walk through a highly opaque medium experienced in the so-called radiative zone. As energy progresses on its way outwards through radiative diffusion, dominant physical processes change gradually as temperature and density decrease. In a less energetic zone, namely the convection

---

<sup>8</sup>Composition of the observed solar spectrum which may be representative of the Sun interior [183].

zone, conditions are met for heavier ions to dwell hindering further radiative diffusion. The pile up of energy destabilises the plasma generating warmer blobs buoying to the surface where part of the energy is released as the surrounding plasma gradually becomes less opaque recovering convective stability in the plasma blobs. In addition to this convective mechanism, the Sun's rotation about its axis is crucial to explain solar plasma flows.

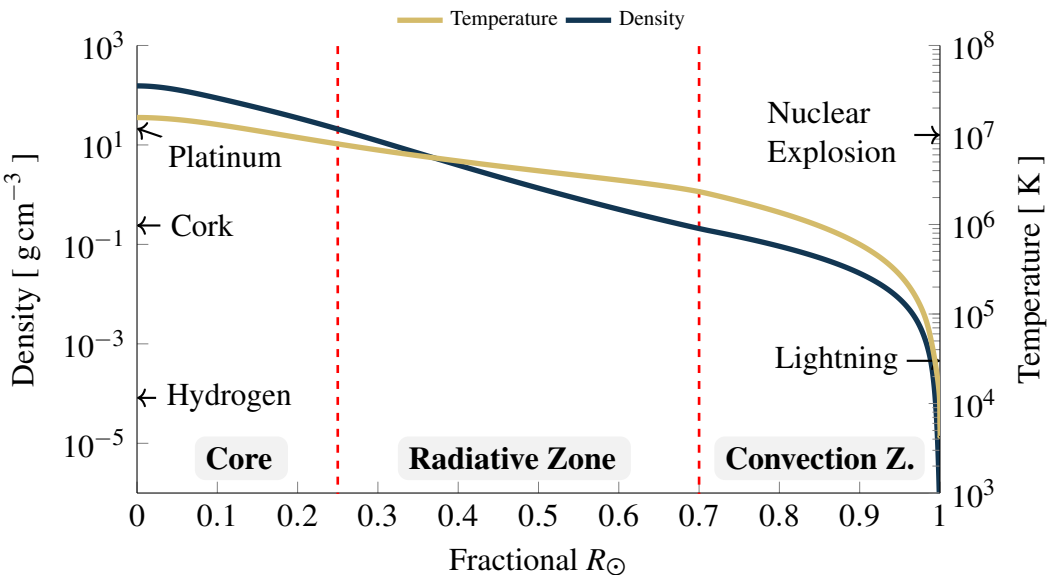


Fig. 4.8 Sun density and temperature depth profile according to the standard model (Model S) [184]. To put these quantities into perspective, some values of phenomena and materials found in Earth in standard conditions are provided.

### 4.5.1 Differential Rotation

Early observations showed that solar plasma at the surface flows at different axial rotation speeds. Doppler analysis of spectral absorption lines identify a surface rotation rate profile, for example the sidereal period near the equator is about 25 days transitioning to 29 days at mid latitudes, to 33 days near the poles. Helioseismology has revealed an extended differential rotation morphology with depth that assists the explanation of sunspot drift phenomena. Fig. 4.9 shows three representations of the longitudinal averaged rotation map as function of latitude and depth, hereinafter referred to as  $\Omega$ . The most common rotation map [185] used in dynamo modelling is shown in

the analytical envelope in Fig. 4.9a. From the comparison between inferred data via helioseismology for various latitudes and its representation in the depth profiles from the analytical fit model, it is possible to identify a rough approximation of the analytical model. On the other hand, Fig. 4.9b derives from insightful mathematical laws [186], where differential rotation is explained through angular entropy gradients and inertial angular velocity. Even though this model's depth profiles show lower agreement to helioseismology data than in the previous case, the fact that this representation is based on mathematical laws makes it relevant towards a deeper understanding of solar physics. Fig. 4.9c shows an O-grid mesh fitted to data from the Global Oscillation Network Group (GONG) [187]. This realistic model captures most characteristics of the average differential rotation morphology that according to the isorotation contour patterns in Fig. 4.9c, can be divided into three main concentric discs.

The innermost disc shows an approximate constant angular velocity, i.e. solid rotation, that is abruptly wrenching at  $\sim 0.7R_\odot$  at various magnitudes with latitude. This region of great shear stress the so-called tachocline, is indispensable in current solar dynamo theory and is marked in all figures with red dashed lines. A mid disk is bounded by the tachocline as inner radius up to  $\sim 0.95R_\odot$ . Within this second disc isorotation contours diverge from radial spokes as latitudes approach the solar equator, in contrast to Fig. 4.9a. In the outer ring extending from  $0.95R_\odot$  to the surface, the isorotation contours shown in Fig. 4.9c gradually match the observed surface rotation profile; it is suspected that this outer ring is dominated by combinations of vigorous turbulent stresses and magnetic braking [186] reducing angular rotation speed. Due to the importance of the flows in the convection zone and shallow phenomena to the current explanation of the solar dynamo (covered later in this section) this investigation departs from the typical analytical model in Fig. 4.9a and employs the model shown in Fig. 4.9c.

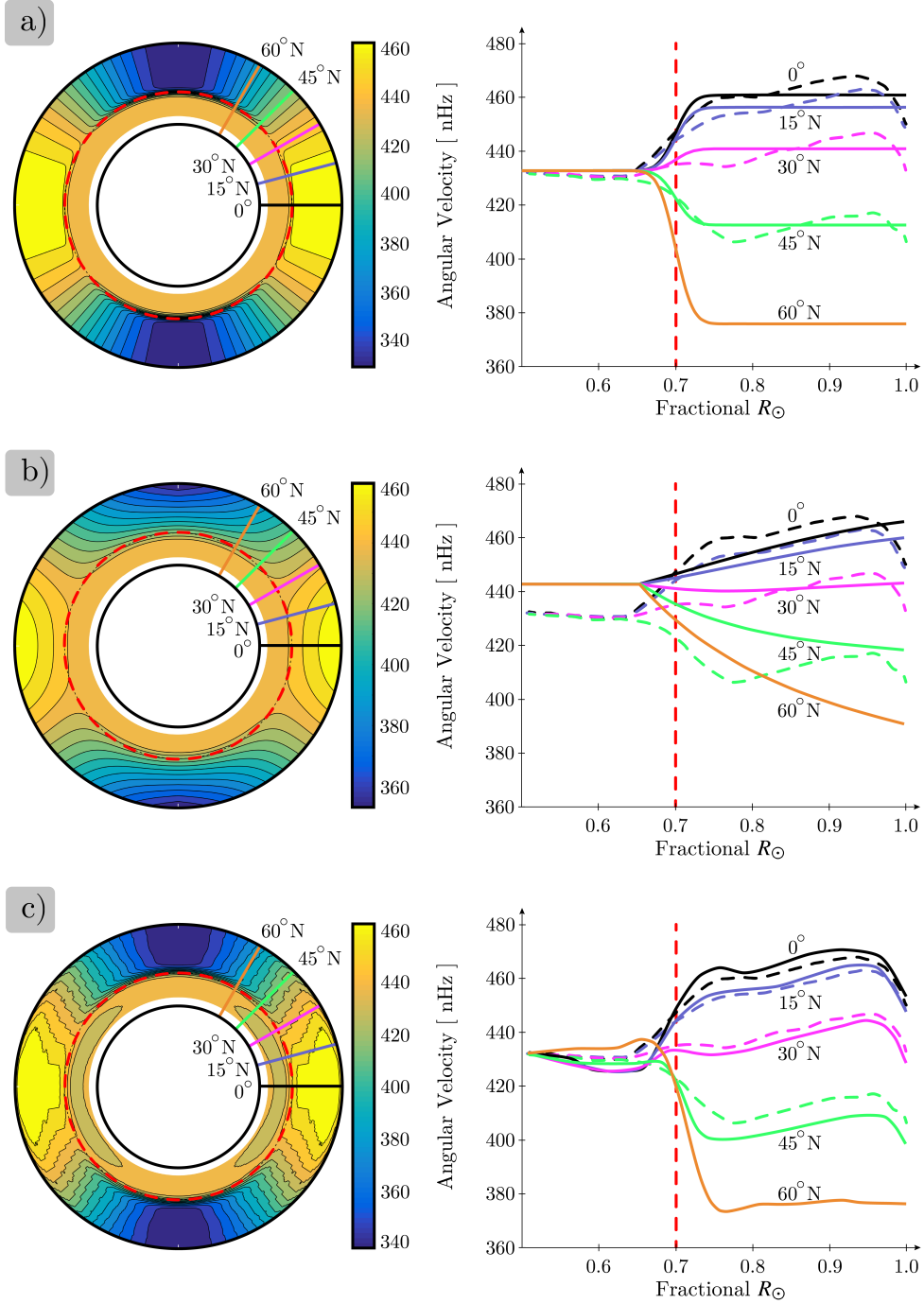


Fig. 4.9 Solar longitudinal averaged isorotation contours (left column) and depth profiles (right column) for selected solar latitudes. The subfigures show examples of axial solar rotation models: a) Analytical fit commonly used in dynamo modelling, b) Mathematical model based on the thermal wind equation, c) Mapping from helioseismology (GONG). Vertical lines in the depth profiles show the core location of the tachocline, solid curves are the velocity profiles of the respective models, and dashed curves correspond to inferred helioseismology.

### 4.5.2 Meridional Circulation

Vigorous rotation acting on anisotropic and compressible plasma in the convection zone generates a second important macroscopic flow. It is believed that the combined effect of plasma in differential axial rotation, pressure gradients, and turbulent buoyant convective plasma generate cellular circulation that collectively may be the cause of the observed meridional circulation on the solar surface. Although there is no direct evidence of the continuation of the meridional flow deep down to the solar interior and subsequently generating a counterflow, the assumption of closed hemispheric meridional cells provides plausible explanations of solar features. The theoretical origin and structure of cellular circulation in stars is investigated by Dikpati [188]. Simulations carried out in that investigation suggest that a two-celled hemispheric counterrotating pattern, a major poleward (at surface) hemispheric cell near the equator and other equatorward at the pole, is likely to happen in stars like the Sun. However, simulations were unable to approach the observed meridional speed using solar parameters. Zhao et al. [189] argued that there is evidence of two radially stacked cells of meridional circulation although this remains unconfirmed by helioseismology. Analysis of the effect of multiple cellular circulation on the reproduction of observed solar activity is studied by Hazra et al. [190]. They concluded that as long as equatorward flow exists at the bottom of the convection zone at low solar latitudes, where an important component of the magnetic field is possibly generated, solar activity is well reproduced in dynamo models. In addition, Hazra et al. [190] assessed the effect of the speed of the meridional flow on the solar cycle period in an array of radially stacked cells. The study indicates a significant influence of the innermost cell speed in determining the length of the solar cycle.

In compliance to the aim of this investigation and due to the reduced meridional flow parameters constrain, the typical single hemispheric cell approach is adopted. For the sake of analysis homogeneity the meridional flow speed profile is kept constant, however observed solar surface meridional circulation indicates that this may vary with

the progress of the solar cycle, e.g. at mid latitudes  $\sim 10 \text{ m s}^{-1}$  during the 23<sup>rd</sup> solar maximum and  $\sim 14 \text{ m s}^{-1}$  by the end of that cycle [191]. In this respect, meridional flow fluctuations may play a fundamental role in determining the duration and influencing the magnitude of solar cycles as suggested by Karak [177]. These analyses imply some degree of uncertainty in solar activity forecast using dynamo based models, which may be attributed in part to lack of deep understanding concerning the nature of meridional flow.

The two-dimensional meridional circulation with velocity  $\vec{v}$  can be expressed through a stream function  $\psi$  as shown in Eq. (4.2), assuming polytropic<sup>9</sup> density stratification given by Eq. (4.3). It is shown by Cardoso and Lopes [192] that a more realistic description of density stratification may lead to noticeable changes in plasma flow evolution. However, considering the current existing uncertainty produced by the meridional circulation structure, the standard polytropic stratification is deemed sufficient for the axisymmetric dynamo model used in this investigation.

$$\rho \vec{v} = \vec{\nabla} \times [\psi(r, \theta) \vec{e}_\phi] \quad (4.2)$$

$$\rho = \left( \frac{R_\odot}{r} - \gamma \right)^m \quad (4.3)$$

$$\psi r \sin \theta = \psi_0 (r - R_p) \sin \left[ \frac{\pi(r - R_p)}{(R_\odot - R_p)} \right] \left[ 1 - e^{-\beta_1 \theta^\epsilon} \right] \left[ 1 - e^{\beta_2 (\theta - \pi/2)} \right] e^{[(r - r_0)/\Gamma]^2} \quad (4.4)$$

Table 4.1 Meridional circulation parameters.

Parameter	Reference model [179]	This model	Unit
$\beta_1$	$1.36 \times 10^{-8}$	$1.50 \times 10^{-8}$	$\text{m}^{-1}$
$\beta_2$	$1.63 \times 10^{-8}$	$1.80 \times 10^{-8}$	$\text{m}^{-1}$
$\gamma$	0.95	0.95	—
$\Gamma$	$3.47 \times 10^8$	$3.47 \times 10^8$	m
$\epsilon$	2.0000001	2.0000001	—
$m$	1.5	1.5	—
$R_p$	$0.61 R_\odot$	$0.61 R_\odot$	m
$v_0$	29	25	$\text{m s}^{-1}$

<sup>9</sup>A polytope is a self-gravitating spherical particle structure model used to roughly approximate some astrophysical systems.

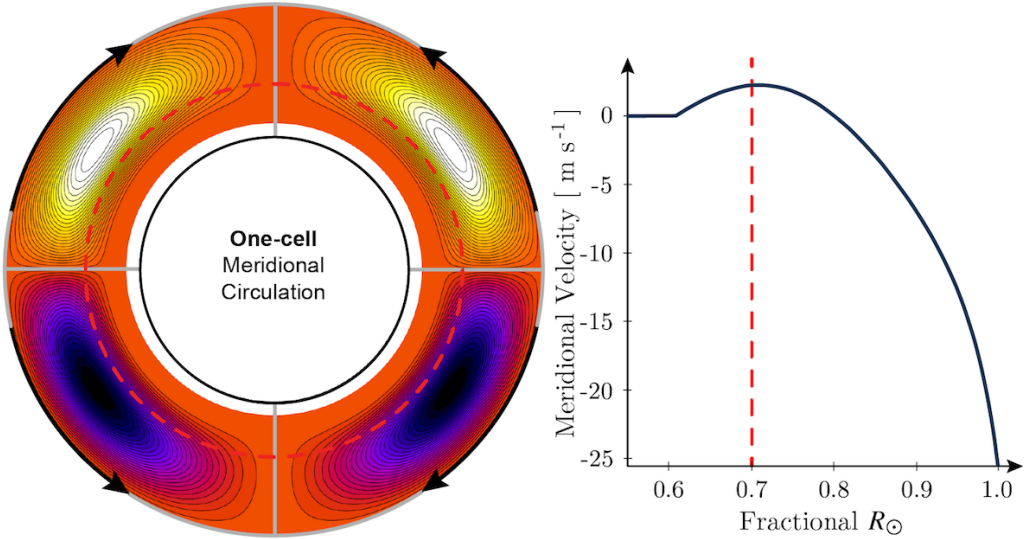


Fig. 4.10 Meridional circulation profile. The disk shows the cells of meridional circulation with varying colatitude  $\theta$  and radius  $r$ . The plot shows the meridional velocity profile at  $\theta = 45^\circ$ . The dashed curve represents the core of the tachocline zone.

The hemispheric stream function model used in this investigation in Eq. (4.4) is reported in the work of Chatterjee et al. [193]. The parameters used in Eq. (4.4) are shown in Table 4.1. With the exception of  $\beta$  values and poleward flow velocity *near* the surface at mid-latitudes ( $v_0$ ), parameters are equal to those reported by Chatterjee et al. [193]. The combination of meridional circulation parameter values used in this investigation, results in the two-dimensional meridional circulation depth profile shown in Fig. 4.10 penetrating up to  $R_p$ . The model generates a maximum equatorward counterflow of  $2.29 \text{ ms}^{-1}$  at the tachocline region congruent with the observed equatorward sunspot drift trend near midlatitudes [194]. In addition the model yields a reference Schwabe cycle of 10.87 years in agreement to the average cycle of interest in this investigation and discussed in the following section (i.e. solar cycles 12 – 23).

### 4.5.3 Flux Transport Dynamo Theory

The strong differential rotation and weaker meridional circulation define the flow used in axisymmetric dynamo models. Knowledge about main solar plasma flows assists the understanding of magnetic field evolution as this is transported by plasma through magnetic freezing. Eq. (4.5) summarises the velocity vector in spherical coordinates

with the axial rotation (azimuthal) and the meridional circulation components.

$$\vec{v}_T = \underbrace{r \sin \theta \Omega(r, \theta) \hat{e}_\phi}_{\text{Axial Rotation}} + \underbrace{\vec{v}}_{\text{Meridional Circulation}} \quad (4.5)$$

The main enigma in solar dynamo theory is how the magnetic field is sustained against diffusion and is recycled periodically. A natural explanation regarding the generation of azimuthal (toroidal) field from meridional (polar) field is that axial rotation in regions of very large shear (tachocline), stretch out the local polar field lines frozen to the moving plasma; the resulting winded magnetic field builds a strong toroidal field. This mechanism of toroidal field generation is termed  $\omega$ -effect. The effect of the strong toroidal magnetic field on the plasma is largely stabilising, acting against convective motion. As a result of the interaction between convection and magnetic tension, bundles of magnetic field lines embedded in nonmagnetic plasma are generated. These bundles of concentrated magnetic field are termed flux tubes. Flux tubes magnetic field endows magnetic tension (stiffness), and magnetic pressure that evacuates plasma from its interior generating magnetic buoyancy against gravity. The restoring effect of magnetic tension keeps local stability unless magnetic buoyancy instabilities, and particularly convective instabilities (blobs), force highly buoyant sections to rise to the surface. The buoyant section would rise radially stretching the flux tube to which it is attached. With respect to the topmost point of the emerging section, the particles conforming the flux tube are moving away from it as a result from the stretching, i.e. particles move away downwards on each opposite connecting branch. This motion of particles relative to the macroscopic axial rotation generates Coriolis forces<sup>10</sup> that tilt the emerging flux tube section with respect to the rest of the tube [195]. When the buoyant section finally reaches the solar surface, it pierces the photosphere forming a tilted bipolar sunspot group in compliance to Joy's law. In addition, as each branch of the emerged tube crosses the surface in opposite directions (in↔out) in each hemisphere, the Hale's

---

<sup>10</sup>The Coriolis force is given by  $\vec{F}_C = -2\rho_i \vec{\Omega} \times \vec{v}_{ft}$ , where  $\Omega$  is the axial rotation and  $\vec{v}$  is the particle's separation rate from the topmost point of the flux tube. Note that  $\vec{v}$  has opposite sign on each connecting branch.

polarity law is fulfilled too. However, considering the sole effect of the Coriolis effect on emerging flux tubes would lead to unrealistic sunspots tilts. It is estimated that the required magnetic field strength, thereby magnetic tension, required to overpower the Coriolis effect to reproduce observed properties of magnetic field groups is of at least  $10^5$  G at the tachocline [196, 180]. This threshold value is therefore important for following descriptions in this chapter.

In a more realistic scenario, turbulent plasma motions may cause premature diffusion and explosion of emerging flux tubes [180], and tilt fluctuation (viz. this explains the statistical quality of Joy's law) and fragmentation in those succeeding to pierce the surface. In order to address these complex interactions detailed MHD analysis of flux tube motion is required, fluid dynamic drag forces, field strength asymmetries arisen from Coriolis forces (e.g. yielding observed stronger and less fragmented leading sunspots [197]), and body-axial flux tube twist [198] are included. Important to the current explanation of solar dynamo are the polar magnetic field component originated by toroidal flux tube rotation under the action of Coriolis forces, termed the  $\alpha$ -effect, the body-axial flux tube twist contributing with poloidal component [180], and diffusion of radial magnetic field from decaying active regions. These chiefly near-surface phenomena are argued to be the source of polar field regeneration [171], in the so-called Babcock-Leighton process. The aleatory quality of polar field generation dominating part of the Schwabe cycle, i.e. mostly from solar maximum to the end of the cycle, is believed to be one of the most important causes of solar cycle irregularities [179]. This theory is supported by the observed regularity and predictability of the rising phase of SSN cycles vis-à-vis the declining (Babcock-Leighton dominated) unstable phase. In continuation with the magnetic cycle, the generated polar magnetic field is advected to the poles by meridional flow (see Fig. 4.5), and magnetic diffusion around evolving photospheric convection cells (supergranule cells). Once near the poles, diffusion and convective stable plasma transport polar field to the base of the convection zone where it is stretched again by differential rotation recovering toroidal field.

The aforementioned processes are the basis of the current flux-transport dynamo theory [180]. Paramount to this investigation is the accumulated polar field by the end of the Schwabe cycle that is apparently the seed of magnetic evolution for the following solar cycle as suggested by historical forecasts [179, 199]. A mathematical representation of the magnetic field evolution in spherical coordinates is given by Eq. (4.6) and Eq. (4.7) for the poloidal and toroidal components respectively.

$$\frac{\partial A}{\partial t} + \frac{1}{r \sin \theta} (\vec{v} \cdot \vec{\nabla}) (rA \sin \theta) = \eta_p \left( \nabla^2 - \frac{1}{r^2 \sin^2 \theta} \right) A + \alpha B \quad (4.6)$$

$$\begin{aligned} \frac{\partial B}{\partial t} + \frac{1}{r} \left[ \frac{\partial}{\partial r} (rv_r B) + \frac{\partial}{\partial \theta} (v_\theta B) \right] &= \eta_t \left( \nabla^2 - \frac{1}{r^2 \sin^2 \theta} \right) B + r \sin \theta (\vec{B}_p \cdot \vec{\nabla}) \Omega + \\ &\quad \frac{1}{r} \frac{d\eta_t}{dr} \frac{\partial}{\partial r} (rB) \end{aligned} \quad (4.7)$$

In these formulae,  $A$  represents the poloidal potential,  $B$  is the toroidal field,  $r$  is the local radius,  $\theta$  is the local colatitude measured from the north solar hemisphere,  $v$  the meridional flow speed,  $\Omega$  the solar axial rotation, and  $\eta_{t,p}$  the magnetic diffusivity. The Babcock-Leighton process in this investigation is phenomenologically represented by  $\alpha$  in Eq. (4.8) modified from Hotta and Yokoyama [200]. The generation of polar field is reasonably concentrated above  $0.95R_\odot$ , and suppressed at poles as shown in Fig. 4.11. This is in contrast to Chatterjee et al. [193] where the latitudinal dependence of the Coriolis effect (represented by factor  $\cos \theta$  in Eq. (4.8)) is only considered. The heuristic value of  $\alpha_0 = 15 \text{ m s}^{-1}$  ensured the relaxation of the model using realistic  $\Omega$  to a stable periodic solution from an initial arbitrary state (super-critical  $\alpha$ ). It is found in this investigation that these  $\alpha$  model requirements are the main consequence of using the realistic  $\Omega$  model.

$$\alpha = \frac{\alpha_0}{4} \cos \theta \left[ 1 + \operatorname{erf} \left( \frac{r - 0.95R_\odot}{0.05R_\odot} \right) \right] \left[ 1 - \operatorname{erf} \left( \frac{r - R_\odot}{0.01R_\odot} \right) \right] \underbrace{\left( \frac{1}{1 + e^{-30\theta}} \right) \sin \theta}_{\text{Suppression at poles}} \quad (4.8)$$

The final critical ingredient to understand macroscopic solar fluctuations, is the turbulent magnetic diffusivity in the convection zone. The importance of the solar

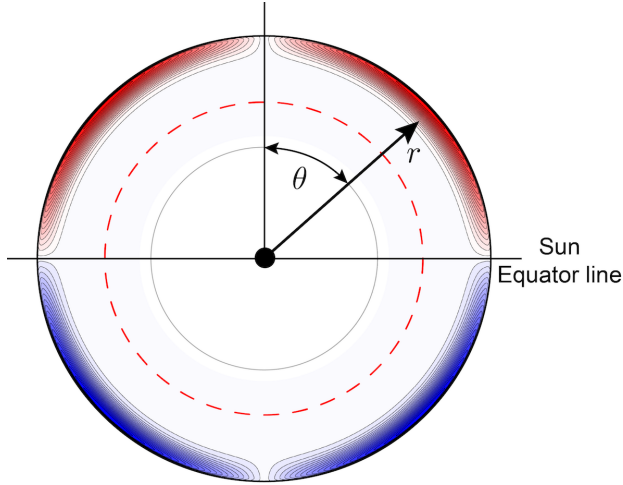


Fig. 4.11 Babcock-Leighton  $\alpha$  profile. The disk shows the contour plot of  $\alpha$  with varying colatitude  $\theta$  and radius  $r$ , within the inner and outer solar radii. The dashed curve represents the core of the tachocline zone.

turbulent diffusivity resides in the interconnecting role between polar and toroidal fields, which as discussed before are generated in separate specific regions of the Sun. Unfortunately, the solar turbulent diffusivity process is currently poorly understood and therefore poorly constrained in solar dynamo models. This uncertainty has lead to two main streams in mean-field dynamo models and philosophies about the diffusivity behaviour in the Sun's interior. With the exception of its near-surface value, where there is apparent consensus supported by mixing-length theory, high or low turbulent magnetic diffusivity values are used as summarised by Muñoz-Jaramillo et al. [201]. Since there is little evidence of the phenomena taking place in the Sun's interior, flux transport dynamo parameters are adjusted within characteristic ranges to match surface phenomena that in both diffusivity cases may reproduce observed patterns. However, the implications on solar activity forecast resulting from each approach are profound. For example, in the low diffusivity scenario<sup>11</sup> where advection is the main mechanism communicating magnetic fields in the majority of the convection zone, a cycle memory effect exists in dynamo models due to high latency in the magnetic field transport. On the other hand, high diffusivity favours faster communication and interaction between

---

<sup>11</sup>Typically  $\eta = 10^6 - 10^{12} \text{ cm}^2 \text{ s}^{-1}$  from bottom to top of the convection zone [202], produce diffusion time across the convection zone of 200 years.

magnetic fields, facilitating the establishment of hemispherical dipolar parity<sup>12</sup> and restraining hemispheric asymmetry, e.g. approximating symmetric butterfly diagrams.

At present the high turbulent diffusivity approach has shown reasonable results in reproducing solar cycles as discussed above implying that long-term solar activity memory, may be unnecessary to explain solar cycles behaviour. Furthermore, the observed lack of correlation between solar activity during a given Schwabe cycle and the polar magnetic field observed by its end [179], highlight the randomness involved in the creation of polar field and thereby the relevance of solar polar magnetic precursor forecasts. The high magnetic diffusivity approach used in this investigation is similar to that reported by various authors [177, 179, 190, 193] with separated poloidal and toroidal diffusivity components in Eq. (4.9) and Eq. (4.10) and plotted in Fig. 4.12. The adequate combination of diffusivity model parameters are obtained by solar dynamo calibration to observed solar activity patterns, e.g. sunspot butterfly diagram, which in this investigation led to the use of  $\eta_{SCZ1} = 3 \times 10^{10} \text{ cm}^2 \text{ s}^{-1}$ , which is slightly lower than the value used in the reference model ( $\eta_{SCZ1} = 4 \times 10^{10} \text{ cm}^2 \text{ s}^{-1}$  [193]), the same  $\eta_{RZ} = 2.2 \times 10^8 \text{ cm}^2 \text{ s}^{-1}$  and  $\eta_{SCZ} = 2.4 \times 10^{12} \text{ cm}^2 \text{ s}^{-1}$  instead of  $\eta_{SCZ} = 2.6 \times 10^{12} \text{ cm}^2 \text{ s}^{-1}$ , all these parameter values are summarised in Table 4.2. The  $\eta_{SCZ1}$  value along with the suppression at poles of the Babcock-Leighton  $\alpha$  profile are related to the use of a realistic rotation map instead of the analytical fit (see Figure 4.9). This is concluded from solar dynamo tests adopting the standard and the proposed combinations of solar parameters.

Table 4.2 Magnetic diffusivity parameters.

Parameter	Reference model [179, 193]	This model	Unit
$\eta_{RZ}$	$2.2 \times 10^8$	$2.2 \times 10^8$	$\text{cm}^2 \text{ s}^{-1}$
$\eta_{SCZ}$	$2.6 \times 10^{12}$	$2.4 \times 10^{12}$	$\text{cm}^2 \text{ s}^{-1}$
$\eta_{SCZ1}$	$4 \times 10^{10}$	$3 \times 10^{10}$	$\text{cm}^2 \text{ s}^{-1}$

<sup>12</sup>Although dipolar parity is observed in the recent record of solar activity, it is argued that quadrupolar parity may appear under specific conditions, e.g. superimposed beating magnetic configuration components. Analysis of J.C. Staudacher sunspot drawings covering the period 1749 – 1796 made by Arlt [203] and further studied by Sokoloff et al. [204] in the context of solar dynamo theory, suggest that cycles 0 and 1 may have shown quadrupolar parity.

$$\eta_p = \eta_{RZ} + \frac{\eta_{SCZ}}{2} \left[ 1 + \operatorname{erf} \left( \frac{r - 0.70R_\odot}{0.025R_\odot} \right) \right] \quad (4.9)$$

$$\eta_t = \eta_{RZ} + \frac{\eta_{SCZ1}}{2} \left[ 1 + \operatorname{erf} \left( \frac{r - 0.72R_\odot}{0.025R_\odot} \right) \right] + \frac{\eta_{SCZ}}{2} \left[ 1 + \operatorname{erf} \left( \frac{r - 0.95R_\odot}{0.025R_\odot} \right) \right] \quad (4.10)$$

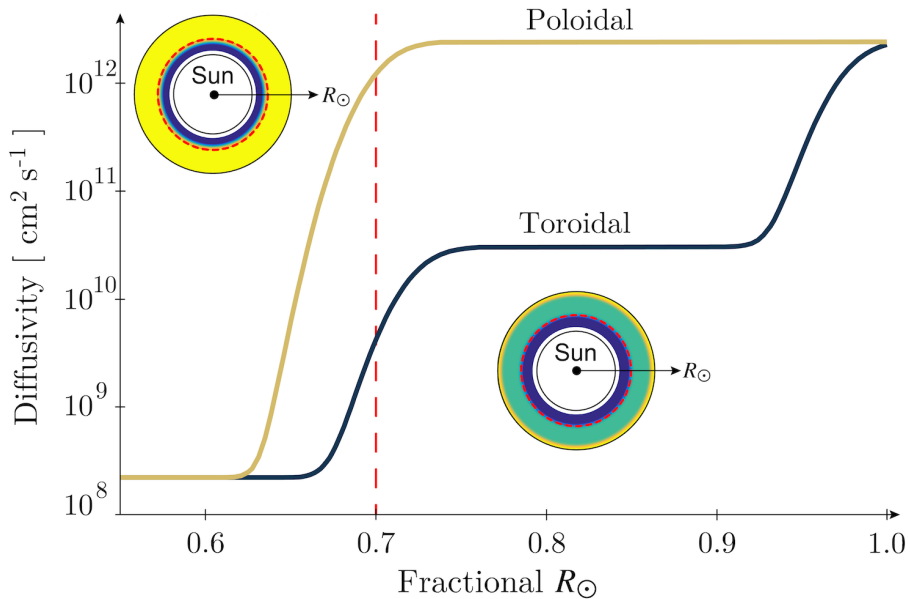


Fig. 4.12 Poloidal and toroidal diffusivity profiles. The disks show the contour plots (minima in dark colour) for each case within the inner and outer solar radii, and the dashed curves represent the core of the tachocline zone.

It is expected that the strong toroidal field at the bottom of the convection zone, where it is generated by high differential rotation, presents suppressed diffusivity. This is a plausible assumption because dynamically stable plasma is found in the near-radiative zone and because strong flux tubes may contribute to reduce turbulent diffusivity. In addition, the extended suppressed toroidal diffusivity in this region, shown in Fig. 4.12, preserves the former high-latitude toroidal field meanwhile is transported (frozen) by the equatorward counter flow (meridional circulation). As the toroidal field is stronger than the poloidal field within the convection zone, a lower diffusivity in the toroidal field is expected until it matches the estimated common diffusivity at the surface. Unlike the double step profile of  $\eta_t$ , the weak poloidal field may be easily diffused throughout the convection zone.

### The Numerical Solar Dynamo Model

Several computational dynamo codes exist based on various numerical techniques centred on the solution of the standard mean field dynamo equations in Eq. (4.6) and Eq. (4.7). An assessment of codes is presented in the work of Jouve et al. [205] showing close agreement amongst the solutions obtained with the different numerical techniques, i.e. finite differences, finite elements, and spectral decomposition. In this investigation a finite differences bespoke code is developed. The bespoke code uses MATLAB<sup>®</sup> language and is based on the openly-available Fortran SURYA code [206]. In order to emulate a suitable proxy of solar activity for comparison to observational data, e.g. sunspots, regions prone to magnetic buoyancy are considered. In this respect, the magnetic growth suppression approach implemented in the SURYA algorithm is used. In this approach the condition of the toroidal field at  $0.71R_{\odot}$  is monitored every 10 simulation days [206]. Wherever the field exceeds the threshold of  $10^5$  G in this layer, half of this field is transferred to upper grid points to emulate a magnetic buoyancy-like effect. Thereby these grid points represent active regions where sunspots may appear. Figure 4.13 and Figure 4.14 show the mean field evolution in a steady dynamo solution (super-critical condition) from the code used in this investigation. The figure shows the characteristic toroidal field evolution during a simulated Schwabe cycle wherein weak fields have been removed for illustration purposes. Note that the solar dynamo simulation using the aforementioned settings would correspond to an average solar cycle and that the number of active regions is defined by the resolution of the simulation, the implications of these are discussed in section 4.6; in this investigation a meridional slab with 256 radial and 256 angular partitions is used.

Figure 4.15 presents the probability density functions (PDF) of emerging active regions during a simulated Schwabe cycle from standard parameterisations and from those used in this investigation. The superimposed shaded areas correspond to the PDFs from observed regular sunspot area activity (greater than 100 millionths of a hemisphere) during the cycles 12 – 23. The approach presented in this investigation

Fig. 4.13 Theoretical magnetic Sun. The image shows the field contours for the toroidal (azimuthal term of the magnetic field or  $B_\phi$ ) and diffuse radial field (radial term of the poloidal component or  $B_r$ ). In both cases the colour bars are in logarithmic scale and the sign in parentheses represents magnetic polarity. Emerging active regions are related to latitudes of sunspot activity. Interactive image in Acrobat Reader, Foxit Reader, or PDF-XChange.

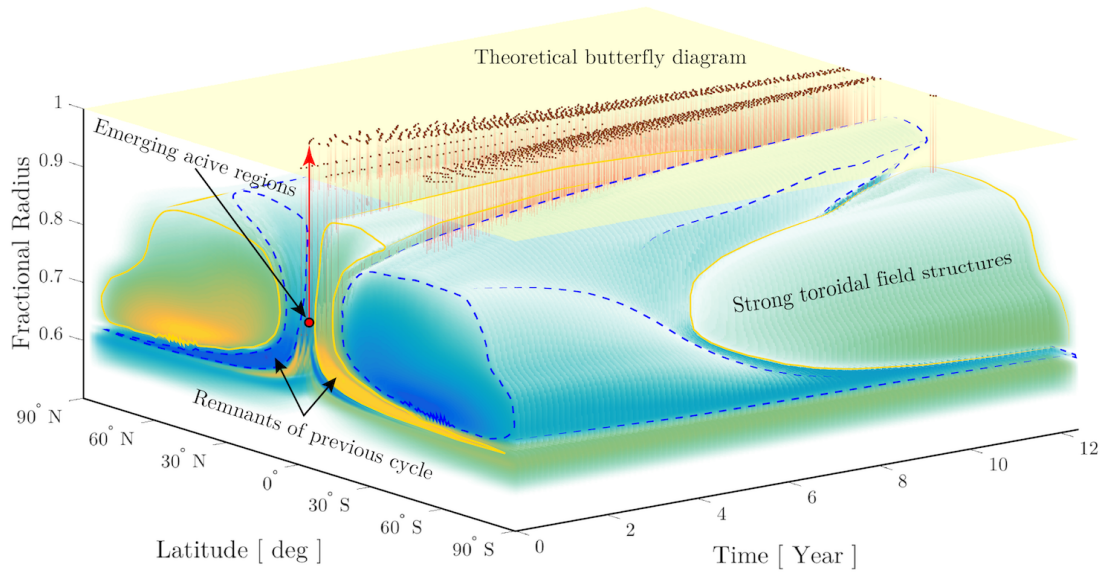


Fig. 4.14 Theoretical toroidal evolution of strong magnetic fields. Weak magnetic field regions, of less than approximately  $10^3$  G, have been removed for illustration purposes. Light solid and dark dashed lines represent magnetic fields of opposite polarity. Active regions correspond to magnetic field strengths higher than  $10^5$  G, which are believed to be the source of buoyant rise of magnetic flux tubes generating sunspots. In this illustration, emerging active regions are projected on the surface plane constituting a theoretical butterfly diagram.

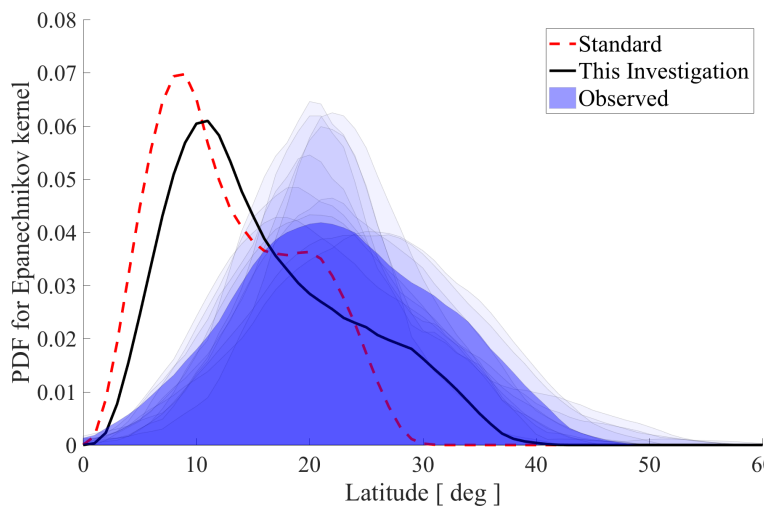


Fig. 4.15 Probability density functions of emerging active regions and regular sunspot areas. The curves represent the simulated average solar cycle activity, superimposed shaded areas correspond to observed solar cycles. The darkest shaded area corresponds to the solar cycle 23 the importance of which for this investigation is discussed in section 4.6.

favours the growth of azimuthal flux in more even fashion at mid-latitudes as seen from the comparison of the right tail of the PDFs. In addition to this, the skewness of the PDF of this investigation shows better resemblance to the PDF from observational data. The PDFs correlation coefficients between observed and simulated solar activity are 0.4921 and 0.6374 for the standard parameterisations and those used in this investigation respectively.

As a final remark in this subsection, it should be pointed out that in general mean field dynamo models are a simplified two-dimensional representation of complicated three-dimensional MHD simulations, i.e. axisymmetrisation of non-axisymmetric parameters. As such, mean field dynamo simulations offer approximations of theoretical three-dimensional MHD simulations; an example of this is presented by Simard et al. [207] on a proposed improvement of mean field dynamo model. Nonetheless, its application in solar dynamo analysis offers an accessible and valuable tool to investigate macroscopic cycle evolution and loosely constrained solar dynamo parameters such as the meridional flow or the magnetic diffusivity discussed in the following section. Therefore the level of detail yielded by three-dimensional MHD dynamo simulations is unnecessary for the purpose of the investigation presented herein.

## **4.6 Solar Cycles Forecast**

After the design of a steady solar-like dynamo model, it is necessary to identify an average observed solar cycle to relate model output characteristics. To this aim in this investigation the total sunspot area record reported in the butterfly diagrams [161] and the monthly average SSN record [151] is evaluated. The SSN record encompasses the last 23 full cycles and the butterfly diagrams, containing hemispheric activity details, the last 12 full cycles. From the SSN record cycle time periods and maximum activity magnitudes are evaluated, whilst from the hemispheric sunspot area record latitudinal activity is evaluated. In this investigation hemispheric sunspot area data (in units of millionths of a hemisphere MSH) is grouped into small sunspots, transition

sunspots, and regular sunspots according to the classification presented by Tlatov and Pevtsov [208]. By processing the complete record of hemispheric sunspot area, it is possible to identify average sunspot activity as function of solar latitude and solar cycle evolution shown in Figure 4.16b. The resulting average butterfly map is then used to quantify differences in hemispheric activity for each solar cycle. The cycle with closest hemispheric activity similarity with respect to the average butterfly map is assigned with rank 1, up to the less similar with rank 13 in this case, i.e. each cycle in the butterfly record is related to a rank value. In a similar way, the identification of the average Schwabe period and SSN magnitude from the SSN record assists the ranking process of the solar cycles. Figure 4.16c summarises the data assessment for the common cycles and identifies the solar cycle 23 as the average cycle according to the cumulative ranking from the three indicators, i.e. butterfly diagrams, SSN maxima, and SSN cycle time periods. This result coincides with the one reported by Jiang et al. [179] although the indicator used in their conclusion is not reported.

Having identified the average solar cycle it is then possible to establish conversion factors to relate observed solar characteristics to the dynamo model output. This fundamental procedure enables the identification of the scaling relationship between the model output, i.e. representing an average solar cycle, and the observed average solar cycle 23. Firstly, in this investigation a conversion factor to relate the theoretical polar magnetic field strength at SSN minimum is of interest, viz. instantaneous initial state, to the corresponding observed value; solar polar magnetic field strength is used as solar activity leading indicator in a similar approach to Jiang et al. [179]. The smoothed polar fields, respective solid lines in Figure 4.17, represent the average observed field in the polar caps with effective latitudes of  $\pm 70^\circ$  [209]. This observable surface indicator of the solar state is of central importance in the dynamo model fine adjustment in this investigation, from the current explanation about the solar cycle 23 to the subsequent scale fitting of other cycle's polar magnetic fields. In this respect, the importance of observed photospheric magnetic fields lies in the belief that its magnitude is related to the poloidal magnetic structures underneath. In order to modulate the poloidal potential

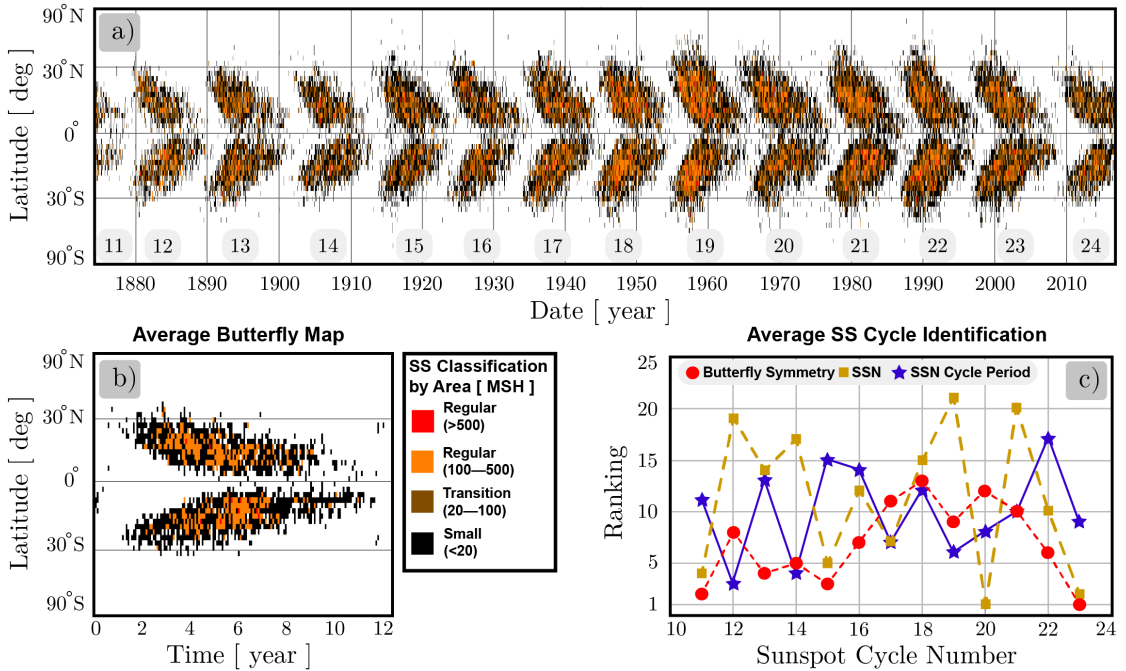


Fig. 4.16 The average solar cycle. Subfigure *a*) presents the record of hemispheric sunspot areas as function of solar latitude and time. Subfigure *b*) shows the average butterfly map computed with data from the observed record. This benchmark map assists in the ranking of the solar cycles, wherein rank 1 corresponds to closest similarity to this benchmark. Data from the SSN record provides two ranking benchmarks, the cycle period and SSN magnitude. The cycle number intersection of the three ranking sets is shown in Subfigure *c*). According to the cumulative ranking from the three indicators, solar cycle 23 is identified as the average cycle.

in dynamo model, the method of meridional slab modification within the region enclosed by  $0.8R_{\odot}$  and the external radius is implemented [179]. This method allows for the even modulation of the polar magnetic field in the dynamo model slab. However, note in Figure 4.17 that the smoothed polar field curves slightly differ at time zero (SSN minimum). In order to include observed hemispheric asymmetries, this investigation uses a sectioned modification meridional slab divided by the solar equator wherein the magnitude of the smoothed south hemisphere polar field is chosen arbitrarily as reference value to compute the model's scale factors; in other words the characteristic southern dynamo polar magnetic field strength at a point near the surface and solar latitude  $70^{\circ}$  is proportional to the respective observed value wherein the constant of proportionality is the scale factor. Finally, scaling the theoretical emerging active

regions profile resulting from the poloidal potential modulation, hereinafter referred to as pseudo-SSN, to observed solar activity is necessary; the maximum smoothed SSN is used for this purpose. Attention of subsequent analysis should be centred only on the relatively stable SSN rising phase as discussed in subsection 4.5, the shaded area encompassing approximately the first lustrum (5 year period) in Figure 4.17.

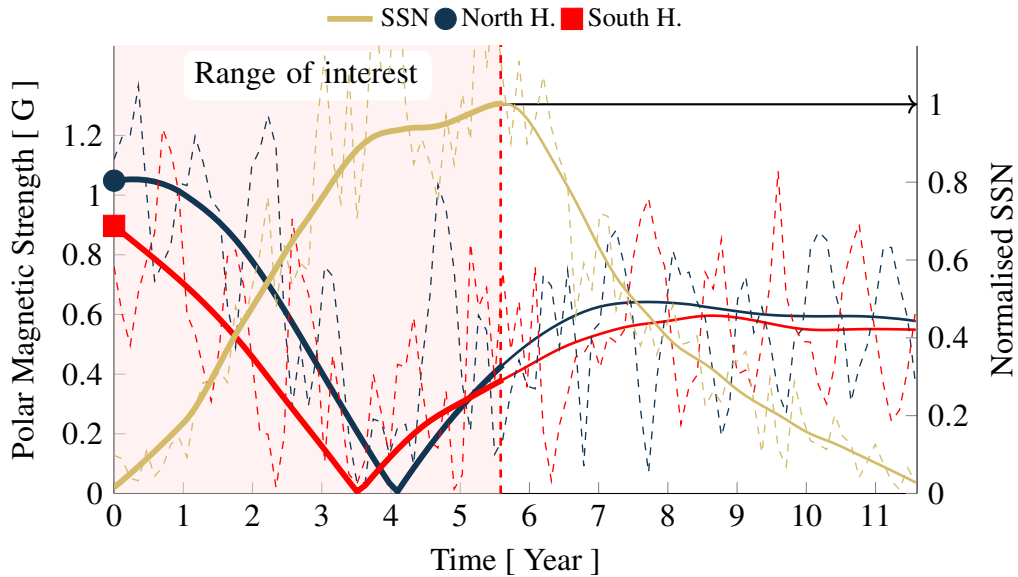


Fig. 4.17 Selected indicators for observed solar cycle 23. The dark solid curves represent smoothed polar magnetic strength magnitudes, left scale, and the solid curve in light colour is the normalised SSN, right scale. In this investigation, the observed polar magnetic field strength values at time zero are used as modification inputs to hemispheric poloidal potential modulation in the dynamo model for each studied solar cycle. On the other hand, the observed maximum SSN value in the solar cycle 23 is used to scale the resulting theoretical dynamo activity output. In this way, observed cycle 23 SSN and pseudo-SSN maxima from the calibrated dynamo model are equivalent.

The calibrated dynamo model for the solar cycle 23, that is the fully scaled dynamo output to the selected solar activity indicators, is shown Figure 4.18. The root-mean-square error (RMSE) of the model pseudo-SSN and the observed SSN for the rising and declining phases are reported in the figure. The effect of forced initial hemispheric asymmetry and values in the model's poloidal potential is observed in the polar magnetic strength magnitude evolution. From the plots in Figure 4.17 and Figure 4.18 *sufficient* resemblance during the rising phase of the SSN cycle is observed as well as the expected incompatibility between simulated and observed data during the declining

phase. The most remarkable incompatibility is observed in the simulated polar fields that as previously discussed, are generated by highly random processes dominating the declining phase of the sunspot cycle. The main factor limiting conclusions about the

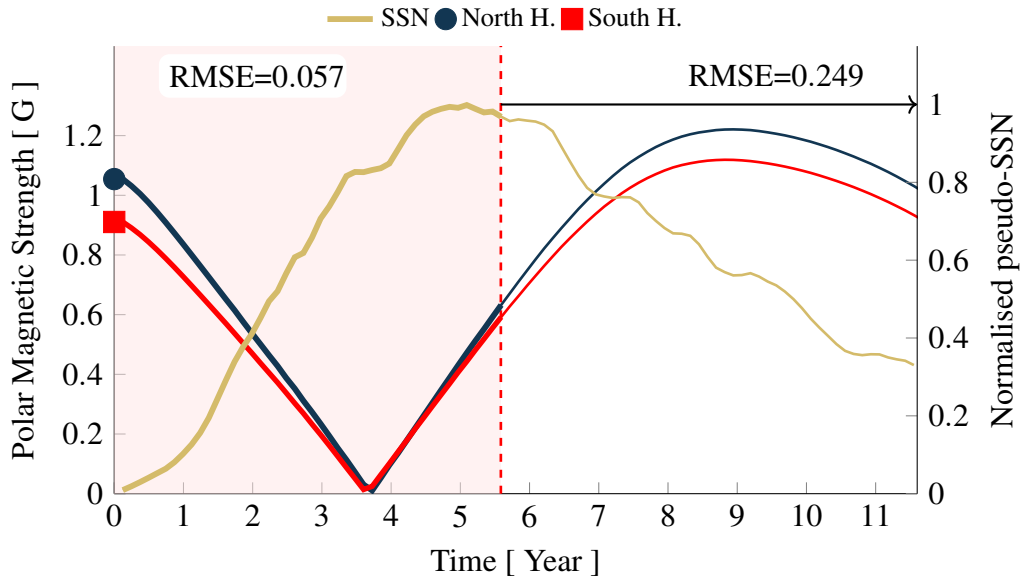


Fig. 4.18 Same as Figure 4.17 for the calibrated dynamo to the observed solar cycle 23. Polar field magnitudes correspond to the solar latitudes  $\pm 70^\circ$ . Starting from the forced initial poloidal potential modulation to match the observed initial polar field magnitudes at time zero, the dynamo model evolves to polar field inversion around the fourth year in close resemblance to the observed trend in Figure 4.17 within the relatively stable SSN rising phase. The maximum value of the pseudo-SSN profile, obtained from the historical number of emerging active regions, is equivalent to the maximum value of observed SSN during the identified average solar cycle 23. Bear in mind that SSN equivalence is ensured only for the solar cycle 23 whereas in other cycles this is not necessarily true as expected from the diverse polar magnetic field strengths initial inputs used in the solar dynamo.

adequacy of the solar dynamo with polar magnetic field as precursor for forecasting purposes, is the reduced record of photospheric magnetic fields and polar solar magnetic activity (Fig. 4.6). For this reason, Jiang et al. [179] tested their model with the information available for the solar cycles 21, 22, and 23. In this investigation the reconstruction of polar field strengths using the longer record of hemispheric sunspot areas is proposed aiming at overcoming this limitation.

#### 4.6.1 Solar Polar Field Strength Reconstruction

Section 4.2 presented the magnetic butterfly diagram and introduced the concept of poleward migration of solar activity remnants. With the advance of the solar cycle and as the generation of poloidal flux from toroidal flux develops near the solar surface, part of the generated flux is advected by meridional flow circulation to the poles where these gradually accumulate building up distinguishable polar fields of maximum strength near the end of the Schwabe cycle. Additionally, remnants of sunspot activity, that is remaining flux after cancellation and submergence, is diffused locally generating unipolar patches. According to the sunspot magnetic flux level, and helicity [210], a small amount may withstand flux fragmentation and cancelation to form long-lasting diffuse unipolar patches. These patches gradually form distinguishable trails of unipolar poleward drift with respect to the surrounding average weak diffuse magnetic field. These characteristic features are easily observable in the averaged photospheric magnetic field reported in magnetic butterfly diagrams, Figure 4.19. However, the surface of the Sun is intrinsically active where magnetic fields are in continuous efficient interaction. Spontaneous magnetic fields emerging throughout the surface are fragmented, redistributed, and diffused in the magnetic carpet renewing itself in a few tens of hours (10 – 40 hours [180]). This inherent surface activity may affect the unipolar trails enhancing their decline. Thus, regular sunspots (flux density above  $\sim 10^{21}$  Mx [208]) are more likely to contribute with long-lasting unipolar patches than small sunspots or pores ( $\lesssim 10^{20}$  Mx). For this reason, the information about past solar activity conveyed to the pole caps is plausibly related to chiefly regular sunspot activity. The phase shift between observed sunspot activity and polar field strength is identified at 4.1 years in this investigation. On the grounds of this reasoning, regular sunspots in the sunspot areas record (Figure 4.16) may contain sufficient information to reconstruct unrecorded polar field cycles. Artificial neural network methods can be suitably used to address this task owing to the complex nature of the relationships involved.

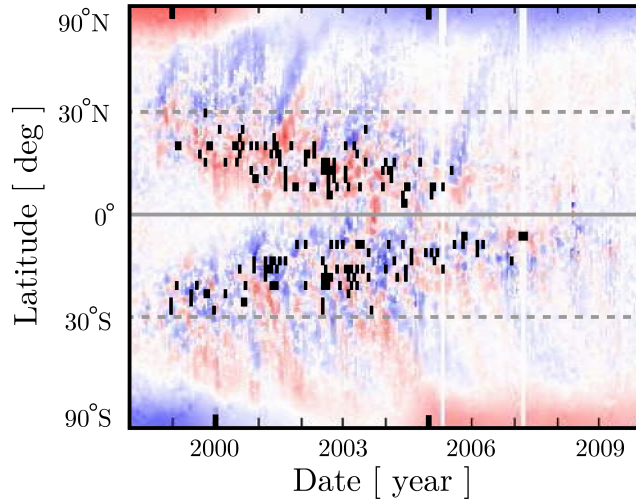


Fig. 4.19 Longitudinally averaged magnetic field (magnetic butterfly) diagram for the solar cycle 23. Reddish colour represents positive flux, and highly active sunspot areas are marked in black. Trails of unipolar poleward drift are observed in both solar hemispheres. In this investigation is argued that regular sunspot activity is likely to be captured in the polar magnetic field pole caps as this is transported by meridional circulation. If the information reaching the pole caps contain sufficient detail about past sunspot activity, then this may open the possibility to reconstruct unrecorded historical polar field from hemispheric sunspot areas. Image adapted from [211]

An artificial neural network (NN) is a computational model built with a collection of interconnected simple processing instances called neurones, resembling in essence a biological neural network. Each neurone consists of adjustable scalar weights to scale inputs, a fixed transfer function to model the neurone shape response, and an adjustable scalar bias to shift the function. The interconnection ensures that every neurone contributes to the collective neural network response. The objective of the NN implementation is to learn from and respond to given data in a desired way, wherein adaptability and capability of generalisation of the NN to new data is the ultimate objective. To this aim, a fundamental design stage in NN implementation is the *training* phase in which the NN learns in unsupervised or supervised manner [212, 213]. During the *training* phase in unsupervised NNs, the adjustable scalars in each neurone are adjusted aiming at the discrimination of data lying within specific criteria. Unsupervised NNs use input data to auto adjust their parameters dynamically. This type of NN are valuable in classification and pattern recognition, e.g. cluster analysis and image

processing for object detection. On the other hand, a supervised NN uses data with labeled responses from input and expected response (target) data<sup>13</sup>. In this case, an iterative process modifies the adjustable scalars in each neurone during the *training* phase aiming at the faithful reproduction of target reference data. Supervised NNs find application in automated classification such as face/voice recognition, and in the modelling of continuous system response as a function of input predictor variables (regression). This later capability of supervised NNs is typically applied in time series predictions such as in financial analyses or even proposed for SSN trend prediction [214] (also discussed in subsection 4.3.1). For the problem at hand, supervised NN training under the regression category was selected because the training dataset, i.e. predictor and target data, encompass sequential vectors.

When dealing with sequential vectors used as NN inputs, adding feedback and delays typically improves the NN performance because these establish memory capability valuable for learning sequential patterns. This type of NN model is called a dynamic network, and relates the history of the input sequence and feedback sequence to establish the NN response. A Nonlinear AutoRegressive network with eXogenous inputs (NARX) is a dynamic model that can use several layers of neurones and independent input series, namely *exogenous series*, which are known influence on the target series. The NARX model output  $y(t)$  is thus a function of past values of  $y(t - n_y)$  (target or feedback data), and exogenous series  $x(t - n_x)$ , Eq. (4.11). The powerful NARX model may be applied in a myriad of applications<sup>14</sup>. In the investigation presented in this chapter, the NARX model is used to represent a nonlinear dynamic system relating present and past data of the driving hemispheric sunspot area series (exogenous), and the record of solar polar fields (target). The selection of this input dataset for the NARX model is justified due to the known influence on the exogenous series on the target series as discussed earlier

---

<sup>13</sup>One of the main differences between supervised and unsupervised NNs is that the later adjusts itself using the network inputs only since no target outputs are available.

<sup>14</sup>For further reading about network theory, architectures, and architecture type choice see Demuth et al. [213]

in this subsection.

$$y(t) = f[y(t-1), y(t-2), \dots, y(t-n_y), x(t-1), x(t-2), \dots, x(t-n_x)] \quad (4.11)$$

The NARX model used for the reconstruction of the polar fields in this investigation is presented in Fig. 4.20. The two exogenous input series ( $x_{1,2}(t)$ ) are the north and south hemispheric regular sunspot areas, and the target series ( $y(t)$ ) is an observed polar field. It should be noted that the two hemispheric exogenous input series are used in the proposed reconstruction of each solar polar field. This is a reasonable approach assuming that sufficient magnetic communication exists between both hemispheres as suggested by the nearly mirrored polar magnetic strength history in Figure 4.17. Hence, possible loss of past solar activity information during the creation of unipolar patches and the subsequent hemispheric poleward drift, may be plausibly recovered from the regular sunspot areas record of both hemispheres. Continuing with the description of the model, a layer of six interconnected sigmoid neurones in the so-called hidden layer, are fed with the exogenous and target series delayed 1 – 10 states (10 Julian days per state). This delay range is heuristically established according to the ultimate performance of the model. The output layer consists of a linear neurone used as a function approximator.

Fig. 4.20 illustrates a parallel NARX architecture (closed loop) useful in the practical application of the model. In a previous step, the model is trained to establish suitable weights and bias values. During the training phase the target series, in this case a polar field series, is available requiring no  $\hat{y}(t)$  feedback. The training algorithm adopted is the standard Levenberg-Marquardt backpropagation, with internal data division of 70% training, 15% validation, and 15% testing. During the training phase, the Levenberg-Marquardt optimisation looks for adequate weights and bias values to reduce the error between the target signal and the model's output. Since internal data division and sampled data for training is stochastic, mainly to prevent target memorisation, computed weights and biases may differ amongst various trained models leading to

## Solar Activity Forecast

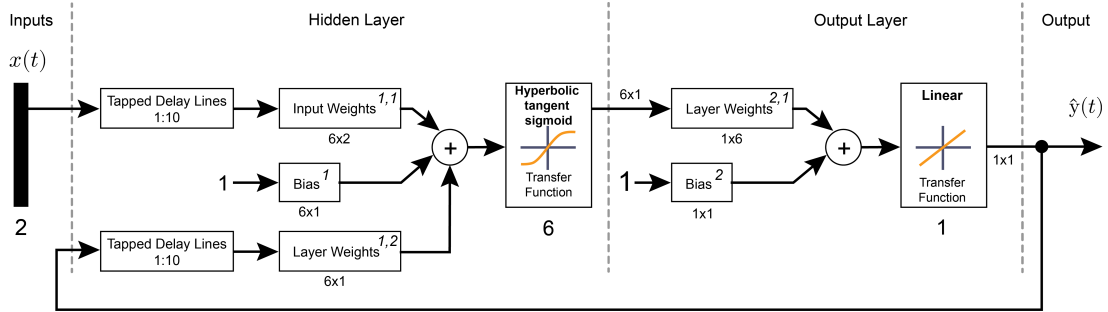


Fig. 4.20 Layer diagram of the Nonlinear AutoRegressive network with eXogenous inputs (NARX) in parallel configuration (closed loop). The network uses 6 hidden layer neurones and the input and feedback delays range from 1 – 10. The two exogenous inputs correspond to the hemispheric regular sunspot area records. During the training phase, that is the procedure to establish weights and biases values, the target series (one observed hemispheric polar field series at a time) is available requiring a series-parallel architecture; after the training phase, model output feedback is used in replacement of the target series in the parallel architecture shown. Architecture change calls for further generalisation performance assessment to discard possible target memorisation during the training phase.

various performance levels. This means that a trained model would have a unique set of bias and weight values related to the *randomly* sampled input data required by the training algorithm. Furthermore, depending on the overall sampled data during the training phase, the NARX may be more or less adaptable to interpret new input data according to its success in building a representative nonlinear dynamic system. Aiming at improving NN generalisation, multiple models may be trained to select the one able to generalise best. In this investigation 200 models for each polar field are trained, and in order to identify the most accurate one, the available target data is divided in two parts: 95% is used for the model training phase, and the remaining 5% is saved for a subsequent best model identification phase.

The optimum trained NARX model for each hemisphere is used to reconstruct the respective polar field. In this implementation phase, the target input  $y(t)$  is substituted by  $\hat{y}(t)$  transforming the series-parallel architecture (open loop), into a parallel architecture. The regular sunspot area record provides sufficient exogenous input series to reconstruct polar fields from the Schwabe cycle 12 to 20, and to forecast their values up to the next sunspot minimum. This last feature is possible due to the the existing phase shift

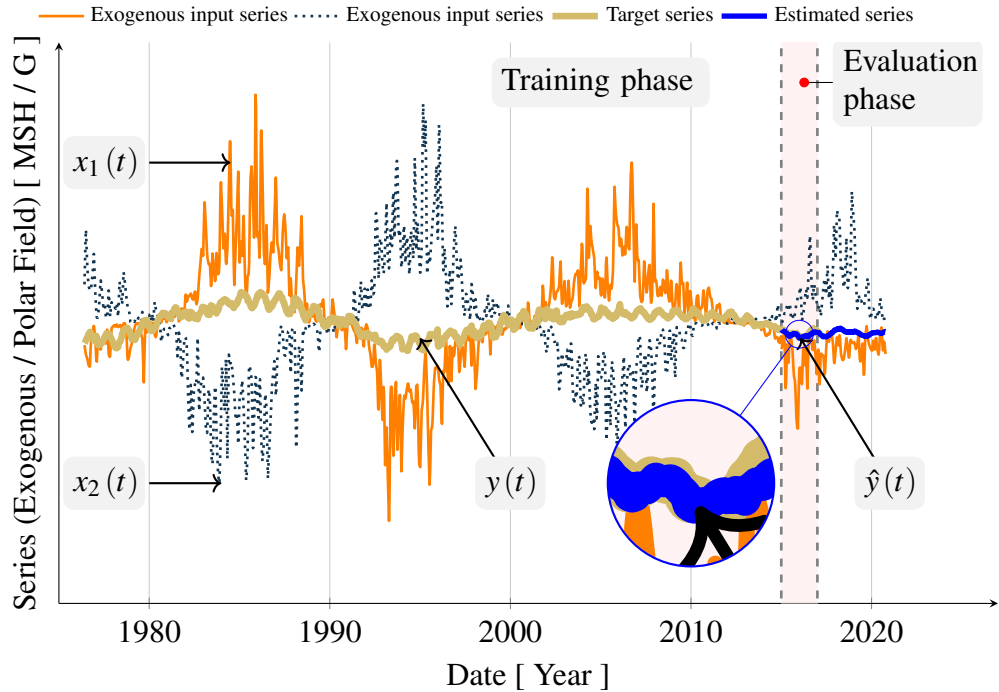


Fig. 4.21 Time series employed for the southern polar field short-term forecast. In this example all relevant time series are superimposed for illustrative purposes only. Phase shift between observed hemispheric sunspot areas (exogenous inputs) and polar field strength (target) is cancelled during computations. Multiple NARX models are trained to finally select one able to generalise best during the evaluation phase. The magnified area shows the target series segment  $y(t)$  and the estimated value of the polar field  $\hat{y}(t)$ . The best NARX model is expected to represent a nonlinear dynamic system relating exogenous input series and target series. In total, a polar magnetic strength forecast and a reconstruction is obtained for each hemisphere.

between the sunspot area record and polar field (section 4.2) as shown in the example in Fig. 4.21. In the figure the exogenous input series, target series, estimated series, and data segmentation for the training and best model identification phases are identified.

The reconstructed and forecasted polar field time series are used to establish the poloidal potential modulation in the dynamo model to reproduce observed solar activity. It is convenient at this point to bear in mind that the poloidal potential modulation is effective only at the start of each simulated solar cycle, which implies natural poloidal potential evolution along the simulated solar cycle. Thus, the polar field time series are sampled at SSN minima to identify the initial poloidal potential modulation for each cycle. With the exception of the starting date of the forthcoming solar cycle 25,

## Solar Activity Forecast

---

all other dates are established. Thus a short-term prediction to estimate the start of the solar cycle 25 is required. To this end, a standard autoregressive model [215] of degree 9 is used on the monthly smoothed SSN as shown in Fig. 4.22. The model short-term prediction sets the start of the solar cycle 25 around the second half of 2018, in agreement to the SILSO [151] forecasts (Kalman-filter optimised forecasts ML and SC). In Fig. 4.23 the magnitude of the full solar polar fields series from the NARX reconstruction and forecasts, as well as from the Wilcox Solar Observatory record [167] (WSO) are presented. Squares in the figure indicate the solar polar field values considered for subsequent solar dynamo input (at the beginning of each solar cycle).

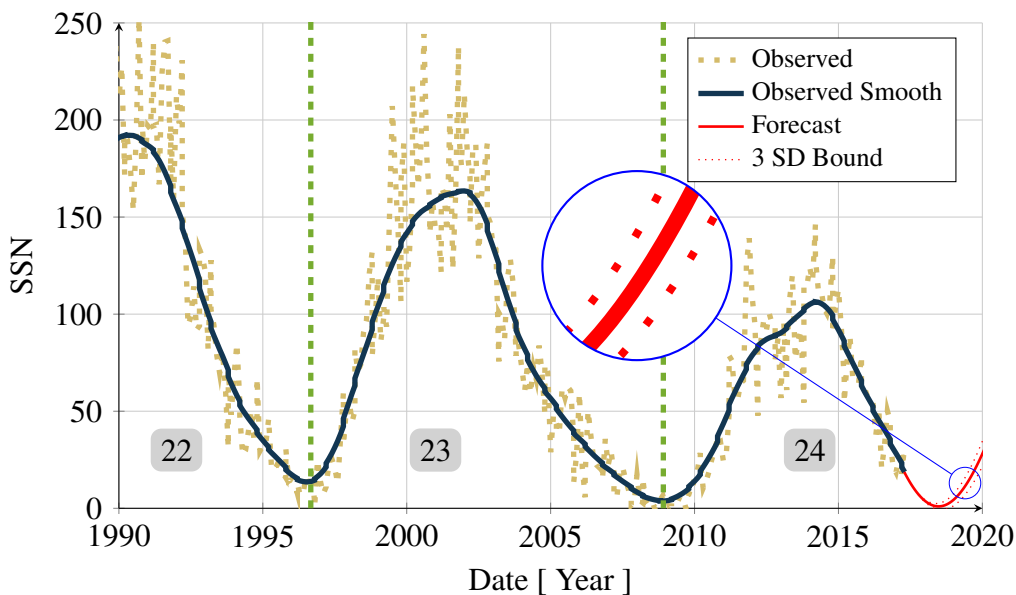


Fig. 4.22 Start of the solar cycle 25 prediction using an autoregressive (AR) model of degree 9 on the monthly smooth SSN.

From Figure 4.23 is observed that the NARX model methodology succeeded in obtaining a nonlinear dynamic system embodying long-term characteristics of the complex processes relating sunspot areas and polar field strengths. However cumulative short-term variations reducing polar field strength representativeness of past solar activity, such as active regions helicity hemispheric compatibility and irregular unipolar poleward migration velocity [210], are arguably an important source of degraded NARX model performance. An immediate apparent discrepancy observed in the NARX

curves is the expected maximum of polar field magnitude at the start of the Schwabe cycles, which is true during the observed magnetic field window in the figure (WSO data). It is essential to acknowledge that the NARX curves are by no means accurate representations of polar field strength history but coarse estimations derived from a small portion of the observed Sun. However, the NARX reconstruction provides interesting clues of possible past behaviour challenging the generalisation of the aforementioned expected trends. In this regard, the consolidated polar faculae (PF) database reported by Muñoz-Jaramillo et al. [216] furnish supporting evidence to the NARX reconstruction validity. For instance, the times of polar faculae maxima (marked as triangles in Figure 4.23) although similar to the times of WSO polar field maxima and in agreement to those of SSN minima, show a local maximum near 1960 differing to the reported start of the solar cycle 20 that took place in 1964; this time of polar faculae maximum and the respective maximum from the NARX reconstruction are similar as shown in Figure 4.23. Acknowledging the possible existence of this behaviour, all sampled reference magnetic states used in the solar dynamo correspond to the start of each Schwabe cycle, independently of the shape of the polar field curves. Hence, the true representativeness of the sampled estimated polar field strength should be assessed by the solar dynamo-NARX combined efficacy in reproducing solar activity.

A possible way to improve the presented NARX model is by incorporating information from other recorded solar activity proxies, e.g. the record of polar faculae, to provide a broader and richer set of scenarios during the development of the model. However, in this investigation solar cycles simulation presented in the following subsection 4.6.2, is carried out using the model developed in this subsection.

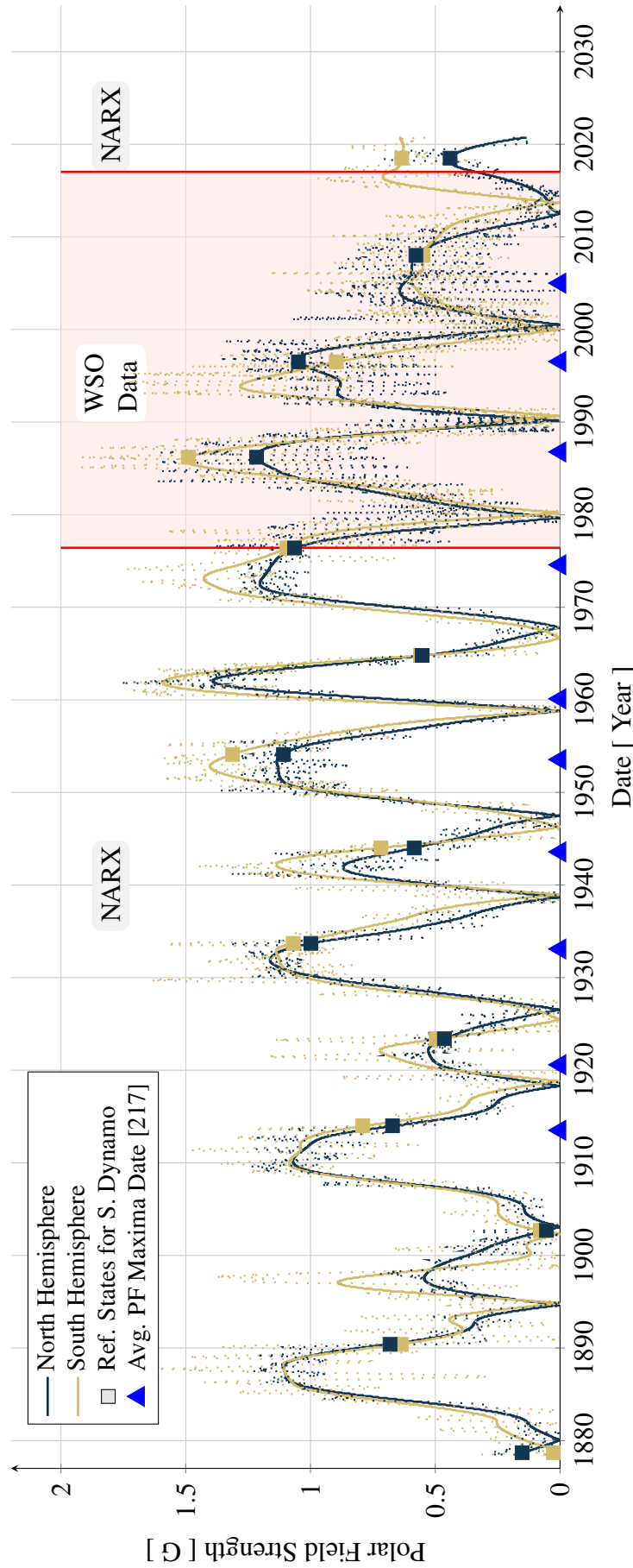


Fig. 4.23 Full solar polar fields series from the NARX reconstruction and forecasts, and from the Wilcox Solar Observatory record. Triangles show dates of reported north-south maxima average polar field strength magnitude according to Muñoz-Jaramillo et al. [217], derived from a consolidated polar faculae database. Dates of peak values from the NARX reconstruction are similar to those from the polar faculae database supporting the reconstruction validity in this respect.

### 4.6.2 Solar Cycles Simulation and Forecast

Solar activity dynamo simulations of the cycles 12 – 25 are presented in Fig. 4.24. The theoretical magnetic and sunspot butterfly diagrams are shown in Fig. 4.24a, and the pseudo-SSN (solid curves) are superimposed on the observed 13-month smoothed monthly SSN [151] (light areas) in the mid and lower plots (b) and (c). Pseudo-SSN are obtained from the normalised and scaled chronological sum of emerging active regions in Fig. 4.24a, with respect to the reference observed solar cycle 23. Note that during the declining phase, the theoretical curves overestimate the observed SSN. This is an expected behaviour as the solar dynamo model gradually adjusts itself from the imposed initial poloidal potential magnitudes and asymmetries to bring back a subsequent average solar cycle. The theoretical curves in Fig. 4.24b show the direct output from the solar dynamo model, whereas Fig. 4.24c shows corrected theoretical curves with the process detailed below.

Raw data in Figure 4.24b shows important characteristics of the dynamo model and its potential use for forecast application. Firstly, theoretical and observed SSN maxima of cycle 23 must match since this cycle serves as data fulcrum to relate theory with observations. Other theoretical and observed maxima show close match such as in cycles 12, 17, 20, and 22; the rest show various levels of differences with the highest found in cycle 19. From these results is evident that the solar dynamo model produces results with limited sensitivity to the simulation initial state, i.e. approximately  $\pm 50$  SSN with respect to the initial observed reference solar cycle. For example, dynamo input data (solar polar fields) from the observed solar cycle 20 produced underestimated pseudo-SSN activity (theoretical curve in the figure) of the cycle 21, albeit with the correct increasing trend. Due to this model limitation simulation results are assessed in pairs, that is in trend transitions from the initial reference observed cycle to the subsequent simulated cycle, rather than direct SSN cycles comparison. Figure 4.25 summarises maxima forward percentage trends between the theoretical and observed SSN. From the theoretical points in Figure 4.25 is seen that the transitions  $17 \rightarrow 18$ , and

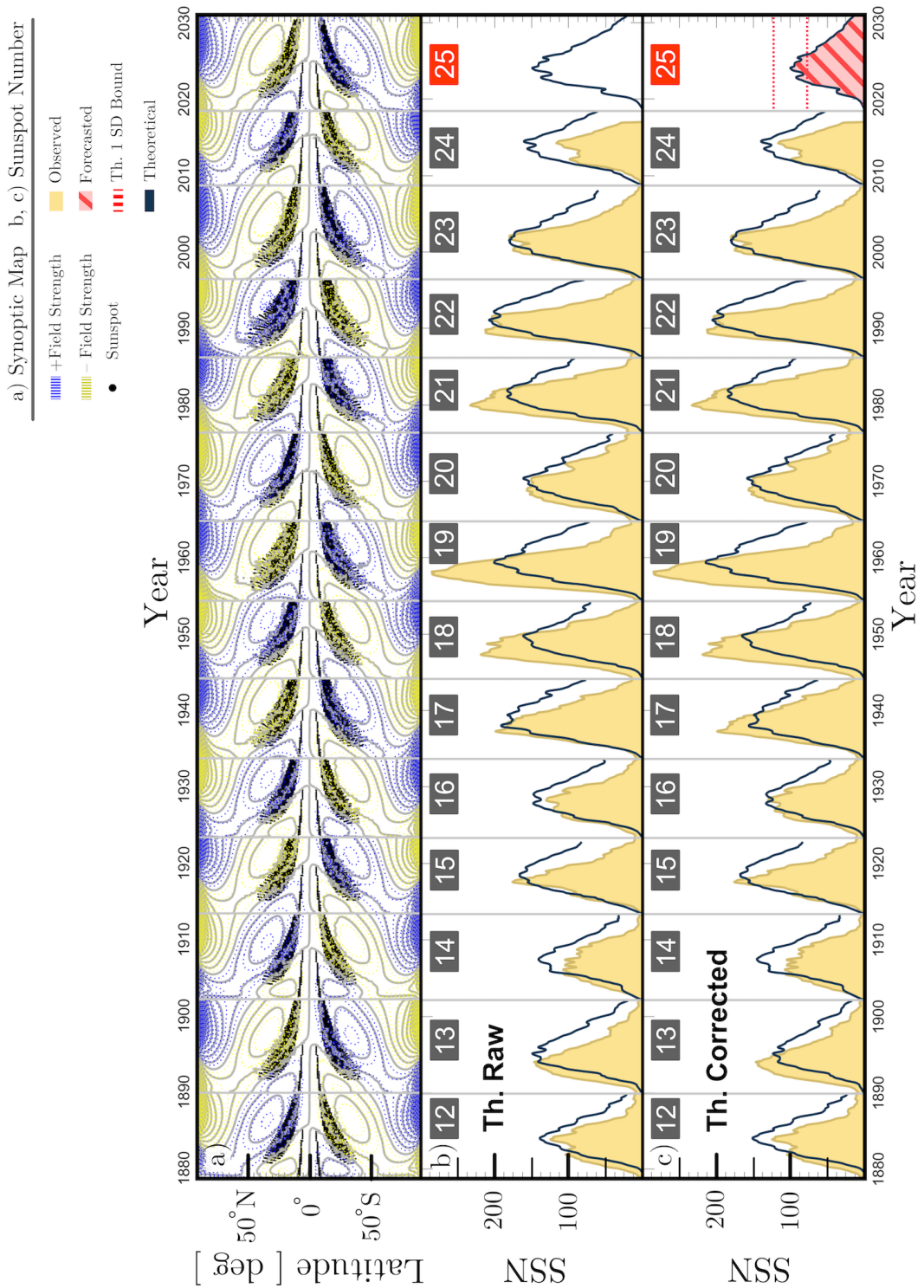


Fig. 4.24 Solar activity simulation results. The theoretical magnetic and sunspot butterfly diagrams are shown in panel (a). Panels (b) and (c) show the raw and corrected pseudo-SSN (solid curves) respectively, superimposed on the 13-month smoothed monthly SSN [151] (light areas).

$21 \rightarrow 22$  are discordant to the observed trends. Or in other words, if forecast had been the case, simulation of cycles 18 and 22 would have lead to incorrect predicted trends with respect to cycles 17 and 21 respectively.

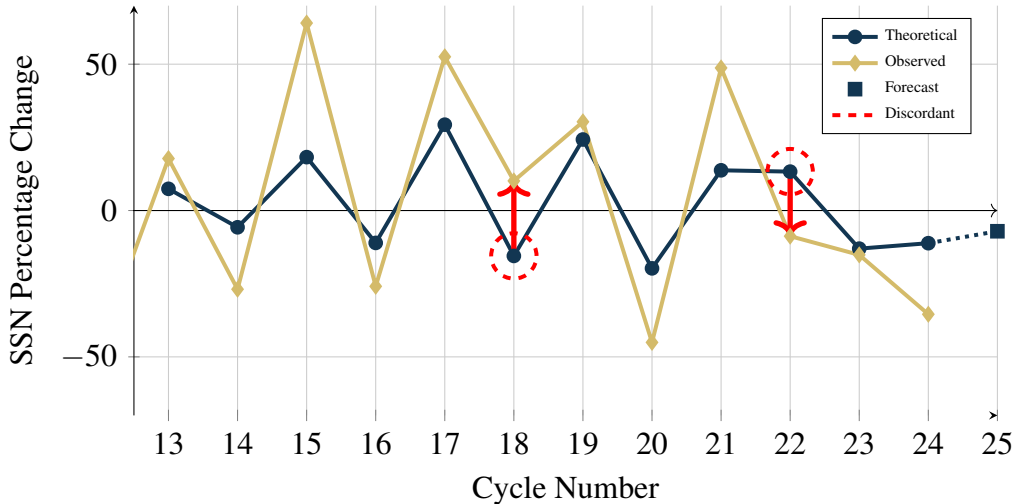


Fig. 4.25 Solar maxima forward change percentage trends from the raw theoretical and observed SSN. Discordant pairs for a given solar cycle have opposite signs, whereas concordant pairs exhibit different levels of agreement. The highest level of agreement (overlapping pair) is observed in the solar cycle 23 because the theoretical response is calibrated on this cycle.

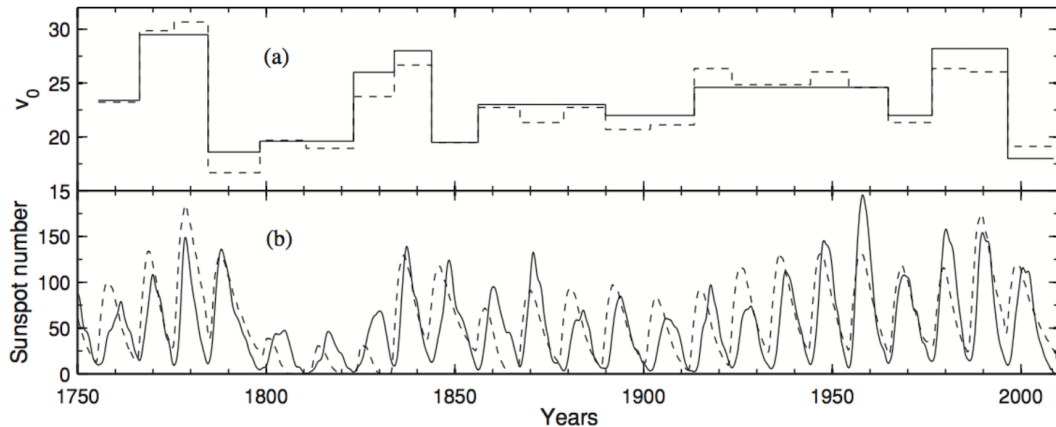
External investigations of solar cycle activity reproduction using high diffusivity mean field axisymmetric dynamo models shown in Fig. 4.26, show similar performances to those in this investigation. In a first example, from Karak's [177] study in Fig. 4.26a, the meridional circulation is adjusted to match observed SSN periods. This parameter variation modified the average dynamo model response producing various levels of solar activity. That approach loosely approximated the magnitude of some solar cycles, with maximum difference found in the solar cycle 19. Regarding the trends between solar cycles and their precursors<sup>15</sup>, cycles 15, 18, and 20 are discordant to observations in Karak's study. In another example, Jiang et al. [179] report simulations using the observed photospheric magnetic fields as cycles' adjusting parameter, thereby encompassing cycle 21 onwards. In Jiang et al. [179] study in Fig. 4.26b, theoretical curves of the cycles 21, 22, 23 show close match to the observed SSN. Additionally a

<sup>15</sup>For the range of interest, from cycle 12 to the latest available cycle 23 [177].

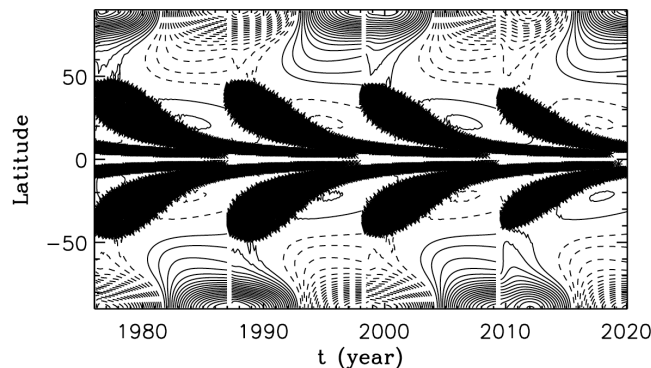
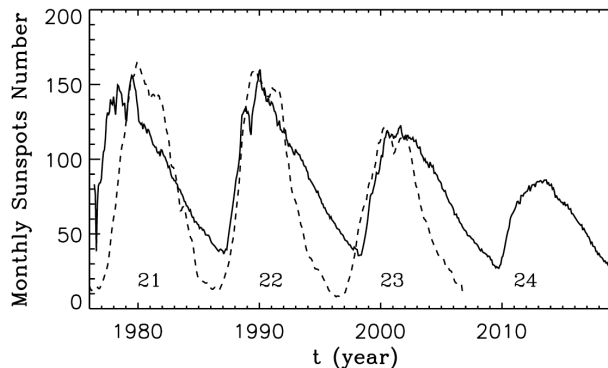
forecast for the cycle 24 is reported that is now known to have successfully anticipated peak observed activity. However, regarding the trends between solar cycles and their precursors, cycle 21 is discordant in that study.

At this point is important to bear in mind that the photospheric magnetic fields precursor approach by Jiang et al. [179], is used as reference in this investigation as mentioned in section 4.4. Thus, due to similarities in approaches, Jiang et al. [179] results can be directly compared to those in this investigation in Fig. 4.24b for the range 21 – 24. Interestingly, discordant cycle 21 → 22 trend and correct reproduction of the solar cycle 24 are observed in both cases. The ability to compare further solar cycles in this investigation, is enabled by the proposed polar fields reconstruction of past solar cycles. The validity of the reconstructed polar fields is tested in their capability to furnish adequate cycle reproduction. Nonetheless, the solar dynamo model as well as the reconstructed polar fields add undifferentiated uncertainty components to the final solar activity simulation. Thus, theoretical cycles in this investigation report weaknesses and virtues of the overall solar parameters and dynamo models, of the reconstructed polar fields for the cycles 12 – 20, and of solar cycles simulation assumptions and methodology. Comparison amongst observed and theoretical cycles in the range 12 – 20 in Fig. 4.24b, highlights the potential of the approach in reproducing observed cycles, however it is seen that high activity cycles are poorly reproduced.

Karak [177] study provides an additional example of solar dynamo model performance. The range of interest for comparison in this case are cycles 12 – 20 in Fig. 4.26a. Albeit comparison of results between Karak’s study and those in Figure 4.24b show that reconstructed polar fields yield better solar cycles reproduction than from observed SSN periods as adjusting dynamo parameter, Karak’s study shows that meridional flow variation is a fundamental ingredient in solar activity simulation. This is a reasonable argument considering that the main relationship between solar activity and meridional flow may be explained by the interaction of equatorward meridional flow at the base of the convection zone. In that possible explanation, plasma flow may encounter motion restriction imposed by magnetic tension found in highly active zones; meridional flow



(a) Solar activity simulation reported by Karak [177]. The upper panel shows the variation of amplitudes of meridional circulation in  $\text{ms}^{-1}$ , the lower panel shows the variation of theoretical sunspot number (dashed line) and observed sunspot number (solid line) with time.



(b) Solar activity simulation reported by Jiang et al. [179]. The upper panel shows the theoretical monthly smoothed SSN (solid line), and the observed SSN (dashed line). The lower panel shows the theoretical butterfly diagram of sunspots superimposed on the contours of radial field for the cycles 21 – 24.

Fig. 4.26 External investigations of solar cycles activity reproduction using high diffusivity mean field axisymmetric dynamo models. Illustrations and information from their respective authors.

is quenched by solar activity. This suggests that a more robust solar dynamo model should include meridional circulation fluctuations along the solar cycles simulation. In this regard, deeper understanding about the meridional flow structure would provide crucial information to improve current solar dynamo models.

Reproduction of past solar cycles is fundamental to the solar dynamo validation process, which in turn improves its reliability for adequate forecasts. The analysis presented above shows that high diffusivity mean field axisymmetric dynamo models do not capture completely the whole range of observed solar activity, at least with the methodologies discussed above. A plausible explanation to the theoretical mismatch found in this investigation, is that the initial adjustment of the dynamo model includes information from only one component of the magnetic field, i.e. poloidal modulation via observed solar polar magnetic fields. In this regard, simulations point out to the possible need of including information about the state of the toroidal component too. Expanding on this possibility, take the theoretical solar cycle 19 in Fig. 4.24b as an example. The initial adjustment of the poloidal potential in the dynamo model introduces partial information of the previous cycle 18 because, without modification, the toroidal field strength corresponds to that of an average solar cycle. With the progress of the simulated cycle, diffusion and the meridional flow gradually transports the modified poloidal field to the tachocline region where it is stretched in the azimuthal direction by the differential rotation. The preexisting and newly produced toroidal fields generate emerging active regions resulting in a small increase of simulated solar activity, i.e. the solar cycle 19. If on the other hand, both fields are adjusted, the newly created toroidal field would find a suitable magnitude of preexisting toroidal field to effectively produce observed activity. The challenge in this case, however, is the identification of an observed proxy of the toroidal field state.

Solar cycles' rise time may give qualitative information of the toroidal field state. This hypothesis is based on an extreme case wherein preexisting saturated toroidal field at the beginning of the solar cycle, would trigger large flux tube buoyant sections emerging rapidly to the solar surface. Conversely to poloidal field, toroidal field

variation is slow, possibly sufficient to retain its main bulk characteristics even after maximum solar activity. If this is true, then a given solar cycle rise time and the polar magnetic field at the end of that cycle, may contain sufficient information to adjust the solar dynamo model for the simulation of the subsequent solar cycle. In order to capture the qualitative state of the toroidal field into a quantitative correction factor, Eq. 4.12 is used in this investigation wherein  $t_i$ ,  $t_f$ , and  $t_{max}$  are solar cycles times at the start, end, and activity peak respectively.

$$C = \frac{t_f - t_{max}}{t_f - t_i} \quad (4.12)$$

The correction is carried out in cycle pairs wherein the cycle  $(n - 1)$  provides the factor  $C$  for the cycle  $n$ . For example, aiming to preserve the magnitude of the reference solar cycle 23, the correction vector is normalised to the cycle 22 as it sets the initial conditions of the cycle 23. The normalised correction vector is then multiplied by the theoretical curves shown in Fig. 4.24b. The corrected theoretical cycles are presented in Fig. 4.24c. This modification results in a dramatic improvement on the magnitudes and trends of simulated cycles with respect to observed activity. Fig. 4.27, shows the corrected simulated cycles trends. SSN percentage change error in solar cycle 22 is reduced in comparison to the same cycle in Fig. 4.25, and the discordant trend in cycle 18 disappears. Nonetheless, two new discordant trends appear in cycles 13 and 14. Interestingly, the erroneous cycle transitions, i.e.  $12 \rightarrow 13$  and  $13 \rightarrow 14$ , coincide with the Maunder's original butterfly diagrams published in 1904 covering the period 1876 – 1902 [218]. In Maunder's original work, butterfly diagrams were built with data of sunspots permanence at a given latitude. Wherever a sunspot centre appeared on the solar surface, and remained for more than one day during a given solar rotation, the latitude was marked in a latitude-time chart [218]. Sunspot area information was added later with the assembly of sunspot observations as formats changed along the years. Unfortunately, recent evaluation of early datasets has identified non-uniform sunspot area data. In an effort to regularise datasets, these were compared with the Mount Wilson photographic plate collection dating from 1917 to 1941 [161]. All this

may suggest that the anomalous transition trends between theoretical and observed data for cycles 13 and 14 in Figure 4.27, may lay in still non-uniform or faulty formatted sunspot area data.

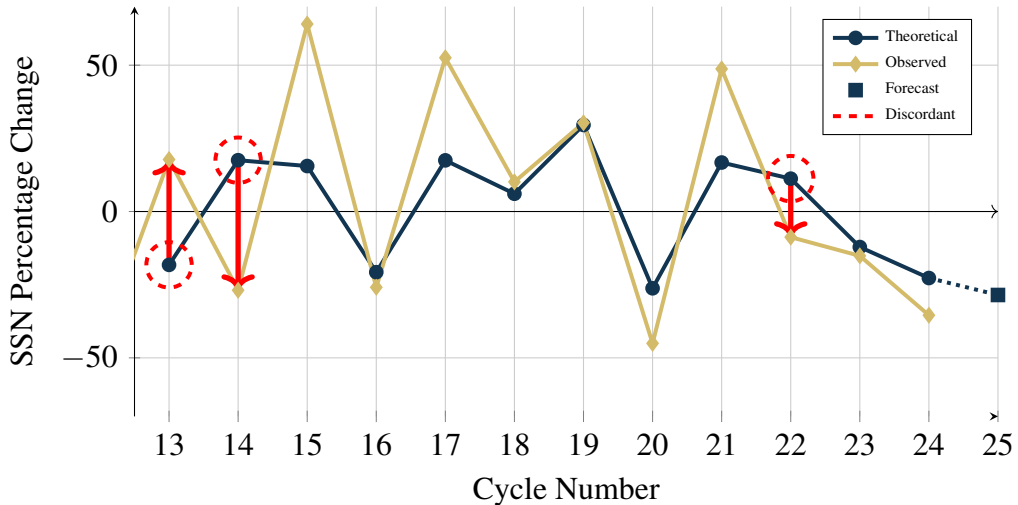


Fig. 4.27 Same as Fig. 4.25 with corrected theoretical SSN. Each cycle correction factor improves the level of agreement observed in the cycle pairs. In addition, possible non-uniform or faulty formatted data in the early cycles record is disclosed.

The solar dynamo model adequate reproduction of solar peak activity and solar maxima forward percentage trends of past solar cycles, allows a forecast for the solar cycle 25 to be proposed. A weak solar cycle 25, with slow rise time and maximum activity  $-14.4\% (\pm 19.5\%)$  with respect to the current cycle 24 is predicted. This represents a peak value of  $99.6 \pm 22.7$  sunspots using the SILSO [151] 13-month smoothed monthly SSN maximum for the solar cycle 24 as reference.

## 4.7 Chapter Conclusions and Further Work

This investigation addresses the problem of solar activity forecast to enable propulsion system design and resources optimisation in nanosatellites. Solar activity forecast becomes an essential task as nanosatellites achieve greater applicability in the commercialisation of space. Reliable solar activity predictions are important because solar activity greatly controls orbital lifespan, body attitude, and survivability in Earth or-

biting nanosatellites. Solar activity repercussion level on propulsion systems varies mostly according to orbit characteristics as this greatly establishes the intensity of Earth atmospheric interaction originating drag. In order to provide an adequate approach to the highly complex task of solar activity prediction, this investigation undertakes the development of a method based on understanding solar cycle underlying process. State-of-the-art solar physics and updated datasets are used, together with advanced time series analysis techniques to develop a robust solar dynamo model. The proposed forecast methodology essentially consists in the use of a suitable calibrated solar dynamo, modulated with observed precursor solar polar magnetic fields and toroidal field proxy information.

Simulations of 13 solar cycles with the proposed solar dynamo approach show satisfactory reproduction of 10 solar maxima and solar cycles peak trends. One anomalous cycle reproduction is likely related to the quality of parameter models and assumptions, the remaining two anomalous cycles are presumably related to observed faulty data employed in the initial set up of the dynamo model. With this acceptable performance, the solar dynamo forecast indicates a weak solar cycle 25,  $-14.4\% (\pm 19.5\%)$  weaker with respect to the current cycle 24. This represents a peak value of  $99.6 \pm 22.7$  sunspots using the SILSO [151] 13-month smoothed monthly SSN maximum for the solar cycle 24 as reference.

The solar activity prediction presented in this chapter should be treated with caution as many fundamental aspects of the solar physics controlling the solar cycle activity are yet to be understood as discussed before. Nonetheless, the combination of the consolidated solar polar magnetic field strengths, and mean field axisymmetric dynamo model parameterisation approach and calibration methodology presented in this investigation, proved to be sufficiently effective to reproduce various historical solar maxima trends. In this regard, further work should use varied sources of data to further enhance the methodologies presented herein. For example, in the proposed solar polar field reconstruction the polar faculae record is used for comparison purposes only; the polar faculae record could potentially be used as a new pair of exogenous input

## **Solar Activity Forecast**

---

series in the neural network to improve the reconstruction, yielding to better polar field precursor definition for dynamo simulations. In addition, the modulation of differential rotation amplitude could also be incorporated in richer mean field axisymmetric dynamo model simulations. Many other unanswered questions about solar activity underlying mechanisms open the possibility for substantial prediction improvement. In this respect, understanding the nature of the solar meridional flow, apparently multicellular, and the actual diffusivity profiles are key to the development of superior solar activity forecasts. Complementary to solar activity prediction, further work may be centred on the heliospheric current sheet analysis due to its interconnecting significance to the space environment.

# **Chapter 5**

## **Atmospheric Interaction with Nanosatellites from Observed Orbital Decay**

This chapter sets out to address a primary application of propulsion technologies for nanosatellite systems. Typical operative altitudes for nanosatellites lie within one thousand kilometres in orbits where the dominant non-conservative disturbing force is the atmospheric drag. Atmospheric interaction with nanosatellite surfaces has a pivotal role in orbital decay, which in turn defines the desired characteristics and size of a convenient atmospheric drag-offsetting propulsion system. Moreover, long term atmosphere-spacecraft interaction variations are key in orbit manoeuvring and orbit maintenance optimisation specifically using EP. In general, the effect of drag on an orbiting object is the monotonic reduction of its eccentricity and semi-major axis. Thereby drag reduces the orbital altitude affecting lifespan, modifying the orbital shape, and ultimately leading to orbit re-entry. Additionally, drag can produce attitude perturbation torques that are in the main undesirable. These aspects are of special relevance to nanosatellites due to reduced mission resources and reduced available space to accommodate components such as extra propellant.

Endeavouring to reveal the nature of drag has shown itself to be a complex task involving constant discoveries and improvements to the original theory of drag force proposed by Lord Rayleigh in the 19<sup>th</sup> century. As an introduction to the main matter of this chapter consider the following concepts.

Drag relates five dimensional variables derived from empirical evidence, namely drag force  $F_D$ <sup>1</sup>, reference area  $A$ , medium density  $\rho$ , relative speed  $v_r$  and kinematic viscosity  $\nu$  with three fundamental physical units kg, m, and s in the International System of Units. In order to obtain a function relating these variables, dimensional analysis states that two sets of dimensionless parameters exist from the combination of the dimensional variables<sup>2</sup>. One of the functional forms of these dimensionless variables is Eq. (5.1). In this case,  $C_D$  is one of the dimensionless parameters expected from dimensional analysis. This inherently requires that  $C_D$  is a function of the remaining functional dimensionless parameter normally the Reynolds number. Acknowledging the dependence of  $C_D$  on another variable is a very insightful concept that finds application in meticulous analysis.

$$C_D = \frac{F_D}{A} \frac{1}{\frac{1}{2}\rho v_r^2} \quad (5.1)$$

The first term in Eq. (5.1) represents the observed pressure produced by in-track drag force acting on an object in relative movement to the surrounding medium. The second term is the reciprocal of the ideal dynamic pressure for an incompressible fluid. In this way,  $C_D$  simply compares a real quantity to an idealised one under specific conditions to quantify the resistance to the movement of an object with respect the surrounding medium. The ideal dynamic pressure concept assumes that the particles comprising an incompressible fluid are able to achieve instantaneous rest at the moment of the impingement on a reference area. As this condition is highly restrictive for most real phenomena, this prompts different levels of variability on  $C_D$  for specific interaction circumstances. For the matter at hand,  $C_D$  encompasses complex dependencies of

---

<sup>1</sup>See general nomenclature table

<sup>2</sup>The Buckingham Pi theorem states that for a physical process with  $n$  variables with  $k$  number of repeating fundamental units exists  $n - k$  independent dimensionless parameters describing the process.

---

medium interactions on the satellite's surfaces such as geometry, surface condition, gas adsorption, and energy and momentum interchange mechanisms.

Atmospheric parameters generally show significant temporal and spatial variations for objects in Low Earth Orbit (LEO). Atmospheric parameters influence the value of  $C_D$  in two main ways. Firstly, the atmospheric density  $\rho$  explicitly modifies  $C_D$  from Eq. (5.1), and implicitly on  $F_D$  through variations in the way different atmospheric species interact with the exposed surfaces. Existing in-situ measurements in low LEO ( $\sim 150 - 300$  km [219]) have shown that atmospheric species may populate exposed surfaces, greatly affecting interactions. This information has been used in the development and refinement of Gas-Surface Interaction (GSI) analytical models and computer-based simulators [220–223], valid within specific altitude ranges. However, current methods to estimate  $C_D$  usually breakdown for orbital altitudes above 500 km [223] and provide poor estimations during high solar activity due to the lack of a range of in-situ measurements to calibrate the models.

In practice, the  $C_D$  approach used to estimate natural orbital evolution in nanosatellites may have a sensible impact on design factors. For the sake of example, assume a 5kg 3U CubeSat capable to accommodate a propulsion system for orbit altitude maintenance. The propulsion system provides a nominal thrust of  $350\mu\text{N}$  and specific impulse of 2000s actuating on a  $30^\circ$  inclined near-circular orbit at 300km of altitude. In this example a continuous thrust manoeuvre aims to recover orbit altitude after 10km decay allowance. Orbit propagations covering a year of solar maximum activity (2001 – 2002), using constant cross-sectional area of  $350\text{cm}^2$  and  $C_D = 2.2$  against a GSI analytical model (explained in detail in subsection 5.1.3), result in 2.7g of propellant mass consumption difference. This is equivalent to a relative error of one week per year of propulsion actuation.

To overcome this shortcoming and acknowledging its repercussion for propulsion systems on nanosatellites, the investigation presented in this chapter, hereinafter referred to as "this investigation", focuses on the assessment of  $C_D$  from observed orbital data. Specifically, this investigation targets standard 3U CubeSats because nanosatellites are

represented by this platform as discussed in Chapter 2. In principle observed orbital decay assessment in standard 3U CubeSats, with acknowledged attitude schemes, may provide valuable information about distinctive drag-entailing phenomena because atmospheric interaction is led by geometric and material features intrinsic to the CubeSat platform.

The estimation of  $C_D$  is achievable by fitting modelled orbit predictions to observed data wherein all other main perturbation forces can be precisely quantified as proposed by Saunders et al. [224] and Pardini et al. [225] in the so-called fitted drag coefficient,  $C_{DF}$ . It is worth mentioning that those authors applied the fitting of variables to orbiting satellites with much higher masses and sizes than those of nanosatellites. Generally, reduced scale implies higher vulnerability to the space environment conditions calling for additional attention on the effect of perturbations over orbital and attitude motions as discussed in section 2.3.2 in Chapter 2. Furthermore smaller geometries increase the difficulty in the acquisition of accurate and precise<sup>3</sup> observed data, deteriorating the performance of a standard fitting of variables procedure. To enable an adequate approach of the fitting of variables to observed data in CubeSats, and therefore profiting in the numerous opportunities of observed data provided by the format, this investigation aims to exploit the asset of the standardised geometry of various missions. Essentially the standardised geometry may bring the opportunity to estimate representative detailed abstractions of dynamic reference areas for improved computations, in contrast to ordinary fixed constant cross-sectional areas. Additionally, this investigation aims to infer values of the energy accommodation coefficient  $\alpha$ , a fundamental constituent of the drag coefficient that provides insightful information about the complex interactions taking place on surfaces.

In general, the assertion of this investigation is that if the means to quantify the drag force contribution amongst other perturbation forces exists, then it opens up the possibility to break it down into its constituents. In this way, the quality of the assessment is

---

<sup>3</sup>In the context of this investigation *accurate* refers to the proximity between a quantity and its true value, and *precise* to the proximity agreement amongst quantities

---

relative to the capability of precisely quantifying those constituents. The drag acceleration can be directly determined by on-board accelerometer measurements or indirectly by observed orbital decay. Since highly accurate on-board measurement resources cannot be feasibly integrated on standard CubeSat missions, indirect estimations have been used in this investigation using data from the North American Aerospace Defense Command (NORAD) open catalogue. NORAD regularly publishes orbital elements of tracked orbiting bodies in the form of Two-Line Elements (TLE) sets. This comprehensive catalogue of space objects constitutes a useful source of information about object's orbital evolution and orbital decay. In spite of the reported low precision of TLE sets, these still support a variety of technical analyses as reported by numerous authors [224–226]. This investigation reports  $C_{DF}$  and  $\alpha$  values along the orbital evolution of the selected three-unit (3U) CubeSats BEVO 2, ExoCube, GEARRS 1, GeneSat-1, PharmaSat 1, RAX-2, SMDC-ONE, SporeSat 1, S-CUBE, and TurkSat-3USat.

These CubeSats describe near-circular LEO orbits at different values of inclination and encompassing orbital altitudes below 630km. The selected CubeSats represent typical orbital insertion opportunities, geometric configurations, form factors, and attitude control schemes. In relation to this last feature, this investigation encompasses Passive Magnetic Attitude Control (PMAC), gravity-gradient stabilisation ( $\nabla G$ ), and random tumbling according to each reported mission profile. Notice that unlike random tumbling, a controlled attitude scheme plays a fundamental role in the way atmospheric particles and incoming solar radiation interact with the nanosatellites' exposed surfaces. In this way a specific controlled attitude scheme defines characteristic reference areas for that scheme in addition to the inherent reduced uncertainty. In a trade-off between onboard resources and performance, the robust and simple PMAC is a common attitude solution for nanosatellites wherein an on-board permanent dipole interacting with the local Earth magnetic field supplies a restoring alignment torque and a magnetically soft material provides energy dissipation. This topic is discussed in more detail in subsection 5.1.4. Assuming that magnetic-locking occurs, it is possible to ease the determination of predictable dynamic cross-sectional areas for any reference vector as

attitude is essentially a function of the known local Earth magnetic field at the satellite's position. In a similar way,  $\nabla G$  stabilisation enables the estimation of predictable reference areas with reduced margins of uncertainty. The use of dynamic cross-sectional areas throughout this investigation is deemed to be relevant in maintaining uncertainties at the level of the TLE sets, i.e. restricting the addition of stochastic variables, that in turn improve the identification and quantification of perturbations.

This chapter is divided into three main sections. Section 5.1 presents background information about Gas-Surface Interactions, the predominant role of atomic oxygen on GSI, and a discussion about analytical drag closed-form models. Section 5.2 presents the simulation criteria and analyses of estimated  $C_{DF}$  values and the related values of  $\alpha$  along the observed orbital evolution of the selected CubeSat missions. Section 5.3 presents the conclusions and contributions of this chapter.

## 5.1 Background

The following subsections present the mathematical background and definitions to interpret the obtained fitted drag coefficients. It is provided as an introduction to Gas-Surface Interactions, the role of Atomic Oxygen in these interactions, and analytical drag models. An introduction to characteristic cross-sectional areas in 3U CubeSats and the proposed dynamic cross-sectional area concept to improve estimations is then provided. Finally, a brief discussion about  $C_D$  estimations from TLE sets is presented.

### 5.1.1 Gas-Surface Interactions

The concept of surface is fundamental in most areas of knowledge because it encompasses the interaction of condensed matter with the external world. In real objects, a surface is primarily characterised by its area and the volume it envelopes. The surface area to volume ratio is generally higher as objects scale down because surface area decreases at a slower rate than volume, e.g. in a cube explicitly  $6l^2/l^3$ . This fact is fundamental when analysing extensive properties of a surface interaction because it

greatly defines its intensity, for example in chemical reactions the surface area to volume ratio leads the reactivity. In particular, the dynamic interaction of atmospheric species with exposed surfaces is of interest throughout this investigation.

The kinetic theory of gases provides the fundamental framework and concepts used in this investigation about the GSI phenomena, in particular those related to the interchange of momentum and energy with a surface which are discussed below. The molecular-surface interaction is usually subdivided into three main regimes depending on the dominating physical phenomena governing the process. One extreme is characterised by prevalent intermolecular collisions giving rise to a continuum fluid interacting with the surface, namely the ordinary regime. The opposite extreme is the free molecular flow regime, which is dominated by discrete molecular-surface interactions. Between these extremes, the transition regime is characterised by alternating intermolecular and molecule-surface collisions. Tsien originally proposed this division and used the non-dimensional Knudsen number as the dividing parameter [227].

$$Kn = \frac{\lambda_a}{L} \quad (5.2)$$

The Knudsen number in Eq. (5.2) is a dimensionless number defined as the ratio of the average distance travelled by a particle between successive collisions, namely the mean free path  $\lambda_a$ , and a characteristic representative length  $L$ . The value of  $\lambda_a$  is given by Eq. (5.3) for the approximation of sphere-like molecules. The value of the number density  $\rho_n$  and the effective collision parameter  $d$  are often approximated for practicality.

$$\lambda_a = \frac{\sqrt{\pi}}{2\pi\rho_n d^2} \quad (5.3)$$

In order to delimit the aforementioned regimes, it is important to notice that the presence of a body does not change the bulk freestream density but it sets local changes. The presence of a body alters  $\rho_n$  in its vicinity modifying the  $\lambda_a$  value locally giving rise to the definition of the freestream and local Knudsen numbers [227]. From Eq. (5.3) we can see that  $\lambda_a$  is inversely proportional to  $\rho_n$ , implying that an increment in  $\rho_n$  due

to presence of the object causes a reduction in the value of the local Knudsen number. This means, for instance, that the conventional freestream Knudsen number of 10 delimiting the transition and free molecular flow regimes, is necessarily different in the vicinity of a body. Furthermore, computer aided simulations show that for a freestream Knudsen number value of approximately 1000 (for a sphere and  $\rho_n \approx 1 \times 10^{16} \text{ m}^{-3}$ ) the local flow is barely on the limit of the transitional regime [223], however experimental evidence shows that this limiting value is in fact highly variable [228]. These concepts are summarised in Fig. 5.1 for a characteristic length of 1 m in a multi-gas mixture Earth atmosphere<sup>4</sup> as function of altitude.

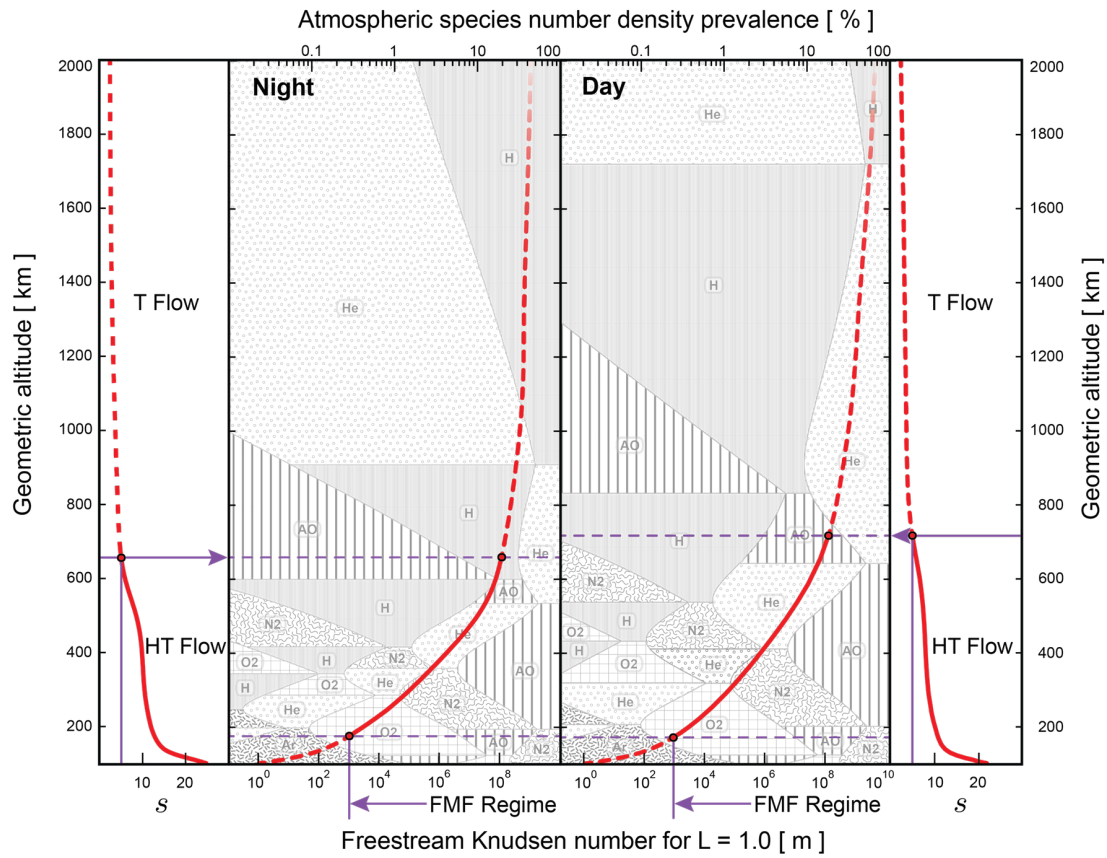


Fig. 5.1 Plots of the Earth atmospheric composition and relative attributes for day (right) and night (left) conditions during solar maximum. The background mosaic illustrates the typical atmospheric species prevalence, and the plotted curves show the Knudsen number and speed ratio values as functions of geometric altitude for both scenarios. Plots prepared assuming an effective collision diameter of 3.65 Å [229] and a test equatorial circular orbit. FMF transition computed assuming  $\rho_n = 1 \times 10^{16} \text{ m}^{-3}$  [223].

<sup>4</sup>Using the JB2008 empirical thermospheric density model [134]

The range of orbital altitudes of interest for this investigation, below 630 km, limit the attention to the free molecular flow regime (FMF) as observed from Fig. 5.1. In the FMF regime, the molecules travel large distances compared to the characteristic length of interest before intermolecular collisions can occur. Note that the definitions given so far refer to intermolecular freedom of movement only. It is therefore necessary to introduce concepts for intermolecular collisions. It is known that a particle in three dimensions has three degrees of freedom associated to its movement, i.e. rotation, translation, and vibration. However, the translational movement usually captures most macroscopic characteristics of the flow dynamics. Consequently it is used to conveniently classify the preferential movement of the particles in the free molecular flow regime. In addition, particles may manifest bulk ordered or random translational motion. In the case of a surface immersed in a stream, the flow of ordered particles would move with a distinctive relative speed  $v_r$  with respect to the surface. To account for the fraction of particles in random translational motion, the flow is typically assumed to follow a Maxwellian velocity distribution so called thermal velocity. In this way, the most probable magnitude of the thermal velocity of the particles is given by Eq. (5.4), where  $k_B$  is the Boltzmann constant,  $T_\infty$  the freestream temperature, and  $\bar{m}_m$  the mean molecular mass.

$$v_s = \sqrt{\frac{2k_B T_\infty}{\bar{m}_m}} \quad (5.4)$$

The bulk and thermal speed contributions of the particles are related in the dimensionless molecular speed ratio  $s$  defined by Eq. (5.5).

$$s = \frac{v_r}{v_s} \quad (5.5)$$

From this relationship note that if the value of  $s$  is large then the bulk motion is dominant, whilst a small value would mean significant randomness in the motion of the particles. It has been proposed by Cook [230] and others that for  $s > 5$  the bulk motion is sufficiently predominant to safely neglect the random thermal motion of the flow in macroscopic analyses. Under this assumption the stream is a collimated beam

of particles customarily termed as the *hyperthermal approximation*. The prefix "hyper" highlights the prevalence of the bulk motion over random thermal motion. However, the terminology for the alternative case of inferior bulk motion has not been standardised. It is thus common to find the terms, "subthermal" "hypothermal" or just "thermal" directly referring to the predominant random thermal motion. The hyperthermal approximation (HT Flow) is a valid assumption in low LEO orbits where heavy atmospheric species and ordered bulk motion prevail. On the other hand, the thermal approximation (T Flow) is a valid assumption at high altitudes where light species in a rarefied atmosphere are easily energised by environment radiation. Fig. 5.1 illustrates the HT Flow and T Flow ranges of domain for an Earth orbiting object with variation of  $s$  as function of altitude. Strictly speaking, the hyperthermal approximation on GSIs is valid only for non-rotating surfaces relative to the flow. However, for orbiting objects at altitudes below  $\sim 500\text{km}$  [231] or high eccentricity orbits [225], the bulk relative speed of the incident atmospheric particles to a body surface is greater than any body rotation allowing for the use of the hyperthermal approximation. In general, the hyperthermal approximation validity on GSIs breaks down mainly for higher altitudes, high solar activity, low relative speed, or any other factor enhancing the effects of thermal motion.

GSIs are complex processes that involve to some extent chemical reactions, mass transfer, and momentum and energy exchange. In this regard, the macroscopic and low resolution orbital observations used in this investigation limit the scope of the analyses to momentum and energy exchange only. The force exerted by the molecules over the surface through collisions depends on the way the impingement is delivered. This interaction is greatly dependent on the surface roughness relative to the size of the colliding particles [228], the quality of which is manifested by the resulting particle reflection. Assuming that the incident particles behave like hard spheres, a rough surface would cause several internal reflections before the particles find a way out through the interstices of the surface. Along each of several internal reflections, as shown in Fig. 5.2c, the particles deliver part of their kinetic energy and receive thermal energy from the surface. Ultimately, the overall energy exchange process may yield to unrelated

incident and reemitted directions. The collective effect of incident particles on a rough material is thus a characteristic diffuse reflection pattern as the bulk incoming direction information is gradually lost. On the other hand, for a hypothetical surface allowing only a single reflection, Fig. 5.2a, the outgoing particles follow a specular pattern with the same angle of incidence, i.e.  $\phi_{rf} = \phi_{ic}$ , but not necessarily the same speeds as the exchange of energy still exists. Complementarily, intermediate cases are possible for a spectrum of surface conditions, resulting in quasi-specular reflection, Fig. 5.2b.

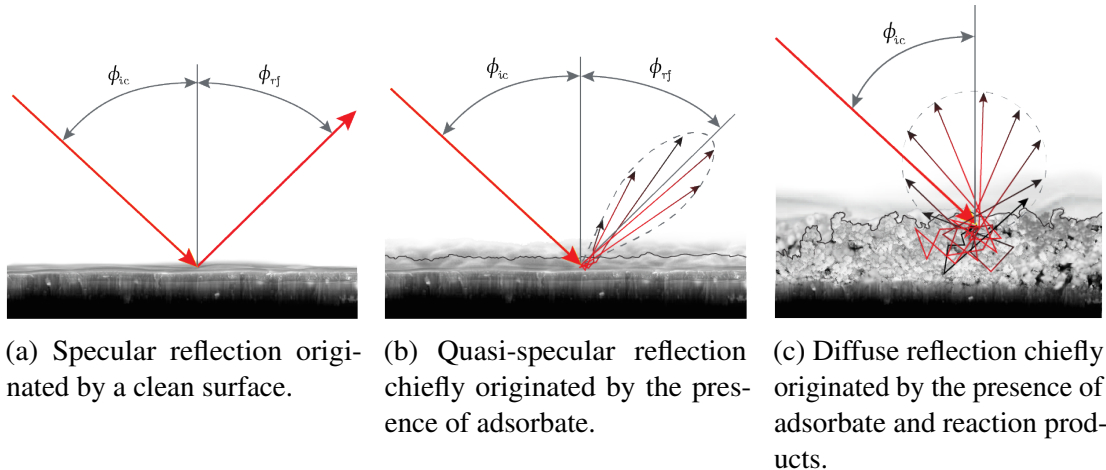


Fig. 5.2 Angular distributions of scattered particles.

The use of coefficients is a common practice in the parametrisation of general phenomena. Coefficients are typically used to weight extreme cases of observed conditions to generate an intermediate continuous range of values. For instance, Maxwell on his theory of gases [232] postulated that a GSI can be approximated by considering weighted proportions of the extreme forms of reflection as in Eq. (5.6), where  $q$  is a flux quantity and  $C$  is a coefficient such that  $0 \leq C \leq 1$ . The particular case of  $C = 0$  corresponds to specular reflection, whereas  $C = 1$  corresponds to pure diffuse reflection. In a real interaction the generalisation assumed in Eq. (5.6) has been proven to be false and the reflected particles are unlikely to be divided as suggested, however the concept embodied in Eq. (5.6) was fundamental in the development of modern GSI theory.

$$q_{rf} = \underbrace{(1 - C) q_{ic}}_{\text{Specular term}} + \underbrace{C q_w}_{\text{Diffuse term}} \quad (5.6)$$

In principle, the force delivered during a GSI can be fully described by momentum transfer. The minimum number of independent components required to parametrise the momentum transfer is two, the so-called normal and tangential *momentum* accommodation coefficients  $\sigma_n$  and  $\sigma_t$  respectively. However, as the *energy* accommodation coefficient  $\alpha$  is traditionally used in the analysis of gas-surface heat transfer in general physics and because in practice energy transfer is often easier to measure than momentum, it is common to find in literature GSI force models using a mix of momentum and energy accommodation coefficients.

### Energy accommodation coefficient

The quality of a GSI is accounted by the fractional energy accommodation coefficient  $\alpha$  in Eq. (5.7). It is used to express the level of equilibrium attained by the kinetic energy of the incident particles with respect to the thermal energy of the surface before re-emission.

$$\alpha = \frac{E_{ic} - E_{rf}}{E_{ic} - E_w} \quad (5.7)$$

If the particles are re-emitted in thermal equilibrium with the surface,  $E_{rf} \equiv E_w$ , then  $\alpha$  is unity. In the case of unchanged energy after the GSI,  $E_{ic} \equiv E_{rf}$ ,  $\alpha$  is equal to zero. It is important to emphasise the unambiguity of the total energy exchange during the GSI and the energy accommodation coefficient concepts. In order to assess the effect of  $\alpha$  and the preexisting energy conditions on the particle's kinetic energy after the GSI permit the following discussion. By solving Eq. (5.7) for  $E_{rf}/E_{ic}$  and assuming uniform equivalence to speeds<sup>5</sup>, i.e.  $E_{rf}/E_{ic} \equiv (v_{rf}/v_{ic})^2$ , the ratio of incident and re-emitted speeds is expressed by Eq. (5.8).

$$\frac{v_{rf}}{v_{ic}} = \sqrt{1 + \alpha \left( \frac{E_w}{E_{ic}} - 1 \right)} \quad (5.8)$$

---

<sup>5</sup>Differences on speed distributions require the factor  $2/3$  to relate  $(v_{rf}/v_{ic})^2$  [223]

The plot of Eq. (5.8) in Fig. 5.3 shows that for the common case of  $E_w < E_{ic}$  in Earth orbiting objects,  $v_{rf}/v_{ic}$  decreases for increasing  $\alpha$ . On the other hand, when  $E_w \geq E_{ic}$ ,  $\alpha$  is positively related to changes in  $v_{rf}/v_{ic}$ .

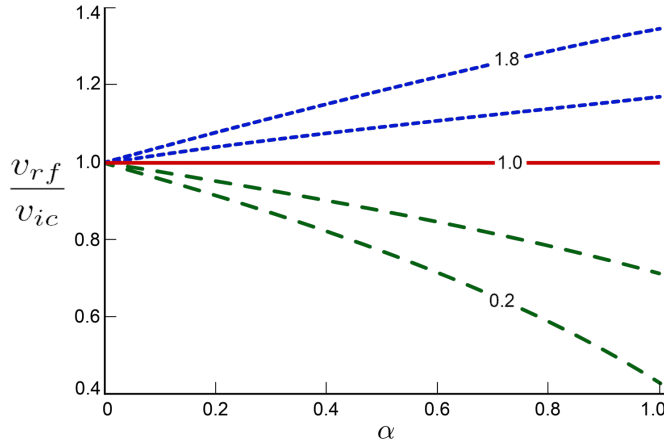


Fig. 5.3 Contour plot for  $E_w/E_{ic}$  as function of  $v_{rf}/v_{ic}$ , and  $\alpha$ .

The preceding analysis can be used to provide an initial approach of  $C_D$  as function of  $\alpha$ . It has been discussed that  $C_D$ , in Eq. (5.1), essentially compares an observed pressure to the ideal dynamic pressure concept. Thus, it can be said that  $C_D \propto v_{rf}/v_{ic}$ , which from Eq. (5.8) and  $E_{ic} > E_w$  (Earth orbiting object), suggests that  $C_D \propto \sqrt{1 - \alpha}$ . Although a simplistic approach, this observation grasps the fundamental relationship between  $C_D$  and  $\alpha$  discussed in detail in following sections.

As a final remark, it is important to recall that actual impinging particles have different degrees of freedom, i.e. translation, rotation and vibration, at the moment of the interaction. Degrees of freedom are particularly relevant when the impinging particle is effectively asymmetric. In that case, it is convenient to introduce separate energy accommodation factors for each degree of freedom [227, 228]. However, for the purpose of this investigation, the particles are assumed symmetric with predominant translational movement as discussed above.

### Momentum accommodation coefficients

The normal and tangential momentum accommodation coefficients are used to parametrise the momentum transfer of a GSI. The tangential momentum accommodation coefficient

in Eq. (5.9) is derived from a general form formula similar to Eq. (5.7) with null surface momentum ( $\tau_w = 0$ ).

$$\sigma_t = 1 - \frac{\tau_{rf}}{\tau_{ic}} \quad (5.9)$$

In order to describe the variables in  $\sigma_t$  we need to turn our attention to the angular distribution of scattered particles in Fig. 5.2. In the ideal case of specular reflection, the incident tangential momentum of a particle,  $\tau_{ic}$ , has to be equal to the reflected tangential momentum  $\tau_{rf}$  that is  $\sigma_t = 0$ . On the other hand, if the surface condition prompts the complete loss of information about the incoming direction of the particle, the axis of the lobe demarcating the possible directions after reflection is centred in the normal surface vector, or  $\tau_{rf} = 0$ . In such a case  $\sigma_t = 1$ . It is interesting to note that if the particle is backscattered  $\tau_{rf} < 0$  and  $\sigma_t$  can be greater than unity. However, the analysis of  $\sigma_t$  is usually restricted to the interval  $[0 - 1]$ . In regard to the relationship between the accommodation coefficients,  $\sigma_t$  is related to  $\alpha$  as long as some degree of specular reflection is present whilst the normal momentum accommodation coefficient  $\sigma_n$  is always related to the value  $\alpha$ .

Empirical evidence shows that  $\sigma$  and  $\alpha$  are positively linked to the mass of the incident particles and the level of surface contamination. On this point, it has been observed in Earth orbiting objects that the atomic oxygen present in the atmosphere greatly interacts with exposed surfaces enhancing accommodation [233]. This topic is covered in subsection 5.1.2.

### 5.1.2 Atomic Oxygen

The atmospheric composition varies with altitude as illustrated in the mosaics in Fig. 5.1. It is expected that through various physical phenomena, e.g. chemical affinity, some atmospheric gas species populate surfaces exposed to the flow. In particular, the presence and interaction of atmospheric atomic oxygen (AO) on spacecraft materials has been identified through in-orbit mass spectrometry measurements [225], and from

the analysis of retrieved materials exposed to the space environment in near LEO orbits [234].

High-energy incoming solar radiation, mainly in the form of EUV and X-ray, causes atomic oxygen to become relatively abundant with increasing altitude up to  $\sim 100\text{km}$  where its number density peaks due to dissociation of oxygen allotropes. Depending on the incoming solar radiation, the relative abundance of AO over other atmospheric species may reach up to 700 km, altitudes normally populated by lighter species i.e. He and H. Atomic oxygen is highly reactive and binds strongly to almost every satellite material causing erosion and oxidation. AO gradually creates adsorbate patches on exposed clean surfaces that can be chemisorbed causing, in the most extreme contamination, complete energy accommodation and diffuse reemission of the particles impinging upon the surfaces through the mechanism described in section 5.1.1. In other words, the effect of AO on Earth orbiting objects is to enhance kinetic energy and momentum transfer from the incident particles to the surface of interaction, e.g. from Eq. (5.8) if  $E_w/E_{ic} \rightarrow 0$  then  $v_{rf} = v_{ic}\sqrt{1-\alpha}$ .

Novel materials may provide the means to reduce the impact of AO on in-orbit spacecraft surfaces. For instance, it has been discovered under laboratory conditions that a single layer of graphene, although easily oxidised by the presence of AO, exhibits strong impermeability to it and multiple layers have shown enhanced erosion resistance providing protection to underlying material [235].

### **5.1.3 GSI Models**

During the 1960s, at the dawn of the space age, various values of drag coefficients were in common use. The employment of the range 2.0 – 2.3, mainly 2.2, was justified by laboratory estimations on clean surfaces [230, 236, 237] and by knowledge gaps about GSI in real space environment conditions. At the present time it is believed that spacecraft surface material properties are likely to be masked by atomic oxygen, even at altitudes of  $\sim 700 - 800\text{km}$  [221, 238], controlling the type of reflection and range

of energy accommodation coefficient. Hence, the value of  $C_D$  is a strong function of AO abundance. With the use of the kinetic theory of gases and available empirical data, GSI models have been developed to enable closed-form solutions for the estimation of physical drag coefficients. At this point it is important to emphasise that free molecular closed-form solutions generally support single re-emission of particles only, like those occurring on convex geometries as illustrated in Fig. 5.4. Conversely, if the satellite geometry is concave , then remitted particles are likely to undergo subsequent reflections making the use of dedicated numerical analysis necessary.

Fig. 5.4 Illustration of multiple specular reflections in a concave CubeSat under HT flow conditions. Interactive image in Acrobat Reader, Foxit Reader, or PDF-XChange.

This investigation uses the Schaaf and Chambre (SC) closed solution for the drag coefficient of a flat plate perpendicular to the flow in free molecular flow (Maxwellian flow) [239]. The SC closed form solution is a function of  $\sigma_n$ ,  $\sigma_t$ ,  $s$ , the average normal speed of diffusely re-emitted particles  $V_w$ , the relative speed of the incident particles  $V$ . In order to transform the SC closed form solution in terms of  $\alpha$  for the purposes of this investigation, we use the Cercignani-Lampis-Lord GSI model modifications reported in the work of Walker et al. [223] yielding Eq. (5.10) where  $C_{I,j}$ ,  $C_{II,j}$ , and  $C_{III,j}$  are given by Eq. (5.11), Eq. (5.12), and Eq. (5.13) respectively. The best-fit parameters,  $\beta$ ,  $\gamma$ ,  $\delta$ , and  $\zeta$ , are presented in Table 5.1. With these modifications the SC closed form solution is expressed in terms of  $\alpha_n$  (part of the kinetic energy due to normal motion [?]) but representative of the total  $\alpha$ ) instead of  $\sigma_n$ , and the surface temperature  $T_s$  and atmospheric translational temperature  $T_\infty$  instead of  $V_w$  and  $V$ . A final remark about this drag coefficient equation is that all portions of the flat plate experience impingement due to the random motion of the molecules (rear and front sides). The total physical drag coefficient  $C_D$  for a mixture of  $N$  number of gases is given by the weighted sum of the individual contribution of the atmospheric species ( $C_{D,j}$ ) in Eq. (5.14), with  $\chi_j$  as their respective mole fraction [221, 223].

$$C_{D,j} = C_{I,j} + C_{II,j} + C_{III,j} \quad (5.10)$$

Eq. (5.10) has been rearranged from its original form and presented conveniently as the sum of three key terms for further discussion in following sections.

$$C_{I,j} = \left(1 + \sqrt{1 - \alpha_n}\right) \left(2 + \frac{1}{s^2}\right) \operatorname{erf} s \quad (5.11)$$

$$C_{II,j} = \frac{2(1 + \sqrt{1 - \alpha_n})}{s\sqrt{\pi}} e^{-s^2} \quad (5.12)$$

$$C_{III,j} = \frac{\sqrt{\pi}}{s^2} \zeta_j \left(\frac{T_w}{T_\infty}\right)^{\delta_j + \frac{1}{2}} e^{-\beta_j(1 - \alpha_n)\gamma_j} \quad (5.13)$$

The total physical drag coefficient  $C_D$  for a mixture of  $N$  number of gases is given by the weighted sum of the individual contribution of the atmospheric species ( $C_{D,j}$ ) in

Table 5.1 Best-fit parameters for a flat plate [223].

Species	$\beta$	$\gamma$	$\delta$	$\zeta$	Atomic mass
O <sub>2</sub>	6.300	0.260	0.420	20.500	32
N <sub>2</sub>	6.600	0.220	0.480	35.000	28
AO	5.850	0.200	0.480	31.000	16
N	4.900	0.320	0.420	8.000	14
He $0.95 < \alpha_n < 1.00$	6.200	0.380	3.300	0.740	4
He $0.90 < \alpha_n < 0.95$	3.800	0.520	3.400	1.120	4
He $0.50 < \alpha_n < 0.90$	3.450	0.520	2.400	0.930	4
He $0.00 < \alpha_n < 0.50$	0.080	0.520	4.200	1.100	4
H $0.95 < \alpha_n < 1.00$	3.900	0.195	1.400	0.300	1
H $0.90 < \alpha_n < 0.95$	3.500	0.420	2.000	0.720	1
H $0.50 < \alpha_n < 0.90$	3.450	0.520	2.400	0.930	1
H $0.00 < \alpha_n < 0.50$	0.095	0.465	2.900	0.920	1

Eq. (5.14), with  $\chi_j$  as their respective mole fraction [221, 223]. In this investigation,  $C_D$  always makes reference to the total physical drag coefficient.

$$C_D = \frac{1}{\bar{m}_m} \sum_{j=1}^N \chi_j m_j C_{D,j} \quad (5.14)$$

### 5.1.4 Characteristic Cross-sectional Areas in CubeSats

All spacecraft surfaces exposed to the space environment are subject to interactions. Nonconservative perturbation forces, e.g. atmospheric drag and solar-radiation pressure, depend strongly on the state of surfaces. The angle of interaction between the perturbing vector and surface elements greatly defines the collective reaction vector on the spacecraft. Therefore, high fidelity perturbation estimations must account for the joint effect of various surface relative dispositions and materials. However, simplified geometric abstractions and material combinations can be used to achieve tailored levels of exactness. A practical example of such surface and material syntheses is given by Fahnestock et al. [240] on the GRAIL spacecraft, wherein combination of surfaces simplified thermo-optical models for perturbation estimations.

In most nanosatellite missions it is unfeasible or impractical to keep continuous track of a spacecraft's attitude to assess precise long term perturbation effects. Coarse estimations of characteristic invariable cross-sectional areas are commonly used instead,

for example those reported by Oltrogge and Leveque [241]. The cross-sectional area is the equivalent total area in view, or projected, by the perturbing source vector. In this fashion, the cross-sectional area in solar-radiation pressure is established by the relative solar vector, and the drag cross-sectional area by the bulk atmospheric relative velocity vector. Fig. 5.5 shows an example of projected cross-sectional area  $A_p$  of a CubeSat. Statistical analysis of multiple projected areas from various angles of incidence defines the characteristic invariable cross-sectional area  $A_{sta}$  of the CubeSat. Acknowledging

Fig. 5.5 Example of the projected cross-sectional area concept. The dark area represents the cross-sectional area from the moving bulk atmosphere perspective assuming HT Flow. Although practical in convex geometry analysis, cross-sectional area assumption in strongly concave geometries like the one shown in this figure may lead to unrepresentativeness in atmospheric drag analysis due to possible single particle multiple reflections. Interactive image in Acrobat Reader, Foxit Reader, or PDF-XChange.

the inevitable low precision of the observed orbital data (TLE sets) and the intended depth of this investigation make it necessary to reduce the level of other uncertainty sources whenever possible. To tackle the level of uncertainty of invariable CubeSat cross-sectional areas, this investigation proposes the use of dynamic cross-sectional areas ( $A_{dyn}$ ) able to capture a higher level of detail along the attitude and orbital motion evolution. To this aim, the ability to effectively estimate attitude dynamics in standard CubeSat geometries is indispensable. In spite of the lack of long-term continuous attitude tracking, as mentioned before, it is still possible to evaluate attitude dynamics in CubeSats furnished with effective passive attitude control systems. The common PMAC and  $\nabla G$  stabilisation methods on CubeSats are considered in this investigation.

However, invariable cross-sectional areas can be used as last resort in specific cases, if the attitude control method or its effectiveness is unverifiable by reported data.

In a trade-off between estimation precision and computational burden,  $A_{dyn}$  values are obtained with analytical models derived from precise orbital and attitude propagations under the desired orbital characteristics. For the sake of illustration, the derivation of the analytical model of PMAC for drag estimation is presented below. Firstly it is necessary to collect sufficient data from orbit and attitude propagations to identify essential features of the cross sectional area variations. High-precision numerical simulations employing a 3D CAD model of a standard 3U CubeSat assigned with typical spacecraft materials [240] is used herein. In PMAC, the CubeSat attitude is defined by the Earth's local magnetic field as shown in Fig. 5.6b. In CubeSats using PMAC and  $\nabla G$  stabilisation, normally one attitude Degree Of Freedom (DOF) remains uncontrolled, e.g. uncontrolled yaw for  $\nabla G$  stabilisation. Thus, assuming complete PMAC magnetic locking, the CubeSats attitude in two DOF is fully dependent upon the position vector and the Earth's magnetic field. The simulations provide the instantaneous weighted average angle of incidence  $\bar{\phi}_{ic,w}$  of the bulk atmosphere on the CubeSat and a characteristic cross-sectional area of the CubeSat. That is, the instantaneous value of  $\bar{\phi}_{ic,w}$  is determined by the surface area elements contributions in the 3D CAD model, note however that only leading area elements can contribute in HT Flow (assumed simplification). Each  $j$ -th surface element contribution with inward area vector  $\vec{n}_{in,j}$  and angle of incidence  $\phi_{ic,j}$  with respect to the relative velocity unit vector  $\hat{v}_{r,j}$  is weighted with Eq. (5.15).

$$\bar{\phi}_{ic,w} = \frac{\sum_{j=1}^N (\vec{n}_{in,j} \cdot \hat{v}_{r,j}) \phi_{ic,j}}{\sum_{j=1}^N \vec{n}_{in,j} \cdot \hat{v}_{r,j}} \quad (5.15)$$

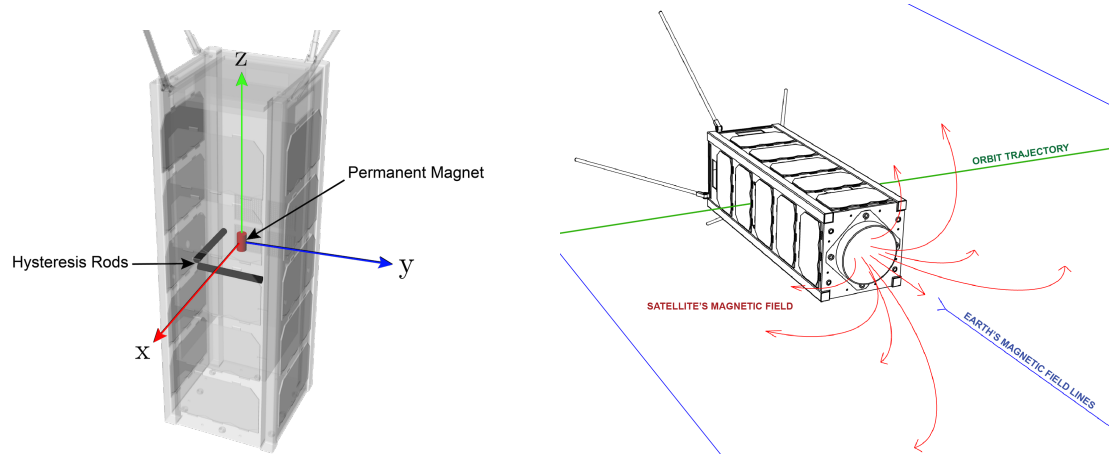
Summarising these concepts yields Eq. (5.16).

$$A_{dyn} = A_{sta} \cos \bar{\phi}_{ic,w} \quad (5.16)$$

Fig. 5.6c illustrates a compound map of simulation results using this methodology for a polar circular orbit. The characteristic two-lobed shaped geometry of  $A_{dyn}/A_{sta}$  is the result of the assembly of collected estimations of PMAC on a 3U CubeSat. The envelope geometry remains essentially invariable under the aforementioned conditions as the near-Earth magnetic field is practically constant for considerable periods of time. Note that a similar analysis for dynamic cross-sectional area for solar radiation pressure, would require the knowledge of the Sun vector for various sample scenarios. In order to capture the identified attributes of the envelope in Fig. 5.6c into mathematical expressions, this investigation employs spherical harmonics. The derived coefficients enable the computation of representative dynamic cross-sectional areas avoiding the use computationally costly attitude propagations. This is a valuable asset in terms of reduced computational burden due to the intrinsic long periods of propagation required in this investigation.

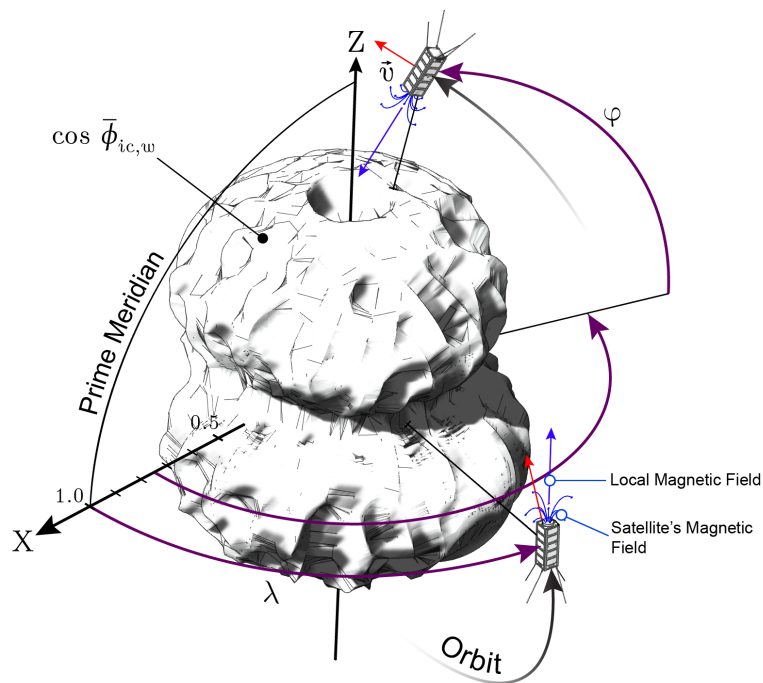
### **5.1.5 $C_D$ Estimations from TLE sets**

The TLE set is a technical tool used to convey condensed orbital information from observations to specialised orbit propagator software. In general terms, the information coded in the two 69-character TLE set lines in punch card format legacy, encloses observed mean orbital elements using the SGP4 orbital model [139]. Observational data is primarily provided by a worldwide network of sensors known as the Space Surveillance Network or SSN, operated by the United States Armed Forces. The SSN consists of radars, phased-array radars, the Ground-based Electro-Optical Deep Space Surveillance system (GEODSS) [242], and the Space Based Space Surveillance system [243]. A key part of the SSN was a network of VHF radars operating in bistatic mode consisting of three transmitter sites and six receiving stations located approximately along the 33rd parallel north stretching across continental the southern US. This so-called Space Fence greatly contributed to the SSN tracking objects with orbital inclinations greater than  $33^\circ$ . It is said that the fence was able to track over 80% of the Earth's population



(a) PMAC system configuration. Hysteresis rods dissipate body kinetic energy and a permanent dipole provides alignment to the external magnetic field.

(b) PMAC system interaction. Two degrees of freedom in attitude are controlled during magnetic locking.



(c) Weighted sum of surface incidence angles as function of the CubeSat's geocentric longitude ( $\lambda$ ), and latitude ( $\varphi$ ).

Fig. 5.6 Characteristic cross-sectional variations under PMAC attitude control.

of artificial satellites [242], nearly 40% of the US Air Force SSN [244], and sensitive enough to detect a 75 cm object at 30000 km altitude. After five decades in operation, this important contributor to the SSN ceased operation in 2013 [244]<sup>6</sup>. A new Space Fence is currently under construction with sites at Marshall Islands, which assets are expected to join the SSN in 2019 [245]. This second generation Space Fence radar will operate in S-band and will be able to track smaller objects than the previous fence. The phased-array radars, are able to track selectable objects dynamically and scan large portions of sky by steering a beam of radio waves formed by the superpose of thousands of individual static wavefronts. The AN/FPS-85, the most important phased-array radar in the network [242], is able to detect a 75 cm object at 40000 km range. On the other hand, there are three operational GEODSS sites around the world providing optical observations to the SSN. GEODSS use telescopes and digital camera technology able to detect a 75 cm object at 20000 km range [246]. Although GEODSS observations are influenced by weather conditions and can only be operated at night, complementary optical observations are fundamental to reduce radar object ambiguity. Finally, the Space Based Space Surveillance is a near-geosynchronous satellite constellation supporting ground-based space surveillance [243]. By 2017 four satellites of this kind were put into orbit. Nanosatellites pose a challenge to existing SSN. Altogether, orbital data acquisition methods and sensor accuracy as well as the high number of orbiting objects in LEO complicates the detection, data collection, correlation, and association of tracked objects. It is argued by Garber [247] that even a the 3U CubeSat geometry, i.e. in the upper limit of nanosatellite definition used in this thesis, represent a scale difficult to process by current space tracking systems. Apart from these, other sources of uncertainty are added to the published data in the form of TLE sets. For example, the reference frame used in TLE sets is the true-equator mean-equinox (TEME). Whilst the true-equator reference is consistent to Earth fixed observations, in which case the Earth-Fixed (ITRF) frame would be the selection [248], the vernal equinox varies with

---

<sup>6</sup>This modification in the SSN may be the cause of TLE sets publication rate modification and noisy data clearly observed in some nanosatellites such as CanX-2 and UWE-2 during 2013.

the Earth's precession and nutation movements. In addition to ambiguity of a precise definition, the TEME reference frame ignores nutation of the Earth's obliquity [249] limiting its accuracyVallado [139]. Another source of errors involves the way mean orbit elements are calculated from batches of observations. The statistical processing cancels high frequency phenomena smoothing the data captured in the TLE set. In addition to the statistical quality of observations, the simplistic TLE format involves numeric rounding impacting the ultimate precision of the reported data. Vallado [139] reports that errors related to the formation of the sets can be on the order of a kilometre or more. Despite the inherent coarse attributes of the TLE sets, these still support a variety of detailed technical analyses [224–226], however the extended applicability to nanosatellites is questionable motivating the investigation presented in this chapter.

The BSTAR drag term ( $B^*$ ) reported in the TLE sets, is a differential correction factor used to fit the SGP4 orbital model to observations. The  $B^*$  may not be related predominantly to atmospheric drag since the correction may be due to solar-radiation pressure, third-body perturbations, or mismodeled factors in the tightly simple SGP4 force model [250]. However in atmospheric drag dominated orbits,  $B^*$  may provide rough information about the ballistic coefficient  $BC$  [139] allowing the estimation of  $C_D$  according to the aerodynamic theory, i.e.  $BC = m/C_{DA}$ . At this point, it is worth considering that nanosatellites detection challenge to current Space Surveillance methods may further contribute  $B^*$  values of reduced representativeness for  $C_D$  estimation even in a drag dominated environment.

The fitting method for drag coefficient estimation aims to infer the level of drag by adjusting iteratively a high fidelity orbital model comprised of precise perturbation models, to the observed orbit evolution profile reported by the TLE sets. The fundamental difference between  $C_D$  estimations from the fitting method and estimations from the  $B^*$ , is that those from a fitting method incorporate modelled information of the space environment to weight perturbation contributions, thus presumably filtering information about observed drag coefficients with more efficiency and reliability.

## 5.2 Simulation and Analysis

For most satellites in near LEO orbits, the drag force contribution on the orbital drift is sufficiently high to be clearly distinguished amongst other perturbations. The successful identification of perturbation components and their contributions is possible by virtue of precise space environment and space-spacecraft interaction models. In this manner, the resolution of the recognised contributions relies largely on the quality of the models. If the models are precise and are able to reproduce spatial and temporal changes of the perturbations, then it is feasible to propagate orbits with high fidelity. In principle, an ideal observed initial orbital state can be propagated over a period of time using a high precision orbit propagator to match a subsequent second ideal observed state obtaining equivalent results. However in practice many real factors alter the equivalence of observed and propagated data, e.g. actual GSIs. Assuming that the initial and final observed orbital states are precise, judicious adjustments on model variables prone to fluctuations may improve propagations disclosing the magnitude of their real variations. In drag dominated orbits, the value of the drag coefficient is the least tightly defined variable subject to fluctuation. In such scenario the fitted drag coefficient,  $C_{DF}$ , would enable analogous observed and propagated orbital states.

The  $C_{DF}$  values presented herein are the result of the comparison of propagated and observed data from open historical NORAD Two-Line Element sets [150] for each of the selected CubeSats. Precise ephemeris knowledge is unattainable with the use of TLE sets as errors could be of more than 1 km due to acquisition method margins, the Kozai mean values used for the semi-major axis and mean motion derivation, and forced rounded values required for publication [251]. In the absence of first-hand resources from which to draw better information about the orbital state of the satellites, such as data from on-board global navigation satellite system receivers, it is convenient to assess the relative statistical self consistency of the batch of TLE sets for each CubeSat. Statistical processing of multiple TLE sets improves data consistency allowing for adequate analysis approaches as proposed by some authors [224–226, 252].

In this respect, this investigation implements two statistical tools. Firstly, the modified Thompson tau method [253] is applied for TLE outliers removal. Secondly, the method of the least squares to report the root-mean square residuals on the semi-major axis in the estimation of  $C_{DF}$  values.

Table 5.2 List of selected 3U CubeSats

Name	Attitude Control	Mass <sup>‡</sup>	Launch Date
BEVO 2	None *	5.0	12/2015
ExoCube <sup>†</sup>	$\nabla G$	4.0	01/2015
GEARRS 1	PMAC	3.9	07/2014
GeneSat-1 <sup>†</sup>	PMAC	4.1	12/2006
PharmaSat 1 <sup>†</sup>	PMAC	4.5	05/2009
RAX-2	PMAC	2.8	10/2011
SMDC-ONE 1	PMAC	4.0	12/2010
SporeSat 1 <sup>†</sup>	PMAC	5.5	04/2014
S-CUBE <sup>†</sup>	$\nabla G$	3.9	08/2015
TurkSat-3USat	PMAC	4.0	04/2013

\* Assumed from failed systems activation

<sup>†</sup> Approximated standard geometry

<sup>‡</sup> In kg

Missions selection for this investigation are based upon open availability of data, reported passive attitude control scheme, and predominant convex geometry in 3U CubeSats. The motivations behind the selection of the 3U size factor are the varied number of available missions covering a rich range of space environment conditions, and the identified relevance of that size factor to enable functional missions with propulsion systems in consonance with the ultimate objective of the thesis. Table 5.2 presents the selected CubeSat missions. From available information nine CubeSat missions fulfilling the investigation criteria are identified. In addition to these missions and profiting from geometric adequacy and data availability, the BEVO 2 CubeSat is incorporated taking into consideration that it was apparently not activated before deployment and presumably its *active* attitude control system is inoperable. Therefore in this investigation BEVO 2 is assumed to be tumbling in an uncontrolled manner. Fig. 5.7 shows the orbital evolution of the selected CubeSats alongside the sunspot number with the purpose of representing general fluctuations in the space environment. From the

figure the varied range of orbital altitudes and space weather conditions analysed in this investigation are observed.

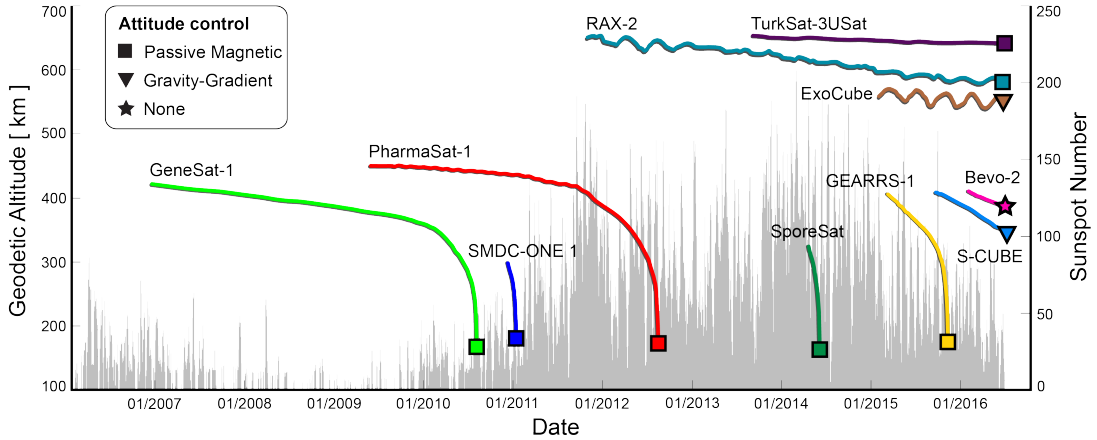


Fig. 5.7 Observed orbital evolution of the analysed CubeSat missions. The sunspot number is used as a proxy for space environment conditions. Plotted data from public sources [148, 151].

The attitude control schemes for each selected mission are provided in Table 5.2 indicating that the PMAC system dominates. Reported steady state attitude behaviour controlled by PMAC systems shows coarse magnetic locking, with worst-case dipole alignment of less than  $\sim 20^\circ$  in RAX-2 [254]. The epicentre of the PMAC dipole misalignment oscillation is the local Earth magnetic vector. In this respect, envelope divergence from Fig. 5.6c due to dipole misalignment is expected to occur at orbit locations with higher local magnetic field gradient, e.g. at mid latitudes in a polar orbit. As misalignment likeliness is unevenly distributed along an orbit and this is of oscillating nature, it is assumed in this investigation that the overall effect on the characteristic envelope is minimum. For this reason and for the sake of analysis homogeneity, this investigation assumes complete alignment of the PMAC dipole to the local Earth magnetic field modelled with the Wold Magnetic Model [88]. In the case of  $\nabla G$  stabilisation, the CubeSats' axis of maximum moment of inertia (in principal axes) is aligned to the local gravitational acceleration vector computed with the GRACE+GOCE Gravity Model GGM05G [140] using harmonics up to 240. As in the PMAC case, perfect alignment is assumed in all instances.

A central element in atmospheric drag analysis is the performance of the atmospheric density model in reproducing actual attributes. The fidelity of the atmospheric density model is fundamental in this investigation because it largely establishes orbital decay estimations and therefore the precision of fitted drag coefficients. This investigation uses the Jacchia-Bowman Thermospheric density model 2008 (JB2008) due to its identified general best performance over other atmospheric density models [115, 144, 255]. In addition, the selection of the JB2008 follows the recommendation of ECSS [142] and the CIRA Working Group [143] for atmospheric density calculations for altitudes above 120km as discussed in Chapter 3. To exemplify an important repercussion of the atmospheric density model fidelity on fitted values, notice that overestimated values of  $\bar{m}_m$  cause proportional increments in  $s$  for fixed  $T_\infty$  and  $v_r$  (Eq. (5.4) and Eq. (5.5)). This in turn reduces  $C_D$  chiefly due to  $C_D \propto 1/s^2$ . It is thus reasonable to compensate the overestimation in the atmospheric density by increasing the  $C_D$  value with the corresponding identified bias percentage [225, 252]. Pardini et al. [252] identified density bias in an earlier version of the JB2008 thermospheric model during the 23<sup>rd</sup> sunspot maximum<sup>7</sup>. However the current version of the JB2008, used in this investigation, has been subject to important empirical corrections [134]. This fact and the conditions of the ongoing 24<sup>th</sup> sunspot cycle make necessary updated studies to identify bias on the current improved JB2008 model.

The fitting algorithm implemented in this investigation can be divided into three main operations. Firstly, it is necessary to precondition collected TLE sets for analysis processing. From the totality of published TLE sets for each CubeSat, statistically inconsistent TLE sets are removed using the Thompson tau technique. Outliers of the temporal semi-major axis rate of change are considered in all instances as shown in the example in Fig. 5.8. The data provided in the final assembly of TLE sets require proper interface from its native SGP4 form to the bespoke special perturbation technique Orbit

---

<sup>7</sup>e.g.  $\sim +7.9\%$  and  $\sim +8.8\%$  at 280 and 600km respectively.

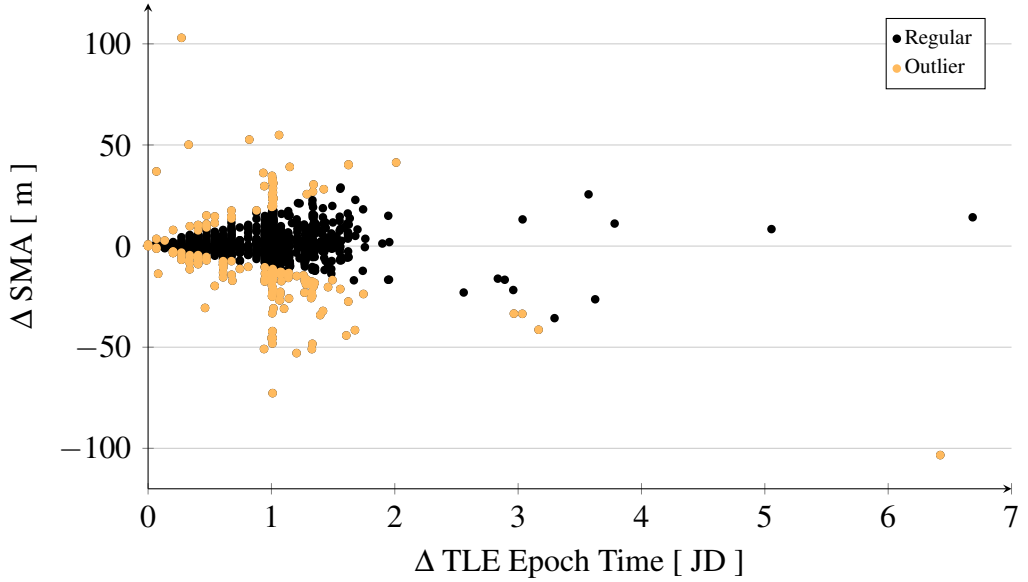


Fig. 5.8 Identification of outliers with respect to the SMA rate of change for RAX-2.

Propagator (OP)<sup>8</sup> designed for the study. To this end the retrieved mean state vector at epoch from a TLE set is converted from its native True Equator Mean Equinox (TEME [148, 139]) coordinate system to the True equator Of the Date (TOD) reference system required by the OP.

The second main operation is the orbital propagation using a seed value of  $C_{D_i}$ . A propagated orbit  $OP_{t_{N-1}}$  in Fig. 5.9 from initial orbital data  $TLE_{N-1}$ , is terminated by the availability of a subsequent observed data  $TLE_N$ . Thus, the new epoch time  $t_N$  defines  $OP_{t_{N_i}}$ . The residual value on SMA between the  $i$ -th propagation and  $N$ -th observation at same epoch,  $R_{SMA_i}$ , is then saved for analysis. At this point is important to bring to mind the existing sensitivity of the OP to the initial state vector and the implications of using TLE sets discussed in Chapter 3. In this regard each pair of TLE sets, i.e.  $TLE_{N-1}$  and  $TLE_N$ , define irregular propagation periods that together with accuracy and resolution concerns imposed by the TLE-OP-TLE assessment may entail unrepresentative  $R_{SMA_i}$  values. Consequently this investigation bounds the analysis to plausible orbital decay values, explained below, as a mitigating measure.

---

<sup>8</sup>In addition to the JB2008 and GGM05G models, the OP incorporates other important perturbations and considerations like Luni-Solar high-precision ephemeris [147], solar irradiance computed with historical empirical data [145], and conical eclipse conditions [146], as presented in Chapter 3.1

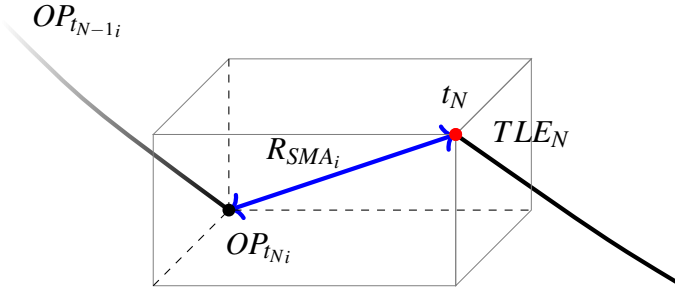


Fig. 5.9 Fitting algorithm. An  $i$  number of  $C_D$  values are used for an equal number of orbital propagations from an initial common observation at time  $t_{N-1}$ . Each propagation would produce a distinctive value of SMA at  $t_N$ , the time of the successive observation ( $TLE_N$ ). The iterative process aims the identification of a drag coefficient value characterising the interval  $t_{N-1}-t_N$  by residual minimisation on SMA ( $R_{SMA_i}$ ) between propagated and observed values.

The third main operation is the fitting of  $C_D$ , through the iterative utilisation of the second main operation. The test range for plausible  $C_D$  values [223] is programmatically bounded to the interval  $[1 - 4]$ . In this regard, the seed value of  $C_D$  used during the first propagation is 1 and two successive propagations test  $C_D$  values for 2.5 and 4. The computed  $R_{SMA_{1,2,3}}$  are analysed for interval convergence. If convergence is found, then fine  $C_D$  fitting is investigated; otherwise the  $OP_{t_{N-1}}$  and  $t_{N-1}$  observation are discarded as the orbit propagation sensitivity or the observed data quality is unsupported for analysis. The final fitted drag coefficient  $C_{DF_{N-1}}$  is determined by three further iterations using variable  $C_D$  values defined by their likeliness to minimise  $R_{SMA}$ . The root-mean square residual on the semi-major axis,  $R\text{-SMA}$ , is computed to report the quality of the estimation. The second and third operations are repeated for all TLE sets available for analysis from the first main operation for each CubeSat.

Note that each reported  $R\text{-SMA}$  is related to one experiment (one  $C_{DF}$ ) and not to a batch of experiments [225]. This approach is adopted because each TLE pair specify an unique experiment with fundamental characteristics, e.g. unique propagation interval (Fig. 5.8). Although it may be argued that there exists some degree of regularity between TLE sets such as in successive TLE epochs allowing for group statistics of fitted values, in this investigation it is preferred to avoid estimated data softening for each analysed

CubeSat. Group statistics is reserved to the eventual compound of  $C_{DF}$  values from a large set of represented conditions.

### 5.2.1 Estimation of $\alpha_n$ from Fitted Drag Coefficients

According to the closed solution for the drag coefficient of a flat plate in free molecular flow used in this investigation, identified values of  $C_{DF}$  may in turn define the values of  $\alpha_n$ . This is possible as long as the average atmospheric composition and bulk temperature, surface temperature, and speed ratio are known. With the exception of the surface temperature, all other variables are well defined by the OP. However, numerical assessment of Eq. (5.10) to (5.13) for the range of conditions of interest in this investigation, shows that the contribution percentage of  $C_I$  in Eq. (5.11) accounts almost invariably for nearly 95% of  $C_D$ . In addition, the sensitivity analysis of Eq. (5.11) to changes in  $\alpha_n$  and  $s$  in Fig. 5.10, shows that  $\alpha_n$  prompts higher variation on the value of  $C_I$ .

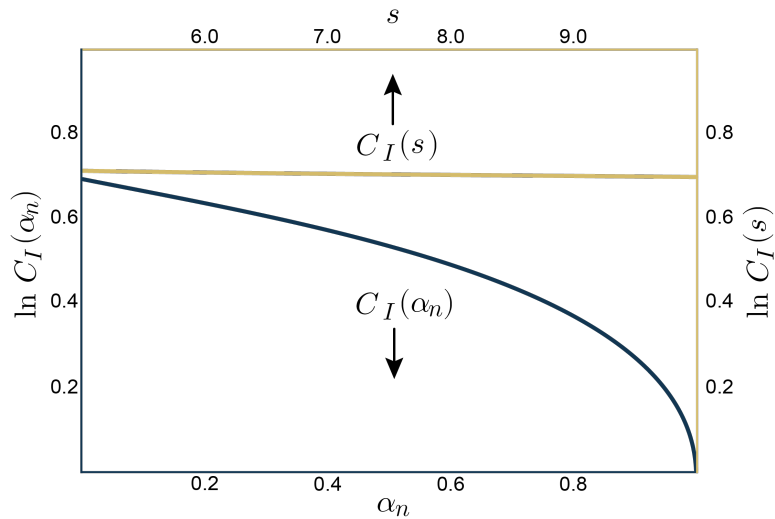


Fig. 5.10 Contribution and variability of term  $C_I$  in Eq. (5.10) to changes in  $\alpha_n$  and  $s$ . The analysed range of  $s$  encompass the values found by the CubeSat missions in this investigation. It is observed that  $\alpha_n$  prompts higher variability on  $C_I$  than  $s$ .

The identified terms contribution and influence of variables allow the simplification of the drag coefficient model for convenient  $\alpha_n$  estimations. Solving Eq. (5.11) for  $\alpha_n$  and substituting  $C_D$  by  $C_{DF}$  yields Eq. (5.17) for the energy accommodation coefficient,

$\alpha_{nF}$ , from fitted drag coefficients.

$$\alpha_{nF} = \frac{C_{DF}s^2(4\operatorname{erf}^2 s + 2\operatorname{erf} s - C_{DF}s^2)}{\operatorname{erf}^2 s(1 + 2s^2)^2} \quad (5.17)$$

### 5.2.2 Analysis of Results

Fig. 5.11 reports relevant parameters from the propagations in box-and-whisker plots. CubeSats data is ordered according to their orbital inclination,  $i$ , in increasing order from left to right. The second row from the top shows the statistics of the total atmospheric density experienced by each CubeSat. Solar activity and orbit altitude establish to a large degree the dispersion, skewness, and values of  $\rho$ .

The reentered GeneSat-1, SMDC-ONE 1, PharmaSat-1, SporeSat, and GEARRS-1, report high values of  $\rho$  with outliers extending to values exceeding  $1 \times 10^{-10} \text{ kg m}^{-3}$ . Outliers in these cases are explained by rapid density increase during the final orbital stage. CubeSats deployed in near Sun-synchronous orbits ( $i \approx 98^\circ$ ) present the lowest atmospheric density values in compliance to their orbital altitudes and little orbital presence in the equatorial bulge.

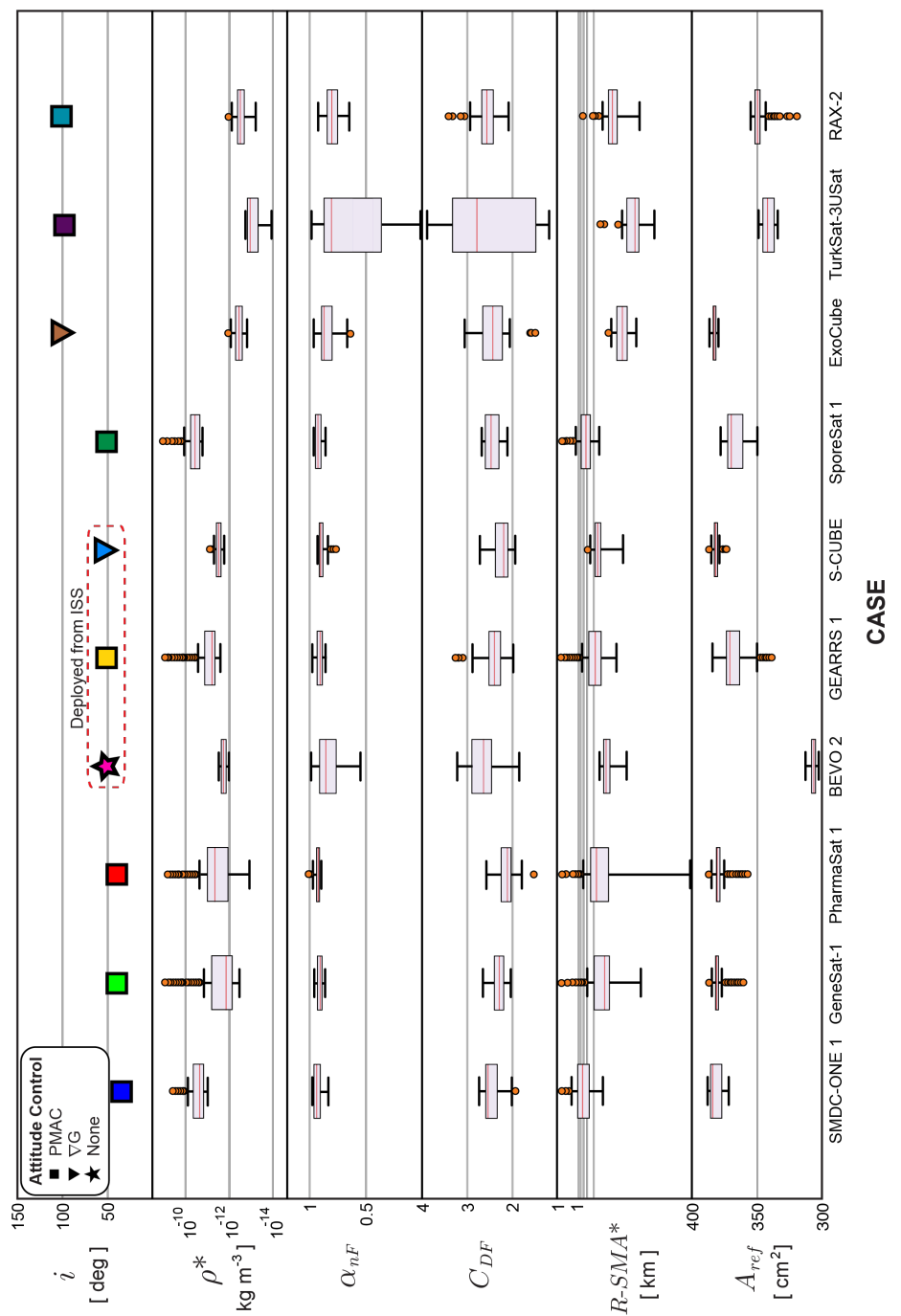


Fig. 5.11 Fitting process summary chart. The line inside the box-and-whisker plots represent the median and the circles represent data outliers.

The third and fourth rows report estimated values of  $\alpha_{nF}$  and  $C_{DF}$  linked by Eq. (5.17). Atmospheric conditions prompting dominant orbital decay enhance the identification of fitted values, which in turn may reveal important characteristics of the surfaces states. In particular, energy accommodation is related to the level of surface contamination as discussed in subsection 5.1.1. It has been hypothesised that AO populates surfaces leading the GSIs as discussed in section 5.1.2. In most cases in Fig. 5.11,  $\alpha_{nF}$  is near to complete accommodation with low degree of data dispersion. These results agree with findings about the possible extended effects of AO at altitudes as high as 650 km. However estimated values of  $\alpha_{nF}$  and  $C_{DF}$  in BEVO 2 and TurkSat-3USat show high levels of dispersion with respect to the rest of the missions. Whilst in TurkSat-3USat the high level of dispersion and skewness in the data may be explained by high AO excursions (in compliance to its orbit altitude) and the reduced number of successful fitted values as reported in Table 5.3, viz. the interquartile range and whiskers may contain unidentifiable outliers in such small data set, data dispersion in BEVO 2 may suggest mostly atypical values. One explanation to this is that data dispersion is showing the forced adjustment of fitted values to suppress the effect of the possible unrepresentativeness of the cross-sectional area approach assumed in BEVO 2. In all instances the inherent sensitivity of TLE-OP-TLE analyses discussed in Chapter 3 is indicated in the low fitting process success percentage reported in Table 5.3, i.e. 40.30% in average.

Table 5.3 Fitting process success percentage.

Name	Analysed TLE sets	Number of $C_{DF}$	Success Percentage
BEVO 2	286	73	25.52
ExoCube	1630	98	6.01
GEARRS 1	588	394	67.01
GeneSat-1	2164	696	32.16
PharmaSat 1	1894	666	35.16
RAX-2	2000	325	16.25
SMDC-ONE 1	83	62	74.70
SporeSat 1	125	116	92.80
S-CUBE	485	255	52.58
TurkSat-3USat	3320	29	0.87

The last two rows report the *R-SMAs* and reference cross-sectional areas ( $A_{ref}$ ) statistics related to the fitting processes. *R-SMA* encompasses values of less than 200 m in most cases. Predominant high solar activity conditions and observed regular orbital decay<sup>9</sup> have a positive influence on the quality of fitted drag coefficient estimations. Specially, the *R-SMA* lower range whisker in PharmaSat 1 demonstrates the effect of a drag dominated orbit on the quality of the fitted values. On the other hand, the  $A_{ref}$  row corresponds to the batch of  $\bar{A}_{dyn}$  values, i.e. average cross-sectional areas over each  $N - 1$  fitted orbit arc under analysis. It is worth recalling that the premise fostering the use of  $A_{dyn}$  in this investigation, is that the relief of cross-sectional area uncertainties would be relevant enough to improve the fitted estimations. In this regard, the overall self-contained results reported so far, need a benchmark for the actual representativeness of the estimated data. Of relevance to this aim are the fitted drag coefficients reported by other investigations and the performance of the identified compound profile of  $C_D$  for 3U CubeSats in reproducing observed orbital decay in a variety of scenarios.

### Discussion

Average fitted drag coefficients ( $\bar{C}_{DF}$ ) for various CubeSats are reported by Oltrogge and Leveque [241] and amongst them values for GeneSat-1, PharmaSat-1, and SMDC-ONE 1 are found. In order to perform adequate comparison of these results to those reported in this investigation it is necessary to make some assumptions. The reported  $\bar{C}_{DF}$  values were computed with four different atmospheric density models, i.e. the Jacchia-Bowman Thermospheric density model 2006 (JB2006), Jacchia 1971, the Standard Atmosphere 1976, and the MSISE2000. Results from the JB2006 are preferred for the purpose of comparison in this investigation because, with the exception of the MSISE2000, the JB2006 is the most recent model based upon total density from satellite drag [139] used in that study. In addition the JB2006 already comprises the improved formulation for high energy incoming solar radiation used in the JB2008 [115].

---

<sup>9</sup>In PharmaSat 1 its consistent observed orbital decay is able to capture peaks in solar activity as shown in Fig. 5.7 near 01/2012

In contrast to this investigation, the Oltrogge and Leveque [241] study assumed fixed mean cross-sectional areas of  $350\text{cm}^2$  in 3U CubeSats. That study encompasses the orbital decay of the CubeSats up to the year 2011. Because the exact date of the analysed time intervals are not provided, it is assumed their analysis is delimited by June 2011, the date of presentation of the work. This assumption has no effect on the comparison of SMDC-ONE 1 and GeneSat-1  $\bar{C}_{DF}$  values because both orbits terminated in early 2011 as shown in Fig. 5.7. On the other hand only  $\bar{C}_{DF}$  values before June 2011 from this investigation are used in the case of PharmaSat 1.

Table 5.4 presents the  $\bar{C}_{DF}$  values from both investigations for the missions in common. In the absence of physical drag coefficient values with which to compare the precision and accuracy of estimations, the relative error with respect to the values of this investigation is reported. Some level of correction for atmospheric density bias is required in both  $\bar{C}_{DF}$  investigations<sup>10</sup>, however this requirement is notable in the discordant PharmaSat 1 value from Oltrogge and Leveque owing to the unattainability of values below 2.0 in free molecular flow as verified from Eq. (5.10) wherein  $\lim_{(\alpha_n,s)\rightarrow(1,\infty)} C_D(\alpha_n,s) = 2$  (HT approximation with complete accommodation), or from Walker et al. [223].

Table 5.4 Comparison of estimated  $\bar{C}_{DF}$  values from this investigation and those reported by Oltrogge and Leveque. Standard deviation reported in parentheses.

Name	This investigation	Oltrogge and Leveque	Relative error*%
GeneSat-1	2.30 (0.14)	2.85	23.91
PharmaSat 1	2.34 (0.16)	1.35	-42.31
SMDC-ONE 1	2.47 (0.18)	2.54	2.83

\* With respect to the values of this investigation

Another aspect to highlight is the variability amongst the results. Reduced variability in the results from this investigation is mostly credited to the effectivity of  $A_{dyn}$  inhibiting the impact of characteristic attitude dynamics on the fitted values. In this regard note that the CubeSats under comparison have similar orbit inclinations and all use

<sup>10</sup>Bias in JB2006 was identified by Pardini et al. [252] from +11.6% to +15.1% at 272 km and 476 km respectively during the 23<sup>rd</sup> sunspot maximum

PMAC systems. Assuming negligible Earth magnetic field variations within the altitude range under analysis, it is reasonable to expect a similar cross-sectional area footprint. This idea can be verified in Fig. 5.11 wherein  $A_{ref}$  is centred around  $\sim 380\text{cm}^2$  in the compared CubeSats, which differs from the invariable  $350\text{cm}^2$  area used in the Oltrogge and Leveque study. Apart from the use of independent results to assess the average performance of the fitted values in this investigation, it is convenient to evaluate other sources of information to identify fitted data evolution performance.

It is discussed in Section 5.1.5 that in an orbiting object subject to the dominant influence of atmospheric drag, the  $B^*$  drag term reported by the TLE sets may bring to light some aspects of drag perturbation fluctuations. Fig. 5.12 presents an example of the evolution of  $C_{DF}$ , the  $C_D$ -like coefficient namely  $C_D^*$  from  $B^{*11}$ , and the respective estimated AO density profile. Although numerical comparison of these different coefficients in this case is trivial due to the incompatibility of data, assessment of fluctuation similarities with AO can be useful.

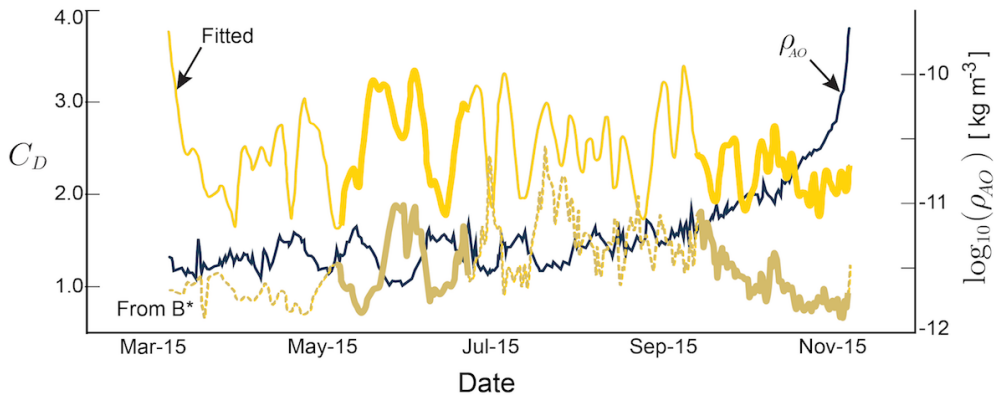


Fig. 5.12 Temporal evolution of drag coefficients and local AO. The light curve, dashed light curve, and dark curve represent the evolution of  $C_{DF}$ ,  $C_D^*$ , and  $\rho_{AO}$  respectively for GEARRS-1.

According to subsection 5.1.1 it is likely that anti-correlation trends between  $C_D$  and AO (through  $\alpha$ ) can be observed. From Fig. 5.12 it is observed that the  $C_D^*$  curve displays nearly-reflected fluctuations with respect to AO, whilst  $C_{DF}$  shows a

---

<sup>11</sup> $C_D^* = \frac{\rho_0 R_\oplus}{2} \frac{A_{ref}}{m_{sc} B^*}$ , with  $\frac{\rho_0 R_\oplus}{2} = \frac{1}{12.741621}$  in  $\text{kg m}^{-2}$  [139], assuming  $m_{sc} = 3.9\text{ kg}$  [256], and  $A_{ref} = 350\text{cm}^2$  for GEARRS-1. In the example, the  $C_D^*$  value is prevalently below two, even using the radar cross section value of  $A_{ref} = 530\text{cm}^2$  (Satellite Catalog (SATCAT) [148] columns 120-127).

less nearly-reflected profile. Similarities between the  $C_D$  curves are observed in some segments like in the interval May-July, and in the final interval September-November. As in this example, weak similarities between  $C_D^*$  and  $C_D$  are observed in all analysed CubeSats, nonetheless  $C_D^*$  values show in general better nearly-reflected variations with respect to AO during drag dominated conditions.  $C_{DF}$  values on the other hand are centred about a plausible range in contrast to  $C_D^*$ .

The comparison of  $C_{DF}$  estimations from this investigation with external estimations and  $C_D^*$ , shows the conforming quality of the fitted values using the methods proposed hereof. However  $C_{DF}$  estimations are valuable only to analyses of 3U CubeSats experiencing analogous space-spacecraft interaction conditions. In such case the use of  $\bar{C}_{DF}$  may be an unnecessary oversimplification of the data profile. Alternatively, a more valuable model may be put forward by profiting from the varied space condition scenarios represented by the compound of  $C_{DF}$  estimations from all analysed missions.

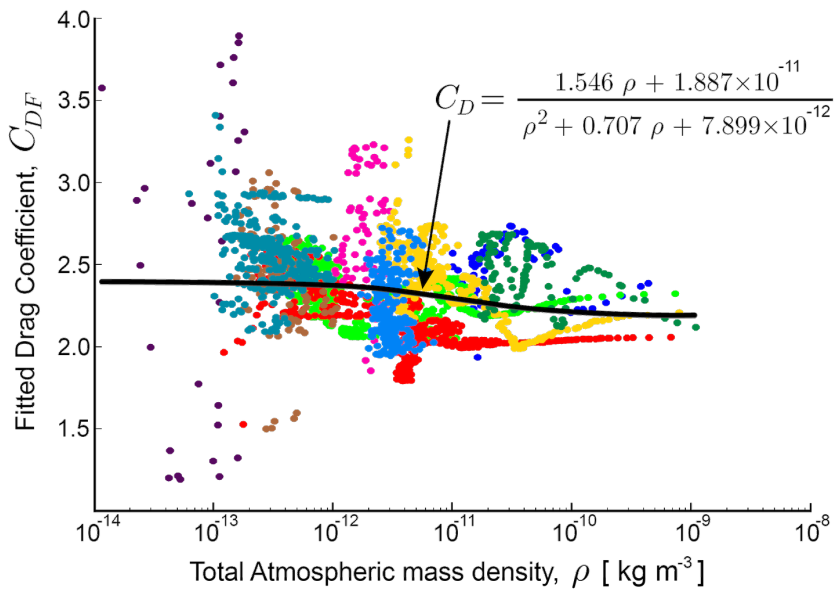


Fig. 5.13 Assembly of  $C_{DF}$  with respect to their average  $\rho$  values. The goodness-of-fit statistics report that the fitted curve describes 98.18% of the total variation of the data about the average (R-Square) with a small random error component (Sum of Squares Due to Error or SSE) of 0.16.

Drag coefficient values are dependent on the molecular speed ratio, temperature, and accommodation coefficients as discussed in previous sections. Acknowledging the lack of sufficient information in this investigation to map an integral spectrum of these

variables, a trade-off between model representativeness of the 3U CubeSat  $C_D$  profile and model simplicity to ease its general application is endeavoured. Regardless of the multivariable dependency of  $C_D$ , the plot of all  $C_{DF}$  values as function of the average total atmospheric density  $\rho$  for each propagation arc, provides sufficient essential information to put forward a representative equation  $C_D(\rho)$  of the 3U CubeSat standard as illustrated in Fig. 5.13. The condition enabling this coarse approximation is that AO (and likely  $\alpha$ ) is strongly and almost invariably correlated to the total atmospheric concentration within the altitude range under analysis, i.e. correlation coefficient of  $\sim 0.98$ , as shown in Fig. 5.14. The performance of  $C_D(\rho)$  in representing a general

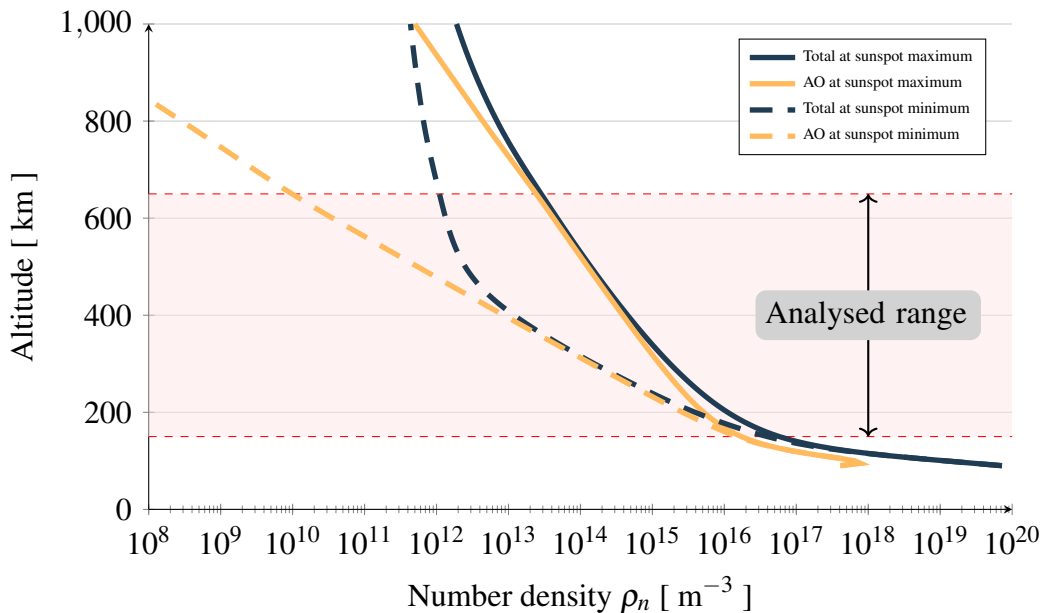


Fig. 5.14 Equatorial total and AO concentration in the JB2008 model under extreme conditions. Maximum and minimum profiles during noon and midnight respectively.

characteristic figure of the standard 3U CubeSats and the convenience of the proposed  $A_{dyn}$  approach can be assessed through the compliance of long-term orbital propagations to observed orbital decay. Figures of merit in this assessment are given by orbit propagations using the typical invariable values of  $C_D = 2.2$  and  $A_{sta} = 350\text{cm}^2$  in standard 3U CubeSats. Table 5.5 summarises the performance of various combinations of these parameters in terms of the semi-major axis root-mean-square residuals per day of propagation ( $R\text{-SMA/day}$ ). Each  $R\text{-SMA}$  is computed with the compound of residual

values between a single full-length orbit propagation and the corresponding observed values selected from the first main operation discussed earlier in this section.

According to Table 5.5 the  $C_D(\rho)$  function in combination with  $A_{dyn}$  successfully approaches the orbital decay of the re-entered GeneSat-1, PharmaSat 1, SMDC-ONE 1, and SporeSat 1 CubeSats. This is concluded from the identification of the lowest value of  $R\text{-SMA}/\text{day}$  amongst combinations. Specially for SMDC-ONE 1 and SporeSat 1 the maximum difference amongst of their respective residuals for each combination,  $\Delta R\text{-SMA}/\text{day}$  reported in the rightmost column, indicates a clear improvement using the proposed approach over typical constant values. These results indicate the suitability of the proposed models over other combinations during moderate-to-high solar activity in LEO orbits below 350km. With respect to the representativeness of  $C_D(\rho)$ , characteristic values of  $\rho$  for SMDC-ONE 1 and SporeSat 1 (see Fig. 5.11) suggests that the function satisfactorily captures  $C_D$  variation for values above  $1 \times 10^{-11} \text{ kg m}^{-3}$ . This can be explained from the low dispersion in  $C_{DF}$  values used for curve fitting for that range of  $\rho$ , see Fig. 5.13. Conversely to these CubeSats, none of the proposed model combinations are strongly representative for GEARRS 1 and S-CUBE. In both cases the proposed models overestimate the product  $A_{dyn}C_D(\rho)$  favouring the use of the conservative values of  $C_D$  and  $A_{sta}$ . The remaining cases show marginal differences amongst the various approaches. That is, the method presented in this investigation is not significantly out-performed by any other combination.

### **5.3 Chapter Conclusions and Further Work**

This investigation aims to improve the optimisation of propulsion technologies for nanosatellite systems through the identification of distinctive drag coefficient development and attributes of gas-surface interactions in standard 3U CubeSats. The selected 3U CubeSats for this investigation, BEVO 2, ExoCube, GEARRS 1, GeneSat-1, PharmaSat 1, RAX-2, SMDC-ONE, SporeSat 1, S-CUBE, and TurkSat-3USat, use passive attitude stabilisation strategies and have similar convex geometry attributes. Dynamic

cross-sectional areas are employed in the fitting of drag coefficients instead of the customary use of constant quantities targeting a better description of the time-varying projected geometry of the standard 3U CubeSat, and therefore representativeness of the results. Additionally, the level of energy accommodation coefficients are estimated by means of the closed form CCL model for a flat plate perpendicular to the flow. The estimated fitted drag coefficients have been consolidated in a representative and simple drag coefficient function as function of atmospheric density. The performance of the proposed function is tested by its ability to reproduce general orbital decay in standard 3U CubeSats.

Based upon the evidence collected in the investigation and the comparison to external reported data, the fitted drag coefficients computed with dynamic cross-sectional areas provide consistent and descriptive data for the geometry and orbital characteristics of the analysed CubeSats undergoing drag-dominated orbits. Additionally, results show that estimating the level of the energy accommodation coefficient in convex CubeSat geometries using fitted drag values is viable. Regarding the proposed drag coefficient function  $C_D(\rho)$  for near-circular orbits, orbital decay simulations show that it captures  $C_D$  variation for values above  $\sim 1 \times 10^{-11} \text{ kg m}^{-3}$ , which is roughly below altitudes of 350 km during moderate-to-high solar activity. However, it should be noted that  $C_D$  is function of a far more complex set of variables as discussed in this chapter, e.g.  $s$ ,  $\sigma$ , the kinetic energy of incident particles, etc., simplified in this case as function of the average total atmospheric density and valid for the JB2008; a supplementary fitting method study on  $C_D$  weak dependencies is presented in Appendix G. A more suitable approach would be to use the results reported in Fig. 5.11 instead of  $C_D(\rho)$  if a valid approximation of orbit characteristics and space environment conditions in a new mission analysis would be feasible.

Further work should focus on the study of a higher number of missions and in situ measurements of atmospheric species dominating the atmospheric-spacecraft interaction. In this regard, atomic oxygen studies from the Flux-Φ-Probe EXperiment (FIPEX) [117] would be valuable. The analysis of various nanosatellite size factors, including

convex and concave geometries under a richer spectrum of space environment conditions, would enhance the study and understanding of atmospheric drag on nanosatellites. Furthermore, future TLE accuracy upgrades (discussed in subsection 5.1.5) in conjunction with the increasing number of nanosatellite missions would make orbital data processing possible for studies considering the weaker parameters of atmospheric drag, e.g. momentum accommodation factors.

Table 5.5 SMA RMS residuals with respect to the values from TLE sets for four combinations of fixed and variable  $A_{ref}$  and  $C_D$ . Minimum values are marked in bold type. Each value is obtained from a single-run orbital propagation from the first valid known orbital state after deployment to the last one available by 5 July, 2016. R-SMA values in [ m ]; re-entry day absolute difference with respect to TLE data is enclosed in parentheses.

Name	Status	R-SMA/day from $C_D(\rho)$		R-SMA/day from $C_D^*$		$\Delta R\text{-SMA}/\text{day}^\S$
		$A_{dyn}$	$A_{sta}^\dagger$	$A_{dyn}$	$A_{sta}^\dagger$	
BEVO 2	In-orbit	30.34	<b>28.14</b>	32.30	28.81	4.16
ExoCube <sup>‡</sup>	In-orbit	30.23	28.23	28.26	<b>27.19</b>	3.04
GEARRS 1	Re-entered	103.22 (24.92)	68.63 (10.30)	69.36 (12.93)	<b>32.54</b> (3.21)	70.68
GeneSat-1 <sup>‡</sup>	Re-entered	<b>9.63</b> (40.38)	12.04 (63.66)	10.80 (50.09)	18.39 (138.26)	8.76
PharmaSat 1 <sup>‡</sup>	Re-entered	<b>7.77</b> (11.99)	22.18 (80.02)	20.74 (67.73)	27.72 (134.35)	19.95
RAX-2	In-orbit	8.93	9.40	<b>7.84</b>	8.08	1.56
SMDDC-ONE 1	Re-entered	<b>334.21</b> (3.28)	507.68 (7.08)	382.83 (4.16)	536.44 (8.02)	<b>202.23</b>
SporeSat 1 <sup>‡</sup>	Re-entered	<b>309.33</b> (4.76)	425.51 (8.02)	368.80 (5.71)	471.61 (9.02)	<b>162.28</b>
S-CUBE <sup>‡</sup>	In-orbit	86.39	51.13	60.13	<b>33.83</b>	52.56
TurkSat-3USat	In-orbit	16.42	16.20	16.19	<b>15.95</b>	0.47

\* Typical value of 2.2

<sup>†</sup> Average cross-sectional area of 350 cm<sup>2</sup>[241]

<sup>‡</sup> Approximated standard geometry

<sup>§</sup> Maximum difference amongst values

Blank page

# **Chapter 6**

## **Spiral Coning Manoeuvre for In-Orbit Low Thrust Characterisation in Nanosatellites**

Of general interest for propulsion system design and operation in nanosatellites is the ability to forecast solar activity, discussed in Chapter 4, in conjunction with the atmosphere-spacecraft interaction through the fitted drag coefficient analysis presented in Chapter 5. Complementary to these essential matters, this chapter covers the onerous in-orbit low thrust characterisation with modest attitude determination resources, which is a fundamental task in propulsion systems characterisation. To this aim, note that the realisation of the analysis presented in Chapter 5 is facilitated by the notable geometric standardisation of nanosatellites in the predominant form of CubeSats. In the same tenor, the investigation presented in this chapter focuses on standard 1.5U and 3U CubeSats to assess a convenient method for in-orbit low thrust characterisation in the range from 50nN to 10 $\mu$ N. This range encompasses high performance propulsion systems with the lowest thrust levels reported in section 2.1 and Appendix F, and typifies a range difficult to characterise with standard attitude determination systems in CubeSats.

The CubeSat geometries in this investigation are assumed standard with near-symmetry in two-axis, namely axisymmetric, and the effect of appendages over the

## Spiral Coning Manoeuvre for In-Orbit Low Thrust Characterisation in Nanosatellites

---

attitude evolution during the thrust characterisation considered negligible. Centroid and moment of inertia tensor variations are also assumed negligible. The CubeSat models employed in this chapter are assumed rigid rectangular parallelepipeds with the  $z$  body axis parallel to the principal moment of inertia  $I_z$  (minor axis of inertia), and the values of  $I_x$  and  $I_y$  nearly equivalent as shown in Fig. 6.1. These assumptions are in close compliance with reported CubeSat configurations [39, 40, 69] and principal moments of inertia values in real missions [30, 257, 258]. Additionally, the investigation is based on the common practice of performing in-orbit thruster characterisation via attitude changes [39, 40, 31]. To this end, a four-element thruster setup configuration is used in the simulations due to the versatile and convenient possible spectrum of manoeuvres.

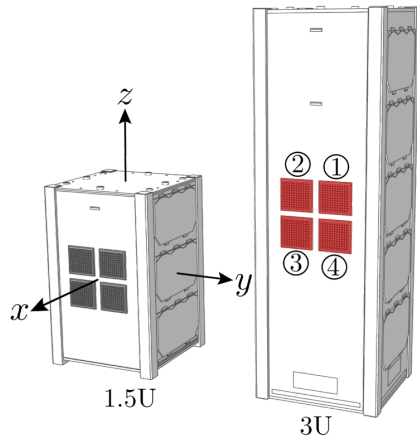


Fig. 6.1 Reference CubeSats, body axes, and thruster patch units definition. The selected generic multi-thruster configuration for this investigation, provides rich manoeuvring possibilities. An instance of this is found in the recent BRICSat-P mission [39].

## 6.1 The Proposed Method

The study presented in this chapter involves the analysis of rigid body motion. For the sake of relevance to the study, the explanations assume motion about the centre of mass instead of generalised mathematical derivations. The displacement of a rigid body can be conveniently separated into translational motion of its centre of mass and the rotational motion about the centre of mass according to the Chasles' theorem<sup>1</sup>.

---

<sup>1</sup>The Chasles' theorem states that every rigid body motion can be realised by a rotation about an axis combined with a translation parallel to that axis [152].

These two sets of movements can be solved independently, requiring expressions for the angular momentum and rotational kinetic energy about the centre of mass in attitude dynamics analysis. The angular momentum vector ( $\vec{L}$  [259]) of a rigid body about its centre of mass in body-fixed reference frame<sup>2</sup> is defined by Eq. (6.1), where  $\vec{r}$  is the position of a mass element ( $dm$ ) from the centre of mass, and  $\vec{\omega}$  is the body angular velocity vector.

$$\vec{L} = \int \vec{r} \times (\vec{\omega} \times \vec{r}) dm \quad (6.1)$$

Expanding Eq. (6.1) into components becomes

$$L_x = \int (r_y^2 + r_z^2) dm\omega_x - \int r_x r_y dm\omega_y - \int r_x r_z dm\omega_z \quad (6.2)$$

$$L_y = - \int r_x r_y dm\omega_x + \int (r_x^2 + r_z^2) dm\omega_y - \int r_y r_z dm\omega_z \quad (6.3)$$

$$L_z = - \int r_x r_z dm\omega_x - \int r_y r_z dm\omega_y + \int (r_x^2 + r_y^2) dm\omega_z \quad (6.4)$$

Eq. (6.2) – (6.4) show that the  $\vec{L}$  is related to  $\vec{\omega}$  by a linear transformation which can be written in matrix form. The linear operator relating both vectors is the symmetric nine component inertia tensor  $\vec{I}$ . The inertia tensor is diagonally composed by the moments of inertia coefficients marked in bold in Eq. (6.2) – (6.4) and off-diagonally by the products of inertia such that  $\vec{I} = \vec{I}^\top$ . Thus, in matrix notation and using this definition, Eq. (6.1) becomes

$$\vec{L} = \vec{I}\vec{\omega} \quad (6.5)$$

In a rigid body with two planes of symmetry with respect to the body reference frame, e.g. a rectangular parallelepiped, the products of inertia elements vanish yielding a diagonal matrix composed solely by the moments of inertia coefficients.

The complementary rotational kinetic energy ( $K$  [259]) is defined by Eq. (6.6)

$$K = \frac{1}{2} \int \dot{r} \cdot \dot{r} dm = \frac{\vec{\omega} \cdot \vec{L}}{2} \quad (6.6)$$

---

<sup>2</sup>Subscripts  $x, y, z$  represent this triad of orthogonal unit vectors.

## Spiral Coning Manoeuvre for In-Orbit Low Thrust Characterisation in Nanosatellites

---

Alternatively, if  $\hat{n}$  is a unit normal vector parallel to  $\vec{\omega}$ , so that  $\vec{\omega} = \omega\hat{n}$ . The moment of inertia about the axis of rotation  $\vec{n}$  can be defined by Eq. (6.7)

$$I = \hat{n} \cdot \vec{I} \hat{n} \quad (6.7)$$

Using this *scalar* value, the rotational kinetic energy can also be written as

$$K = \frac{1}{2} I \omega^2 \quad (6.8)$$

In a rigid body in torque-free motion, the rotational kinetic energy is constant and the total angular momentum vector is fixed in inertial space [152]. Otherwise the angular momentum rate of change in a rigid body can be related to the action of an external moment  $\vec{M}$  acting about the centre of mass having the expression

$$\dot{\vec{L}} = \vec{M} \quad (6.9)$$

The rate of change of the vector  $\vec{L}$  with respect to an inertial reference frame (space) is given by Eq. (6.10) [260]

$$\dot{\vec{L}}_{space} = \dot{\vec{L}}_{body} + (\vec{\omega} \times \vec{L})_{rotation} \quad (6.10)$$

Now, with Eq. (6.10) in Eq. (6.9), the rotational motion about the centre of mass (relative to the body axes) is therefore given by Eq. (6.11)

$$\vec{M} = \dot{\vec{L}} + \vec{\omega} \times \vec{L} \quad (6.11)$$

The specific solution of Eq. (6.11) for the problem at hand is discussed in the following subsection. At the moment a geometrical description of the torque-free motion in principal axes is convenient to assist the proposed method explanation. Here, the Poinsot's construction provides a useful geometrical description of the rigid body

motion by allowing the visualisation of  $\vec{\omega}$  in terms of the constants of the motion. Consider the vector description given by Eq. (6.12) [260] for the Poinsot's construction in which the direction of  $\vec{\rho}$  is defined by  $\vec{\omega}$  and its magnitude by the relative inertial properties of the body.

$$\vec{\rho} = \frac{\hat{n}}{\sqrt{I}} = \frac{\vec{\omega}}{\sqrt{2K}} \quad (6.12)$$

Assume the definition in Eq. (6.13) leads to a function that has the form of a triaxial ellipsoid in cartesian  $\vec{\rho}$  coordinates for constant values of  $f$ . It is of interest for the intended explanation, the particular case wherein  $f(\rho) = 1$ , known as inertial ellipsoid.

$$f(\rho) = \vec{\rho} \cdot \vec{I} \vec{\rho} = I_x \rho_x^2 + I_y \rho_y^2 + I_z \rho_z^2 \quad (6.13)$$

The gradient of function Eq. (6.13), furnishes information about the normal vectors of the inertial ellipsoid surface.

$$\nabla_{\rho} f = 2\vec{I} \cdot \vec{\rho} = \sqrt{\frac{2}{K}} \vec{L} \quad (6.14)$$

A relevant aspect of the motion arises from Eq. (6.14) that the surface normals of the inertial ellipsoid are parallel to the constant vector  $\vec{L}$ . Furthermore, by considering the projection,  $h$ , of the time dependent  $\vec{\rho}$  on  $\vec{L}$  in Eq. (6.15) it becomes evident that  $h$  remains constant as it is defined solely by constants of the motion.

$$h = \frac{\vec{\rho} \cdot \vec{L}}{L} = \frac{\sqrt{2K}}{L} \quad (6.15)$$

By joining and applying the aforementioned inferences to a tumbling regular prolate cuboid ( $I_x \approx I_y > I_z$ ) it is possible to illustrate the state of  $\vec{\omega}$  as shown in Fig. 6.2. The construction of the illustration in inertial space can be realised by first defining the invariant  $\vec{L}$ . The vector  $\vec{L}$  starts at the cuboid's centre of mass, and has been chosen pointing downwards in Fig. 6.2 for illustrative purposes. Following with the construction of other geometry elements around this vector, we know from Eq. (6.15)

## Spiral Coning Manoeuvre for In-Orbit Low Thrust Characterisation in Nanosatellites

that there exists a fixed distance  $h$  from the centre of mass to the projection of  $\vec{\rho}$  on  $\vec{L}$  at any time. Furthermore, Eq. (6.14) establishes that the inertial ellipsoid has to have its instantaneous surface normal, parallel to  $\vec{L}$  for any  $\vec{\rho}$ . These two conditions are fulfilled by a plane at a fixed distance  $h$  from the centre of mass of the body, named the invariable plane, over which the inertial ellipsoid rolls to preserve the constant relationship of  $\vec{L}$  and  $\vec{\rho}$  for any time<sup>3</sup>. In this way, the instantaneous contact point between the inertial ellipsoid and the invariable plane in intermediate axis spinners trace out two circles, the polhode and herpolhode respectively. Finally, note that with respect to the body axes,  $\vec{\rho}$  sweeps out a cone, referred to as the body cone. Likewise, the swept out cone in inertial space is called the space cone. Both idealised cones are always in contact, rolling one over the other through the contact line defined by  $\vec{\rho}$ . For

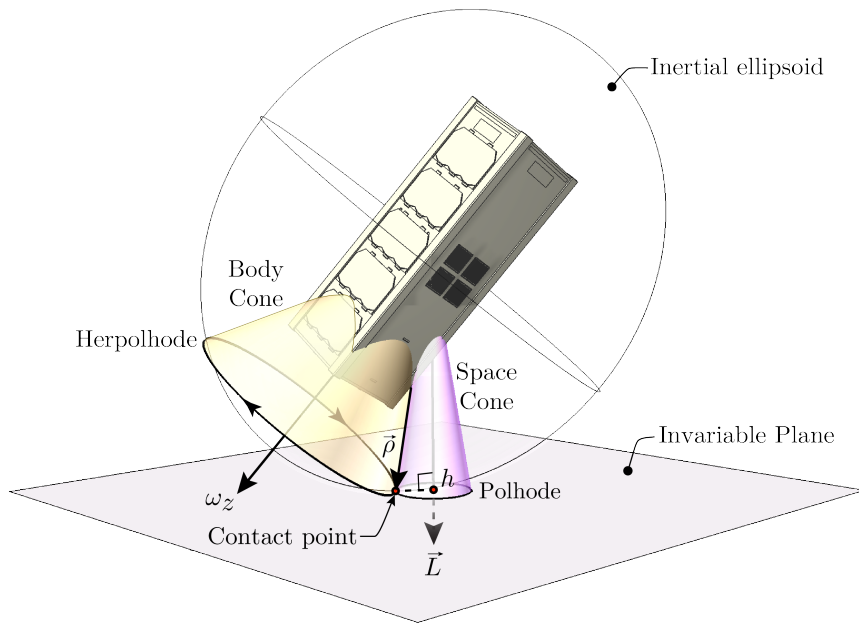


Fig. 6.2 Poinsot's construction. The 3U CubeSat geometry has been included for illustrative purposes to emphasise the precession of  $\vec{\rho}$  in body axes for a intermediate axis spinner. The herpolhode sweep-out frequency outlines the proposed methodology for in-orbit low thrust characterisation in CubeSats.

the purpose of this investigation, the interpretation of Fig. 6.2 in body axes, wherein  $\vec{\rho}$  has prograde precession around  $\omega_z$  in an intermediate axis spinner is of relevance.

<sup>3</sup>The Poinsot's Theorem [261] states that the moment of inertia ellipsoid in space rolls without slipping on the invariable plane.

Bearing in mind that  $\vec{\rho}$  and  $\vec{\omega}$  are collinear, this investigation employs the pre and post manoeuvre body cones of  $\vec{\omega}$  to draw information about the thrust magnitude. The two cones can be idealised as two concentric nested cones with their apices located at the CubeSat's centre of mass and having different heights. In this particular case, concentricity in the body cones implies that the values of  $\omega_x$  and  $\omega_y$  remain constant during the test manoeuvre that aims change in  $\omega_z$ , which in turn modifies the inertial ellipsoid size. A distinctive open spiral cone, not used in the following descriptions, transitions from the pre to the post manoeuvre body cones. The conventional way to assess thrust action using body angular velocities is by observing the rate of change in body cone *height*, or put in another way, by assessing the rate of change in  $\omega_z$  during the thrust manoeuvre. Provided that the thrust magnitude and sensing resources allow it, this method gives a simple and reliable method to evaluate thrust. Conversely, this investigation proposes the use of *sweep-out frequency* change of the the herpolhode, identifiable from  $\omega_x$  or  $\omega_y$ , to draw information about the thrust magnitude. In principle, if the *height* difference of the body cones (or rate of change) is difficult to resolve, e.g. noisy signal and weak angular rates, then it is still possible to identify changes in their characteristic and definable transversal (*xy* plane) sweep-out frequencies. Note that there exists redundancy in the data source of the sweep-out frequency<sup>4</sup> conferring additional flexibility to the proposed method.

Another important aspect to consider in the proposed method is that the cone angles of aperture are dictated by the values of  $\vec{I}$  and the magnitude of the transversal component of  $\vec{\omega}$ , henceforth referred to as  $\omega_t$ . Two relevant cases are formed when the inertial ellipsoid becomes a sphere for  $I_x \approx I_y \approx I_z$ , and when  $\omega_t = 0$ . In both cases  $\vec{\rho}$  and  $\vec{L}$  become collinear implying the disappearance of the space cone. The first case nullifies the sweep-out frequency of interest by establishing constant values of  $\omega_x$  or  $\omega_y$ . Further discussion on the matter is presented in subsection 6.1.1. At this point it is worth mentioning that the parallelism between  $\vec{\rho}$  and  $\vec{L}$  implies stable rotation under kinetic energy dissipative processes. However only unstable rotation in a prolate body

---

<sup>4</sup>Both  $\omega_x$  and  $\omega_y$  equally define the sweep-out herpolhode frequency.

(intermediate axis spinner) is of interest for this investigation as the analysis is based on the body cone sweep-out frequency.

The effects of spacecraft mass variations and unstable rotation under energy dissipative phenomena, e.g. flexible elements such as antennae, become important over attitude evolution normally after long periods of time in comparison to the average thrust test. These topics are addressed in subsections 6.1.2 and 6.1.3 respectively, after the derivation of the pertinent analytical solutions of the rigid body motion.

### 6.1.1 Analytic Solutions

In order to develop the analytical framework of this investigation, consider the Euler's equations of motion of a rotating rigid body with principal axes at the centre of mass under the action of a total perturbing torque vector  $\vec{M}$  derivable from Eq. (6.11).

$$M_x = I_x \dot{\omega}_x + (I_z - I_y) \omega_y \omega_z \quad (6.16)$$

$$M_y = I_y \dot{\omega}_y + (I_x - I_z) \omega_z \omega_x \quad (6.17)$$

$$M_z = I_z \dot{\omega}_z + (I_y - I_x) \omega_x \omega_y \quad (6.18)$$

These equations are a set of coupled nonlinear equations describing the temporal evolution of the angular velocity in body axes. Their general solution requires numeric integration, but in specific cases it is possible to obtain analytical solutions. One such case is for an axisymmetric body. Assuming that  $I_x$  is nearly equivalent to  $I_y$ , Eq. (6.18) is simplified to Eq. (6.19) prompting decoupling and the solution of the system of equations.

$$\omega_z = \frac{M_z}{I_z} t + \omega_{z0} \quad (6.19)$$

The simplest solution, excluding the trivial one, is found when the values of  $M_x$  or  $M_y$ , and  $M_z$  are negligible. This case describes a slender rigid body in forced rotation about its minimum axis of inertia. However, for the purpose of this investigation  $M_z \neq 0$ , i.e. in the characterising manoeuvre thrust modifies  $M_z$ . Under this scenario, finding

analytical solutions requires a far more complex approach. This investigation uses the methodology proposed in the work of Tsiotras and Longuski [262] to find a suitable solution for the problem at hand. Eq. (6.20) presents the differential equation in complex notation for the transversal angular velocities.

$$F = \dot{\vec{\Omega}} + iD\vec{\Omega} \quad (6.20)$$

The variables in this equation are described by Eqs. (6.21) to (6.26) with  $A \equiv \omega_z$ .

$$\vec{\Omega} \equiv \omega_1 \sqrt{C_2} + i\omega_2 \sqrt{C_1} \quad (6.21)$$

$$F \equiv \frac{M_x}{I_x} \frac{I_z}{M_z} \sqrt{C_2} + i \frac{M_y}{I_y} \frac{I_z}{M_z} \sqrt{C_1} \quad (6.22)$$

$$C_1 \equiv \frac{I_z - I_y}{I_x} \quad (6.23)$$

$$C_2 \equiv \frac{I_z - I_x}{I_y} \quad (6.24)$$

$$C \equiv \sqrt{C_1 C_2} \quad (6.25)$$

$$D \equiv C \frac{I_z}{M_z} \quad (6.26)$$

With Eq. (6.20)–(6.26) from Tsiotras and Longuski [262], the customised analytic solution for the investigation presented in this chapter is developed as follows. The integral of Eq. (6.20) with respect to  $A$  and solved for  $\vec{\Omega}$  represents the solution for the transversal angular velocities given by Eq. (6.27)

$$\vec{\Omega} = \vec{\Omega}_0 e^{i\frac{D}{2}(A^2 - A_0^2)} + F e^{i\frac{DA^2}{2}} \int_{A_0}^A e^{-i\frac{Du^2}{2}} du \quad (6.27)$$

By neglecting  $M_x$ ,  $M_y$ , and substituting  $\vec{\Omega}_0 = \omega_{x_0} \sqrt{C_2} + i\omega_{y_0} \sqrt{C_1}$ ,  $A_0 \equiv \omega_{z_0}$ , and  $I_x$  and  $I_y$  with  $I_t$  for simplification purposes, yields Eq. (6.28)

$$\vec{\Omega} = (\omega_{x_0} + i\omega_{y_0}) e^{i \frac{(I_t - I_z)(M_z t^2 + 2I_z \omega_{z_0} t)}{2I_z I_t}} \quad (6.28)$$

## Spiral Coning Manoeuvre for In-Orbit Low Thrust Characterisation in Nanosatellites

---

Or equivalently in trigonometric form

$$\vec{\Omega} = (\omega_{x_0} + i\omega_{y_0}) (\cos wt + i \sin wt) \quad (6.29)$$

in which the angular frequency,  $w$ , is given by Eq. (6.30). Notice the explicit dependence of this spinning axisymmetric forced frequency on time in a characteristic linear chirp signal.

$$w = \frac{(I_t - I_z)(M_z t + 2I_z \omega_{z_0})}{2I_z I_t} \quad (6.30)$$

The real and imaginary components in Eq. (6.29) constitute the transversal angular velocities  $\omega_x$  and  $\omega_y$  respectively

$$\omega_x = \frac{\Re(\vec{\Omega})}{\sqrt{C_2}} \quad (6.31)$$

$$\omega_y = \frac{\Im(\vec{\Omega})}{\sqrt{C_1}} \quad (6.32)$$

Finally, the rigid body angular velocities for  $M_x = M_y = 0$ , and  $M_z \neq 0$  are

$$\omega_x = \omega_{x_0} \cos wt + \omega_{y_0} \sin wt \quad (6.33)$$

$$\omega_y = \omega_{y_0} \cos wt - \omega_{x_0} \sin wt \quad (6.34)$$

$$\omega_z = \frac{M_z}{I_z} t + \omega_{z_0} \quad (6.35)$$

Furthermore, the *free spin* condition is fulfilled for  $M_z = 0$ . In that case Eq. (6.33) to Eq. (6.35) are simplified to

$$\omega_x = \omega_{x_0} \cos w_n t + \omega_{y_0} \sin w_n t \quad (6.36)$$

$$\omega_y = \omega_{y_0} \cos w_n t - \omega_{x_0} \sin w_n t \quad (6.37)$$

$$\omega_z = \omega_{z_0} \quad (6.38)$$

with the spinning axisymmetric natural frequency defined by

$$w_n = \omega_{z0} \left( 1 - \frac{I_z}{I_t} \right) \quad (6.39)$$

As a final remark in this subsection note that the projection of  $\vec{\omega}$  on the  $xy$  plane in body axes draw circles representing the herpolhode for both the free and forced spin conditions. In addition, it has been discussed earlier in this Section 6 that for  $I_x \approx I_y \approx I_z$  in torque-free motion, the body angular velocities are constant. This argument is now validated by Eq. (6.39) by providing a null transversal natural frequency in full symmetry conditions.

### 6.1.2 Induced Error due to Temporal Mass Variation

Temporal changes in mass quantity and distribution, e.g. propellant consumption, can be incorporated in the proposed method. However, it is convenient to recall that this investigation assumes  $I_t \equiv I_x \approx I_y$ . If important variation within the transversal component exists or is expected to occur implying necessary asymmetry, then bespoke analytical solutions may be still available [262], enabling thrust estimation with the proposed method. Fig. 6.3 presents the percent relative error of Eq. (6.30) to variations in  $I_t$  and  $I_z$  for standard 1.5U and 3U CubeSats, and the empirical value  $w = 0.01 \text{ rad s}^{-1}$  (distinctive for 10 min of micro-thrust in a 1.5U CubeSat). The exhaust mass flow rate is computed with  $\dot{m}_e = M_z / d_m I_{sp} g_0$  [152, pp. 557], being  $d_m$  the effective moment arm reasonably equivalent to one fourth of the CubeSat face width accommodating a symmetric thruster array, namely 2.5 cm, and  $g_0$ , the standard surface gravity. The value of  $\chi$  is the product of  $I_{sp}$  and  $d_m$ . The value of  $I_{sp}$  according to Fig. 2.4 in Chapter 2 and Appendix F, is typically higher than 1000 s for propulsion systems natively below  $\mu\text{N}$  yielding  $\chi > 25$ . Under these assumptions, the induced error due to neglecting temporal mass variations is lower than ten thousandths percent.

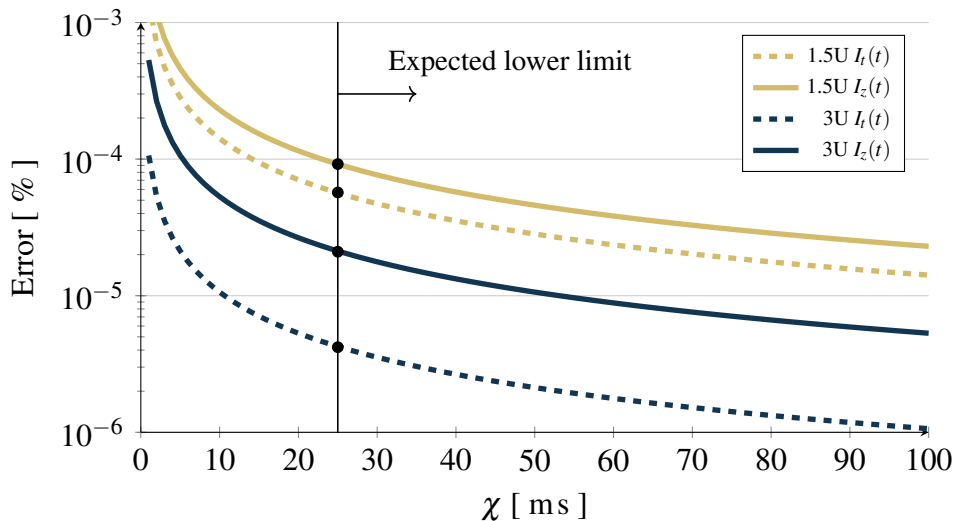


Fig. 6.3 Log-lin plot of the percent relative error of the method due to transversal,  $I_t(t)$ , and longitudinal,  $I_z(t)$ , moment of inertia variations. The figure accounts for the propellant mass consumption led by  $I_{sp}$  through  $\chi$ , the product of  $I_{sp}$  and the moment arm, in standard CubeSat form factors.

### 6.1.3 Rotation Stability and Energy Dissipation

Stable rotation in a simple axisymmetric spinner occurs around two *preferred* orthogonal axes satisfying parallelism between  $\vec{\rho}$  and  $\vec{L}$  as discussed before. Under non-conservative circumstances, an intermediate axis spinner, as in Fig. 6.2, would nutate until it spins about the major axis of inertia and minimum energy state. An explanation can be formulated by considering the constants of the motion and the moment of inertia as seen by  $\vec{\omega}$ . Given the body rotation energy by  $K = 1/2I\omega^2$  and the body angular momentum magnitude by  $L = I\omega$ , a torque-free spinner is then governed by  $I = L^2/2K$ . Energy loss mechanisms lower the value of  $K$  giving rise to an increment in  $I$ . In this way the spinner would gradually move to stable rotation about the maximum moment of inertia (flat spin).

The source of predominant energy dissipation varies significantly amongst satellite designs. However, rotational power loss  $\dot{K}$  is commonly related to hysteretic damping, for instance in flexible elements such as antennae booms being periodically bent by the action of the gravity-gradient field or in propellant slosh. The interaction of the Earth's magnetic field with metallic structural elements, i.e. eddy-current damping, is apparently

a highly relevant factor in rotational energy dissipation in CubeSats [263, 264]. As a dimensioning example on this point, consider that for an aluminium–7075<sup>5</sup> outer shell in a 3U CubeSat immersed in a fluctuating magnetic field with flux density of 30 µT, the magnitude of eddy-current power loss is around 27 orders of magnitude lower than the input rotational power due to 1 µN thrust.

$$\frac{d\omega_t^2}{dt} = 2 \frac{I_z}{I_t} \frac{\dot{K}}{I_z - I_t} \quad (6.40)$$

Eq. (6.40) [152, pp. 489] describes the temporal evolution of  $\omega_t$  due to energy dissipation in a prolate spinner. Although the sensitivity in  $\omega_t$  due to energy dissipation is higher as  $I_t \rightarrow I_z$ , as shown in the plot of Eq. (6.40) in Fig. 6.4, it is safe to neglect its effects during the time span for the proposed thrust characterisation method without any loss of generality. Nonetheless, the proposed method may not be applicable to CubeSats with abnormal sources of attitude uncertainty like passive magnetic attitude control systems.

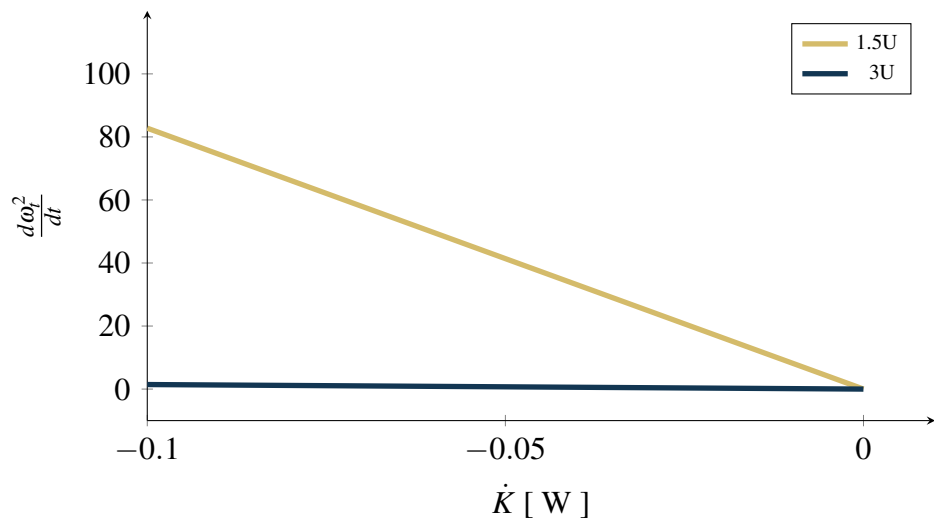


Fig. 6.4 Effect of dissipative processes over the transversal angular velocities evolution in standard CubeSats. Values different from zero in  $d\omega_t^2/dt$  amount to instability in a prolate spinner. The value of  $\dot{K}$  is negative in power loss. 3U CubeSats are less prone to  $\omega_t$  variation due to rotational power loss.

<sup>5</sup>Material in compliance with the CubeSat Design Specification [86], CubeSat configuration assumed in this investigation,  $\omega_z = 10^\circ/\text{s}$ , magnetic field acting parallel to the transversal plane and magnitude equivalent to the average at 100 km Earth altitude, and formulae from Barranger [265].

## 6.2 Application Example

In order to estimate the desired thrust value, from the quotient of  $M_z$  and the moment arm, it is necessary to solve Eq. (6.30) for  $M_z$ . Eq. (6.41) describes the temporal evolution of  $M_z$  as a function of the spinning forced frequency  $w$  and the initial angular velocity  $\omega_{z0}$  during the manoeuvre.

$$M_z = \frac{I_t I_z}{(I_t - I_z)t} w - \frac{I_z \omega_{z0}}{t} \quad (6.41)$$

Typically spin-despin manoeuvres are used to estimate thrust levels through  $M_z$  by assessing the imposed angular acceleration in one axis, e.g. assuming  $I_x \approx I_y$  then simply  $M_z = I_z \dot{\omega}_z$ . On the other hand, estimations using Eq. (6.41) are dependent upon  $\omega_z$  and  $w$ . By considering actual electronic angular rate sensors, both methods are affected by inherent signal noise and satisfactory definition of the magnitude of  $\omega$ . Moreover, thrust estimations from noisy signals using Eq. (6.41) can be poorer than those from the typical method (from  $\dot{\omega}_z$ ) due to the additional dependence on  $w$ . The convenience of using Eq. (6.41) is evident when the analysis is centred in the pre/post manoeuvre transversal angular velocity responses, because transversal spinning axisymmetric natural frequencies can be determined with greater efficacy than magnitudes in signals difficult to resolve. In order to eliminate the dependency of Eq. (6.41) on  $\omega_{z0}$ , we can use Eq. (6.30) to obtain the difference of the pre/post transversal natural frequencies  $\Delta w$  yielding the alternative solution in Eq. (6.42). In this way, the proposed method provides a better approach using standard attitude sensor resources in CubeSats for the characterisation of weak thrust levels otherwise strongly linked to sensor noise.

$$M_z = \frac{I_t I_z}{I_t - I_z} \frac{\Delta w}{t} \quad (6.42)$$

Simulated digital MEMS Gyro signals in three-axis are used in the following example. Basically, the sensor model comprises a second order transfer function with band-limited white noise wherein the noise power is defined by the Rate Noise Density reported

in Table 6.1. The simulation parameters aim to describe a distinctive low Earth orbit insertion opportunity for the typical CubeSat mission. The propagations use perturbation forces from gravitation, third-body, solar radiation pressure, atmospheric drag, and gravity gradient, acting on 3D models of the 1.5U and 3U CubeSats. Additionally, the cartesian coordinate axes coincide with the mutually orthogonal principal axes of rotation (principal moments of inertia), as assumed along this investigation. In actual circumstances the proposed method for in-orbit thrust characterisation might encompass two manoeuvres. A preliminary manoeuvre would bring the periodic transversal component of the angular velocity vector into the range of the sensing capabilities of the on-board attitude determination system resources in order to determine the axisymmetric natural frequency during a first coast period. As the level of thrust required for this first manoeuvre depends on specific mission conditions and constraints, such as signal noise level and initial body angular rates, this investigation focuses only on the second manoeuvre aimed to characterise the thrust level. However, typical after deployment tumbling rates in CubeSats may range over a few degrees per second providing an adequate baseline natural frequency during the initial coasting period to dispense with a first manoeuvre. In this example the arbitrary but representative [266, 267] after deployment values of  $\omega_{x0} = 1.1^\circ/\text{s}$ ,  $\omega_{y0} = 1.3^\circ/\text{s}$ , and  $\omega_{z0} = 1.6^\circ/\text{s}$  are used. These initial rate values in conjunction with sensor capabilities used in this example, allow to dispense with the first manoeuvre.

Fig. 6.5 and Fig. 6.6 present the sequence of key events during the proposed thrust characterisation. Of interest for the proposed method are the plots of  $\omega_x$  and  $\omega_y$  describing the sweep-out cone in transversal components. Note from the analytical solutions derived in subsection 6.1.1 that these two functions share the angular frequency value, this implies redundancy in the data source employed to determine the first and second coast natural frequencies required in  $\Delta w$ , which in turn enables the use of Eq. (6.42). The existing redundancy represents an advantage of the proposed method that becomes relevant in a real scenario wherein angular rate readings for each axis may differ in quality even from the same source rate sensor. Similarly to the discussion about

## Spiral Coning Manoeuvre for In-Orbit Low Thrust Characterisation in Nanosatellites

---

Table 6.1 Main simulation parameters

Variable	Value	Remarks
<b>Keplerian orbital elements*</b>		
Geometric altitude	400	km
Eccentricity	0.0014	—
Inclination	51	°
Longitude of the ascending node	0	°
Argument of periapsis	0	°
True anomaly	270	°
<b>CubeSats</b>		
Mass per U CubeSat	1.3	kg
$I_t$	$0.0056 - 0.0372^\dagger$	$\text{kg m}^2$
$I_z$	$0.0039 - 0.0079^\dagger$	$\text{kg m}^2$
$\omega_{x_0}$	1.1	°/s
$\omega_{y_0}$	1.3	°/s
$\omega_{z_0}$	1.6	°/s
Total Thruster Area	95	$\text{cm}^2$
<b>Digital gyroscope readings<sup>‡</sup></b>		
Sensitivity	73.26	$\text{mdps/digit}$
Rate Noise Density	200 $^\S$	$\text{mdps}/\sqrt{\text{Hz}}$
<b>Miscellaneous</b>		
Date and time for the simulation	2014/03/20 12 : 00 : 00	Near to vernal equinox
Gravity model	GGM05G	10 <sup>th</sup> Degree and order
Thermospheric density model	JB2008	—
Solar irradiance data	SORCE	—
Moment arm	0.02375	m

\* Alluding an ISS CubeSat deployment

$^\dagger$  For the 1.5U and 3U CubeSat respectively

$^\ddagger$  Compensated for gyroscopic bias drift

$^\S$  Four times higher than the typical value [268, 269]

the first manoeuvre, the span of the coasting periods under analysis are greatly dependent on specific mission constraints. For example, test energy consumption or eclipse conditions may be delimiting factors of the allowed interval. Nevertheless, relatively short intervals would be sufficient for resolving well-defined natural frequencies in CubeSats as observed in Fig. 6.6.

Six different values of thrust have been used for the characterisation test simulation (second manoeuvre), namely 0.05  $\mu\text{N}$ , 0.1  $\mu\text{N}$ , 0.5  $\mu\text{N}$ , 1  $\mu\text{N}$ , 5  $\mu\text{N}$ , and 10  $\mu\text{N}$ . These values correspond to the thrust delivered by each of the patch elements acting during the characterisation manoeuvre, specifically 1 and 4 in Fig. 6.1, adding spin about the  $z$  body axis. A standard thrust characterisation based on  $\omega_z$  has been used as

figure of merit in the following descriptions. In all instances, the raw data has been conditioned using a Savitzky-Golay digital filter<sup>6</sup>. Note from Fig. 6.6 that the standard and proposed characterisation methods differ solely in the source component of  $\vec{\omega}$  used in the computations. In the standard characterisation, the thrust magnitude is estimated directly from the temporal rate of change of  $\omega_z$ , namely angular acceleration  $\alpha$ , during the thrust campaign as illustrated in Fig. 6.6. In order to compute  $\alpha$ , a regression line has been fitted in the least-squares sense to the  $\omega_z$  values using the Vandermonde matrix<sup>7</sup>. On the other hand,  $\omega_y$  is picked to obtain  $\Delta w$  from the coasting periods 1 and 2. To this end, a Fast Fourier Transform has been used to identify the signal frequency of maximum energy that is subsequently used as initial guess in a fitting procedure aiming the refinement of the estimation. Finally, the provided spectrogram of  $w$  in Fig. 6.6 illustrates the frequency evolution of  $\omega_y$ . Despite the apparent similarity between the plot of  $\omega_z$  and the spectrogram of  $w$ , it is convenient to bear in mind that the first describes a magnitude whilst the latter describes the sweep-out frequency of the body cone. A Matlab script summarising the analysis procedure is presented in Appendix H and sample test data is available upon request.

Fig. 6.7 and Fig. 6.8 present the simulation results for a 1.5U and 3U CubeSat respectively. The statistical analysis comprises 20 samples for each of the 6 thrust levels for a total of 120 simulation samples for each CubeSat. The error percentage has been computed with respect to the nominal thrust value. Amplitude changes are highly susceptible to noise effects mostly when these approximate. In that case, thrust estimations from  $\alpha$  are better represented from instantaneous changes during the manoeuvre instead that from pre and post manoeuvre data. Conversely, the intrinsic ease of identifying frequency changes rather than amplitude ones in rate noisy signals, confers the proposed method with the ability to utilise bigger portions of data. In

---

<sup>6</sup>Savitzky-Golay FIR smoothing filter with polynomial order 1 and frame length ( $sl$ ) of 1001 samples. Smoothed values within the frame length are given by  $\hat{\boldsymbol{\omega}} = \mathbf{B}\boldsymbol{\omega}$ , with the smoothing filter matrix  $\mathbf{B} = \mathbf{S}(\mathbf{S}^T\mathbf{S})^{-1}\mathbf{S}^T$  where  $\mathbf{S}_{i,j} = \mathbf{Z}_i^{j-1}$  such that  $(1-sl)/2 \leq \mathbf{Z} \leq (sl-1)/2$  and  $sl$  is an odd number [270, pp. 427].

<sup>7</sup>If  $\boldsymbol{\omega}_z$  and  $\mathbf{t}$  are the analysed rate and time data vectors for respectively, then  $\alpha = \mathbf{y}_{2,1} = [(\mathbf{V}^T\mathbf{V}^{-1})\mathbf{V}^T]\boldsymbol{\omega}_z^T$  where  $\mathbf{V}$  is the Vandermonde matrix given in this case by  $\mathbf{V}_{i,j} = \mathbf{t}_i^{j-1}$  [271, pp. 116].

## Spiral Coning Manoeuvre for In-Orbit Low Thrust Characterisation in Nanosatellites

---

Fig. 6.5 Example of body angular velocities response to thrust action. Interactive image in Acrobat Reader, Foxit Reader, or PDF-XChange.

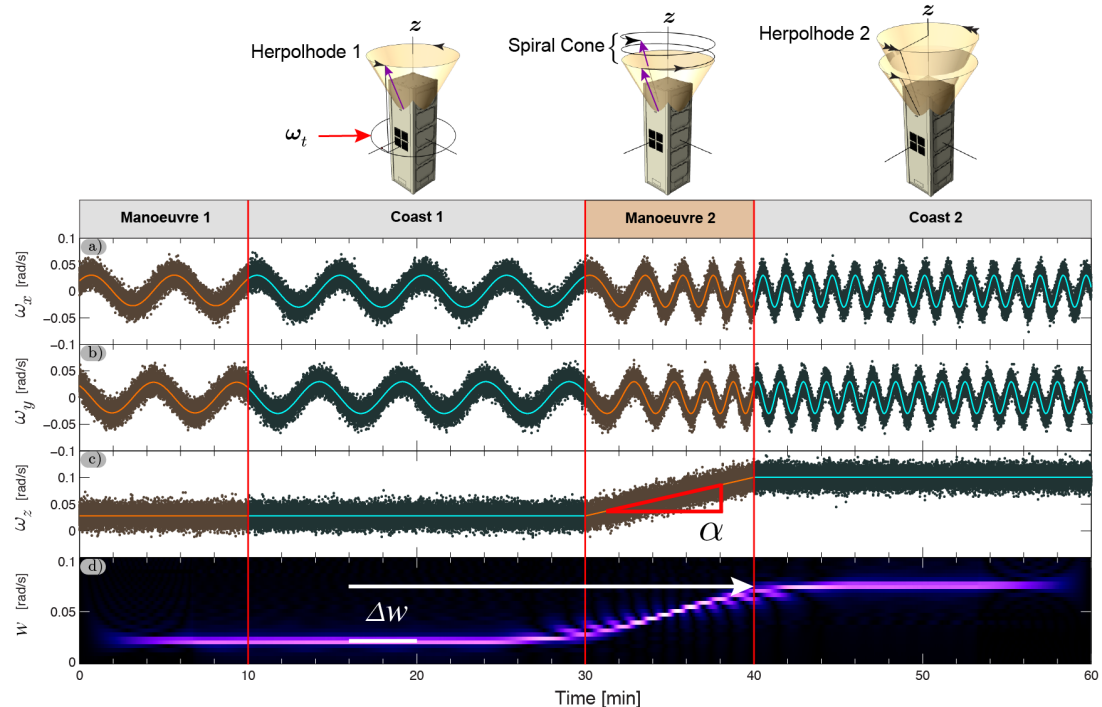


Fig. 6.6 Example of body angular velocities response. Plots a), b), and c) show noisy angular velocity signal outputs from the emulated digital gyro. Plot d) presents the Wigner-Ville spectrogram of  $\omega_y$  evidencing a linear up-chirp signal along the manoeuvring time. Signal spectrum analysis is used in the example to identify component frequencies in the data.

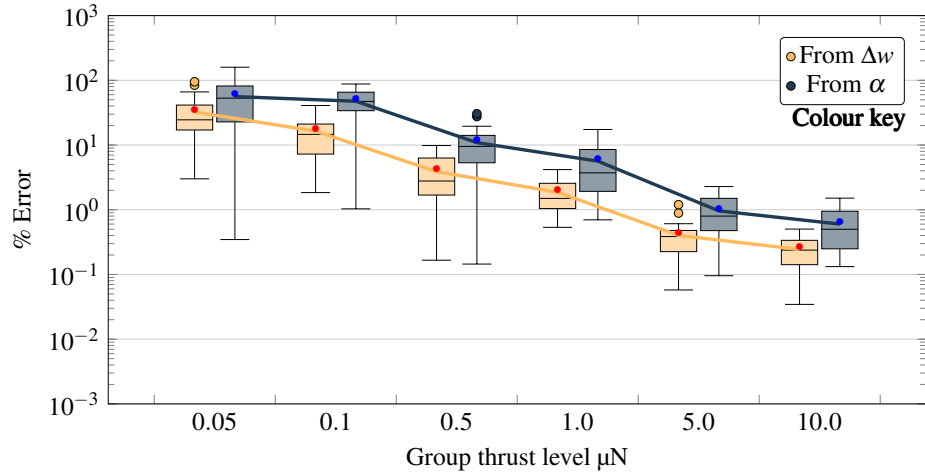


Fig. 6.7 Log box-and-whisker plot of the error percentage with respect to the actual thrust level. Using estimations from the angular acceleration in  $z$  body axis,  $\alpha$ , and from the difference in pre/post manoeuvre transversal natural frequencies,  $\Delta w$ , in a 1.5U CubeSat. Each box plot pair constitute a thrust test instance.

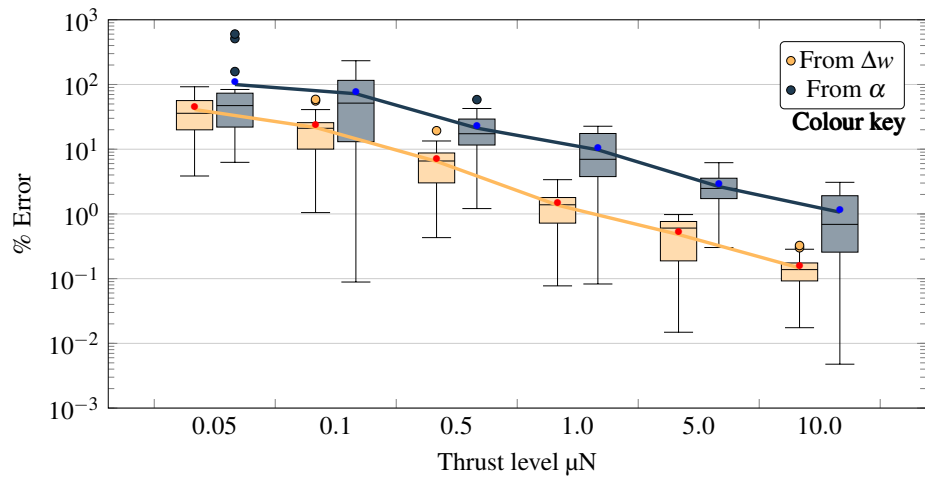


Fig. 6.8 Log box-and-whisker plot of the error percentage with respect to the actual thrust level. Using estimations from the angular acceleration in  $z$  body axis,  $\alpha$ , and from the difference in pre/post manoeuvre transversal natural frequencies,  $\Delta w$ , in a 3U CubeSat. Each box plot pair constitute a thrust test instance.

this way, the observed consistent improved relative performance is clearly foreseen, considering that estimations from  $\Delta w$  encompass four times the time span than those from  $\alpha$  as shown in Fig. 6.6. This important feature of the proposed method enables enhanced thrust estimations.

As a final remark in this section on the applicability of the proposed method, note from subplots *a*) or *b*) in Fig. 6.6 that the angular sweep-out frequency has necessarily an upper limit before the appearance of frequency ambiguity in noisy signals. That limit is clearly defined by the quality of the signal under analysis, e.g. sensor properties.

## 6.3 Chapter Conclusions and Further Work

The investigation presented in this chapter set out to evaluate an alternative method to enhance in-orbit micro thrust characterisation using standard attitude determination elements in nanosatellites.

Simulation results presented in this investigation show that it is possible to improve estimations of low thrust levels from weak and noisy sensor signals by evaluating the angular frequency of the transversal component of the angular velocity vector in rigid axisymmetric bodies as intermediate axis spinners, over estimations from angular acceleration. In addition, the proposed method adds versatility to the thrust analysis process by allowing selectable angular velocity transversal component.

Further work should focus on establishing the practical full range of the spiral coning manoeuvre effectiveness due to real sensor limitations and sensor operational condition fluctuations. In addition, the presented study focuses on the analysis of a generic case wherein one angular velocity component is used. However, in a real application the attitude determination system commonly processes multiple noisy sensor measurements to establish improved joint probability distributions. Although this may imply enhanced performance of the proposed method, which also needs verification, a similar filtering approach could be used to profit from both angular velocity transversal components enabled by the proposed spiral coning manoeuvre method.

# **Chapter 7**

## **Conclusions**

Nanosatellite systems technological progress is based on accessibility, innovation, and versatility. These ingredients and the prospective access to space, have motivated the development of a significant number of mission concepts. The most ambitious and versatile mission concepts integrate propellant-based propulsion technologies to facilitate orbit and attitude fine control. Current propulsion options for nanosatellites include commercial and bespoke systems. However, most commercial devices wait for space operation verification, whilst bespoke systems are usually projected for specific short-term technology demonstration experiments. Nanosatellites' propulsion systems rudimentary stage of development is chiefly explained by scale incompatibility of most heritage technologies. Some conventional propulsion technologies are scalable to some extent, for example cold gas propulsion, albeit inconveniently voluminous for general application. Other propulsion technologies show higher miniaturisation suitability for nanosatellite application such as pulsed plasma thruster and colloid thruster electric propulsion systems. Yet, characteristic thrust levels are rather low in these electric propulsion concepts, limited to few tens of micro Newton, which are difficult to measure with standard nanosatellite onboard sensors. Numerous deficiencies and underdeveloped components add to the complexity of propulsion systems operation in nanosatellites. For example poor electronics radiation shielding is one of the technical reasons limiting most nanosatellite operations to low LEO orbits wherein space environment pertur-

## **Conclusions**

---

bations can easily overwhelm electric propulsion actuation. Moreover, nanosatellites are inherently vulnerable to space environment due to their physical characteristics. That is, surface-area-to-volume ratio is higher in nanosatellites than in major satellites, drawing particular attention to surface interaction phenomena. The understanding of such surface interactions in nanosatellites is in turn, key to the optimisation of onboard propulsion system resources for aspired long-term mission objectives.

As a propulsion system viability and limitations are reified by specific nanosatellite mission requirements and assets, the research effort presented in this thesis is directed towards general overlapping urgencies for the favourable development and operation of such systems. The following section appraises research findings and discusses their relevance for the thesis hypotheses.

### **7.1 Conclusions of the Developed Methodologies**

This thesis addresses concerns of general interest for the designer of a nanosatellite mission equipped with propulsion system. The thesis topics are classified in three main subjects covering: the preponderant role of solar activity in establishing space weather conditions, and the characteristic atmospheric interaction with nanosatellites for propulsion systems design and optimisation; and an innovative method for effective low thrust characterisation from noisy signals or low resolution sensing resources. Solar activity investigation focuses on the development of a robust forecast method to assist tight propulsion system sizing and onboard resources optimisation. In addition solar activity forecast establishes other systems margins related to spacecraft survivability. The investigation of atmospheric interaction with nanosatellites targets the identification of the scarcely known drag coefficient, which critically encompasses the atmospheric interaction with exposed surfaces. Lastly, the low thrust characterisation method is devised to overcome typical attitude determination limitations found in nanosatellites. These limitations may include low quality or low resolution signals as sensors are

generally taken from standard commercial off-the-shelf technologies rather than from suited specialised sensors.

**The solar activity forecast** investigation in Chapter 4, hypothesised that solar activity forecast reliability can be improved by assembling historical sparse accumulated knowledge about solar attributes because it allows the refinement of current solar physics models. In order to test this hypothesis, a solar dynamo computational model was developed prioritising the use of updated observational data and complemented with adequate solar parameter analytic models. The resulting solar dynamo model was verified through its ability to reproduce historical solar activity, by employing meaningful solar polar magnetic field precursor information. In this regard, current solar activity reproduction using solar dynamo models with polar precursor, is limited to few solar cycles, i.e. solar polar data available after 1976. In order to extend the verification of the solar dynamo model throughout a broader number of solar activity scenarios, the missing solar polar magnetic field was reconstructed from the year 1880. Solar polar magnetic field reconstruction was possible after the judicious selection of an adequate solar proxy in conjunction to artificial neural network technology.

Reconstructed polar magnetic fields enabled extended verification of the solar dynamo model for thirteen solar cycles, rather than for just the recorded four cycles. The model showed consistent solar cycles reproduction and activity trends in agreement to most observed solar activity in the form of sunspot number. In addition, the extended model verification permitted the identification of a correction factor to improve solar dynamo prediction. Corrected solar dynamo predictions showed remarkable agreement to maximum solar activity in the SSN record. Further, possible anomalous historical adaptation in proxy observational data is identified in early solar cycle reports. The satisfactory performance of the solar dynamo model permitted the forecast of most likely solar activity during the next 25<sup>th</sup> solar cycle. According to the results of this investigation, a weaker solar cycle 25 – 14.4% ( $\pm 19.5\%$ ) is expected in comparison to the current cycle 24. This represents a peak value of  $99.6 \pm 22.7$  sunspots using the

## **Conclusions**

---

SILSO [151] 13-month smoothed monthly SSN maximum for the solar cycle 24 as reference.

This investigation distinguishes itself from other related research in its characteristic set of solar dynamo parameterisations employed for simulation. The main distinction between this investigation and other approaches is the incorporation of the observed differential rotation profile, yielding to a series of necessary adjustments to complementary analytic models within the solar dynamo model. Additionally, a method to include solar polar hemispheric asymmetries into the solar dynamo model has been developed. A unique feature of this investigation with respect to other related research is the incorporation of a simulated solar activity correction factor plausibly relating the effect of the toroidal field. The main contribution of this investigation is considered to be the reconstruction of polar solar magnetic field strengths, for the year interval 1880 – 1976. The reconstructed polar fields render extended solar cycle simulation with the solar dynamo model based on polar field precursor information possible. Importantly, the availability of varied solar simulation conditions permit extended dynamo model performance verification that in turn improves the value of solar activity predictions. Lastly, these elements coalesce into a solar forecast method based on and supported by observational data and solar physics contributing to the current body of knowledge towards improved nanosatellite mission planification.

**The atmospheric interaction with nanosatellites from observed orbital decay** investigation in Chapter 5, hypothesised that observed orbital decay assessment in standard nanosatellites furnish valuable information about distinctive drag-entailing phenomena because atmospheric interaction is led by geometric and material features intrinsic to nanosatellites. The assessment of this hypothesis was realised with the comparison of observed and simulated orbit decay. The premise in this investigation is that if the means to quantify the drag force contribution amongst other perturbation forces exists, then it opens the possibility to break it down into its constituents. In this way, the quality of the assessment is relative to the capability of precisely quantifying those

constituents. Readily available orbit information in the form of TLE sets, is the only existing long-term record to evaluate orbital evolution. Therefore, orbit perturbation contributions are inferred via the evaluation of observed orbital decay.

In principle, the estimation of characteristic drag coefficients is achievable by fitting modelled orbit decay predictions to observed data wherein all other main perturbation forces can be precisely quantified. This investigation reports fitted drag coefficients and related energy accommodation values along the orbital evolution of the selected three-unit CubeSats BEVO 2, ExoCube, GEARRS 1, GeneSat-1, PharmaSat 1, RAX-2, SMDC-ONE, SporeSat 1, S-CUBE, and TurkSat-3USat. These nanosatellites were selected because their geometries are characteristic of the CubeSat standard. In other words, the effect of antennae and other external components do not vary significantly from the general CubeSat standard in these selected missions. Additionally, the 3U size factor is historically related to propulsion system demonstration missions and is forecasted the preferred nanosatellite size in the near-future. Selected CubeSat missions describe near-circular LEO orbits at different values of inclination and encompassing orbital altitudes below 630km. The selected CubeSats represent typical orbital insertion opportunities, geometric configurations, form factors, and attitude control schemes. In relation to this last feature, this investigation encompasses Passive Magnetic Attitude Control, gravity-gradient stabilisation, and random tumbling according to each reported mission profile. The attitude control scheme plays a fundamental role in the way atmospheric particles and incoming solar radiation interact with the nanosatellites' exposed surfaces. In this way a specific controlled attitude scheme defines characteristic reference areas for that scheme, in addition to the inherent reduced uncertainty. In a trade-off between onboard resources and performance, the robust and simple PMAC is a common attitude control solution for nanosatellites wherein an on-board permanent dipole interacting with the local Earth magnetic field supplies a restoring alignment torque and a magnetic soft material provides energy dissipation. Assuming that magnetic-locking occurs, it is possible to ease the determination of predictable dynamic cross-sectional areas for any reference vector as attitude is essen-

## Conclusions

---

tially a function of the known local Earth magnetic field at the satellite's position. In a similar way,  $\nabla G$  stabilisation enables the estimation of predictable reference areas with plausible reduced margins of uncertainty. Throughout this investigation, the use of dynamic cross-sectional areas is deemed relevant in maintaining uncertainties at the level of the TLE sets, i.e. restricting the addition of stochastic variables, which in turn improve the identification and quantification of perturbations. Investigation results show coherent fitted drag coefficient evolution according to the respective space environment conditions. Furthermore, the results were compared to those of an external investigation using static cross-sectional areas. In contrast to the external investigation, the approach presented herein provided more consistent results although it was not possible to individuate the source of improvement due to lack of detailed external data for a deeper assessment. The overall results were merged into a drag coefficient analytic expression representative of the 3U CubeSat standard, as function of total atmospheric density for accessible utilisation. The performance of the characteristic drag coefficient function was evaluated through its capability to reproduce observed orbit decay of the selected nanosatellite missions. Orbit propagations using possible combinations of drag coefficient, i.e. constant and variable, and cross-sectional areas, i.e. static and dynamic, were carried out in each instance. Results indicate the suitability of the proposed dynamic cross-sectional areas and drag coefficient function approaches over other combinations during moderate-to-high solar activity in LEO orbits below 350km. With respect to the representativeness of the drag coefficient function, results suggest that the function satisfactorily captures the 3U CubeSat drag coefficient variation for total atmospheric density values above  $1 \times 10^{-11} \text{ kg m}^{-3}$ .

In contribution to the current body of knowledge, the variable-fitting approach proposed for the assessment of atmospheric interaction evolution from observed orbital decay, shows suitability for the application on the standard nanosatellite. Results reported in this investigation employing the proposed methodology, point out the identification of characteristic fitted drag coefficients of the selected nanosatellites. Furthermore, the statistical consolidation of fitted drag coefficients permitted the iden-

tification of a simplified standard 3U CubeSat drag coefficient profile for a range of altitudes of interest. These specific and consolidated drag coefficient profiles derived from observational data are essential in nanosatellite LEO mission design for onboard propulsive resources optimisation.

**The spiral coning manoeuvre for in-orbit low thrust characterisation in nanosatellites** investigation in Chapter 6, hypothesised that low thrust levels are effectively characterised using COTS sensors through the analysis of induced low frequency responses since long term changes are more easily identifiable by non-specialised low resolution sensors. The assessment of this hypothesis was done via precise attitude and orbit propagations of 3D nanosatellite models. In compliance to the thesis general approach of standard far-reaching solutions, typical nanosatellite geometries as well as thruster configuration are employed; and the method is based on the common practice of performing in-orbit thruster characterisation via attitude changes. According to historic and estimated trends of propulsion systems in nanosatellites, 1.5U and 3U standard CubeSat geometries are considered. A four-element thruster setup configuration is used in the simulations due to the versatile and convenient possible spectrum of manoeuvres. Under these assumptions, the method aims to exploit the characteristic axisymmetric geometry and mass distribution of CubeSats, and the effect of appendages over the attitude evolution during the thrust characterisation is considered negligible. The low thrust characterisation method consists of low thrust operations acting on an intermediate axis spinner, yielding distinctive body cone sweep-out frequency variations. Observed sweep-out frequency response of the intermediate axis spinner is then analysed with a reference analytic model to obtain an estimation of thrust magnitude.

Preliminary simulations were used to assess the impact of the simplifications used in the derivation of the analytic solution on the estimation of thrust. For example, in practice nanosatellite mass variations are expected due to propellant consumption, therefore the induced error due to temporal mass variation was analysed. Results show that the induced error due to neglecting temporal mass variations is lower than ten

## Conclusions

---

thousandths percent, in a propulsion system with specific impulse of 1000 s. Body rotation variation due to energy dissipation is another source of diversion from the analytic solution. The interaction of the Earth's magnetic field with metallic structural elements, i.e. eddy-current damping, is a major factor in rotational energy dissipation in nanosatellites. Simulations showed that this energy dissipation phenomenon is negligible during the proposed thrust actuation timespans. However, greater vulnerability of small size factors is evinced. Thrust characterisation simulations required the emulation of digital MEMS Gyro signals in three-axis. To this aim a second order transfer function with band-limited white noise equivalent to that observed in commercial components was employed. Six different values of thrust were used for the characterisation test simulation, namely  $0.05\text{ }\mu\text{N}$ ,  $0.1\text{ }\mu\text{N}$ ,  $0.5\text{ }\mu\text{N}$ ,  $1\text{ }\mu\text{N}$ ,  $5\text{ }\mu\text{N}$ , and  $10\text{ }\mu\text{N}$ . These values typify a range difficult to characterise with standard attitude determination systems in CubeSats. The performance of the proposed method was compared to the customary method of thrust inference via body angular acceleration. Simulation results show that body cone sweep-out frequency variation is a better indicator of low thrust actuation than body angular acceleration, in both 1.5U and 3U CubeSat form factors. The proposed method permits analysis versatility by facilitating the assessment of interchangeable data source as the body cone sweep-out frequency can be obtained from two body axes. Additionally, the proposed methodology can be applied to general nearly symmetric geometries wherein appendages do not represent an important source of short-term attitude changes.

This investigation contributes to the current body of knowledge of in-orbit thrust characterisation in rigid axisymmetric nanosatellites by providing a simple and accessible method particularly valuable to missions with challenging thrust level determination.

## 7.2 Concluding Remarks

The main characteristic of this thesis is that it represents a comprehensive examination of topics of general interest for nanosatellite propulsion systems design and operation.

The contribution of this thesis has been to provide fundamental tools to tackle important gaps in the current general development of nanosatellites. Each one of the presented investigations was judiciously designed in terms of findings significance and applicability to propulsion systems design and operation. In addition, the broad scope of the investigations opens up the possibility to customise the methodologies herein presented to specific requirements as intended.

The envisaged prosperous future of flourishing miniaturised satellite concepts rely on exceptionally efficient propulsion management. It is hoped that the accessible tools developed for this thesis in combined or independent usage, contribute to the practical advancement of propulsion technologies for nanosatellite systems.

Blank page

# References

- [1] Tony Azzarelli. International regulations for nano/pico satellites. In *ITU Seminar*, pages 2–2, 2014.
- [2] Bill Doncaster, Caleb Williams, and Jordan Shulman. 2017 nano/microsatellite market assessment. Technical report, Space Works Inc., 2017.
- [3] Gottapu Sasibhushana Rao. *Global Navigation Satellite Systems: With Essentials of Satellite Communications*. Tata McGraw Hill, 2010.
- [4] David Homan. The challenges of developing an operational nanosatellite. In *22nd Annual AIAA/USU Conference on Small Satellites*, 2009.
- [5] Harry Culver. Nano-satellite avionics. Technical Report 19990079773, NASA Goddard Space Flight Center, 1999.
- [6] Rainer Sandau, Hans Peter Roser, and Arnoldo Valenzuela, editors. *Small Satellite Missions for Earth Observation*. Springer, 2010.
- [7] Mark Hans. *Encyclopedia of Space Science and Technology*, volume 1. Wiley-Interscience, 2003.
- [8] MS Rhee, CM Zakrzewski, and MA Thomas. Highlights of nanosatellite propulsion development program at nasa-goddard space flight center. Technical Report 20000091529, NASA, 2000.
- [9] D DePasquale and A Charania. Nano/microsatellite launch demand assessment 2011. *SpaceWorks Commercial, November*, 2011.
- [10] Morehead State University. Robert j. twiggs, 2017. URL <https://www.moreheadstate.edu/College-of-Science/Earth-and-Space-Sciences/Faculty-Staff/Robert-J-Twiggs>.
- [11] Purdue University. Jordi puig-suari, 2017. URL <https://engineering.purdue.edu/AAE/people/alumni/distinguished/oaе/2017/Jordi-Puig-Suari>.
- [12] NANORACKS. Nanoracks the operating system of space, 2017. URL <http://nanoracks.com/products/smallsat-deployment/>.
- [13] Virgin Orbit. Virgin orbit: Launcherone, 2017. URL <https://virginorbit.com>.
- [14] RCI. Intrepid-1, 2017. URL <http://rocketcrafters.space/>.
- [15] Jeroen Rotteveel, Abe Bonnema, and Julien Hennequin. Nano-profitability a review of the financial success of nanosatellite industrial companies. *Small Satellite Conference*, 1(7), 2014.

## References

---

- [16] Marcel J Sidi. *Spacecraft dynamics and control: a practical engineering approach*, volume 7. Cambridge university press, 1997.
- [17] David Hinkley. A novel cold gas propulsion system for nanosatellites and picosatellites. *22nd Annual AIAA/USU Conference on Small Satellites*, 2008.
- [18] Cardin J.M. A cold gas micro-propulsion system for CubeSats. In *17th Annual AIAA/USU Conference on Small Satellites*, 2003.
- [19] Stephen Mauthe, Freddy Pranajaya, and Robert Zee. The design and test of a compact propulsion system for CanX nanosatellite formation flying. *Small Satellite Conference*, 2005.
- [20] Steve Overton, May Allen, Bob Massee, Ron Spores, and Liz Driscoll. CubeSat mission benefits and integration of high thrust, high  $\Delta V$  green propulsion. In *13<sup>th</sup> Annual CubeSat Developer's Workshop*. Aerojet Rocketdyne, 2016.
- [21] George P Sutton and Oscar Biblarz. *Rocket propulsion elements*. John Wiley & Sons, 2016.
- [22] V Lappas, S Pottinger, A Knoll, P Shaw, D Lamprou, T Harle, B Melly, and M Perren. Micro-electric propulsion (EP) solutions for small satellite missions. In *Space Technology (ICST), 2011 2nd International Conference on*, pages 1–4. IEEE, 2011.
- [23] Aerojet Rocketdyne. CubeSat modular propulsion systems, 2017. URL <http://www.rocket.com/cubesat>.
- [24] GomSpace. Product categories, 2017. URL <http://gomspace.com/>.
- [25] Nano-Avionics. Small satellite and CubeSat propulsion systems, 2017. URL <http://n-avionics.com/propulsion-systems/>.
- [26] VACCO. CubeSat propulsion systems, 2017. URL <http://www.cubesat-propulsion.com/vacco-systems/>.
- [27] BUSEK Space Propulsion Systems. Propulsion for CubeSats and nanosats, 2017. URL [http://www.busek.com/cubesatprop\\_main.htm](http://www.busek.com/cubesatprop_main.htm).
- [28] ClydeSpace. Products, 2017. URL <https://www.clyde.space/products/>.
- [29] CUAerospace. Propulsion unit for CubeSats, 2017. URL <http://www.cuaerospace.com/Products/SmallSatellitePropulsion.aspx>.
- [30] Microspace Srl. The power of microspace, 2017. URL <http://www.micro-space.org/power.html>.
- [31] Shaun Kenyon and Christopher Bridges. STRAND-1: Use of a \$500 smartphone as the central avionics of a nanosatellite. In *62nd International Astronautical Congress*, volume IAC-11-B4.6B.8, 2011.
- [32] CP Bridges, S Kenyon, P Shaw, E Simons, L Visagie, T Theodorou, B Yeomans, J Parsons, V Lappas, C Underwood, et al. A baptism of fire: The strand-1 nanosatellite. *27th Annual AIAA/USU Conference on Small Satellites*, 2013.

- [33] David Krejci, Fernando Mier-Hicks, Corey Fucetola, Paulo Lozano, Andrea Hsu Schouten, and Francois Martel. Design and characterization of a scalable ion electrospray propulsion system. *IEPC*, 1(149), 2015.
- [34] Douglas Spence, Nathaniel Demmons, and Thomas Roy. A compact low-power high-Isp thruster for microsatellites. *22nd Annual AIAA/USU Conference on Small Satellites*, 2008.
- [35] ENPULSION. Enabling CubeSats: IFM 350 nano, 2017. URL <https://enpulsion.com/cubesatpropulsion/>.
- [36] Mars-Space. PPTCUP: Pulsed plasma thruster for CubeSat propulsion, 2017. URL <http://www.mars-space.co.uk/projects/pptcup>.
- [37] Andrew J Jamison, Andrew D Ketsdever, and EP Muntz. Accurate measurement of nano-newton thrust for micropropulsion system characterization. In *27th International Electric Propulsion Conference, Pasadena, California, USA, IEPC-01-236*, 2001.
- [38] M Pollard and D Lamprou. The design, development, manufacture and test of an electric propulsion system for small spacecraft. In *Proceedings of the Space Propulsion Conference*, 2012.
- [39] Christopher Dinelli, Haque Samudra, Hang Jin, Michael Keidar, and Kristen Castonguay. Ballistic reinforced communication satellite (BRICSat-P): The first flight of an electric micropropulsion system for CubeSat mission applications. In *The Interplanetary CubeSat Workshop*, volume 2014.B.2.4. iCubeSat, 2014.
- [40] Siegfried W Janson and Richard P Welle. The NASA optical communication and sensor demonstration program: An update. Technical Report SSC14-VI-1, The Aerospace Corporation, August 2014.
- [41] Richard P Welle. The aerospace nano/picosatellite program. Technical report, The Aerospace Corporation, July 2014.
- [42] CubeSatShop, 2017. URL <http://www.cubesatshop.com/>.
- [43] Christoph Steiger, Andrea Da Costa, Pier P Emanuelli, Rune Floberghagen, and Michael Fehringer. Evolution of flight operations for ESA's gravity mission GOCE. In *SpaceOps 2012*, page 1262715, 2012.
- [44] Massimo Romanazzo, Christoph Steiger, Gianfranco Sechi, Massimiliano Saponara, Mehrdad Rezazad, A Piris Niño, A Da Costa, M Fehringer, R Floberghagen, G André, et al. In-orbit Experience with the Drag-Free Attitude and Orbit Control system of ESA's Gravity Mission GOCE. In *8th International ESA Conference on Guidance, Navigation & Control Systems, Karlovy Vary, Czech Republic*, 2011.
- [45] FM Pranajaya and Robert E Zee. Generic nanosatellite bus for responsive mission. In *5th Responsive Space Conference*. Citeseer, 2007.
- [46] Gunter Krebs. Orbital launches of 2017, 2017. URL <http://space.skyrocket.de>.
- [47] eoPortal Directory. Satellite missions database, 2017. URL <https://directory.eoportal.org>.

## References

---

- [48] Erik Kulu. Nanosatellite database, 2017. URL <http://www.nanosats.eu/>.
- [49] Malcolm Macdonald. *Advances in solar sailing*. Springer Science & Business Media, 2014.
- [50] Jiri Blazek. *Computational fluid dynamics: principles and applications*. Butterworth-Heinemann, 2015.
- [51] Dan M Goebel and Ira Katz. *Fundamentals of electric propulsion: ion and Hall thrusters*, volume 1. John Wiley & Sons, 2008.
- [52] Wiley J Larson and James Richard Wertz. Space mission analysis and design. Technical report, Microcosm, Inc., Torrance, CA (US), 1992.
- [53] AMR Propulsion. AMR propulsion innovations, 2017. URL <https://www.propulsion.at/cubesatpropulsion/>.
- [54] Tethers Unlimited. Water Electrolysis Thruster, 2017. URL <http://www.tethers.com>.
- [55] Accion Systems. Linear thrust satellite electric propulsion system, 2017. URL <http://www.accion-systems.com/tile/>.
- [56] Chad Frost, E Agasid, et al. Small spacecraft technology state of the art. *Moffett Field, California: NASA Ames Research Center*, 2015.
- [57] Manuel Gamero-Castaño. A torsional balance for the characterization of micronewton thrusters. *Review of Scientific Instruments*, 74(10), 2003.
- [58] AN Grubišić and SB Gabriel. Development of an indirect counterbalanced pendulum optical-lever thrust balance for micro-to millinewton thrust measurement. *Measurement Science and Technology*, 21(10):105101, 2010.
- [59] SM Merkowitz, PG Maghami, A Sharma, WD Willis, and CM Zakrzewski. A  $\mu$ newton thrust-stand for LISA. *Classical and Quantum Gravity*, 19(7):1745, 2002.
- [60] Denis Packan, Jean Bonnet, and Simone Rocca. Thrust Measurements with the ONERA Micronewton Balance. *30th International Electric Propulsion Conference*, 118, 2007.
- [61] Freddy M Pranajaya and Mark A Cappelli. Performance studies of a colloid thruster system. In *Proceedings of the 27th International Electric Propulsion Conference*, volume 202, 2001.
- [62] L Boccaletto and L d'Agostino. Design and testing of a micro-newton thrust stand for FEEP. In *36th AIAA/ASME/SAE/ASEE Joint Propulsion Conference*, volume AIAA 2000-3268, 2000.
- [63] J Soni and S Roy. Design and characterization of a nano-newton resolution thrust stand. *Review of Scientific Instruments*, 84(9):095103, 2013.
- [64] Giulio Manzoni and Yesie L. Brama. CubeSat micropropulsion characterisation in low earth orbit. In *29th Annual AIAA/USU Conference on Small Satellites*, volume SSC15-IV-5. Microspace Rapid Pte Ltd, 2015.

- [65] Giulio Manzoni and Yesie L Brama. CubeSat micropropulsion characterization in low earth orbit. *Small Satellite Conference*, 2015.
- [66] SPL. MIT SPL delivers the scalable ion electrospray propulsion system (S-iEPS) for CubeSats to NASA, 2016. URL <http://web.mit.edu>.
- [67] Michael Keidar, Taisen Zhuang, Alexey Shashurin, George Teel, Dereck Chiu, Joseph Lukas, Samudra Haque, and Lubos Brieda. Electric propulsion for small satellites. *Plasma Physics and Controlled Fusion*, 57(1):014005, 2014.
- [68] Gilbert Moore. 3D printing and MEMS propulsion for the RAMPART 2U CubeSat. In *24th Annual AIAA/USU Conference on Small Satellites*, volume SSC10-III-8, 2010.
- [69] Karan Sarda, Cordell Grant, Stuart Eagleson, Daniel D Kekez, and Robert E Zee. Canadian advanced nanospace experiment 2: On-orbit experiences with a three-kilogram satellite. In *22nd Annual AIAA/USU Conference on Small Satellites*, volume SSC08-II-5. Space Flight Laboratory, University of Toronto Institute for Aerospace Studies, 2008.
- [70] Steven Arestie, E Glenn Lightsey, and Brian Hudson. Development of a modular, cold gas propulsion system for small satellite applications. *Journal of Small Satellites*, 1(2):63–74, 2012.
- [71] VACCO. *Reaction Control Propulsion Module X13003000-01*. VACCO Industries, 7/14 edition, 2014.
- [72] C Muller, L Perez, B Zandbergen, G Brouwer, R Amini, D Kajon, and B Sanders. Implementation of the T3 $\mu$ PS in the Delfi-n3Xt satellite. *Small Satellite Missions for Earth Observation*, 2010.
- [73] DelfiSpace. Delfi-n3xt micropropulsion payload, 2016. URL <http://www.delfispace.nl>.
- [74] University of Michigan. PEPL Thrusters: CubeSat Ambipolar Thruster, 2017. URL <http://pepl.engin.umich.edu>.
- [75] ClydeSpace. Pulsed plasma thrusters, 2017. URL <https://www.clyde.space/products/50-cubesat-pulsed-plasma-thruster>.
- [76] K Harris, M McGarvey, H Chang, M Ryle, T Ruscitti, B Udrea, and M Nayak. Application for RSO Automated Proximity Analysis and IMAGING (ARAPAIMA): Development of a nanosat-based space situational awareness mission. In *CubeSat Summer Workshop 2013*. Embry-Riddle Aeronautical University, 2013.
- [77] BUSEK. ION thrusters BIT-3, 2017. URL [http://busek.com/technologies\\_ion.htm](http://busek.com/technologies_ion.htm).
- [78] Ashish Tewari. *Automatic Control of Atmospheric and Space Flight Vehicles: Design and Analysis with MATLAB® and Simulink®*. Springer Science & Business Media, 2011.
- [79] ISIS Innovative Solutions in Space. Small satellite launch services, 2017. URL <https://www.isispace.nl/launch-services/>.
- [80] NH Crisp, Katharine Smith, and Peter Hollingsworth. Launch and deployment of distributed small satellite systems. *Acta Astronautica*, 114:65–78, 2015.

## References

---

- [81] Peter B de Selding. 1 in 5 CubeSats violates international orbit disposal guidelines, 2015. URL <http://spacenews.com/1-in-5-cubesats-violate-international-orbit-disposal-guidelines/>.
- [82] A Kato, B Lazare, D Oltrogge, and H Stokes. Debris mitigation strategies, standards and best practices with sample application to CubeSats. In *Space Operations and Support Technical Committee (SOSTC) Space Operations Workshop, San Antonio, TX*, volume 3, 2013.
- [83] P. Meador-Anz. A review of space environment implications of CubeSat traffic, 2013-2014. *The NASA Orbital Debris Program Office*, 19(3), 2015.
- [84] International Organization for Standardization. Iso 16164:2915, 2015. URL <https://www.iso.org/standard/55741.html>.
- [85] Jordi Puig-Suari, Clark Turner, and William Ahlgren. Development of the standard cubesat deployer and a cubesat class picosatellite. In *Aerospace Conference, 2001, IEEE Proceedings.*, volume 1, pages 1–347. IEEE, 2001.
- [86] Cal Poly. *CubeSat Design Specification (CDS) Rev 13*. Cal Poly SLO, 2015 edition, 2015.
- [87] Air force space command. *Range safety user requirements manual volume 3 launch vehicles, payloads, and ground support systems requirements*. Air force space command, December 2015.
- [88] BGS and NCEI. World magnetic model, 2017. URL <http://geomag.bgs.ac.uk/research/modelling/WorldMagneticModel.html>.
- [89] A de Brito and PB Saganti. Plasma events in the south atlantic anomaly: Correlations with the interplanetary magnetic field reconnection processes. In *International Cosmic Ray Conference*, volume 2, page 353, 2005.
- [90] AzurSpace. Space solar cells, 2017. URL <http://www.azurspace.com/index.php/en/products/products-space/space-solar-cells>.
- [91] THOTH Technology. Services and products for space applications, 2017. URL <http://thothx.com/products/>.
- [92] Michael Swartwout. The first one hundred cubesats: A statistical look. *Journal of Small Satellites*, 2(2):213–233, 2013.
- [93] Mike Sandor. Plastic Encapsulated Microcircuits (PEMs) Reliability/Usage Guidelines For Space Applications. *Jet Propulsion Laboratory California Institute of Technology Pasadena, California*, 2000.
- [94] Siegfried Janson, Brian Hardy, Andrew Chin, Daniel Rumsey, Daniel Ehrlich, and David Hinkley. Attitude control on the pico satellite solar cell testbed-2. *SSC12*, II(1), 2012.
- [95] EU. Directive 2011/65/eu of the european parliament and of the council. *Official Journal of the European Union*, 1(L 174/88), 2011.
- [96] NASA. Tin and other metal whisker homepage, 2017. URL <https://nepp.nasa.gov/whisker/background/>.

- [97] Joseph F Lemaire, Konstantin I Gringauz, David L Carpenter, and V Bassolo. *The Earth's plasmasphere*. Cambridge University Press, 2005.
- [98] NASA. Imager for magnetopause-to-aurora global exploration, 2017. URL <https://image.gsfc.nasa.gov>.
- [99] Yan Yan, Hua-Ning Wang, Han He, Fei He, Bo Chen, Jian-Qing Feng, Jin-Song Ping, Chao Shen, Rong-Lan Xu, and Xiao-Xin Zhang. Analysis of observational data from Extreme Ultra-Violet Camera onboard Chang'E-3 mission. *Astrophysics and Space Science*, 361(2):1–7, 2016.
- [100] ECSS. Methods for the calculation of radiation received and its effects, and a policy for design margins. Technical Report ECSS-E-ST-10-12C, European Cooperation for Space Standardization, 2008.
- [101] Electronic Systems Laboratory. *Cubecomputer v4.1: General Purpose on-board computer*. CubeSpace, 1.1 edition, 2017.
- [102] ESA. Space environment information system, 2017. URL <http://www.spenvis.oma.be>.
- [103] Michael Dowd. How rad hard do you need? the changing approach to space parts selection? *Application notes, Maxwell technologies*, 2003.
- [104] DC Thompson, C Bonifazi, BE Gilchrist, SD Williams, W Jo Raitt, J-P Lebreton, WJ Burke, NH Stone, and KH Wright. The current-voltage characteristics of a large probe in low earth orbit: TSS-1R results. *Geophysical research letters*, 25(4):413–416, 1998.
- [105] Adam Piotrowski and Szymon Tarnowski. Compiler-level implementation of single event upset errors mitigation algorithms. In *Mixed Design of Integrated Circuits & Systems, 2009. MIXDES'09. MIXDES-16th International Conference*, pages 89–92. IEEE, 2009.
- [106] M Nohmi. Initial Orbital Performance Result of Nano-Satellite STARS-II. In *International Symposium on Artificial Intelligence, Robotics and Automation in Space (I-SAIRAS)*, 2014.
- [107] Shu T Lai. *Fundamentals of spacecraft charging: spacecraft interactions with space plasmas*. Princeton University Press, 2011.
- [108] JG Laframboise. Is there a good way to model spacecraft charging in the presence of space-charge coupling, flow, and magnetic fields? Technical report, DTIC Document, 1983.
- [109] M Tajmar. Electric propulsion plasma simulations and influence on spacecraft charging. *Journal of spacecraft and Rockets*, 39(6):886–893, 2002.
- [110] Jean-Francois Roussel, Francois Rogier, Dominique Volpert, Julien Forest, Guillaume Rousseau, and Alain Hilgers. Spacecraft plasma interaction software (SPIS): Numerical solvers. Methods and architecture. In *9th Spacecraft Charging Technology Conference 9th Spacecraft Charging Technology Conference*, page 462, 2005.
- [111] Myron J Mandell, Victoria A Davis, David L Cooke, Adrian T Wheelock, and CJ Roth. Nascap-2k spacecraft charging code overview. *IEEE transactions on plasma science*, 34(5):2084–2093, 2006.

## References

---

- [112] Wiley Williams and Charles Thompson. The perimeter of a polyomino and the surface area of a polycube. *The College Mathematics Journal*, 39(3):233–237, 2008.
- [113] ESA. Thermospheric density and crosswind speed along the GOCE orbit. Technical report, ESA Earth Observation, 2017.
- [114] YL Zhou, SY Ma, H Lühr, C Xiong, and C Reigber. An empirical relation to correct storm-time thermospheric mass density modeled by NRLMSISE-00 with CHAMP satellite air drag data. *Advances in Space Research*, 43(5):819–828, 2009.
- [115] Bruce R Bowman, W Kent Tobiska, Frank A Marcos, Cheryl Y Huang, Chin S Lin, and William J Burke. A new empirical thermospheric density model JB2008 using new solar and geomagnetic indices. In *AIAA/AAS astrodynamics specialist conference and exhibit, Honolulu, Hawaii*, 2008.
- [116] M. Picone, A. E. Hedin, and D. Drob. NRLMSISE-00 Model 2001. Technical report, Naval Research Laboratory NASA, 2001.
- [117] VZLU. Czech technological nanosatellite, 2017. URL <http://vzlusat1.cz/en/>.
- [118] James Armstrong, Craig Casey, Glenn Creamer, and Gilbert Dutchover. Pointing control for low altitude triple CubeSat space darts. *23rd Annual AIAA/USU Conference on Small Satellites*, 2009.
- [119] John C Springmann, James W Cutler, and Hasan Bahcivan. Magnetic sensor calibration and residual dipole characterization for application to nanosatellites. *Toronto, Ontario Canada*, 2010.
- [120] International Laser Ranging Service. Blits, 2017. URL [https://ilrs.cddis.eosdis.nasa.gov/missions/satellite\\_missions/current\\_missions/blit\\_general.html](https://ilrs.cddis.eosdis.nasa.gov/missions/satellite_missions/current_missions/blit_general.html).
- [121] K Loh. Solar cells for space applications. *Academia*, 2013.
- [122] Elwood Agasid, D Biggs, J Conley, AD Perez, N Faber, A Genova, A Gonzales, A Grasso, J Harpur, S Hu, et al. Small spacecraft technology state of the art. Technical report, NASA/TP-2014-216648/REV1 (Mission Design Division Staff, Ames Research Center, Moffett Field, CA), 2014.
- [123] Sanjay Jayaram, Darren Pais, Sonia Hernez, Paul Lemon, Nathaniel Clark, Benjamin Corrado, Brian Vitale, Justin Kerber, Elena Nogales, Jorge Moya, et al. Billikensat-ii: The first bio-fuel cell test platform for space. *21st Annual AIAA/USU Conference on Small Satellites*, 2007.
- [124] Thomas G Roberts, Edward L Wilkinson, and Lee O Webster. Tether power generator for earth orbiting satellites, May 8 1990. US Patent 4,923,151.
- [125] M. A. Green. *Third Generation Photovoltaics*. Springer, 2006.
- [126] *Advanced Triple-Junction Solar Cell for Space Applications: BTJ Photovoltaic Cell*. Emcore Corporation, 2012.
- [127] KDG Imalka Jayawardena, Lynn J Rozanski, Chris A Mills, Michail J Beliatis, N Aamina Nismy, and S Ravi P Silva. Inorganics-in-Organics: recent developments and outlook for 4G polymer solar cells. *Nanoscale, The Royal Society of Chemistry*, 5(18):8411–8427, 2013.

- [128] R. L. Easton and M. J. Votaw. Vanguard I IGY Satellite. *Review of Scientific Instruments*, 1959.
- [129] Spectrolab. Triangular Advanced Solar Cells (TASC), 2017. URL [http://www.spectrolab.com/DataSheets/PV/PV\\_NM\\_TASC\\_ITJ.pdf](http://www.spectrolab.com/DataSheets/PV/PV_NM_TASC_ITJ.pdf).
- [130] NREL. Photovoltaic research, 2017. URL <https://www.nrel.gov/pv/>.
- [131] JC Bourgoin, R Kiliulis, C Gonzales, G Strobl, C Flores, K Bogus, and C Signorini. Deep space degradation of Si and GaAs solar cells. In *Photovoltaic Specialists Conference, 1996., Conference Record of the Twenty Fifth IEEE*, pages 211–214. IEEE, 1996.
- [132] Nathan Tardiff, Jason Kang, and Ben Todd. SNAPS: Satellite Power Simulation. EPS Team Final Report, Stanford Space and Systems Development Laboratory, 2012.
- [133] Tenergy. Rechargeable battery cells, 2017. URL <http://www.tenergy.com/Rechargeable-Batteries-Category>.
- [134] Space Environment Technologies. The Jacchia-Bowman 2008 Empirical Thermospheric Density Model, 2017. URL <http://sol.spacenvironment.net/~jb2008/>.
- [135] Andreas Zoellner. The drag-free CubeSat. In *CubeSat Developers Workshop*. Stanford University, 2012.
- [136] Nick Maclarens. Why (and why not) to use fortran instead of c++, matlab, python, etc. University of Cambridge Computing Service, June 2012.
- [137] NASA. Comparing Python, NumPy, Matlab, Fortran, etc, 2009. URL <https://modelingguru.nasa.gov/docs/DOC-1762>.
- [138] Petre Stoica, Randolph L Moses, et al. *Spectral analysis of signals*, volume 452. Pearson Prentice Hall Upper Saddle River, NJ, 2005.
- [139] David A Vallado. *Fundamentals of Astrodynamics and Applications*. Space Technology Library, 2013.
- [140] S. Bettadpur, J. Ries, R. Eanes, P. Nagel, N. Pie, S. Poole, T. Richter, and H. Save. Evaluation of the GGM05 Mean Earth Gravity Model. In *EGU General Assembly Conference Abstracts*, volume 17 of *EGU General Assembly Conference Abstracts*, page 4153, April 2015.
- [141] International Centre for Global Earth Models. Global Gravity Field Model Database, 2017. URL <http://icgem.gfz-potsdam.de>.
- [142] ECSS. Ecss space engineering-space environment. Technical report, Technical Report ECSS-E-ST-10-04C, ESA, 2008.
- [143] CIRA Working Group. Cospar international reference atmosphere – 2012. Technical report, The Committee on Space research, July 2012.
- [144] WW Vaughan. Guide to reference and standard atmosphere models. Technical report, AIAA-G-003C-2010, American Institute of Aeronautics and Astronautics, Reston, VA, 2010.

## References

---

- [145] University of Colorado. SORCE SOlar Radiation and Climate Experiment, 2017. URL <http://lasp.colorado.edu>.
- [146] Beny Neta and David Vallado. On satellite umbra/penumbra entry and exit positions. Technical report, Monterey, California. Naval Postgraduate School, 1997.
- [147] Ibrahim Reda. Solar eclipse monitoring for solar energy applications using the solar and moon position algorithms. *Publications (E)*, 2010.
- [148] Thomas Sean Kelso. Satellite catalog (SATCAT), 2017. URL <https://celestrak.com/satcat/>.
- [149] F te Hennepe, BT Zandbergen, and R Hamann. Simulation of the attitude behaviour and available power profile of the DELFI-C3 spacecraft with application of the OPSIM platform. In *1st CEAS European Air and Space Conference, Berlin, Germany*, pages 10–13, 2007.
- [150] Space-Track. Two Line Element (TLE) Data, 2017. URL <https://www.space-track.org/>.
- [151] SILSO. Sunspot number, 2017. URL <http://www.sidc.be/silso/datafiles>.
- [152] HD Curtis. Orbital mechanics for engineering students, 2005.
- [153] XU Zhentao. The basic forms of ancient chinese sunspot records. *Chinese Science*, 9:19–28, 1989.
- [154] FR Stephenson. Historical evidence concerning the Sun: interpretation of sunspot records during the telescopic and pretelescopic eras. *Philosophical Transactions of the Royal Society of London A: Mathematical, Physical and Engineering Sciences*, 330(1615):499–512, 1990.
- [155] Ralph Neuhaeuser and Dagmar L Neuhaeuser. Sunspot numbers based on historic records in the 1610s: Early telescopic observations by simon marius and others. *Astronomische Nachrichten*, 337(6):581–620, 2016.
- [156] National Oceanic and Atmospheric Administration. Solar indices data, 2017. URL <https://www.ngdc.noaa.gov/stp/spaceweather.html>.
- [157] Heinrich Schwabe and Hofrath Schwabe. Sonnen—Beobachtungen im Jahre 1843. *Astronomische Nachrichten*, 21(15):234–235, 1844.
- [158] Ilya G Usoskin. A history of solar activity over millennia. *Living Reviews in Solar Physics*, 10(1):1–94, 2013.
- [159] Friedhelm Steinhilber, Jose A Abreu, Jürg Beer, Irene Brunner, Marcus Christl, Hubertus Fischer, Ulla Heikkilä, Peter W Kubik, Mathias Mann, Ken G McCracken, et al. 9,400 years of cosmic radiation and solar activity from ice cores and tree rings. *Proceedings of the National Academy of Sciences*, 109(16):5967–5971, 2012.
- [160] Jack B Zirker. *Sunquakes: probing the interior of the Sun*. JHU Press, 2003.
- [161] NASA. Royal Observatory, Greenwich - USAF/NOAA Sunspot Data, 2017. URL <https://solarscience.msfc.nasa.gov/greenwch.shtml>.

- [162] P Zeeman. On the influence of magnetism on the nature of the light emitted by a substance (Part I). *Communications from the Physical Laboratory at the University of Leiden*, 33:1–8, 1896.
- [163] J Brookes Spencer. The discovery of the Zeeman effect in sunspots. *Leaflet of the Astronomical Society of the Pacific*, 9:273, 1965.
- [164] NASA. Technology Through Time Issue 46: The Magnetic Sun, 2017. URL <https://sunearthday.nasa.gov/2006/locations/magneticsun.php>.
- [165] Harold D Babcock. The Sun’s polar magnetic field. *The Astrophysical Journal*, 130:364, 1959.
- [166] Robert Howard. Magnetic fields on the Sun. Technical report, Smithsonian Astrophysical Observatory, NASA Astrophysics Data System, 1982.
- [167] WSO. The Wilcox Solar Observatory, 2017. URL <http://wso.stanford.edu/>.
- [168] Franz-Ludwig Deubner and Douglas Gough. Helioseismology: Oscillations as a diagnostic of the solar interior. *Annual review of astronomy and astrophysics*, 22(1):593–619, 1984.
- [169] R.B. Leighton. Untitled comments on observations of supergranulation and five-minute oscillations. In *Aerodynamic Phenomena in Stellar Atmospheres: IAU Symposium*, volume 12 of 10 22:321–327, 1961.
- [170] Michael J Thompson, Jørgen Christensen-Dalsgaard, Mark S Miesch, and Juri Toomre. The internal rotation of the Sun. *Annual Review of Astronomy and Astrophysics*, 41(1):599–643, 2003.
- [171] Arnab Rai Choudhuri, SS Hasan, and D Banerjee. An elementary introduction to solar dynamo theory. In *AIP Conference Proceedings*, volume 919, pages 49–73. AIP, 2007.
- [172] W Dean Pesnell. Solar cycle predictions. *Solar Physics*, 281(1):507–532, 2012.
- [173] National Oceanic and Atmospheric Administration. Sunspot number progression, 2017. URL <http://www.swpc.noaa.gov/products/solar-cycle-progression>.
- [174] SILSO. 2014: maximum year for solar cycle 24, 2017. URL <http://www.sidc.be/silso/news004>.
- [175] David H Hathaway, Robert M Wilson, and Edwin J Reichmann. The shape of the sunspot cycle. *Solar Physics*, 151(1):177–190, 1994.
- [176] M Dikpati. Predicting cycle 24 using various dynamo-based tools. In *Annales Geophysicae*, volume 26, pages 259–267. Copernicus GmbH, 2008.
- [177] Bidya Binay Karak. Importance of meridional circulation in flux transport dynamo: the possibility of a maunder-like grand minimum. *The Astrophysical Journal*, 724(2):1021, 2010.
- [178] I Kitiashvili and AG Kosovichev. Application of data assimilation method for predicting solar cycles. *The Astrophysical Journal Letters*, 688(1):L49, 2008.

## References

---

- [179] Jie Jiang, Piyali Chatterjee, and Arnab Rai Choudhuri. Solar activity forecast with a dynamo model. *Monthly Notices of the Royal Astronomical Society*, 381(4):1527–1542, 2007.
- [180] Eric Priest. *Magnetohydrodynamics of the Sun*. Cambridge University Press, 2014.
- [181] Hannes Alfvén. Existence of electromagnetic-hydrodynamic waves. *Nature*, 150(3805):405–406, 1942.
- [182] Zhu-Xing Liang and Yi Liang. Significance of polarization charges and isomagnetic surface in magnetohydrodynamics. *PloS one*, 10(8):e0136936, 2015.
- [183] Eric Chaisson and Stephen McMillan. *Astronomy today*. Pearson/Prentice Hall, 2005.
- [184] J Christensen-Dalsgaard, Wc Dappen, SV Ajukov, ER Anderson, et al. The current state of solar modeling. *Science*, 272(5266):1286, 1996.
- [185] Paul Charbonneau, J Christensen-Dalsgaard, Reyco Henning, RM Larsen, J Schou, MJ Thompson, and S Tomczyk. Helioseismic constraints on the structure of the solar tachocline. *The Astrophysical Journal*, 527(1):445, 1999.
- [186] Steven A Balbus, Henrik Latter, and Nigel Weiss. Global model of differential rotation in the Sun. *Monthly Notices of the Royal Astronomical Society*, 420(3):2457–2466, 2012.
- [187] Andrés Muñoz-Jaramillo, Dibyendu Nandy, and Petrus CH Martens. Helioseismic data inclusion in solar dynamo models. *The Astrophysical Journal*, 698(1):461, 2009.
- [188] M Dikpati. Generating the Sun’s global meridional circulation from differential rotation and turbulent Reynolds stresses. *Monthly Notices of the Royal Astronomical Society*, page stt2353, 2014.
- [189] Junwei Zhao, RS Bogart, AG Kosovichev, TL Duvall Jr, and Thomas Hartlep. Detection of equatorward meridional flow and evidence of double-cell meridional circulation inside the Sun. *The Astrophysical Journal Letters*, 774(2):L29, 2013.
- [190] Gopal Hazra, Bidya Binay Karak, and Arnab Rai Choudhuri. Is a deep one-cell meridional circulation essential for the flux transport solar dynamo? *The Astrophysical Journal*, 782(2):93, 2014.
- [191] David H Hathaway and Lisa Upton. The solar meridional circulation and sunspot cycle variability. *Journal of Geophysical Research: Space Physics*, 119(5):3316–3324, 2014.
- [192] Elisa Cardoso and Ilídio Lopes. Impact of a realistic density stratification on a simple solar dynamo calculation. *The Astrophysical Journal*, 757(1):71, 2012.
- [193] Piyali Chatterjee, Dibyendu Nandy, and Arnab Rai Choudhuri. Full-sphere simulations of a circulation-dominated solar dynamo: Exploring the parity issue. *Astronomy & Astrophysics*, 427(3):1019–1030, 2004.
- [194] David H Hathaway, Dibyendu Nandy, Robert M Wilson, and Edwin J Reichmann. Evidence that a deep meridional flow sets the sunspot cycle period. *The Astrophysical Journal*, 589(1):665, 2003.

- [195] S D’silva and AR Choudhuri. A theoretical model for tilts of bipolar magnetic regions. *Astronomy and Astrophysics*, 272:621, 1993.
- [196] Dibyendu Nandy and Arnab Rai Choudhuri. Toward a mean field formulation of the Babcock-Leighton type solar dynamo. i.  $\alpha$ -coefficient versus Durney’s double-ring approach. *The Astrophysical Journal*, 551(1):576, 2001.
- [197] George H Fisher, Yuhong Fan, Dana W Longcope, Mark G Linton, and Alexei A Pevtsov. The solar dynamo and emerging flux. *Solar Physics*, 192:119, 2000.
- [198] Kirill M Kuzanyan, Valerij V Pipin, and Norbert Seehafer. The alpha effect and the observed twist and current helicity of solar magnetic fields. *Solar Physics*, 233(2):185–204, 2006.
- [199] Kenneth Schatten, Daniel J Myers, and Sabatino Sofia. Solar activity forecast for solar cycle 23. *Geophysical research letters*, 23(6):605–608, 1996.
- [200] H Hotta and T Yokoyama. Solar parity issue with flux-transport dynamo. *The Astrophysical Journal Letters*, 714(2):L308, 2010.
- [201] Andrés Muñoz-Jaramillo, Dibyendu Nandy, and Petrus CH Martens. Magnetic quenching of turbulent diffusivity: reconciling mixing-length theory estimates with kinematic dynamo models of the solar cycle. *The Astrophysical Journal Letters*, 727(1):L23, 2010.
- [202] Mausumi Dikpati and Peter A Gilman. Simulating and predicting solar cycles using a flux-transport dynamo. *The Astrophysical Journal*, 649(1):498, 2006.
- [203] Rainer Arlt. The butterfly diagram in the eighteenth century. *Solar Physics*, 255 (1), 2009.
- [204] Dmitry Sokoloff, Rainer Arlt, David Moss, Steven H Saar, and Ilya Usoskin. Sunspot cycles and grand minima. *Proceedings of the International Astronomical Union*, 5(S264):111–119, 2009.
- [205] L Jouve, AS Brun, R Arlt, A Brandenburg, M Dikpati, A Bonanno, PJ Käpylä, D Moss, Matthias Rempel, P Gilman, et al. A solar mean field dynamo benchmark. *Astronomy & Astrophysics*, 483(3):949–960, 2008.
- [206] AR Choudhuri. The user’s guide to the solar dynamo code Surya. *Indian Institute of Science*, 2005.
- [207] Corinne Simard, Paul Charbonneau, and Amélie Bouchat. Magnetohydrodynamic simulation-driven kinematic mean field model of the solar cycle. *The Astrophysical Journal*, 768(1):16, 2013.
- [208] Andrey G Tlatov and Alexei A Pevtsov. Bimodal distribution of magnetic fields and areas of sunspots. *arXiv preprint arXiv:1308.0535*, 2013.
- [209] Leif Svalgaard, Thomas L Duvall, and Philip H Scherrer. The strength of the Sun’s polar fields. *Solar Physics*, 58(2):225–239, 1978.
- [210] Tyler C. McMaken and Gordon J. D. Petrie. The great solar active region NOAA 12192: Helicity transport, filament formation, and impact on the polar field. *The Astrophysical Journal*, 840(2):100, 2017. URL <http://stacks.iop.org/0004-637X/840/i=2/a=100>.

## References

---

- [211] GJD Petrie. Solar magnetic activity cycles, coronal potential field models and eruption rates. *The Astrophysical Journal*, 768(2):162, 2013.
- [212] Daniel Graupe. *Principles of artificial neural networks*. World Scientific, 2007.
- [213] Howard B Demuth, Mark H Beale, Orlando De Jess, and Martin T Hagan. *Neural network design*. Martin Hagan, 2014.
- [214] Ming Li, Kishan Mehrotra, Chilukuri K Mohan, and Sanjay Ranka. Forecasting sunspot numbers using neural networks. 1990.
- [215] R Werner. Sunspot number prediction by an autoregressive model. *Sun and Geosphere*, 7:75–80, 2012.
- [216] Andrés Muñoz-Jaramillo, María Dasi-Espuig, Laura A Balmaceda, and Edward E DeLuca. Solar cycle propagation, memory, and prediction: insights from a century of magnetic proxies. *The Astrophysical Journal Letters*, 767(2):L25, 2013.
- [217] Andrés Muñoz-Jaramillo, Neil R Sheeley, Jie Zhang, and Edward E DeLuca. Calibrating 100 years of polar faculae measurements: implications for the evolution of the heliospheric magnetic field. *The Astrophysical Journal*, 753(2):146, 2012.
- [218] E Walter Maunder. Note on the distribution of sunspots in heliographic latitude, 1874-1902. *Monthly Notices of the Royal Astronomical Society*, 64:747–761, 1904.
- [219] Kenneth Moe and Mildred M Moe. Gas-surface interactions and satellite drag coefficients. *Planetary and Space Science*, 53(8):793–801, 2005.
- [220] Kenneth Moe and Mildred M Moe. The effect of adsorption on densities measured by orbiting pressure gauges. *Planetary and Space Science*, 15(8):1329–1332, 1967.
- [221] Marcin D Pilinski, Brian M Argow, and Scott E Palo. Drag coefficients of satellites with concave geometries: comparing models and observations. *Journal of Spacecraft and Rockets*, 48(2):312–325, 2011.
- [222] David A Vallado and David Finkleman. A critical assessment of satellite drag and atmospheric density modeling. In *AIAA/AAS astrodynamics specialist conference and exhibit*, pages 18–21, 2008.
- [223] Andrew Walker, Piyush Mehta, and Josef Koller. Drag Coefficient Model Using the Cercignani–Lampis–Lord Gas–Surface Interaction Model. *Journal of Spacecraft and Rockets*, 51(5):1544–1563, 2014.
- [224] Arrun Saunders, Graham G Swinerd, and Hugh G Lewis. Deriving accurate satellite ballistic coefficients from two-line element data. *Journal of Spacecraft and Rockets*, 49(1):175–184, 2012.
- [225] C Pardini, L Anselmo, K Moe, and MM Moe. Drag and energy accommodation coefficients during sunspot maximum. *Advances in Space Research*, 45(5):638–650, 2010.
- [226] Alan Li and Sigrid Close. Mean thermospheric density estimation derived from satellite constellations. *Advances in Space Research*, 56(8):1645–1657, 2015.

- [227] Ching Shen. *Rarefied gas dynamics: fundamentals, simulations and micro flows*. Springer Science & Business Media, 2006.
- [228] Lee H Sentman. Free molecule flow theory and its application to the determination of aerodynamic forces. Technical report, DTIC Document, 1961.
- [229] David R Lide. *CRC handbook of chemistry and physics*, volume 85. CRC press, 2004.
- [230] GE Cook. Satellite drag coefficients. *Planetary and Space Science*, 13(10): 929–946, 1965.
- [231] Dennis R Imbro, Mildred M Moe, and Kenneth Moe. On fundamental problems in the deduction of atmospheric densities from satellite drag. *Journal of Geophysical Research*, 80(22):3077–3086, 1975.
- [232] James Clerk Maxwell. *The Scientific Papers of James Clerk Maxwell...*, volume 2. J. Hermann, 1890.
- [233] Kenneth Moe, Mildred M Moe, Deborah A Levin, Ingrid J Wysong, and Alejandro L Garcia. Gas-surface interactions in Low-Earth Orbit. In *AIP Conference Proceedings*, volume 1333, pages 1313–1318. AIP, 2011.
- [234] Kim K De Groh and Terry R McCue. Analyses of contaminated solar array handrail samples retrieved from Mir. Technical report, SAE Technical Paper, 1999.
- [235] Wen Zhang, Min Yi, Zhigang Shen, Xiaohu Zhao, Xiaojing Zhang, and Shulin Ma. Graphene-reinforced epoxy resin with enhanced atomic oxygen erosion resistance. *Journal of Materials Science*, 48(6):2416–2423, 2013.
- [236] MN Izakov. Some problems of investigating the structure of the upper atmosphere and constructing its models. *Space Research*, 5:1191, 1965.
- [237] Raymond W Wolverton. *Flight performance handbook for orbital operations*. John Wiley and Sons, 1961.
- [238] K Moe and BR Bowman. The effects of surface composition and treatment on drag coefficients of spherical satellites, AAS 2005-258. *American Astronautical Society Publications Office, San Diego, CA*, 2005.
- [239] JA Storch. Aerodynamic disturbances on spacecraft in free-molecular flow. Technical report, DTIC Document, 2002.
- [240] Eugene G Fahnstock, Ryan S Park, Dah-Ning Yuan, and Alex S Konopliv. Spacecraft thermal and optical modeling impacts on estimation of the GRAIL lunar gravity field. In *AIAA/AAS Astrodynamics Specialist Conference*, pages 13–16, 2012.
- [241] D Oltrogge and K Leveque. An evaluation of CubeSat orbital decay. In *AIAA/USU Conference on Small Satellites*, volume SSC11-VII-2 AIAA/USU, USA, 2011.
- [242] Thomas Sean Kelso. Space surveillance, 2014. URL <https://celestrak.com/columns/v04n01/>.

## References

---

- [243] Air Force Space Command. Two new satellites now operational, expand U.S. space situational awareness, 2017. URL <http://www.afspc.af.mil/News/Article-Display/Article/1310272/two-new-satellites-now-operational-expand-us-space-situational-awareness/>.
- [244] Mike Gruss. Shelton Orders Shutdown of Space Fence, 2017. URL <http://spacenews.com/36655shelton-orders-shutdown-of-space-fence/>.
- [245] Mike Gruss. Haney: U.S. Partners To Have Indirect Access to Space Fence Data, 2017. URL <http://spacenews.com/42619haney-us-partners-to-have-indirect-access-to-space-fence-data/>.
- [246] Air Force Space Command. Ground-Based Electro-Optical Deep Space Surveillance, 2017. URL <http://www.afspc.af.mil/About-Us/Fact-Sheets/Article/249016/ground-based-electro-optical-deep-space-surveillance/>.
- [247] Darren D Garber. The CubeSat Challenge: A Review of CubeSat Dependencies and Requirements for Space Tracking Systems. In *9th Space Surveillance Workshop, Listvyanka, Russia*, August 27–30 2012.
- [248] David A Vallado and Paul Crawford. SGP4 orbit determination. In *Proceedings of AIAA/AAS Astrodynamics Specialist Conference and Exhibit*, pages 18–21. AIAA Reston, VA, 2008.
- [249] Thomas Sean Kelso. More frequently asked questions, 2014. URL <https://celestrak.com/columns/v04n05/index.asp#FAQ08>.
- [250] David A Vallado, Paul Crawford, Richard Hujšák, and TS Kelso. Revisiting spacetrack report# 3. AIAA, 6753:2006, 2006.
- [251] David A Vallado and Wayne D McClain. *Fundamentals of astrodynamics and applications*, volume 12. Springer Science & Business Media, 2001.
- [252] C. Pardini, K. Moe, and L. Anselmo. Thermospheric density model biases at the 23rd sunspot maximum. *Planetary and Space Science*, 67(1):130 – 146, 2012. ISSN 0032-0633. doi: <http://dx.doi.org/10.1016/j.pss.2012.03.004>. URL <http://www.sciencedirect.com/science/article/pii/S0032063312000621>.
- [253] R Thompson. A note on restricted maximum likelihood estimation with an alternative outlier model. *Journal of the Royal Statistical Society. Series B (Methodological)*, pages 53–55, 1985.
- [254] John Springmann, Benjamin Kempke, James Cutler, and Hasan Bahcivan. Initial flight results of the RAX-2 satellite. *26th Annual AIAA/USU Conference on Small Satellites*, 2012.
- [255] JS Shim, M Kuznetsova, L Rastätter, M Hesse, D Bilitza, M Butala, M Codrescu, B Emery, B Foster, T Fuller-Rowell, et al. CEDAR electrodynamics thermosphere ionosphere (ETI) challenge for systematic assessment of ionosphere/thermosphere models: NmF2, hmF2, and vertical drift using ground-based observations. *Space Weather*, 9(12), 2011.
- [256] Kyle D. Kemble. AFRL Small satellite portfolio. In *Ground system architectures workshop*, 2015.

- [257] Andrew J Auman. *Geometric attitude estimation & orbit modelling*. PhD thesis, University of Surrey, 2015.
- [258] J Reijneveld and D Choukroun. Attitude control system of the Delfi-n3Xt satellite. *Progress in Flight Dynamics, GNC, and Avionics 6* (2013) 189-208, 2013.
- [259] B Wie. Space vehicle dynamics and control second edition, aiaa education series, american institute of aeronautics and astronautics, 2008.
- [260] Herbert Goldstein, Charles P Poole, and John L Safko. *Classical Mechanics: Pearson New International Edition*. Pearson Higher Ed, 2014.
- [261] Jerrold E Marsden and Tudor S Ratiu. *Introduction to mechanics and symmetry: a basic exposition of classical mechanical systems*, volume 17. Springer Science & Business Media, 2013.
- [262] Panagiotis Tsotras and James M Longuski. Analytic solution of Euler's equations of motion for an asymmetric rigid body. *Journal of applied mechanics*, 63(1): 149–155, 1996.
- [263] Siegfried Janson and David Hinkley. Spin dynamics of the pico satellite solar cell testbed spacecraft. *Small Satellite Conference*, 2009.
- [264] Tim Neilsen, Cameron Weston, Chad Fish, and Bryan Bingham. Dice: Challenges of spinning CubeSat. In *37th Annual AAS Guidance and Control Conference, Breckenridge, CO*, 2014.
- [265] J Barranger. Hysteresis and eddy-current losses of a transformer lamination viewed as an application of the pointing theorem. *Washington: NASA Technical note*, 1965.
- [266] Yudintsev Vadim. CubeSat separation dynamics. In *II Latin American IAA CubeSat WorkShop*, 2016.
- [267] Robbert Hamann, Jasper Bouwmeester, and Geert Brouwer. Delfi-C3 preliminary mission results. *23rd Annual AIAA/USU Conference on Small Satellites*, SSC09-IV(7), 2009.
- [268] CubeSatShop. Nanopower solar P110U-A/B, 2016. URL <http://www.cubesatshop.com/>.
- [269] Analog. *ADIS16251 Programmable Low Power Gyroscope*. Analog Devices Inc., Norwood, MA, USA, PrA edition, 2006.
- [270] Sophocles J Orfanidis. *Introduction to signal processing*. Prentice-Hall, Inc., 2010.
- [271] W. Gander, M.J. Gander, and F. Kwok. *Scientific Computing - An Introduction using Maple and MATLAB*. Texts in Computational Science and Engineering. Springer International Publishing, 2014. ISBN 9783319043258.
- [272] L. Blitzer. Satellite resonances and librations associated with tesseral harmonics of the geopotential. *Journal of Geophysical Research*, 71(14), 1966.
- [273] A De Vos and H Pauwels. On the thermodynamic limit of photovoltaic energy conversion. *Applied physics*, 25(2):119–125, 1981.

## References

---

- [274] FHWN. Pegasus design, 2017. URL <http://www.pegasus-fhwn.at/project-info/pegasus-design/>.
- [275] SSCSpace. Micropropulsion for nanosatellites, 2017. URL [www.sscspace.com/nanospace](http://www.sscspace.com/nanospace).
- [276] Eamonn P Glennon, Joseph P Gauthier, Mazher Choudhury, Kevin Parkinson, and Andrew G Dempster. Project Biarri and the Namuru V3.2 Spaceborne GPS Receiver. In *International Global Navigation Satellite Systems Society Symposium*, 2013.
- [277] Fabrizio Piergentili, Marco Balucani, Rocco Crescenzi, Jacopo Piattoni, Fabio Santoni, Barbara Betti, Francesco Nasuti, and Marcello Onofri. *MEMS cold gas microthruster on Ursa Maior CubeSat*, volume 9, pages 7137–7143. International Astronautical Federation, IAF, 2013.
- [278] Nano-Avionics. LituanicaSAT-2, 2017. URL <http://n-avionics.com/projects/lituanicasat2-satellite-mission/>.
- [279] P. Elliott Hardy. Orbital maneuver applications and capabilities of the ALL-STAR CubeSat propulsion system, 2013. URL <http://ccar.colorado.edu>.
- [280] SSTL. WARP DRiVE, 2017. URL <http://www.sstl.co.uk>.
- [281] Alexandra Bulit, Matthias Gollor, Pierre Lionnet, Jean-Charles Treuet, and Ines Alonso Gomez. D2.1 Database on EP (and EP-related) technologies and TRL. Technical report, EPIC-CNES, 2015.
- [282] VACCO. JPL MarCO micro propulsion system, 2017. URL <http://www.cubesat-propulsion.com/jpl-marco-micro-propulsion-system/>.
- [283] Joseph Lukas, George Teel, Samudra Hague, Alexey Shashurin, and Michael Keidar. Thruster subsystem design for the ballistic reinforced communication satellite. In *CubeSat Developers Workshop*, volume SSC14-WK-18. The George Washington University, 2014.
- [284] Earl D Knechtel and William C Pitts. Normal and tangential momentum accommodation for earth satellite conditions. *Acta Astronautica*, 18(112784):171–184, 1973.
- [285] Michael Paluszek. *Spacecraft attitude and orbit control*. Princeton Satellite Systems, Incorporated, 2008.

# A: List of historic nanosatellite missions

Table 1 Historical nanosatellites missions. Excerpt from the Satellite Catalog (SATCAT) [148].

International Designator	NORAD Catalog Number	Operational Status Code	Satellite Name(s)	Source or Ownership
2013-009B	39087	Nonoperational	AAUSAT3	Denmark
2008-021F	32788	Partially Op.	AAUSAT-II	Denmark
2009-028E	35005	Decayed	AEROCUBE 3	United States
1998-067EQ	39571	Decayed	UAPSAT 1	Peru
1998-067DC	39414	Decayed	ARDUSAT-X	United States
1998-067DA	39412	Decayed	ARDUSAT-1	United States
2011-061E	37854	Operational	AUBIESAT-1 (AO-71)	United States
2009-051C	35933	Operational	BEEESAT	Germany
2013-015G	39136	Operational	BEEESAT-2	Germany
2013-015E	39134	Operational	SOMP	Germany
2007-012P	31130	Nonoperational	CAPE1	United States
2013-064AB	39405	Decayed	CHARGERSAT	United States
2008-021E	32787	Partially Op.	COMPASS-1	Germany
2007-012N	31129	Nonoperational	POLYSAT CP3	United States
2007-012Q	31132	Nonoperational	POLYSAT CP4	United States
2009-028C	35003	Decayed	POLYSAT CP6	United States
2007-012F	31122	Nonoperational	CSTB1	United States
2003-031J	27848	Operational	CUBESAT XI-IV (CO-57)	Japan
2005-043F	28895	Operational	CUBESAT XI 5	Japan
2003-031E	27844	Operational	CUTE-1 (CO-55)	Japan
2013-021C	39161	Operational	ESTCUBE 1	Estonia
2012-006C	38079	Decayed	E-ST@R	Italy
1998-067CP	38853	Decayed	FITSAT-1 (NIWAKA)	Japan
2013-066AE	39444	Operational	FUNCUBE-1 (AO-73)	United Kingdom

## A: List of historic nanosatellite missions

---

2012-006D	38080	Decayed	GOLIAT	Romania
2009-028D	35004	Decayed	HAWKSAT 1	United States
2014-009F	39577	Decayed	INVADER (CO-77)	Japan
2014-009B	39573	Decayed	ITF-1	Japan
2009-051E	35935	Operational	ITUPSAT 1	Turkey
2014-009G	39578	Decayed	KSAT-2	Japan
2007-012M	31128	Nonoperational	LIBERTAD-1	Colombia
2012-006E	38081	Decayed	MASAT 1 (MO-72)	Hungary
2007-012K	31126	Nonoperational	MAST	United States
2011-061F	37855	Operational	M-CUBED & EXP-1 PRIME	United States
2013-018B	39151	Partially Op.	NEE-01 PEGASUS	Ecuador
2013-066AB	39441	Operational	NEE-02 KRYSAOR	Ecuador
2010-020C	36575	Decayed	NEGAI	Japan
2014-009D	39575	Decayed	OPUSAT	Japan
2013-016A	39142	Decayed	BELL	United States
2013-016E	39146	Decayed	GRAHAM	United States
2013-016C	39144	Decayed	ALEXANDER	United States
2013-066AC	39442	Nonoperational	PUCP-SAT 1	Peru
2012-006G	38083	Decayed	PW-SAT	Poland
2008-021J	32791	Operational	SEEDS II (CO-66)	Japan
1998-067EL	39567	Decayed	SKYCUBE	United States
2013-015F	39135	Nonoperational	BEESAT-3	Germany
2010-035B	36796	Nonoperational	STUDSAT	India
2009-051B	35932	Operational	SWISSCUBE	Switzerland
1998-067CQ	38854	Decayed	TECHEDSAT	United States
2010-035E	36799	Operational	TISAT 1	Switzerland
1998-067EM	39568	Decayed	LITSAT-1	Lithuania
2012-006J	38085	Decayed	UNICUBESAT GG	Italy
2009-051D	35934	Nonoperational	UWE-2	Germany
2014-034E	40057	Operational	VELOX 1	Singapore
2013-066Y	39438	Nonoperational	VELOX-II	Singapore
2013-064AD	39407	Decayed	VERMONT LUNAR	United States
2010-020B	36574	Decayed	WASEDA-SAT2	Japan
2012-006F	38082	Decayed	XATCOBEO	Spain
2008-021H	32790	Operational	CANX-2	Canada
2008-021G	32789	Partially Op.	DELFI-C3 (DO-64)	Netherlands
2013-066N	39428	Nonoperational	DELFI-N3XT	Netherlands
2013-064AA	39404	Operational	FIREFLY	United States
2006-058C	29655	Decayed	GENESAT-1	United States
2011-058B	37839	Operational	JUGNU	India
2010-066J	37252	Decayed	MAYFLOWER	United States
2009-028B	35002	Decayed	PHARMASAT	United States
2010-066F	37249	Decayed	QBX1	United States
2010-066B	37245	Decayed	QBX2	United States

2003-031F	27845	Nonoperational	QUAKESAT	United States
2011-061D	37853	Nonoperational	RAX-2	United States
2010-066C	37246	Decayed	SMDC ONE	United States
2013-009E	39090	Operational	STRAND-1	United Kingdom
2016-051B	41732	Operational	3CAT-2	Spain
2016-025E	41460	Operational	AAUSAT 4	Denmark
2014-033AM	40045	Operational	AEROCUBE 6A	United States
2014-033AN	40046	Operational	AEROCUBE 6B	United States
2016-067F	41853	Operational	AEROCUBE 8C	United States
2016-067E	41852	Operational	AEROCUBE 8D	United States
1998-067HP	41313	Operational	AGGIESAT 4	United States
2010-035C	36797	Operational	AISSAT 1	Norway
2014-037G	40075	Operational	AISSAT 2	Norway
2013-015D	39133	Operational	AIST-2	CIS (former USSR)
2016-059G	41789	Operational	ALSAT 1N	Algeria
2014-033AA	40034	Operational	ANELSAT	Uruguay
2016-062E	41873	Operational	LEMUR-2-ANUBHAVTHAKUR	United States
1998-067KX	41935	Operational	AOBA-VELOX 3	Singapore
2015-077C	41168	Operational	ATHENOXAT 1	Singapore
2016-040W	41619	Operational	BEESEN-4	Germany
1998-067HQ	41314	Operational	BEVO 2	United States
2009-049G	35871	Nonoperational	BLITS	CIS (former USSR)
2016-019C	41596	Operational	LEMUR-2-BRIDGEMAN	United States
2013-009F	39091	Operational	BRITE-AUSTRIA	Austria
2013-066R	39431	Operational	BRITE-PL	Poland
2014-049B	40119	Operational	BRITE-PL 2	Poland
2014-049B	40119	Operational	BRITE-PL 2	Poland
2014-033L	40020	Operational	BRITE-TORONTO	Canada
2016-083C	41909	Decayed	BY70-1	PR of China
2016-059F	41788	Operational	CANX-7	Canada
2016-067C	41850	Operational	CELTEE 1	United States
2015-052D	40933	Operational	LEMUR-2-CHRIS	United States
2013-064R	39395	Decayed	COPPER	United States
2013-018D	39153	Operational	CUBEBUG-1 (CAPITAN BETO)	Argentina
2013-066AA	39440	Operational	CUBEBUG-2 (LO-74)	Argentina
2016-019D	41597	Operational	LEMUR-2-CUBECHEESE	United States
2008-021C	32785	Operational	CUTE-1.7+APD II (CO-65)	Japan
2008-021C	32785	Operational	CUTE-1.7+APD II (CO-65)	Japan
2015-032E	40719	Operational	DEORBITSAIL	United Kingdom
1998-067HT	41463	Operational	DIWATA-1	Philippines
2013-016B	39143	Decayed	DOVE 1	United States
2013-015C	39132	Nonoperational	DOVE 2	United States
2013-066P	39429	Operational	DOVE 3	United States
2013-066U	39434	Nonoperational	DOVE 4	United States

## A: List of historic nanosatellite missions

---

2016-019B	41595	Operational	LEMUR-2-DRMUZZ	United States
2014-033M	40021	Operational	DUCHIFAT-1	Israel
2013-066W	39436	Operational	EAGLE 2	United States
1998-067KW	41934	Operational	EGG	Japan
2015-052G	40936	Operational	EXACTVIEW 9	Canada
2015-003E	40380	Operational	EXOCUBE	United States
1993-061C	22825	Partially Op.	EYESAT-1 (AO-27)	United States
2016-025D	41459	Operational	E-ST@R-II	Italy
2015-003B	40377	Operational	FIREBIRD 3	United States
2015-003C	40378	Operational	FIREBIRD 4	United States
2014-033T	40027	Operational	FLOCK 1C-1	United States
2014-033P	40023	Operational	FLOCK 1C-10	United States
2014-033Z	40033	Operational	FLOCK 1C-11	United States
2014-033V	40029	Operational	FLOCK 1C-2	United States
2014-033AH	40041	Operational	FLOCK 1C-3	United States
2014-033X	40031	Operational	FLOCK 1C-4	United States
2014-033AE	40038	Operational	FLOCK 1C-5	United States
2014-033AC	40036	Operational	FLOCK 1C-6	United States
2014-033S	40026	Operational	FLOCK 1C-7	United States
2014-033AG	40040	Operational	FLOCK 1C-8	United States
2014-033AB	40035	Operational	FLOCK 1C-9	United States
1998-067GP	40737	Decayed	FLOCK 1E-10	United States
1998-067GQ	40738	Decayed	FLOCK 1E-11	United States
1998-067GR	40739	Decayed	FLOCK 1E-12	United States
1998-067GS	40740	Decayed	FLOCK 1E-13	United States
1998-067GT	40741	Decayed	FLOCK 1E-14	United States
1998-067GM	40729	Decayed	FLOCK 1E-6	United States
1998-067GJ	40726	Decayed	FLOCK 1E-7	United States
1998-067DH	39513	Decayed	FLOCK 1-1	United States
1998-067DR	39526	Decayed	FLOCK 1-10	United States
1998-067DS	39527	Decayed	FLOCK 1-11	United States
1998-067DT	39528	Decayed	FLOCK 1-12	United States
1998-067DU	39529	Decayed	FLOCK 1-13	United States
1998-067DV	39530	Decayed	FLOCK 1-14	United States
1998-067DW	39531	Decayed	FLOCK 1-15	United States
1998-067DX	39532	Decayed	FLOCK 1-16	United States
1998-067DY	39555	Decayed	FLOCK 1-17	United States
1998-067DZ	39556	Decayed	FLOCK 1-18	United States
1998-067EC	39559	Decayed	FLOCK 1-19	United States
1998-067DJ	39514	Decayed	FLOCK 1-2	United States
1998-067ED	39560	Decayed	FLOCK 1-20	United States
1998-067EA	39557	Decayed	FLOCK 1-21	United States
1998-067EB	39558	Decayed	FLOCK 1-22	United States
1998-067EE	39561	Decayed	FLOCK 1-23	United States

---

1998-067EF	39562	Decayed	FLOCK 1-24	United States
1998-067EG	39563	Decayed	FLOCK 1-25	United States
1998-067EH	39564	Decayed	FLOCK 1-26	United States
1998-067EJ	39565	Decayed	FLOCK 1-27	United States
1998-067EK	39566	Decayed	FLOCK 1-28	United States
1998-067DG	39512	Decayed	FLOCK 1-3	United States
1998-067DK	39515	Decayed	FLOCK 1-4	United States
1998-067DL	39518	Decayed	FLOCK 1-5	United States
1998-067DM	39519	Decayed	FLOCK 1-6	United States
1998-067DN	39520	Decayed	FLOCK 1-7	United States
1998-067DP	39521	Decayed	FLOCK 1-8	United States
1998-067DQ	39525	Decayed	FLOCK 1-9	United States
1998-067HB	40950	Decayed	FLOCK 2B-1	United States
1998-067HK	40962	Decayed	FLOCK 2B-10	United States
1998-067HM	40979	Decayed	FLOCK 2B-13	United States
1998-067HN	40980	Decayed	FLOCK 2B-14	United States
1998-067HC	40951	Decayed	FLOCK 2B-2	United States
1998-067HD	40952	Decayed	FLOCK 2B-3	United States
1998-067HE	40953	Decayed	FLOCK 2B-4	United States
1998-067HF	40954	Decayed	FLOCK 2B-5	United States
1998-067HG	40955	Decayed	FLOCK 2B-6	United States
1998-067HH	40956	Decayed	FLOCK 2B-7	United States
1998-067HL	40963	Decayed	FLOCK 2B-9	United States
1998-067HZ	41479	Operational	FLOCK 2E'-1	United States
1998-067KA	41576	Operational	FLOCK 2E'-10	United States
1998-067KB	41577	Operational	FLOCK 2E'-11	United States
1998-067KC	41578	Operational	FLOCK 2E'-12	United States
1998-067KH	41761	Operational	FLOCK 2E'-13	United States
1998-067KJ	41762	Operational	FLOCK 2E'-14	United States
1998-067KL	41764	Operational	FLOCK 2E'-15	United States
1998-067KK	41763	Operational	FLOCK 2E'-16	United States
1998-067KN	41776	Operational	FLOCK 2E'-17	United States
1998-067KM	41769	Operational	FLOCK 2E'-18	United States
1998-067KP	41777	Operational	FLOCK 2E'-19	United States
1998-067JB	41481	Operational	FLOCK 2E'-2	United States
1998-067KQ	41782	Operational	FLOCK 2E'-20	United States
1998-067JA	41480	Operational	FLOCK 2E'-3	United States
1998-067JC	41482	Operational	FLOCK 2E'-4	United States
1998-067JR	41567	Operational	FLOCK 2E'-5	United States
1998-067JS	41568	Operational	FLOCK 2E'-6	United States
1998-067JU	41570	Operational	FLOCK 2E'-7	United States
1998-067JT	41569	Operational	FLOCK 2E'-8	United States
1998-067JZ	41575	Operational	FLOCK 2E'-9	United States
1998-067JD	41483	Operational	FLOCK 2E-1	United States

## A: List of historic nanosatellite missions

---

1998-067JW	41572	Operational	FLOCK 2E-10	United States
1998-067JW	41572	Operational	FLOCK 2E-10	United States
1998-067JY	41574	Operational	FLOCK 2E-11	United States
1998-067JY	41574	Operational	FLOCK 2E-11	United States
1998-067JX	41573	Operational	FLOCK 2E-12	United States
1998-067JX	41573	Operational	FLOCK 2E-12	United States
1998-067KH	41761	Operational	FLOCK 2E'-13	United States
1998-067KJ	41762	Operational	FLOCK 2E'-14	United States
1998-067KL	41764	Operational	FLOCK 2E'-15	United States
1998-067KK	41763	Operational	FLOCK 2E'-16	United States
1998-067KN	41776	Operational	FLOCK 2E'-17	United States
1998-067KM	41769	Operational	FLOCK 2E'-18	United States
1998-067KP	41777	Operational	FLOCK 2E'-19	United States
1998-067JD	41483	Operational	FLOCK 2E-1	United States
1998-067JE	41484	Operational	FLOCK 2E-2	United States
1998-067KQ	41782	Operational	FLOCK 2E'-20	United States
1998-067JE	41484	Operational	FLOCK 2E-2	United States
1998-067JG	41486	Operational	FLOCK 2E-3	United States
1998-067JG	41486	Operational	FLOCK 2E-3	United States
1998-067JH	41487	Operational	FLOCK 2E-4	United States
1998-067JH	41487	Operational	FLOCK 2E-4	United States
1998-067JN	41564	Operational	FLOCK 2E-5	United States
1998-067JN	41564	Operational	FLOCK 2E-5	United States
1998-067JM	41563	Operational	FLOCK 2E-6	United States
1998-067JS	41568	Operational	FLOCK 2E'-6	United States
1998-067JP	41565	Operational	FLOCK 2E-7	United States
1998-067JP	41565	Operational	FLOCK 2E-7	United States
1998-067JQ	41566	Operational	FLOCK 2E-8	United States
1998-067JQ	41566	Operational	FLOCK 2E-8	United States
1998-067JV	41571	Operational	FLOCK 2E-9	United States
1998-067JV	41571	Operational	FLOCK 2E-9	United States
2016-040U	41617	Operational	FLOCK 2P-1	United States
2016-040P	41612	Operational	FLOCK 2P-10	United States
2016-040K	41608	Operational	FLOCK 2P-11	United States
2016-040R	41614	Operational	FLOCK 2P-12	United States
2016-040L	41609	Operational	FLOCK 2P-2	United States
2016-040V	41618	Operational	FLOCK 2P-3	United States
2016-040N	41611	Operational	FLOCK 2P-4	United States
2016-040T	41616	Operational	FLOCK 2P-5	United States
2016-040H	41606	Operational	FLOCK 2P-6	United States
2016-040S	41615	Operational	FLOCK 2P-7	United States
2016-040Q	41613	Operational	FLOCK 2P-8	United States
2016-040M	41610	Operational	FLOCK 2P-9	United States
2015-077E	41170	Operational	GALASSIA	Singapore

---

2013-066Q	39430	Operational	GOMX 1	Denmark
1998-067HA	40949	Decayed	GOMX 3	Denmark
2015-003D	40379	Operational	GRIFEX	United States
2013-064T	39397	Operational	HORUS	United States
2012-025D	38340	Operational	HORYU 2	Japan
2016-012D	41340	Operational	HORYU-IV	Japan
2013-066T	39433	Operational	HUMSAT-D	Spain
1998-067KU	41932	Operational	ITF-2	Japan
1998-067JL	41490	Operational	LEMUR-2-JEFF	United States
2015-052E	40934	Operational	LEMUR-2-JEROEN	United States
2015-049P	40912	Operational	KAITOU 1B	PR of China
2009-002H	33499	Operational	KKS-1 (KISEKI)	Japan
2014-033AL	40044	Operational	LEMUR-1	United States
2016-062E	41873	Operational	LEMUR-2-ANUBHAVTHAKUR	United States
2016-019C	41596	Operational	LEMUR-2-BRIDGETMAN	United States
2015-052D	40933	Operational	LEMUR-2-CHRIS	United States
2016-019D	41597	Operational	LEMUR-2-CUBECHEESE	United States
2016-019B	41595	Operational	LEMUR-2-DRMUZZ	United States
1998-067JL	41490	Operational	LEMUR-2-JEFF	United States
2015-052E	40934	Operational	LEMUR-2-JEROEN	United States
2015-052C	40932	Operational	LEMUR-2-JOEL	United States
1998-067JK	41489	Operational	LEMUR-2-KANE	United States
1998-067JJ	41488	Operational	LEMUR-2-NICK-ALLAIN	United States
2016-019E	41598	Operational	LEMUR-2-NATE	United States
2015-052F	40935	Operational	LEMUR-2-PETER	United States
2016-062D	41872	Operational	LEMUR-2-SOKOLSKY	United States
1998-067JF	41485	Operational	LEMUR-2-THERESACONDOR	United States
2016-062F	41874	Operational	LEMUR-2-WINGO	United States
2016-062C	41871	Operational	LEMUR-2-XIAOQING	United States
2002-052B	27562	Decayed	MEPSI	United States
2006-055B	29660	Decayed	MEPSI	United States
1998-067HU	41474	Operational	MINXSS	United States
2014-033Q	40024	Operational	NANOSATC-BR1	Brazil
1998-067HY	41478	Operational	NODES 1	United States
1998-067HX	41477	Operational	NODES 2	United States
2013-064K	39389	Decayed	NPS-SCAT	United States
2015-049B	40900	Operational	NUDT-PHONESAT	PR of China
2016-067D	41851	Operational	OPTICUBE 04	United States
2013-066E	39420	Operational	OPTOS	Spain
1998-067KZ	41939	Operational	OSNSAT	United States
2016-025C	41458	Operational	OUFTI-1	Belgium
2001-043C	26931	Partially Op.	PCSAT (NO-44)	United States
2014-033AF	40039	Operational	PERSEUS-M1	CIS (former USSR)
2014-033AD	40037	Operational	PERSEUS-M2	CIS (former USSR)

## A: List of historic nanosatellite missions

---

2013-064B	39381	Decayed	PHONESAT 2.4	United States
2014-033AJ	40042	Operational	POLYITAN-1	Ukraine
2013-055D	39268	Operational	POPACS 1	United States
2013-055E	39269	Operational	POPACS 2	United States
2013-055F	39270	Operational	POPACS 3	United States
2014-033U	40028	Operational	POPSAT-HIP-1	Singapore
2009-002B	33493	Operational	PRISM (HITOMI)	Japan
2016-067G	41854	Operational	PROMETHEUS 2-1	United States
2016-067H	41855	Operational	PROMETHEUS 2-3	United States
2014-033R	40025	Operational	QB50P1	Belgium
2014-033Y	40032	Operational	QB50P2	Belgium
2016-067B	41849	Operational	RAVAN	United States
2016-026C	41466	Operational	SAMSAT-218D	CIS (former USSR)
2016-040B	41600	Operational	SATHYABAMASAT	India
2002-058C	27607	Operational	SAUDISAT 1C (SO-50)	Saudi Arabia
2014-029E	39770	Operational	SPROUT	Japan
2009-002G	33498	Operational	STARS (KUKAI)	Japan
1998-067KR	41895	Operational	STARS-C	Japan
1998-067HW	41476	Operational	STMSAT-1	United States
2016-040J	41607	Operational	SWAYAM	India
1998-067GY	40898	Decayed	S-CUBE	Japan
1998-067KT	41931	Operational	TANCREDO-1	Brazil
2015-051B	40926	Operational	TIANWANG 1C (TW-1C)	PR of China
2015-051D	40928	Operational	TIANWANG 1A (TW-1A)	PR of China
2015-051C	40927	Operational	TIANWANG 1B (TW-1B)	PR of China
2014-033AK	40043	Operational	TIGRISAT	Iraq
2013-066M	39427	Operational	TRITON-1	United Kingdom
1998-067KY	41936	Operational	TUPOD	Italy
2014-037F	40074	Operational	UKUBE-1	United Kingdom
2013-009G	39092	Operational	UNIBRITE	Austria
2013-066AG	39446	Operational	UWE-3	Germany
2015-077F	41171	Operational	VELOX 2	Singapore
1998-067KV	41933	Operational	WASEDA-SAT3	Japan
2013-066H	39423	Operational	WNISAT-1	Japan
2013-066V	39435	Nonoperational	WREN	Germany
2015-049N	40911	Operational	XW-2B	PR of China
2015-049H	40906	Operational	XW-2C	PR of China
2015-049J	40907	Operational	XW-2D	PR of China
2015-049L	40909	Nonoperational	XW-2E	PR of China
2015-049M	40910	Operational	XW-2F	PR of China
2013-066B	39417	Operational	ZACUBE-1 (TSHEPISOSAT)	South Africa
2010-047B	37166	Operational	ZHEDA PIXING 1B	PR of China
2010-047C	37167	Operational	ZHEDA PIXING 1C	PR of China
2012-048C	38760	Operational	AENEAS	United States

---

2012-048K	38767	Operational	AEROCUBE 4.5A	United States
2012-048L	38768	Operational	AEROCUBE 4.5B	United States
2013-072D	39465	Operational	AEROCUBE 5A	United States
2013-072E	39466	Operational	AEROCUBE 5B	United States
2015-058B	40965	Operational	AEROCUBE 5C	United States
2015-058C	40966	Operational	AEROCUBE 7	United States
2015-025J	40659	Operational	AEROCUBE 8A	United States
2015-025K	40660	Operational	AEROCUBE 8B	United States
2013-072F	39467	Operational	ALICE	United States
2015-058F	40969	Operational	ARC-1	United States
2015-058E	40968	Operational	BISONSAT	United States
2012-048G	38764	Operational	CINEMA	United States
2012-048D	38761	Operational	CSSWE	United States
2013-072B	39463	Operational	FIREBIRD A	United States
2013-072C	39464	Operational	FIREBIRD B	United States
2015-058D	40967	Operational	FOX-1	United States
2015-025G	40657	Operational	GEARRS-2	United States
2015-058H	40971	Operational	LMRST-SAT	United States
2010-062C	37224	Operational	O/OREOS (USA 219)	United States
2015-025D	40654	Operational	PARKINSONSAT (PSAT)	United States
2015-058N	40976	Operational	PROPCUBE 1	United States
2015-058K	40973	Operational	PROPCUBE 3	United States
2015-058L	40974	Operational	SINOD-D 1	United States
2015-058P	40977	Operational	SINOD-D 3	United States
2012-048J	38766	Operational	SMDC ONE 1.1	United States
2012-048B	38759	Operational	SMDC ONE 1.2	United States
2013-072N	39474	Operational	SMDC ONE 2.3	United States
2013-072L	39472	Operational	SMDC ONE 2.4	United States
2015-058G	40970	Operational	SNAP-3 ALICE	United States
2015-058J	40972	Operational	SNAP-3 EDDIE	United States
2015-058M	40975	Operational	SNAP-3 JIMI	United States

---

Blank page

## B: Nanosatellite missions for 2017

Table 2 Projected nanosatellite launches for 2017.

Number	Name	CubeSat Factor	Vehicle	Launch Site	Date	Propulsion system	Country	Developer
1	XY S1 (Xingyun Shiyan 1)	2U	Kuaizhou-1A	JSLC (Mongolia)	09/01/201	--	China	Univ.
2	Kaidun 1 (Caton 1)	2U	Kuaizhou-1A	JSLC (Mongolia)	09/01/201	--	China	Univ. + Comm.
3	TRICOM 1	3U	SS-520-4 nano-satellite launcher	KSCUT (Japan)	14/01/201	--	Japan	Univ.
4 – 5	INS 1 A – B	--	PSLV-XL	SDSC (India)	15/02/201	--	India	Gov.
6 – 94	Flock 3p 1 – 88	3U	PSLV-XL	SDSC (India)	15/02/201	--	USA	Comm.
95 – 103	Lemur-2 22 – 29	3U	PSLV-XL	SDSC (India)	15/02/201	--	USA	Comm.
104	BGUSat	3U	PSLV-XL	SDSC (India)	15/02/201	--	Israel	Univ.
105	DIDO 2 (Chen Jiayong 1)	3U	PSLV-XL	SDSC (India)	15/02/201	--	Israel, Switzerland	Comm.
106	PEASSS	3U	PSLV-XL	SDSC (India)	15/02/201	--	Netherlands, Germany, Belgium, Israel	Comm.
107	Al-Farabi 1	2U	PSLV-XL	SDSC (India)	15/02/201	--	Kazakhstan	Univ.
108	Nayif 1 (FUNcube 5)	1U	PSLV-XL	SDSC (India)	15/02/201	--	United Arab Emirates	Gov. + Univ.
109	ALTAIR 1	6U	ISS	WLPIS (USA)	--	--	USA	Comm.
110	SUSat (QB50 AU01)	2U	ISS	CCAFS (USA)	--	--	Australia	Univ.
111	UNSW-ECO (QB50 AU02)	2U	ISS	CCAFS (USA)	--	--	Australia	Univ.
112	i-INSPIRE 2 (QB50 AU03)	2U	ISS	CCAFS (USA)	--	--	Australia	Univ.
113	ZA-AeroSat (QB50 AZ01)	2U	ISS	CCAFS (USA)	--	--	South Africa	Univ.
114	nSIGHT 1 (QB50 AZ02)	2U	ISS	CCAFS (USA)	--	--	South Africa	Univ. + Comm.
115	Ex-Alta 1 (QB50 CA03)	3U	ISS	CCAFS (USA)	--	--	Canada	Univ.
116	LilacSat 1 (QB50 CN02)	2U	ISS	CCAFS (USA)	--	--	China	Univ.
117	NJUST 1 (QB50 CN03)	2U	ISS	CCAFS (USA)	--	--	China	Univ.
118	Aoxiang 1 (QB50 CN04)	2U	ISS	CCAFS (USA)	--	--	China	Univ.
119	SOMP 2 (QB50 DE02)	2U	ISS	CCAFS (USA)	--	--	Germany	Univ.
120	QBITO (QB50 ES01)	2U	ISS	CCAFS (USA)	--	--	Spain	Univ.
121	Aalto 2 (QB50 FI01)	2U	ISS	CCAFS (USA)	--	--	Finland	Univ.
122	X-CubeSat (QB50 FR01)	2U	ISS	CCAFS (USA)	--	--	France	Univ.
123	SpaceCube (QB50 FR05)	2U	ISS	CCAFS (USA)	--	--	France	Univ.
124	DUTHSat (QB50 GR01)	2U	ISS	CCAFS (USA)	--	--	Greece	Univ.
125	UPSat (QB50 GR02)	2U	ISS	CCAFS (USA)	--	--	Greece	Univ.
126	Hoopoe (QB50 IL01)	2U	ISS	CCAFS (USA)	--	--	Greece	Civil
127	LINK (QB50 KR01)	2U	ISS	CCAFS (USA)	--	--	South Korea	Univ.

## B: Nanosatellite missions for 2017

---

128	SNUSAT 1 (QB50 KR02)	2U	ISS	CCAFS (USA)	--	--	South Korea	Univ.
129	qbee50-LTU-OC (QB50 SE01)	2U	ISS	CCAFS (USA)	--	--	Sweden	Univ.
130	BeEagleSat (QB50 TR01)	2U	ISS	CCAFS (USA)	--	--	Turkey	Univ.
131	HAVELSAT (QB50 TR02)	2U	ISS	CCAFS (USA)	--	--	Turkey	Univ.
132	Phoenix (QB50 TW01)	2U	ISS	CCAFS (USA)	--	--	Taiwan	Univ.
133	PolyITAN 2-SAU (QB50 UA01)	2U	ISS	CCAFS (USA)	--	--	Ukraine	Univ.
134	QBUS 1 (QB50 US01)	2U	ISS	CCAFS (USA)	--	--	USA	Univ.
135	QBUS 2 (QB50 US02)	2U	ISS	CCAFS (USA)	--	--	USA	Univ.
136	QBUS 4 (QB50 US04)	2U	ISS	CCAFS (USA)	--	--	USA	Univ.
137	IceCube (Earth 1)	3U	ISS	CCAFS (USA)	--	--	USA	Gov.
138	CSUNSat 1	2U	ISS	CCAFS (USA)	--	--	USA	Gov.
139	CXBN 2	2U	ISS	CCAFS (USA)	--	--	USA	Univ.
140	Biarri-Point	3U	ISS	CCAFS (USA)	--	--	Australia, USA, Canada, UK	Gov.
141	Venta 1	3U	PSLV-XL	SDSC (India)	--	--	Latvia	Univ.
142 –	R – G – B Diamonds	3U	PSLV-XL	SDSC (India)	--	--	UK, Israel,	Comm.
144							Australia	
145	PicSat	3U	PSLV-XL	SDSC (India)	--	--	France	Gov.
146	COMPASS 2 (QB50 DE04)	3U	PSLV-XL	SDSC (India)	--	--	Germany	Univ.
147	InflateSail (QB50 GB06)	3U	PSLV-XL	SDSC (India)	--	--	UK	Univ.
148	LituaniaSAT 2 (QB50 LT01)	3U	PSLV-XL	SDSC (India)	--	Chemical	Lithuania	Univ.
149	URSA MAIOR (QB50 IT02)	3U	PSLV-XL	SDSC (India)	--	Cold gas	Italy	Univ.
150	NUDTSat (QB50 CN06)	2U	PSLV-XL	SDSC (India)	--	--	China	Univ.
151	Pegasus (QB50 AT03)	2U	PSLV-XL	SDSC (India)	--	PPT	Austria	Univ.
152	UCLSat (QB50 GB03)	2U	PSLV-XL	SDSC (India)	--	--	UK	Univ.
153	VZLUsat 1 (QB50 CZ02)	2U	PSLV-XL	SDSC (India)	--	--	Czech Republic	Univ.
154	Aalto 1	3U	PSLV-XL	SDSC (India)	--	--	Finland	Univ.
155	ROBUSTA 1B	1U	PSLV-XL	SDSC (India)	--	--	France	Univ.
156	COPPER 2 (SLU 03)	3U	Minotaur-C- 3210	VBG (USA)	--	--	USA	Univ.
157 –	CPOD A – B	3U	Minotaur-C- 3210	VBG (USA)	--	Cold gas	USA	Comm.
158	MinXSS 2	3U	Minotaur-C- 3210	VBG (USA)	--	--	USA	Univ.
160 –	RANGE A – B	1.5U	Minotaur-C- 3210	VBG (USA)	--	--	USA	Univ.
161								
162	ASTERIA	6U	Falcon-9 v1.2	CCAFS (USA)	--	--	USA	Univ.
163	LAICE	6U	Falcon-9 v1.2	CCAFS (USA)	--	--	USA	Univ.
164	RBLE	6U	Falcon-9 v1.2	CCAFS (USA)	--	--	USA	Gov.
165	OPAL	3U	Falcon-9 v1.2	CCAFS (USA)	--	--	USA	Univ.
166	OSIRIS-3U	3U	Falcon-9 v1.2	CCAFS (USA)	--	--	USA	Univ.
167	HARP	3U	Falcon-9 v1.2	CCAFS (USA)	--	--	USA	Univ.
168	OPEN	1U	Falcon-9 v1.2	CCAFS (USA)	--	--	USA	Univ.
169	Overview 1	3U	Falcon-9 v1.2	CCAFS (USA)	--	--	USA	Univ.
170 –	Corvus-BC 1 – 2	6U	Soyuz-2-1a	TYMSC	--	--	USA	Comm.
171			Fregat-M (Kazakhstan)					
172 –	Perseus-O 1 – 4	6U	Soyuz-2-1a	TYMSC	--	--	Russia, South	Comm.
175			Fregat-M (Kazakhstan)				Korea	
176 –	MKA-N 1 – 2	6U	Soyuz-2-1a	TYMSC	--	--	Russia	Gov. + Comm.
177			Fregat-M (Kazakhstan)					
178 –	Flock-2k 1 – 48	3U	Soyuz-2-1a	TYMSC	--	--	USA	Comm.
225			Fregat-M (Kazakhstan)					
226	Mayak	3U	Soyuz-2-1a	TYMSC	--	--	Russia	Univ.
			Fregat-M (Kazakhstan)					

227 –	SAMSON 1 – 3	6U	Vega	FRGUI (French Guiana)	--	PPT (?)	Israel	Comm.
229								
230	LightSail B	3U	Falcon-Heavy	CCAFS (USA)	--	--	USA	Civil
231	ARMADILLO	3U	Falcon-Heavy	CCAFS (USA)	--	--	USA	Univ.
232	FalconSat 7 (Peregrine)	3U	Falcon-Heavy	CCAFS (USA)	--	--	USA	Mil.
233 –	TBEx A – B	3U	Falcon-Heavy	CCAFS (USA)	--	--	USA	Civil
234								
235 –	Prometheus 2.2 – 2.10	1.5U	Falcon-Heavy	CCAFS (USA)	--	--	USA	Gov.
242								
243	PSat 2	1.5U	Falcon-Heavy	CCAFS (USA)	--	--	USA	Univ.
244	BRICSat 2	1.5U	Falcon-Heavy	CCAFS (USA)	--	$\mu$ -CAT	USA	Univ.
245 –	TEPCE 1 – 2	3U	Falcon-Heavy	CCAFS (USA)	--	--	USA	Mil.
246								
247	CP 9 (LEO)	2U	Falcon-Heavy	CCAFS (USA)	--	--	USA	Univ.
248	StangSat	1U	Falcon-Heavy	CCAFS (USA)	--	--	USA	Univ.
249	Buccaneer RMM	3U	Delta-7920-10C	VBG (USA)	--	--	Australia	Univ.
250	MiRaTA	3U	Delta-7920-10C	VBG (USA)	--	--	USA	Univ.
251	EagleSat	1U	Delta-7920-10C	VBG (USA)	--	--	USA	Univ.
252	RadFxSat (Fox 1B)	1U	Delta-7920-10C	VBG (USA)	--	--	USA	Civil
253	MakerSat 0	1U	Delta-7920-10C	VBG (USA)	--	--	USA	Univ.
254	INCA	6U	LauncherOne	MHV (USA)	--	--	USA	Univ.
255	ALBus	3U	LauncherOne	MHV (USA)	--	--	USA	Gov.
256	CACTUS 1	3U	LauncherOne	MHV (USA)	--	--	USA	Univ.
257	+ExoCube 2	3U	LauncherOne	MHV (USA)	--	--	USA	Gov. + Univ.
258	MicroMAS 2b	3U	LauncherOne	MHV (USA)	--	--	USA	Univ.
259	MiTEE 1	3U	LauncherOne	MHV (USA)	--	--	USA	Univ.
260	PolarCube	3U	LauncherOne	MHV (USA)	--	--	USA	Univ.
261	Q-PACE (Cu-PACE)	2U	LauncherOne	MHV (USA)	--	--	USA	Univ.
262	SurfSat	2U	LauncherOne	MHV (USA)	--	--	USA	Univ.
263	CAPE 3	1U	LauncherOne	MHV (USA)	--	--	USA	Univ.
264	RadFxSat 2 (Fox 1E)	1U	LauncherOne	MHV (USA)	--	--	USA	Civil
265 –	PICS 1 – 2	1U	LauncherOne	MHV (USA)	--	--	USA	Univ.
266								
267	AISSat 3	--	Soyuz-2-1b Fregat-M	VOSTO (Russia)	--	--	Norway	Gov.
268	SEAM	3U	Soyuz-2-1b Fregat-M	VOSTO (Russia)	--	--	Sweden	Univ.
269	ANDESITE	6U	Electron	MRLLS (New Zealand)	--	--	USA	Univ.
270	CeREs	3U	Electron	MRLLS (New Zealand)	--	--	USA	Gov.
271	CHOMPTT	3U	Electron	MRLLS (New Zealand)	--	--	USA	Univ.
272	Da Vinci	3U	Electron	MRLLS (New Zealand)	--	--	USA	Univ.
273	ISX (CP 11)	3U	Electron	MRLLS (New Zealand)	--	--	USA	Univ.
274	NMTSat	3U	Electron	MRLLS (New Zealand)	--	--	USA	Univ.
275	RSat-P	3U	Electron	MRLLS (New Zealand)	--	--	USA	Univ.
276	Shields 1	3U	Electron	MRLLS (New Zealand)	--	--	USA	Gov.
277	STF 1	3U	Electron	MRLLS (New Zealand)	--	--	USA	Gov.
278 –	CubeSail 1 – 2	1.5U	Electron	MRLLS (New Zealand)	--	--	USA	Univ.
279								
280 –	Lemur – 2	3U	--	--	--	--	USA	Comm.
--	Flock –	3U	--	--	--	--	USA	Comm.

Blank page

## C: Total Ionising Dose (TID)

Table 3 Dose at transmission surface of aluminium slab shields. Data from the ESA's Space Environment Information System [102] using the AE-8/AP-8 Radiation Belt Models and the SHIELDOSE-2 dose model.

Altitude [km]	Inclination [deg]	Absorber Thickness [mm]	Dose [rad]			
			Total	Electrons	Bremsstrahlung	Trapped Protons
500	0	5.0000E-02	3.9361E-02	3.9287E-02	7.3869E-05	0.0000E+00
500	0	1.0000E-01	3.4759E-02	3.4686E-02	7.3187E-05	0.0000E+00
500	0	2.0000E-01	2.7775E-02	2.7709E-02	6.6391E-05	0.0000E+00
500	0	3.0000E-01	2.2779E-02	2.2719E-02	6.0944E-05	0.0000E+00
500	0	4.0000E-01	1.9307E-02	1.9250E-02	5.6937E-05	0.0000E+00
500	0	5.0000E-01	1.6892E-02	1.6838E-02	5.4417E-05	0.0000E+00
500	0	6.0000E-01	1.5152E-02	1.5099E-02	5.2450E-05	0.0000E+00
500	0	8.0000E-01	1.2752E-02	1.2702E-02	4.9704E-05	0.0000E+00
500	0	1.0000E+00	1.1080E-02	1.1033E-02	4.7786E-05	0.0000E+00
500	0	1.5000E+00	8.3775E-03	8.3331E-03	4.4413E-05	0.0000E+00
500	0	2.0000E+00	6.6631E-03	6.6221E-03	4.1014E-05	0.0000E+00
500	0	2.5000E+00	5.3641E-03	5.3265E-03	3.7597E-05	0.0000E+00
500	0	3.0000E+00	4.2765E-03	4.2424E-03	3.4160E-05	0.0000E+00
500	0	4.0000E+00	2.4953E-03	2.4671E-03	2.8228E-05	0.0000E+00
500	0	5.0000E+00	1.2220E-03	1.1983E-03	2.3722E-05	0.0000E+00
500	0	6.0000E+00	4.6019E-04	4.3982E-04	2.0377E-05	0.0000E+00
500	0	7.0000E+00	1.2567E-04	1.0783E-04	1.7838E-05	0.0000E+00
500	0	8.0000E+00	2.8078E-05	1.2179E-05	1.5899E-05	0.0000E+00
500	0	9.0000E+00	1.4755E-05	3.2307E-07	1.4432E-05	0.0000E+00
500	0	1.0000E+01	1.3338E-05	8.1713E-09	1.3330E-05	0.0000E+00
500	0	1.2000E+01	1.1692E-05	0.0000E+00	1.1692E-05	0.0000E+00
500	0	1.4000E+01	1.0586E-05	0.0000E+00	1.0586E-05	0.0000E+00
500	0	1.6000E+01	9.7764E-06	0.0000E+00	9.7764E-06	0.0000E+00
500	0	1.8000E+01	9.0819E-06	0.0000E+00	9.0819E-06	0.0000E+00
500	0	2.0000E+01	8.4651E-06	0.0000E+00	8.4651E-06	0.0000E+00

## C: Total Ionising Dose (TID)

---

600	0	5.0000E-02	9.1103E-01	8.2135E-01	1.5254E-03	8.8157E-02
600	0	1.0000E-01	7.2365E-01	6.5101E-01	1.3374E-03	7.1302E-02
600	0	2.0000E-01	4.9732E-01	4.3267E-01	1.0007E-03	6.3644E-02
600	0	3.0000E-01	3.5989E-01	2.9912E-01	7.9097E-04	5.9981E-02
600	0	4.0000E-01	2.7600E-01	2.1805E-01	6.5557E-04	5.7300E-02
600	0	5.0000E-01	2.2457E-01	1.6881E-01	5.7234E-04	5.5189E-02
600	0	6.0000E-01	1.9150E-01	1.3760E-01	5.1255E-04	5.3391E-02
600	0	8.0000E-01	1.5151E-01	1.0065E-01	4.3398E-04	5.0423E-02
600	0	1.0000E+00	1.2731E-01	7.8927E-02	3.8332E-04	4.7995E-02
600	0	1.5000E+00	9.3829E-02	5.0286E-02	3.0739E-04	4.3236E-02
600	0	2.0000E+00	7.5616E-02	3.5809E-02	2.6080E-04	3.9546E-02
600	0	2.5000E+00	6.3287E-02	2.6513E-02	2.2721E-04	3.6547E-02
600	0	3.0000E+00	5.3767E-02	1.9637E-02	2.0059E-04	3.3929E-02
600	0	4.0000E+00	3.9557E-02	1.0005E-02	1.6056E-04	2.9392E-02
600	0	5.0000E+00	2.9869E-02	4.3749E-03	1.3314E-04	2.5361E-02
600	0	6.0000E+00	2.3347E-02	1.4937E-03	1.1394E-04	2.1739E-02
600	0	7.0000E+00	1.8912E-02	3.5051E-04	9.9797E-05	1.8462E-02
600	0	8.0000E+00	1.5809E-02	3.9202E-05	8.9237E-05	1.5680E-02
600	0	9.0000E+00	1.3432E-02	1.0480E-06	8.1229E-05	1.3350E-02
600	0	1.0000E+01	1.1585E-02	2.6318E-08	7.5076E-05	1.1510E-02
600	0	1.2000E+01	9.1382E-03	0.0000E+00	6.5932E-05	9.0722E-03
600	0	1.4000E+01	7.5904E-03	0.0000E+00	5.9496E-05	7.5309E-03
600	0	1.6000E+01	6.3952E-03	0.0000E+00	5.4566E-05	6.3407E-03
600	0	1.8000E+01	5.3013E-03	0.0000E+00	5.0400E-05	5.2509E-03
600	0	2.0000E+01	4.2913E-03	0.0000E+00	4.6794E-05	4.2445E-03
700	0	5.0000E-02	3.8369E+01	1.7872E+01	3.3242E-02	2.0463E+01
700	0	1.0000E-01	2.9673E+01	1.2247E+01	2.5185E-02	1.7400E+01
700	0	2.0000E-01	2.1671E+01	6.4447E+00	1.5393E-02	1.5210E+01
700	0	3.0000E-01	1.7715E+01	3.5957E+00	1.0419E-02	1.4109E+01
700	0	4.0000E-01	1.5496E+01	2.1559E+00	7.6259E-03	1.3332E+01
700	0	5.0000E-01	1.4163E+01	1.4179E+00	6.0437E-03	1.2739E+01
700	0	6.0000E-01	1.3292E+01	1.0189E+00	5.0127E-03	1.2269E+01
700	0	8.0000E-01	1.2184E+01	6.2516E-01	3.7868E-03	1.1555E+01
700	0	1.0000E+00	1.1462E+01	4.3156E-01	3.0776E-03	1.1028E+01
700	0	1.5000E+00	1.0323E+01	2.2189E-01	2.1428E-03	1.0099E+01
700	0	2.0000E+00	9.5619E+00	1.3841E-01	1.6725E-03	9.4218E+00
700	0	2.5000E+00	8.9753E+00	9.3028E-02	1.3920E-03	8.8809E+00
700	0	3.0000E+00	8.4964E+00	6.3555E-02	1.1996E-03	8.4316E+00
700	0	4.0000E+00	7.7266E+00	2.7953E-02	9.3867E-04	7.6977E+00
700	0	5.0000E+00	7.1143E+00	1.0704E-02	7.7159E-04	7.1028E+00
700	0	6.0000E+00	6.6183E+00	3.2864E-03	6.5829E-04	6.6143E+00
700	0	7.0000E+00	6.1927E+00	7.0541E-04	5.7597E-04	6.1914E+00
700	0	8.0000E+00	5.8339E+00	7.3781E-05	5.1476E-04	5.8333E+00

700	0	9.0000E+00	5.5170E+00	1.9231E-06	4.6766E-04	5.5166E+00
700	0	1.0000E+01	5.2404E+00	4.9779E-08	4.3013E-04	5.2400E+00
700	0	1.2000E+01	4.7573E+00	0.0000E+00	3.7323E-04	4.7569E+00
700	0	1.4000E+01	4.3505E+00	0.0000E+00	3.3165E-04	4.3502E+00
700	0	1.6000E+01	4.0079E+00	0.0000E+00	2.9888E-04	4.0076E+00
700	0	1.8000E+01	3.7066E+00	0.0000E+00	2.7175E-04	3.7064E+00
700	0	2.0000E+01	3.4478E+00	0.0000E+00	2.4890E-04	3.4475E+00
800	0	5.0000E-02	5.0661E+02	3.7638E+02	7.0058E-01	1.2952E+02
800	0	1.0000E-01	3.5072E+02	2.3581E+02	4.8763E-01	1.1443E+02
800	0	2.0000E-01	2.0823E+02	1.0444E+02	2.6269E-01	1.0353E+02
800	0	3.0000E-01	1.4665E+02	4.8501E+01	1.6072E-01	9.7990E+01
800	0	4.0000E-01	1.1799E+02	2.3993E+01	1.0844E-01	9.3890E+01
800	0	5.0000E-01	1.0390E+02	1.3164E+01	8.0597E-02	9.0658E+01
800	0	6.0000E-01	9.6217E+01	8.1458E+00	6.3699E-02	8.8008E+01
800	0	8.0000E-01	8.8163E+01	4.0683E+00	4.5096E-02	8.4050E+01
800	0	1.0000E+00	8.3704E+01	2.4310E+00	3.5209E-02	8.1237E+01
800	0	1.5000E+00	7.7475E+01	9.7439E-01	2.3089E-02	7.6478E+01
800	0	2.0000E+00	7.3607E+01	5.1936E-01	1.7361E-02	7.3070E+01
800	0	2.5000E+00	7.0675E+01	3.1215E-01	1.4178E-02	7.0348E+01
800	0	3.0000E+00	6.8211E+01	1.9467E-01	1.2096E-02	6.8005E+01
800	0	4.0000E+00	6.4194E+01	7.2278E-02	9.3812E-03	6.4113E+01
800	0	5.0000E+00	6.0945E+01	2.3611E-02	7.6679E-03	6.0914E+01
800	0	6.0000E+00	5.8236E+01	6.3767E-03	6.5044E-03	5.8223E+01
800	0	7.0000E+00	5.5854E+01	1.2417E-03	5.6569E-03	5.5847E+01
800	0	8.0000E+00	5.3780E+01	1.2207E-04	5.0199E-03	5.3775E+01
800	0	9.0000E+00	5.1888E+01	3.1216E-06	4.5214E-03	5.1883E+01
800	0	1.0000E+01	5.0147E+01	8.2646E-08	4.1152E-03	5.0143E+01
800	0	1.2000E+01	4.7011E+01	0.0000E+00	3.4908E-03	4.7007E+01
800	0	1.4000E+01	4.4164E+01	0.0000E+00	3.0287E-03	4.4161E+01
800	0	1.6000E+01	4.1624E+01	0.0000E+00	2.6661E-03	4.1622E+01
800	0	1.8000E+01	3.9295E+01	0.0000E+00	2.3725E-03	3.9293E+01
800	0	2.0000E+01	3.7189E+01	0.0000E+00	2.1303E-03	3.7187E+01
900	0	5.0000E-02	4.7974E+03	4.3472E+03	8.0917E+00	4.4206E+02
900	0	1.0000E-01	3.0385E+03	2.6298E+03	5.4577E+00	4.0321E+02
900	0	2.0000E-01	1.4591E+03	1.0861E+03	2.8097E+00	3.7022E+02
900	0	3.0000E-01	8.1789E+02	4.6646E+02	1.6599E+00	3.4977E+02
900	0	4.0000E-01	5.4565E+02	2.1055E+02	1.0901E+00	3.3401E+02
900	0	5.0000E-01	4.2734E+02	1.0455E+02	7.9356E-01	3.2200E+02
900	0	6.0000E-01	3.7191E+02	5.8897E+01	6.1827E-01	3.1239E+02
900	0	8.0000E-01	3.2389E+02	2.5520E+01	4.3070E-01	2.9794E+02
900	0	1.0000E+00	3.0118E+02	1.3731E+01	3.3403E-01	2.8711E+02
900	0	1.5000E+00	2.7185E+02	4.5210E+00	2.1783E-01	2.6711E+02
900	0	2.0000E+00	2.5406E+02	2.1028E+00	1.6310E-01	2.5179E+02

## C: Total Ionising Dose (TID)

---

900	0	2.5000E+00	2.4077E+02	1.1449E+00	1.3290E-01	2.3949E+02
900	0	3.0000E+00	2.2993E+02	6.6119E-01	1.1316E-01	2.2916E+02
900	0	4.0000E+00	2.1323E+02	2.1512E-01	8.7553E-02	2.1293E+02
900	0	5.0000E+00	2.0068E+02	6.1758E-02	7.1365E-02	2.0055E+02
900	0	6.0000E+00	1.9077E+02	1.4677E-02	6.0325E-02	1.9070E+02
900	0	7.0000E+00	1.8230E+02	2.5389E-03	5.2272E-02	1.8225E+02
900	0	8.0000E+00	1.7503E+02	2.3226E-04	4.6190E-02	1.7498E+02
900	0	9.0000E+00	1.6844E+02	5.8514E-06	4.1405E-02	1.6840E+02
900	0	1.0000E+01	1.6244E+02	1.5770E-07	3.7491E-02	1.6240E+02
900	0	1.2000E+01	1.5186E+02	0.0000E+00	3.1462E-02	1.5183E+02
900	0	1.4000E+01	1.4256E+02	0.0000E+00	2.7002E-02	1.4253E+02
900	0	1.6000E+01	1.3449E+02	0.0000E+00	2.3526E-02	1.3446E+02
900	0	1.8000E+01	1.2720E+02	0.0000E+00	2.0736E-02	1.2718E+02
900	0	2.0000E+01	1.2065E+02	0.0000E+00	1.8450E-02	1.2064E+02
1000	0	5.0000E-02	3.0059E+04	2.8726E+04	5.3489E+01	1.2799E+03
1000	0	1.0000E-01	1.8245E+04	1.7019E+04	3.5447E+01	1.1908E+03
1000	0	2.0000E-01	7.8959E+03	6.7868E+03	1.7869E+01	1.0912E+03
1000	0	3.0000E-01	3.8490E+03	2.8178E+03	1.0414E+01	1.0207E+03
1000	0	4.0000E-01	2.1967E+03	1.2245E+03	6.7784E+00	9.6539E+02
1000	0	5.0000E-01	1.5107E+03	5.8281E+02	4.9043E+00	9.2295E+02
1000	0	6.0000E-01	1.2076E+03	3.1498E+02	3.8078E+00	8.8881E+02
1000	0	8.0000E-01	9.6723E+02	1.2796E+02	2.6458E+00	8.3663E+02
1000	0	1.0000E+00	8.6470E+02	6.5667E+01	2.0526E+00	7.9698E+02
1000	0	1.5000E+00	7.4553E+02	1.9752E+01	1.3415E+00	7.2444E+02
1000	0	2.0000E+00	6.8066E+02	8.5554E+00	1.0048E+00	6.7110E+02
1000	0	2.5000E+00	6.3496E+02	4.3916E+00	8.1845E-01	6.2975E+02
1000	0	3.0000E+00	5.9903E+02	2.4150E+00	6.9631E-01	5.9592E+02
1000	0	4.0000E+00	5.4571E+02	7.2041E-01	5.3793E-01	5.4445E+02
1000	0	5.0000E+00	5.0732E+02	1.8775E-01	4.3782E-01	5.0669E+02
1000	0	6.0000E+00	4.7795E+02	3.9682E-02	3.6949E-01	4.7754E+02
1000	0	7.0000E+00	4.5339E+02	5.9199E-03	3.1966E-01	4.5307E+02
1000	0	8.0000E+00	4.3265E+02	4.6225E-04	2.8196E-01	4.3236E+02
1000	0	9.0000E+00	4.1410E+02	1.0710E-05	2.5227E-01	4.1385E+02
1000	0	1.0000E+01	3.9746E+02	3.1629E-07	2.2798E-01	3.9724E+02
1000	0	1.2000E+01	3.6889E+02	0.0000E+00	1.9057E-01	3.6870E+02
1000	0	1.4000E+01	3.4463E+02	0.0000E+00	1.6293E-01	3.4447E+02
1000	0	1.6000E+01	3.2416E+02	0.0000E+00	1.4145E-01	3.2402E+02
1000	0	1.8000E+01	3.0600E+02	0.0000E+00	1.2426E-01	3.0588E+02
1000	0	2.0000E+01	2.8988E+02	0.0000E+00	1.1022E-01	2.8977E+02
500	30	5.0000E-02	7.8369E+03	7.7373E+03	1.4592E+01	8.5046E+01
500	30	1.0000E-01	3.8832E+03	3.7967E+03	8.4148E+00	7.8061E+01
500	30	2.0000E-01	1.3188E+03	1.2445E+03	3.8412E+00	7.0467E+01
500	30	3.0000E-01	5.6323E+02	4.9591E+02	2.2045E+00	6.5114E+01

500	30	4.0000E-01	2.8624E+02	2.2371E+02	1.4582E+00	6.1075E+01
500	30	5.0000E-01	1.7393E+02	1.1475E+02	1.0780E+00	5.8103E+01
500	30	6.0000E-01	1.2454E+02	6.7908E+01	8.5495E-01	5.5778E+01
500	30	8.0000E-01	8.5807E+01	3.2894E+01	6.1209E-01	5.2301E+01
500	30	1.0000E+00	6.9677E+01	1.9475E+01	4.8234E-01	4.9720E+01
500	30	1.5000E+00	5.3077E+01	7.5147E+00	3.1899E-01	4.5243E+01
500	30	2.0000E+00	4.6201E+01	3.7364E+00	2.3897E-01	4.2226E+01
500	30	2.5000E+00	4.2257E+01	2.0394E+00	1.9334E-01	4.0024E+01
500	30	3.0000E+00	3.9576E+01	1.1451E+00	1.6329E-01	3.8267E+01
500	30	4.0000E+00	3.6020E+01	3.3428E-01	1.2484E-01	3.5561E+01
500	30	5.0000E+00	3.3620E+01	7.2357E-02	1.0098E-01	3.3447E+01
500	30	6.0000E+00	3.1793E+01	1.0566E-02	8.4848E-02	3.1698E+01
500	30	7.0000E+00	3.0235E+01	1.0722E-03	7.3158E-02	3.0161E+01
500	30	8.0000E+00	2.8889E+01	6.3654E-05	6.4339E-02	2.8825E+01
500	30	9.0000E+00	2.7669E+01	1.3932E-06	5.7416E-02	2.7612E+01
500	30	1.0000E+01	2.6560E+01	4.3541E-08	5.1786E-02	2.6508E+01
500	30	1.2000E+01	2.4611E+01	0.0000E+00	4.3168E-02	2.4568E+01
500	30	1.4000E+01	2.2907E+01	0.0000E+00	3.6835E-02	2.2871E+01
500	30	1.6000E+01	2.1441E+01	0.0000E+00	3.1936E-02	2.1409E+01
500	30	1.8000E+01	2.0129E+01	0.0000E+00	2.8027E-02	2.0101E+01
500	30	2.0000E+01	1.8964E+01	0.0000E+00	2.4842E-02	1.8939E+01
600	30	5.0000E-02	2.4905E+04	2.4613E+04	4.6472E+01	2.4495E+02
600	30	1.0000E-01	1.2318E+04	1.2070E+04	2.6782E+01	2.2129E+02
600	30	2.0000E-01	4.1732E+03	3.9647E+03	1.2230E+01	1.9633E+02
600	30	3.0000E-01	1.7674E+03	1.5808E+03	7.0194E+00	1.7965E+02
600	30	4.0000E-01	8.8376E+02	7.1185E+02	4.6409E+00	1.6727E+02
600	30	5.0000E-01	5.2520E+02	3.6353E+02	3.4281E+00	1.5824E+02
600	30	6.0000E-01	3.6754E+02	2.1361E+02	2.7168E+00	1.5122E+02
600	30	8.0000E-01	2.4459E+02	1.0187E+02	1.9424E+00	1.4078E+02
600	30	1.0000E+00	1.9422E+02	5.9655E+01	1.5293E+00	1.3304E+02
600	30	1.5000E+00	1.4309E+02	2.2716E+01	1.0104E+00	1.1936E+02
600	30	2.0000E+00	1.2189E+02	1.1230E+01	7.5679E-01	1.0990E+02
600	30	2.5000E+00	1.0969E+02	6.1081E+00	6.1233E-01	1.0297E+02
600	30	3.0000E+00	1.0144E+02	3.4212E+00	5.1726E-01	9.7498E+01
600	30	4.0000E+00	9.0621E+01	9.9692E-01	3.9553E-01	8.9228E+01
600	30	5.0000E+00	8.3442E+01	2.1672E-01	3.1995E-01	8.2905E+01
600	30	6.0000E+00	7.8068E+01	3.2355E-02	2.6881E-01	7.7767E+01
600	30	7.0000E+00	7.3571E+01	3.5940E-03	2.3172E-01	7.3336E+01
600	30	8.0000E+00	6.9773E+01	2.8844E-04	2.0375E-01	6.9569E+01
600	30	9.0000E+00	6.6406E+01	1.1849E-05	1.8178E-01	6.6224E+01
600	30	1.0000E+01	6.3407E+01	2.7751E-07	1.6391E-01	6.3243E+01
600	30	1.2000E+01	5.8278E+01	6.9374E-10	1.3657E-01	5.8141E+01
600	30	1.4000E+01	5.3906E+01	0.0000E+00	1.1647E-01	5.3790E+01

## C: Total Ionising Dose (TID)

---

600	30	1.6000E+01	5.0194E+01	0.0000E+00	1.0094E-01	5.0093E+01
600	30	1.8000E+01	4.6896E+01	0.0000E+00	8.8547E-02	4.6807E+01
600	30	2.0000E+01	4.3978E+01	0.0000E+00	7.8452E-02	4.3899E+01
700	30	5.0000E-02	6.0481E+04	5.9784E+04	1.1291E+02	5.8408E+02
700	30	1.0000E-01	3.0048E+04	2.9464E+04	6.5297E+01	5.1863E+02
700	30	2.0000E-01	1.0235E+04	9.7568E+03	2.9924E+01	4.4831E+02
700	30	3.0000E-01	4.3219E+03	3.9014E+03	1.7188E+01	4.0329E+02
700	30	4.0000E-01	2.1380E+03	1.7556E+03	1.1359E+01	3.7103E+02
700	30	5.0000E-01	1.2498E+03	8.9351E+02	8.3834E+00	3.4787E+02
700	30	6.0000E-01	8.5887E+02	5.2214E+02	6.6377E+00	3.3010E+02
700	30	8.0000E-01	5.5501E+02	2.4600E+02	4.7388E+00	3.0427E+02
700	30	1.0000E+00	4.3221E+02	1.4284E+02	3.7277E+00	2.8564E+02
700	30	1.5000E+00	3.0994E+02	5.3818E+01	2.4608E+00	2.5366E+02
700	30	2.0000E+00	2.6015E+02	2.6467E+01	1.8428E+00	2.3184E+02
700	30	2.5000E+00	2.3164E+02	1.4348E+01	1.4914E+00	2.1581E+02
700	30	3.0000E+00	2.1237E+02	8.0183E+00	1.2602E+00	2.0309E+02
700	30	4.0000E+00	1.8720E+02	2.3320E+00	9.6404E-01	1.8391E+02
700	30	5.0000E+00	1.7075E+02	5.0775E-01	7.7998E-01	1.6946E+02
700	30	6.0000E+00	1.5869E+02	7.6221E-02	6.5538E-01	1.5796E+02
700	30	7.0000E+00	1.4878E+02	8.6061E-03	5.6499E-01	1.4821E+02
700	30	8.0000E+00	1.4051E+02	7.5292E-04	4.9678E-01	1.4001E+02
700	30	9.0000E+00	1.3325E+02	4.1166E-05	4.4322E-01	1.3281E+02
700	30	1.0000E+01	1.2685E+02	1.1652E-06	3.9966E-01	1.2645E+02
700	30	1.2000E+01	1.1602E+02	4.0043E-09	3.3296E-01	1.1569E+02
700	30	1.4000E+01	1.0693E+02	0.0000E+00	2.8395E-01	1.0664E+02
700	30	1.6000E+01	9.9276E+01	0.0000E+00	2.4606E-01	9.9030E+01
700	30	1.8000E+01	9.2514E+01	0.0000E+00	2.1583E-01	9.2298E+01
700	30	2.0000E+01	8.6553E+01	0.0000E+00	1.9120E-01	8.6362E+01
800	30	5.0000E-02	1.2791E+05	1.2641E+05	2.3850E+02	1.2567E+03
800	30	1.0000E-01	6.4159E+04	6.2924E+04	1.3892E+02	1.0962E+03
800	30	2.0000E-01	2.2056E+04	2.1070E+04	6.4006E+01	9.2157E+02
800	30	3.0000E-01	9.3055E+03	8.4523E+03	3.6802E+01	8.1640E+02
800	30	4.0000E-01	4.5666E+03	3.7990E+03	2.4301E+01	7.4325E+02
800	30	5.0000E-01	2.6351E+03	1.9271E+03	1.7917E+01	6.9015E+02
800	30	6.0000E-01	1.7843E+03	1.1212E+03	1.4171E+01	6.4896E+02
800	30	8.0000E-01	1.1230E+03	5.2375E+02	1.0102E+01	5.8919E+02
800	30	1.0000E+00	8.5717E+02	3.0234E+02	7.9407E+00	5.4689E+02
800	30	1.5000E+00	5.9536E+02	1.1294E+02	5.2386E+00	4.7718E+02
800	30	2.0000E+00	4.9095E+02	5.5260E+01	3.9229E+00	4.3177E+02
800	30	2.5000E+00	4.3223E+02	2.9862E+01	3.1760E+00	3.9919E+02
800	30	3.0000E+00	3.9301E+02	1.6659E+01	2.6846E+00	3.7367E+02
800	30	4.0000E+00	3.4260E+02	4.8440E+00	2.0549E+00	3.3570E+02
800	30	5.0000E+00	3.1040E+02	1.0593E+00	1.6631E+00	3.0768E+02

800	30	6.0000E+00	2.8731E+02	1.6051E-01	1.3978E+00	2.8575E+02
800	30	7.0000E+00	2.6858E+02	1.8372E-02	1.2053E+00	2.6736E+02
800	30	8.0000E+00	2.5308E+02	1.6722E-03	1.0600E+00	2.5202E+02
800	30	9.0000E+00	2.3952E+02	1.0135E-04	9.4590E-01	2.3858E+02
800	30	1.0000E+01	2.2760E+02	3.1491E-06	8.5305E-01	2.2674E+02
800	30	1.2000E+01	2.0756E+02	1.0985E-08	7.1086E-01	2.0685E+02
800	30	1.4000E+01	1.9086E+02	0.0000E+00	6.0636E-01	1.9025E+02
800	30	1.6000E+01	1.7689E+02	0.0000E+00	5.2552E-01	1.7636E+02
800	30	1.8000E+01	1.6460E+02	0.0000E+00	4.6102E-01	1.6414E+02
800	30	2.0000E+01	1.5380E+02	0.0000E+00	4.0846E-01	1.5339E+02
900	30	5.0000E-02	2.4412E+05	2.4122E+05	4.5449E+02	2.4454E+03
900	30	1.0000E-01	1.2420E+05	1.2182E+05	2.6749E+02	2.1150E+03
900	30	2.0000E-01	4.3334E+04	4.1460E+04	1.2424E+02	1.7495E+03
900	30	3.0000E-01	1.8314E+04	1.6717E+04	7.1560E+01	1.5255E+03
900	30	4.0000E-01	8.9267E+03	7.5106E+03	4.7220E+01	1.3688E+03
900	30	5.0000E-01	5.0904E+03	3.8001E+03	3.4776E+01	1.2556E+03
900	30	6.0000E-01	3.3997E+03	2.2040E+03	2.7473E+01	1.1682E+03
900	30	8.0000E-01	2.0858E+03	1.0238E+03	1.9553E+01	1.0425E+03
900	30	1.0000E+00	1.5585E+03	5.8859E+02	1.5355E+01	9.5456E+02
900	30	1.5000E+00	1.0426E+03	2.1836E+02	1.0124E+01	8.1413E+02
900	30	2.0000E+00	8.4101E+02	1.0631E+02	7.5812E+00	7.2712E+02
900	30	2.5000E+00	7.3037E+02	5.7281E+01	6.1403E+00	6.6695E+02
900	30	3.0000E+00	6.5803E+02	3.1915E+01	5.1929E+00	6.2092E+02
900	30	4.0000E+00	5.6744E+02	9.2879E+00	3.9776E+00	5.5417E+02
900	30	5.0000E+00	5.1137E+02	2.0417E+00	3.2210E+00	5.0611E+02
900	30	6.0000E+00	4.7211E+02	3.1200E-01	2.7083E+00	4.6909E+02
900	30	7.0000E+00	4.4065E+02	3.6022E-02	2.3363E+00	4.3828E+02
900	30	8.0000E+00	4.1472E+02	3.3821E-03	2.0554E+00	4.1266E+02
900	30	9.0000E+00	3.9205E+02	2.2303E-04	1.8348E+00	3.9022E+02
900	30	1.0000E+01	3.7212E+02	7.4030E-06	1.6553E+00	3.7047E+02
900	30	1.2000E+01	3.3867E+02	2.6042E-08	1.3802E+00	3.3729E+02
900	30	1.4000E+01	3.1084E+02	0.0000E+00	1.1779E+00	3.0966E+02
900	30	1.6000E+01	2.8765E+02	0.0000E+00	1.0213E+00	2.8663E+02
900	30	1.8000E+01	2.6729E+02	0.0000E+00	8.9623E-01	2.6640E+02
900	30	2.0000E+01	2.4946E+02	0.0000E+00	7.9433E-01	2.4866E+02
1000	30	5.0000E-02	4.3457E+05	4.2930E+05	8.0767E+02	4.4612E+03
1000	30	1.0000E-01	2.2419E+05	2.1989E+05	4.8025E+02	3.8161E+03
1000	30	2.0000E-01	7.9289E+04	7.5961E+04	2.2475E+02	3.1028E+03
1000	30	3.0000E-01	3.3553E+04	3.0756E+04	1.2964E+02	2.6672E+03
1000	30	4.0000E-01	1.6255E+04	1.3808E+04	8.5481E+01	2.3622E+03
1000	30	5.0000E-01	9.1717E+03	6.9672E+03	6.2882E+01	2.1416E+03
1000	30	6.0000E-01	6.0495E+03	4.0281E+03	4.9619E+01	1.9718E+03
1000	30	8.0000E-01	3.6244E+03	1.8606E+03	3.5258E+01	1.7285E+03

## C: Total Ionising Dose (TID)

---

1000	30	1.0000E+00	2.6534E+03	1.0650E+03	2.7667E+01	1.5607E+03
1000	30	1.5000E+00	1.7110E+03	3.9208E+02	1.8229E+01	1.3007E+03
1000	30	2.0000E+00	1.3506E+03	1.8990E+02	1.3651E+01	1.1470E+03
1000	30	2.5000E+00	1.1572E+03	1.0203E+02	1.1061E+01	1.0441E+03
1000	30	3.0000E+00	1.0331E+03	5.6790E+01	9.3590E+00	9.6691E+02
1000	30	4.0000E+00	8.8090E+02	1.6551E+01	7.1738E+00	8.5718E+02
1000	30	5.0000E+00	7.8929E+02	3.6621E+00	5.8120E+00	7.7981E+02
1000	30	6.0000E+00	7.2653E+02	5.6652E-01	4.8890E+00	7.2108E+02
1000	30	7.0000E+00	6.7687E+02	6.6628E-02	4.2189E+00	6.7258E+02
1000	30	8.0000E+00	6.3614E+02	6.6585E-03	3.7131E+00	6.3242E+02
1000	30	9.0000E+00	6.0061E+02	5.2791E-04	3.3157E+00	5.9729E+02
1000	30	1.0000E+01	5.6940E+02	2.4361E-05	2.9921E+00	5.6641E+02
1000	30	1.2000E+01	5.1716E+02	7.0187E-08	2.4961E+00	5.1466E+02
1000	30	1.4000E+01	4.7388E+02	0.0000E+00	2.1312E+00	4.7174E+02
1000	30	1.6000E+01	4.3794E+02	0.0000E+00	1.8485E+00	4.3609E+02
1000	30	1.8000E+01	4.0651E+02	0.0000E+00	1.6227E+00	4.0489E+02
1000	30	2.0000E+01	3.7903E+02	0.0000E+00	1.4386E+00	3.7760E+02
500	60	5.0000E-02	3.8240E+04	3.7971E+04	7.3303E+01	1.9595E+02
500	60	1.0000E-01	1.8666E+04	1.8514E+04	4.2552E+01	1.0931E+02
500	60	2.0000E-01	7.5194E+03	7.4244E+03	2.1938E+01	7.3131E+01
500	60	3.0000E-01	4.1943E+03	4.1192E+03	1.4536E+01	6.0588E+01
500	60	4.0000E-01	2.7546E+03	2.6901E+03	1.0872E+01	5.3605E+01
500	60	5.0000E-01	1.9936E+03	1.9359E+03	8.8331E+00	4.8834E+01
500	60	6.0000E-01	1.5372E+03	1.4844E+03	7.4881E+00	4.5317E+01
500	60	8.0000E-01	1.0210E+03	9.7480E+02	5.8021E+00	4.0449E+01
500	60	1.0000E+00	7.3390E+02	6.9192E+02	4.7464E+00	3.7234E+01
500	60	1.5000E+00	3.7853E+02	3.4292E+02	3.2403E+00	3.2377E+01
500	60	2.0000E+00	2.1898E+02	1.8712E+02	2.4518E+00	2.9400E+01
500	60	2.5000E+00	1.3545E+02	1.0618E+02	1.9815E+00	2.7286E+01
500	60	3.0000E+00	8.8946E+01	6.1598E+01	1.6716E+00	2.5676E+01
500	60	4.0000E+00	4.5927E+01	2.1386E+01	1.2755E+00	2.3266E+01
500	60	5.0000E+00	2.9852E+01	7.3505E+00	1.0380E+00	2.1463E+01
500	60	6.0000E+00	2.3380E+01	2.4527E+00	8.8270E-01	2.0044E+01
500	60	7.0000E+00	2.0395E+01	7.9036E-01	7.7210E-01	1.8832E+01
500	60	8.0000E+00	1.8734E+01	2.4256E-01	6.9054E-01	1.7801E+01
500	60	9.0000E+00	1.7575E+01	7.0853E-02	6.2754E-01	1.6877E+01
500	60	1.0000E+01	1.6655E+01	1.9447E-02	5.7681E-01	1.6059E+01
500	60	1.2000E+01	1.5108E+01	9.5210E-04	4.9943E-01	1.4607E+01
500	60	1.4000E+01	1.3812E+01	1.5380E-05	4.4199E-01	1.3370E+01
500	60	1.6000E+01	1.2718E+01	1.8802E-07	3.9639E-01	1.2322E+01
500	60	1.8000E+01	1.1756E+01	5.2575E-09	3.5889E-01	1.1397E+01
500	60	2.0000E+01	1.0927E+01	0.0000E+00	3.2739E-01	1.0600E+01
600	60	5.0000E-02	6.4274E+04	6.3559E+04	1.2234E+02	5.9312E+02

600	60	1.0000E-01	3.1100E+04	3.0697E+04	7.0407E+01	3.3277E+02
600	60	2.0000E-01	1.2043E+04	1.1793E+04	3.5367E+01	2.1370E+02
600	60	3.0000E-01	6.4478E+03	6.2540E+03	2.2897E+01	1.7095E+02
600	60	4.0000E-01	4.1035E+03	3.9396E+03	1.6836E+01	1.4709E+02
600	60	5.0000E-01	2.9111E+03	2.7659E+03	1.3515E+01	1.3170E+02
600	60	6.0000E-01	2.2203E+03	2.0883E+03	1.1365E+01	1.2066E+02
600	60	8.0000E-01	1.4647E+03	1.3500E+03	8.7247E+00	1.0604E+02
600	60	1.0000E+00	1.0547E+03	9.5094E+02	7.1054E+00	9.6636E+01
600	60	1.5000E+00	5.5471E+02	4.6752E+02	4.8306E+00	8.2353E+01
600	60	2.0000E+00	3.3163E+02	2.5438E+02	3.6499E+00	7.3607E+01
600	60	2.5000E+00	2.1468E+02	1.4407E+02	2.9495E+00	6.7660E+01
600	60	3.0000E+00	1.4913E+02	8.3423E+01	2.4882E+00	6.3221E+01
600	60	4.0000E+00	8.7628E+01	2.8824E+01	1.8987E+00	5.6905E+01
600	60	5.0000E+00	6.3722E+01	9.8482E+00	1.5440E+00	5.2330E+01
600	60	6.0000E+00	5.3314E+01	3.2738E+00	1.3112E+00	4.8729E+01
600	60	7.0000E+00	4.7883E+01	1.0559E+00	1.1451E+00	4.5682E+01
600	60	8.0000E+00	4.4471E+01	3.2565E-01	1.0222E+00	4.3124E+01
600	60	9.0000E+00	4.1891E+01	9.5914E-02	9.2714E-01	4.0868E+01
600	60	1.0000E+01	3.9748E+01	2.6629E-02	8.5050E-01	3.8871E+01
600	60	1.2000E+01	3.6211E+01	1.3477E-03	7.3356E-01	3.5476E+01
600	60	1.4000E+01	3.3253E+01	2.2514E-05	6.4689E-01	3.2606E+01
600	60	1.6000E+01	3.0764E+01	2.6977E-07	5.7831E-01	3.0186E+01
600	60	1.8000E+01	2.8574E+01	7.8693E-09	5.2210E-01	2.8052E+01
600	60	2.0000E+01	2.6652E+01	0.0000E+00	4.7506E-01	2.6177E+01
700	60	5.0000E-02	1.0356E+05	1.0194E+05	1.9549E+02	1.4176E+03
700	60	1.0000E-01	5.0203E+04	4.9317E+04	1.1246E+02	7.7382E+02
700	60	2.0000E-01	1.8947E+04	1.8415E+04	5.5526E+01	4.7679E+02
700	60	3.0000E-01	9.7768E+03	9.3688E+03	3.5253E+01	3.7274E+02
700	60	4.0000E-01	6.0251E+03	5.6838E+03	2.5517E+01	3.1585E+02
700	60	5.0000E-01	4.1830E+03	3.8832E+03	2.0250E+01	2.7957E+02
700	60	6.0000E-01	3.1526E+03	2.8819E+03	1.6897E+01	2.5385E+02
700	60	8.0000E-01	2.0644E+03	1.8311E+03	1.2853E+01	2.2039E+02
700	60	1.0000E+00	1.4888E+03	1.2789E+03	1.0422E+01	1.9942E+02
700	60	1.5000E+00	7.9805E+02	6.2242E+02	7.0572E+00	1.6857E+02
700	60	2.0000E+00	4.9251E+02	3.3709E+02	5.3246E+00	1.5010E+02
700	60	2.5000E+00	3.3201E+02	1.9024E+02	4.3024E+00	1.3747E+02
700	60	3.0000E+00	2.4132E+02	1.0977E+02	3.6296E+00	1.2792E+02
700	60	4.0000E+00	1.5457E+02	3.7640E+01	2.7701E+00	1.1416E+02
700	60	5.0000E+00	1.1923E+02	1.2746E+01	2.2513E+00	1.0424E+02
700	60	6.0000E+00	1.0265E+02	4.2062E+00	1.9096E+00	9.6535E+01
700	60	7.0000E+00	9.3125E+01	1.3526E+00	1.6652E+00	9.0107E+01
700	60	8.0000E+00	8.6670E+01	4.1765E-01	1.4841E+00	8.4769E+01
700	60	9.0000E+00	8.1572E+01	1.2354E-01	1.3437E+00	8.0105E+01

## C: Total Ionising Dose (TID)

---

700	60	1.0000E+01	7.7273E+01	3.4557E-02	1.2304E+00	7.6008E+01
700	60	1.2000E+01	7.0182E+01	1.7858E-03	1.0573E+00	6.9122E+01
700	60	1.4000E+01	6.4298E+01	3.0443E-05	9.2922E-01	6.3369E+01
700	60	1.6000E+01	5.9381E+01	3.6053E-07	8.2813E-01	5.8553E+01
700	60	1.8000E+01	5.5062E+01	1.0788E-08	7.4555E-01	5.4316E+01
700	60	2.0000E+01	5.1277E+01	0.0000E+00	6.7665E-01	5.0600E+01
800	60	5.0000E-02	1.6035E+05	1.5723E+05	3.0052E+02	2.8156E+03
800	60	1.0000E-01	7.8328E+04	7.6625E+04	1.7353E+02	1.5286E+03
800	60	2.0000E-01	2.9124E+04	2.8113E+04	8.4716E+01	9.2596E+02
800	60	3.0000E-01	1.4550E+04	1.3782E+04	5.2904E+01	7.1502E+02
800	60	4.0000E-01	8.6849E+03	8.0472E+03	3.7740E+01	5.9996E+02
800	60	5.0000E-01	5.8924E+03	5.3364E+03	2.9621E+01	5.2641E+02
800	60	6.0000E-01	4.3818E+03	3.8831E+03	2.4525E+01	4.7415E+02
800	60	8.0000E-01	2.8418E+03	2.4171E+03	1.8485E+01	4.0626E+02
800	60	1.0000E+00	2.0490E+03	1.6701E+03	1.4921E+01	3.6398E+02
800	60	1.5000E+00	1.1149E+03	8.0177E+02	1.0061E+01	3.0302E+02
800	60	2.0000E+00	7.0678E+02	4.3156E+02	7.5805E+00	2.6764E+02
800	60	2.5000E+00	4.9287E+02	2.4276E+02	6.1255E+00	2.4399E+02
800	60	3.0000E+00	3.7126E+02	1.3974E+02	5.1687E+00	2.2635E+02
800	60	4.0000E+00	2.5279E+02	4.7564E+01	3.9464E+00	2.0128E+02
800	60	5.0000E+00	2.0251E+02	1.5930E+01	3.2059E+00	1.8337E+02
800	60	6.0000E+00	1.7747E+02	5.2023E+00	2.7165E+00	1.6955E+02
800	60	7.0000E+00	1.6208E+02	1.6621E+00	2.3658E+00	1.5805E+02
800	60	8.0000E+00	1.5113E+02	5.1183E-01	2.1051E+00	1.4852E+02
800	60	9.0000E+00	1.4226E+02	1.5156E-01	1.9028E+00	1.4021E+02
800	60	1.0000E+01	1.3471E+02	4.2625E-02	1.7392E+00	1.3293E+02
800	60	1.2000E+01	1.2225E+02	2.2524E-03	1.4893E+00	1.2076E+02
800	60	1.4000E+01	1.1196E+02	3.9281E-05	1.3044E+00	1.1065E+02
800	60	1.6000E+01	1.0340E+02	4.5901E-07	1.1589E+00	1.0224E+02
800	60	1.8000E+01	9.5891E+01	1.4118E-08	1.0403E+00	9.4851E+01
800	60	2.0000E+01	8.9322E+01	0.0000E+00	9.4175E-01	8.8380E+01
900	60	5.0000E-02	2.4361E+05	2.3822E+05	4.5390E+02	4.9379E+03
900	60	1.0000E-01	1.2048E+05	1.1753E+05	2.6406E+02	2.6876E+03
900	60	2.0000E-01	4.4511E+04	4.2759E+04	1.2809E+02	1.6245E+03
900	60	3.0000E-01	2.1613E+04	2.0288E+04	7.8885E+01	1.2458E+03
900	60	4.0000E-01	1.2492E+04	1.1399E+04	5.5523E+01	1.0370E+03
900	60	5.0000E-01	8.2672E+03	7.3203E+03	4.3121E+01	9.0377E+02
900	60	6.0000E-01	6.0553E+03	5.2108E+03	3.5432E+01	8.0908E+02
900	60	8.0000E-01	3.8806E+03	3.1689E+03	2.6465E+01	6.8524E+02
900	60	1.0000E+00	2.7920E+03	2.1632E+03	2.1271E+01	6.0753E+02
900	60	1.5000E+00	1.5340E+03	1.0233E+03	1.4290E+01	4.9650E+02
900	60	2.0000E+00	9.9263E+02	5.4770E+02	1.0756E+01	4.3418E+02
900	60	2.5000E+00	7.0975E+02	3.0752E+02	8.6944E+00	3.9354E+02

Performance Metrics for Various Parameters						
Parameter A	Parameter B	Value C	Value D	Value E	Value F	Value G
900	60	3.0000E+00	5.4788E+02	1.7688E+02	7.3396E+00	3.6366E+02
900	60	4.0000E+00	3.8741E+02	5.9911E+01	5.6076E+00	3.2189E+02
900	60	5.0000E+00	3.1704E+02	1.9839E+01	4.5543E+00	2.9264E+02
900	60	6.0000E+00	2.8067E+02	6.4039E+00	3.8555E+00	2.7041E+02
900	60	7.0000E+00	2.5742E+02	2.0326E+00	3.3538E+00	2.5204E+02
900	60	8.0000E+00	2.4043E+02	6.2474E-01	2.9800E+00	2.3683E+02
900	60	9.0000E+00	2.2642E+02	1.8524E-01	2.6893E+00	2.2355E+02
900	60	1.0000E+01	2.1439E+02	5.2334E-02	2.4540E+00	2.1188E+02
900	60	1.2000E+01	1.9444E+02	2.8194E-03	2.0944E+00	1.9234E+02
900	60	1.4000E+01	1.7794E+02	5.0451E-05	1.8285E+00	1.7611E+02
900	60	1.6000E+01	1.6423E+02	5.8036E-07	1.6197E+00	1.6261E+02
900	60	1.8000E+01	1.5224E+02	1.8431E-08	1.4501E+00	1.5079E+02
900	60	2.0000E+01	1.4177E+02	0.0000E+00	1.3094E+00	1.4046E+02
1000	60	5.0000E-02	3.5820E+05	3.4984E+05	6.6442E+02	7.6888E+03
1000	60	1.0000E-01	1.7993E+05	1.7527E+05	3.9040E+02	4.2678E+03
1000	60	2.0000E-01	6.6424E+04	6.3634E+04	1.8887E+02	2.6008E+03
1000	60	3.0000E-01	3.1485E+04	2.9375E+04	1.1500E+02	1.9948E+03
1000	60	4.0000E-01	1.7655E+04	1.5918E+04	7.9988E+01	1.6573E+03
1000	60	5.0000E-01	1.1398E+04	9.8968E+03	6.1530E+01	1.4393E+03
1000	60	6.0000E-01	8.2190E+03	6.8858E+03	5.0208E+01	1.2830E+03
1000	60	8.0000E-01	5.2025E+03	4.0883E+03	3.7195E+01	1.0770E+03
1000	60	1.0000E+00	3.7344E+03	2.7575E+03	2.9782E+01	9.4718E+02
1000	60	1.5000E+00	2.0704E+03	1.2874E+03	1.9951E+01	7.6301E+02
1000	60	2.0000E+00	1.3627E+03	6.8614E+02	1.5007E+01	6.6158E+02
1000	60	2.5000E+00	9.9283E+02	3.8422E+02	1.2137E+01	5.9647E+02
1000	60	3.0000E+00	7.7980E+02	2.2042E+02	1.0251E+01	5.4912E+02
1000	60	4.0000E+00	5.6572E+02	7.4084E+01	7.8373E+00	4.8380E+02
1000	60	5.0000E+00	4.6928E+02	2.4171E+01	6.3638E+00	4.3875E+02
1000	60	6.0000E+00	4.1793E+02	7.6675E+00	5.3831E+00	4.0488E+02
1000	60	7.0000E+00	3.8414E+02	2.4025E+00	4.6778E+00	3.7706E+02
1000	60	8.0000E+00	3.5899E+02	7.3142E-01	4.1515E+00	3.5410E+02
1000	60	9.0000E+00	3.3802E+02	2.1498E-01	3.7415E+00	3.3407E+02
1000	60	1.0000E+01	3.1995E+02	6.0237E-02	3.4093E+00	3.1649E+02
1000	60	1.2000E+01	2.8998E+02	3.2469E-03	2.9012E+00	2.8707E+02
1000	60	1.4000E+01	2.6524E+02	6.0124E-05	2.5258E+00	2.6271E+02
1000	60	1.6000E+01	2.4473E+02	6.7592E-07	2.2315E+00	2.4250E+02
1000	60	1.8000E+01	2.2682E+02	2.2467E-08	1.9930E+00	2.2483E+02
1000	60	2.0000E+01	2.1119E+02	0.0000E+00	1.7956E+00	2.0939E+02
500	90	5.0000E-02	3.4557E+04	3.4338E+04	6.6406E+01	1.5231E+02
500	90	1.0000E-01	1.6924E+04	1.6795E+04	3.8628E+01	8.9728E+01
500	90	2.0000E-01	6.8854E+03	6.8035E+03	2.0012E+01	6.1872E+01
500	90	3.0000E-01	3.8582E+03	3.7932E+03	1.3290E+01	5.1711E+01
500	90	4.0000E-01	2.5350E+03	2.4791E+03	9.9437E+00	4.5897E+01

## C: Total Ionising Dose (TID)

---

500	90	5.0000E-01	1.8310E+03	1.7810E+03	8.0748E+00	4.1875E+01
500	90	6.0000E-01	1.4073E+03	1.3615E+03	6.8385E+00	3.8886E+01
500	90	8.0000E-01	9.2806E+02	8.8808E+02	5.2864E+00	3.4696E+01
500	90	1.0000E+00	6.6292E+02	6.2672E+02	4.3150E+00	3.1882E+01
500	90	1.5000E+00	3.3747E+02	3.0699E+02	2.9335E+00	2.7545E+01
500	90	2.0000E+00	1.9287E+02	1.6580E+02	2.2145E+00	2.4861E+01
500	90	2.5000E+00	1.1805E+02	9.3287E+01	1.7877E+00	2.2979E+01
500	90	3.0000E+00	7.6834E+01	5.3752E+01	1.5075E+00	2.1575E+01
500	90	4.0000E+00	3.9124E+01	1.8452E+01	1.1501E+00	1.9522E+01
500	90	5.0000E+00	2.5222E+01	6.2765E+00	9.3608E-01	1.8009E+01
500	90	6.0000E+00	1.9691E+01	2.0724E+00	7.9619E-01	1.6823E+01
500	90	7.0000E+00	1.7167E+01	6.6106E-01	6.9652E-01	1.5810E+01
500	90	8.0000E+00	1.5772E+01	2.0105E-01	6.2299E-01	1.4948E+01
500	90	9.0000E+00	1.4800E+01	5.8272E-02	5.6619E-01	1.4176E+01
500	90	1.0000E+01	1.4029E+01	1.5892E-02	5.2039E-01	1.3493E+01
500	90	1.2000E+01	1.2735E+01	7.8032E-04	4.5048E-01	1.2284E+01
500	90	1.4000E+01	1.1653E+01	1.3188E-05	3.9855E-01	1.1255E+01
500	90	1.6000E+01	1.0741E+01	1.5618E-07	3.5730E-01	1.0383E+01
500	90	1.8000E+01	9.9376E+00	4.6648E-09	3.2335E-01	9.6142E+00
500	90	2.0000E+01	9.2441E+00	0.0000E+00	2.9485E-01	8.9493E+00
600	90	5.0000E-02	5.7191E+04	5.6626E+04	1.0903E+02	4.5669E+02
600	90	1.0000E-01	2.7812E+04	2.7481E+04	6.2959E+01	2.6820E+02
600	90	2.0000E-01	1.0847E+04	1.0637E+04	3.1740E+01	1.7792E+02
600	90	3.0000E-01	5.8149E+03	5.6499E+03	2.0565E+01	1.4441E+02
600	90	4.0000E-01	3.6944E+03	3.5539E+03	1.5112E+01	1.2541E+02
600	90	5.0000E-01	2.6133E+03	2.4882E+03	1.2119E+01	1.1303E+02
600	90	6.0000E-01	1.9867E+03	1.8725E+03	1.0179E+01	1.0406E+02
600	90	8.0000E-01	1.3025E+03	1.2027E+03	7.7951E+00	9.2038E+01
600	90	1.0000E+00	9.3298E+02	8.4244E+02	6.3350E+00	8.4207E+01
600	90	1.5000E+00	4.8558E+02	4.0905E+02	4.2906E+00	7.2237E+01
600	90	2.0000E+00	2.8821E+02	2.2010E+02	3.2348E+00	6.4868E+01
600	90	2.5000E+00	1.8598E+02	1.2360E+02	2.6114E+00	5.9772E+01
600	90	3.0000E+00	1.2919E+02	7.1101E+01	2.2020E+00	5.5888E+01
600	90	4.0000E+00	7.6201E+01	2.4272E+01	1.6801E+00	5.0249E+01
600	90	5.0000E+00	5.5680E+01	8.1810E+00	1.3664E+00	4.6132E+01
600	90	6.0000E+00	4.6745E+01	2.6784E+00	1.1606E+00	4.2906E+01
600	90	7.0000E+00	4.2056E+01	8.5059E-01	1.0136E+00	4.0192E+01
600	90	8.0000E+00	3.9086E+01	2.5858E-01	9.0484E-01	3.7923E+01
600	90	9.0000E+00	3.6825E+01	7.5229E-02	8.2067E-01	3.5930E+01
600	90	1.0000E+01	3.4942E+01	2.0690E-02	7.5274E-01	3.4169E+01
600	90	1.2000E+01	3.1834E+01	1.0392E-03	6.4902E-01	3.1184E+01
600	90	1.4000E+01	2.9237E+01	1.7533E-05	5.7209E-01	2.8665E+01
600	90	1.6000E+01	2.7054E+01	2.0849E-07	5.1117E-01	2.6542E+01

Performance Metrics for Various Parameters						
Parameter A	Parameter B	Value 1	Value 2	Value 3	Value 4	Value 5
600	90	1.8000E+01	2.5132E+01	6.1773E-09	4.6124E-01	2.4671E+01
600	90	2.0000E+01	2.3447E+01	0.0000E+00	4.1947E-01	2.3027E+01
700	90	5.0000E-02	8.9913E+04	8.8629E+04	1.6989E+02	1.1138E+03
700	90	1.0000E-01	4.3871E+04	4.3136E+04	9.8141E+01	6.3702E+02
700	90	2.0000E-01	1.6654E+04	1.6200E+04	4.8589E+01	4.0492E+02
700	90	3.0000E-01	8.5838E+03	8.2330E+03	3.0836E+01	3.1997E+02
700	90	4.0000E-01	5.2706E+03	4.9756E+03	2.2286E+01	2.7266E+02
700	90	5.0000E-01	3.6446E+03	3.3845E+03	1.7657E+01	2.4242E+02
700	90	6.0000E-01	2.7371E+03	2.5014E+03	1.4710E+01	2.2097E+02
700	90	8.0000E-01	1.7823E+03	1.5781E+03	1.1161E+01	1.9295E+02
700	90	1.0000E+00	1.2801E+03	1.0958E+03	9.0322E+00	1.7519E+02
700	90	1.5000E+00	6.8163E+02	5.2699E+02	6.0959E+00	1.4854E+02
700	90	2.0000E+00	4.1945E+02	2.8257E+02	4.5912E+00	1.3228E+02
700	90	2.5000E+00	2.8320E+02	1.5833E+02	3.7071E+00	1.2116E+02
700	90	3.0000E+00	2.0681E+02	9.0885E+01	3.1267E+00	1.1280E+02
700	90	4.0000E+00	1.3405E+02	3.0854E+01	2.3863E+00	1.0081E+02
700	90	5.0000E+00	1.0438E+02	1.0311E+01	1.9396E+00	9.2132E+01
700	90	6.0000E+00	9.0336E+01	3.3478E+00	1.6453E+00	8.5343E+01
700	90	7.0000E+00	8.2136E+01	1.0575E+00	1.4348E+00	7.9644E+01
700	90	8.0000E+00	7.6501E+01	3.2006E-01	1.2786E+00	7.4903E+01
700	90	9.0000E+00	7.2012E+01	9.2641E-02	1.1575E+00	7.0762E+01
700	90	1.0000E+01	6.8215E+01	2.5344E-02	1.0597E+00	6.7130E+01
700	90	1.2000E+01	6.1950E+01	1.2673E-03	9.1018E-01	6.1038E+01
700	90	1.4000E+01	5.6757E+01	2.1290E-05	7.9945E-01	5.5958E+01
700	90	1.6000E+01	5.2421E+01	2.5381E-07	7.1203E-01	5.1709E+01
700	90	1.8000E+01	4.8613E+01	7.4708E-09	6.4063E-01	4.7972E+01
700	90	2.0000E+01	4.5275E+01	0.0000E+00	5.8108E-01	4.4694E+01
800	90	5.0000E-02	1.3611E+05	1.3378E+05	2.5559E+02	2.0682E+03
800	90	1.0000E-01	6.6839E+04	6.5498E+04	1.4804E+02	1.1937E+03
800	90	2.0000E-01	2.4930E+04	2.4101E+04	7.2358E+01	7.5647E+02
800	90	3.0000E-01	1.2419E+04	1.1779E+04	4.5128E+01	5.9445E+02
800	90	4.0000E-01	7.3779E+03	6.8419E+03	3.2129E+01	5.0383E+02
800	90	5.0000E-01	4.9841E+03	4.5135E+03	2.5172E+01	4.4541E+02
800	90	6.0000E-01	3.6942E+03	3.2698E+03	2.0809E+01	4.0365E+02
800	90	8.0000E-01	2.3861E+03	2.0217E+03	1.5647E+01	3.4876E+02
800	90	1.0000E+00	1.7166E+03	1.3900E+03	1.2611E+01	3.1405E+02
800	90	1.5000E+00	9.3308E+02	6.6129E+02	8.4835E+00	2.6331E+02
800	90	2.0000E+00	5.9349E+02	3.5350E+02	6.3841E+00	2.3360E+02
800	90	2.5000E+00	4.1642E+02	1.9771E+02	5.1565E+00	2.1355E+02
800	90	3.0000E+00	3.1601E+02	1.1324E+02	4.3505E+00	1.9842E+02
800	90	4.0000E+00	2.1816E+02	3.8196E+01	3.3218E+00	1.7664E+02
800	90	5.0000E+00	1.7627E+02	1.2655E+01	2.6986E+00	1.6092E+02
800	90	6.0000E+00	1.5511E+02	4.0754E+00	2.2865E+00	1.4875E+02

## C: Total Ionising Dose (TID)

---

800	90	7.0000E+00	1.4188E+02	1.2802E+00	1.9910E+00	1.3861E+02
800	90	8.0000E+00	1.3237E+02	3.8617E-01	1.7714E+00	1.3021E+02
800	90	9.0000E+00	1.2462E+02	1.1157E-01	1.6008E+00	1.2291E+02
800	90	1.0000E+01	1.1801E+02	3.0528E-02	1.4628E+00	1.1651E+02
800	90	1.2000E+01	1.0710E+02	1.5342E-03	1.2518E+00	1.0584E+02
800	90	1.4000E+01	9.8093E+01	2.5968E-05	1.0957E+00	9.6997E+01
800	90	1.6000E+01	9.0604E+01	3.0815E-07	9.7287E-01	8.9631E+01
800	90	1.8000E+01	8.4039E+01	9.1600E-09	8.7283E-01	8.3166E+01
800	90	2.0000E+01	7.8291E+01	0.0000E+00	7.8965E-01	7.7502E+01
900	90	5.0000E-02	1.9982E+05	1.9593E+05	3.7307E+02	3.5214E+03
900	90	1.0000E-01	9.9327E+04	9.7065E+04	2.1764E+02	2.0442E+03
900	90	2.0000E-01	3.6767E+04	3.5371E+04	1.0563E+02	1.2908E+03
900	90	3.0000E-01	1.7790E+04	1.6716E+04	6.4942E+01	1.0090E+03
900	90	4.0000E-01	1.0230E+04	9.3335E+03	4.5608E+01	8.5077E+02
900	90	5.0000E-01	6.7402E+03	5.9568E+03	3.5352E+01	7.4811E+02
900	90	6.0000E-01	4.9223E+03	4.2191E+03	2.9002E+01	6.7423E+02
900	90	8.0000E-01	3.1464E+03	2.5485E+03	2.1614E+01	5.7632E+02
900	90	1.0000E+00	2.2628E+03	1.7315E+03	1.7347E+01	5.1402E+02
900	90	1.5000E+00	1.2473E+03	8.1221E+02	1.1632E+01	4.2344E+02
900	90	2.0000E+00	8.1216E+02	4.3180E+02	8.7460E+00	3.7161E+02
900	90	2.5000E+00	5.8548E+02	2.4096E+02	7.0675E+00	3.3745E+02
900	90	3.0000E+00	4.5602E+02	1.3784E+02	5.9655E+00	3.1221E+02
900	90	4.0000E+00	3.2758E+02	4.6250E+01	4.5578E+00	2.7678E+02
900	90	5.0000E+00	2.7071E+02	1.5137E+01	3.7016E+00	2.5187E+02
900	90	6.0000E+00	2.4084E+02	4.8104E+00	3.1333E+00	2.3289E+02
900	90	7.0000E+00	2.2141E+02	1.4986E+00	2.7251E+00	2.1718E+02
900	90	8.0000E+00	2.0704E+02	4.5012E-01	2.4209E+00	2.0417E+02
900	90	9.0000E+00	1.9511E+02	1.2967E-01	2.1842E+00	1.9279E+02
900	90	1.0000E+01	1.8483E+02	3.5404E-02	1.9925E+00	1.8280E+02
900	90	1.2000E+01	1.6773E+02	1.7919E-03	1.6994E+00	1.6603E+02
900	90	1.4000E+01	1.5358E+02	3.0968E-05	1.4826E+00	1.5209E+02
900	90	1.6000E+01	1.4180E+02	3.6254E-07	1.3124E+00	1.4049E+02
900	90	1.8000E+01	1.3149E+02	1.1079E-08	1.1742E+00	1.3032E+02
900	90	2.0000E+01	1.2248E+02	0.0000E+00	1.0596E+00	1.2142E+02
1000	90	5.0000E-02	2.8979E+05	2.8375E+05	5.3862E+02	5.4943E+03
1000	90	1.0000E-01	1.4602E+05	1.4247E+05	3.1692E+02	3.2297E+03
1000	90	2.0000E-01	5.3892E+04	5.1693E+04	1.5323E+02	2.0458E+03
1000	90	3.0000E-01	2.5445E+04	2.3755E+04	9.3108E+01	1.5971E+03
1000	90	4.0000E-01	1.4196E+04	1.2789E+04	6.4616E+01	1.3424E+03
1000	90	5.0000E-01	9.1239E+03	7.8991E+03	4.9607E+01	1.1751E+03
1000	90	6.0000E-01	6.5592E+03	5.4651E+03	4.0414E+01	1.0537E+03
1000	90	8.0000E-01	4.1405E+03	3.2188E+03	2.9871E+01	8.9181E+02
1000	90	1.0000E+00	2.9710E+03	2.1584E+03	2.3883E+01	7.8867E+02

---

1000	90	1.5000E+00	1.6538E+03	9.9733E+02	1.5968E+01	6.4053E+02
1000	90	2.0000E+00	1.0976E+03	5.2775E+02	1.2000E+01	5.5781E+02
1000	90	2.5000E+00	8.0795E+02	2.9403E+02	9.7027E+00	5.0421E+02
1000	90	3.0000E+00	6.4119E+02	1.6802E+02	8.1942E+00	4.6498E+02
1000	90	4.0000E+00	4.7278E+02	5.6029E+01	6.2654E+00	4.1048E+02
1000	90	5.0000E+00	3.9584E+02	1.8100E+01	5.0873E+00	3.7266E+02
1000	90	6.0000E+00	3.5409E+02	5.6789E+00	4.3028E+00	3.4411E+02
1000	90	7.0000E+00	3.2610E+02	1.7613E+00	3.7382E+00	3.2060E+02
1000	90	8.0000E+00	3.0503E+02	5.3059E-01	3.3167E+00	3.0119E+02
1000	90	9.0000E+00	2.8738E+02	1.5404E-01	2.9881E+00	2.8424E+02
1000	90	1.0000E+01	2.7213E+02	4.2528E-02	2.7217E+00	2.6936E+02
1000	90	1.2000E+01	2.4678E+02	2.2233E-03	2.3142E+00	2.4447E+02
1000	90	1.4000E+01	2.2585E+02	4.0601E-05	2.0131E+00	2.2383E+02
1000	90	1.6000E+01	2.0847E+02	4.5938E-07	1.7770E+00	2.0670E+02
1000	90	1.8000E+01	1.9329E+02	1.5073E-08	1.5859E+00	1.9170E+02
1000	90	2.0000E+01	1.8002E+02	0.0000E+00	1.4278E+00	1.7860E+02

---

Blank page

# D: Main orbit perturbations

This appendix expands on the orbit perturbation models used in the orbit propagator (OP) design presented in Chapter 3. The models represent main sources of orbit and attitude perturbation, the mathematical forms of which allow adaptability in assuming new observations if necessary. In a trade-off between orbit propagation precision and computational burden for the investigations reported in this thesis, selected perturbations with negligible effect on reported results are excluded. In this respect, some examples include the minor effects of ocean, solid, and pole tides.

The following subsections present the base models of geopotential, lunisolar perturbation, solar radiation pressure, and atmospheric drag used by the OP.

## Geopotential

The Earth can be mathematically represented as an oblate spheroid with bulges out of the equator caused by the effect of the Earth's rotation rate about its axis. The sole effect of the equatorial bulge causes important latitudinal variations in the relative gravitational acceleration acting on orbiting objects. This major well-known effect is used in basic calculations through the second zonal harmonic  $J_2$ , the main mathematical contributor to the Earth oblateness. However, for precise perturbation estimations, other Earth shape irregularities must be considered requiring a higher number of zonal harmonics (Fig. 1).

The GRACE+GOCE Gravity Model GGM05G [140] with maximum spherical harmonic degree  $l$  and order  $m$  of 240 is used in this thesis. The acceleration originated by the aspheric gravitational potential  $U$  is estimated with Eq. (1)–(3). For detailed

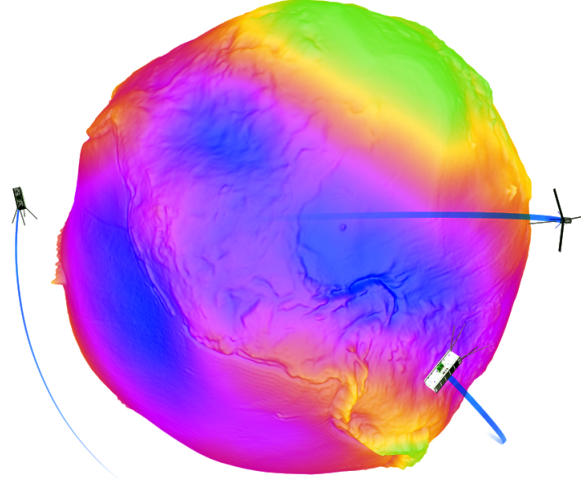


Fig. 1 Earth oblateness. Geoid height model exaggerated 15000 times.

derivation and description of this formulas refer to Vallado [139].

$$\ddot{\vec{r}}_{gp} = \begin{bmatrix} \left( \frac{1}{r} \frac{\partial U}{\partial r} - \frac{r_k}{r^2 \sqrt{r_I^2 + r_J^2}} \frac{\partial U}{\partial \phi_{gc_{sat}}} \right) r_I - \left( \frac{1}{r_I^2 + r_J^2} \frac{\partial U}{\partial \lambda_{sat}} \right) r_J - \frac{\mu r}{r^3} \\ \left( \frac{1}{r} \frac{\partial U}{\partial r} - \frac{r_k}{r^2 \sqrt{r_I^2 + r_J^2}} \frac{\partial U}{\partial \phi_{gc_{sat}}} \right) r_J + \left( \frac{1}{r_I^2 + r_J^2} \frac{\partial U}{\partial \lambda_{sat}} \right) r_I - \frac{\mu r}{r^3} \\ \frac{1}{r} \frac{\partial U}{\partial r} r_K + \frac{\sqrt{r_I^2 + r_J^2}}{r^2} \frac{\partial U}{\partial \phi_{gc_{sat}}} - \frac{\mu r}{r^3} \end{bmatrix} \quad (1)$$

In these equations,  $\phi_{gc_{sat}}$  is the geocentric latitude of the satellite,  $\lambda_{sat}$  is the satellite's longitude and  $\mu_{\oplus}$  is the standard gravitational parameter of the Earth. The partial derivatives of the gravitational potential are given by

$$\frac{\partial U}{\partial \phi_{gc_{sat}}} = \frac{\mu_{\oplus}}{r} \sum_{l=2}^{\infty} \sum_{m=0}^l \left( \frac{R_{\oplus}}{r} \right)^l (P_{l,m+1} \sin \phi_{gc_{sat}} - m \tan \phi_{gc_{sat}} P_{l,m} \sin \phi_{gc_{sat}}) \\ (C_{l,m} \cos m \lambda_{sat} + S_{l,m} \sin m \lambda_{sat}) \quad (2)$$

$$\frac{\partial U}{\partial \lambda_{sat}} = \frac{\mu_{\oplus}}{r} \sum_{l=2}^{\infty} \sum_{m=0}^l \left( \frac{R_{\oplus}}{r} \right)^l m P_{l,m} \sin \phi_{gc_{sat}} (S_{l,m} \cos m \lambda_{sat} - C_{l,m} \sin m \lambda_{sat}) \quad (3)$$

$$\frac{\partial U}{\partial r} = -\frac{\mu_{\oplus}}{r^2} \sum_{l=2}^{\infty} \sum_{m=0}^l \left( \frac{R_{\oplus}}{r} \right)^l (l+1) P_{l,m} \sin \phi_{gc_{sat}} [C_{l,m} \cos m \lambda_{sat} + S_{l,m} \sin m \lambda_{sat}] \quad (4)$$

The values of  $P_{l,m}$  are the associated Legendre functions, and  $C_{l,m}$  and  $S_{l,m}$  represent coefficients capturing various details of the average Earth's shape. Hence, ocean and

solid tides can be incorporated into the model through the suitable modification of  $C_{l,m}$  and  $S_{l,m}$ .

Under specific circumstances, the mixed effect of gravitational irregularities and orbit characteristics may produce orbital resonance. This effect is produced by the gradual interchange of momentum, which may greatly modify some orbit parameters. For this reason identifying its possible occurrence and influence on analyses is important. In this respect, there exists two main types of resonances, that arising from the averaged longitudinal geopotential at critical orbital inclination ( $63.4^\circ$ ), and that acting on equatorial orbits. For further details on this subject see Blitzer [272]. Although typical nanosatellite orbits cover a different range of inclinations at present, future mission orbits could be associated to some of these resonant effects.

### Lunisolar Perturbations

The commonly weak third body perturbations such as the solar and lunar gravitational pulls may become comparable to other perturbations experienced by a satellite at high orbital altitudes (see Fig. 2.15 in Chapter 2). Precise estimation of third body perturbations is complicated by the long relative distances used in computations, e.g. Moon-Earth and Moon-satellite distances in Fig. 2, and the fact that the third body perturbation is inversely proportional to the cube of those distances. These may yield to small terms prone to computational rounding introducing error to estimations. A suitable mathematical representation of third body perturbations for numerical estimations is presented in Eq. (5)–Eq. (7).

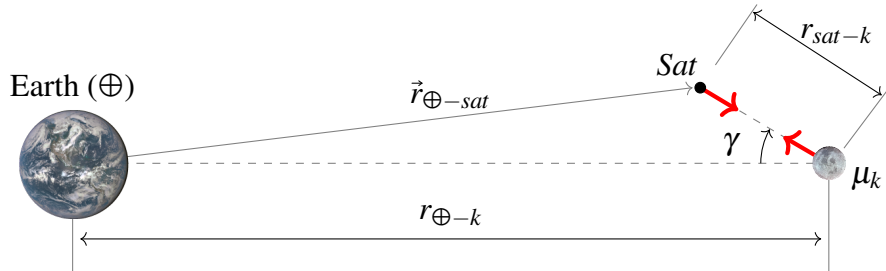


Fig. 2 Third-body perturbation elements.

## D: Main orbit perturbations

---

Lunisolar accelerations on a satellite are computed with Eq. (5).

$$\ddot{\vec{r}}_{\odot-\mathbb{C}-sat} = -\frac{\mu_{\odot}}{r_{\oplus-\odot}^3}(\vec{r}_{\oplus-sat} - \beta_{\odot}\vec{r}_{sat-\odot}) - \frac{\mu_{\mathbb{C}}}{r_{\oplus-\mathbb{C}}^3}(\vec{r}_{\oplus-sat} - \beta_{\mathbb{C}}\vec{r}_{sat-\mathbb{C}}) \quad (5)$$

In this equation, the value of  $\beta$  is suitably given in terms of  $B$ , a variable based on Legendre polynomials ( $P_j$ ).

$$\beta_k = 3B_k + 3B_k^2 + B_k^3 \quad (6)$$

$$B_k = \sum_{j=1}^{\infty} P_j(\cos \gamma) \left( \frac{r_{\oplus-sat}}{r_{\oplus-k}} \right)^j \quad (7)$$

## Solar Radiation Pressure

Another major perturbation acting on satellites is the Solar Radiation Pressure (SRP). Unlike gravitational perturbations, covered in the two previous cases, SRP is a non-conservative perturbation. The effect of SRP on orbit parameters may be small in comparison to other perturbations in standard satellite shapes, or deliberately amplified and used in specialised satellites, e.g. solar sails. However, SRP is mostly related to undesired attitude perturbations in standard satellites. The SRP perturbation magnitude depends on the area and angle at which the Sun radiation exerts force on it. Solar activity and the relative distance of the Sun are also important in the definition of the level of incoming radiation experienced by the satellite surfaces. The following set of equations have been compiled to provide a fundamental mathematical description to the standard SRP formula.

SRP is originated by traveling electromagnetic waves. Assuming that solar radiation travels in plane sinusoidal waves, the energy flux density transported by the electromagnetic field is given by the Poynting vector in Eq. (8)

$$\vec{S} = \frac{1}{\mu_0} \vec{E} \times \vec{B} \quad (8)$$

In this equation  $\mu_0$ ,  $\vec{E}$  and  $\vec{B}$  are the vacuum permeability, electric and magnetic fields respectively. Now, the power flux ( $P$ ) passing through a surrounding closed surface is

---

given by the energy flux density and the surface area vector ( $\hat{n}dA$ ) as in Eq. (9)

$$P = \iint_{Surf} \vec{S} \cdot \hat{n} dA \quad (9)$$

The time averaged solar power can thus be written in the form of Eq. (10)

$$P_\odot = \langle |\vec{S}_\odot| \rangle A_\odot = \frac{d\langle \mathcal{E}_\odot \rangle}{dt} \quad (10)$$

or equivalently as the temporal rate of change of the energy transported by the fields ( $\mathcal{E}_\odot$ ) enclosed by the surface. Assuming that the control volume is a sphere concentric to the Sun, the time averaged energy flux density is given by Eq. (11)

$$\langle |\vec{S}_R| \rangle = \frac{P_\odot}{4\pi R^2} \quad (11)$$

Complementary, the energy-momentum relation is given by Eq. (12), where  $\mathcal{L}$  is the momentum of a particle with rest mass  $m_0$ , and  $c$  is the speed of light.

$$\mathcal{E}^2 = \mathcal{L}^2 c^2 + m_0^2 c^4 \quad (12)$$

In the current problem  $m_0 = 0$  for photons, allowing the simplification of Eq. (12) to Eq. (13)

$$\mathcal{L} = \frac{\mathcal{E}}{c} \quad (13)$$

Acknowledging that the temporal rate of change of  $\mathcal{L}$  is proportional to the force  $F$ , or equivalently to the rate of change of the total energy, Eq. (13) yields Eq. (14)

$$F = \lim_{\Delta t \rightarrow 0} \frac{\Delta \mathcal{L}}{\Delta t} = \lim_{\Delta t \rightarrow 0} \frac{1}{c} \frac{\Delta \mathcal{E}}{\Delta t} \quad (14)$$

Finally, the SRP force in (15) is obtained by substituting Eq. (11) in Eq. (14)

$$F_{srp} = \frac{1}{c} \frac{d\mathcal{E}_R}{dt} \equiv \frac{1}{c} \langle |\vec{S}_R| \rangle A_{srp} \quad (15)$$

## D: Main orbit perturbations

---

In terms of radiated power from a black body (Stefan-Boltzmann law), the SRP pressure ( $p_{srp}$ ) can be written in the form of Eq. (16). This equation incorporates  $R$ , the relative distance to the Sun from the perturbed object.

$$p_{srp} = \frac{1}{c} \frac{P_\odot}{4\pi R^2} = \frac{\sigma T_\odot^4}{c} \left( \frac{R_\odot}{R} \right)^2 \quad (16)$$

Eq. (16) is typically used in SRP perturbation models in the form of Eq. (17). This simple function incorporates observational data through the solar irradiance value  $I_\odot$ . The sole effect of the Earth orbit eccentricity, note the  $R$  relationship in Eq. (16), causes a variation of  $\sim \pm 3.4\%$  on the observed average total solar irradiance of  $1361 \text{ W/m}^2$  at 1 AU throughout the Earth translation.

$$p_{srp} = \frac{I_\odot}{c} \quad (17)$$

This  $p_{srp}$  equation can be incorporated in a more descriptive force equation incorporating surface interaction characteristics. For example, Eq. (18) relates various practical parameters such as an  $i$ -th flat area element of interaction  $A_{sp_i}$ , its radiation angle of incidence  $\phi_{inc_i}$ , surface material specular reflectivity  $C_{Rs_i}$  and diffuse reflectivity  $C_{Rd_i}$  (e.g. Table 4), and satellite mass  $m$ .

$$\ddot{\vec{r}}_{srp} = - \sum_{i=1} \frac{p_{srp} A_{sp_i} \cos \phi_{inc_i}}{m} \left[ 2 \left( \frac{C_{Rd_i}}{3} + C_{Rs_i} \cos \phi_{inc_i} \right) \hat{n} + (1 - C_{Rs_i}) \hat{s} \right] \quad (18)$$

The  $i$ -th outward surface normal vector  $\hat{n}$  and the Sun-spacecraft surface vector  $\hat{s}$  are illustrated in Fig. 3.

### Atmospheric Drag

Atmospheric drag is discussed in detail in Chapter 5. In a brief description, drag acceleration is typically modelled through Eq. (19). Drag acceleration is antiparallel to the satellite's relative velocity vector with respect to the surrounding atmosphere and is a strong function of its magnitude. In this respect, a common simplification is

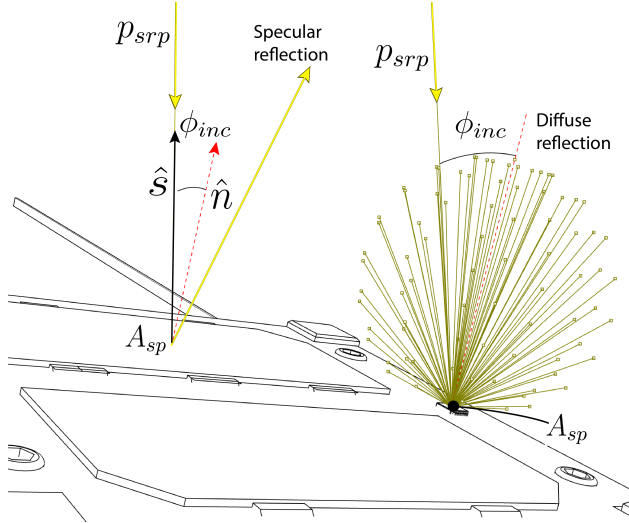


Fig. 3 Incident solar radiation. Reflection may occur in specular or diffuse pattern depending on the exposed surface optical characteristics.

Table 4 Optical properties for common surface materials. Data from Fahnestock et al. [240].

Material	Beginning of life (BOL)				End of life (EOL)			
	$\alpha$	$\epsilon$	$C_{Rs}$	$C_{Rd}$	$\alpha$	$\epsilon$	$C_{Rs}$	$C_{Rd}$
MLI (Aluminized Kapton)	0.410	0.720	0.550	0.040	0.470	0.720	0.490	0.040
Silver Teflon	0.090	0.780	0.850	0.060	0.140	0.780	0.800	0.060
White Paint Z-93C55	0.160	0.910	0.040	0.800	0.210	0.910	0.040	0.750
Solar Cells	0.910	0.840	0.090	0.000	0.910	0.840	0.090	0.000
Bare M55J	0.920	0.700	0.000	0.080	0.920	0.700	0.000	0.080
Warm Gas Radiator	0.250	0.890	0.040	0.710	0.300	0.890	0.035	0.070
Aluminium Foil	0.180	0.010	0.660	0.160	0.180	0.010	0.660	0.160

## D: Main orbit perturbations

---

to assume that the atmosphere rotates with the Earth at the same angular speed  $\omega_{\oplus}$ . In reality the atmosphere follows a velocity profile with slower bulk velocities with increasing altitude i.e. the lower atmosphere rotates close to  $\omega_{\oplus}$  whilst higher strata lag slightly behind [139]. Furthermore, the thermosphere is subject to wind variations according to the local time and season. An example of observed thermospheric wind speed fluctuations is presented in Fig. 4 from the GOCE mission at 270km. This topic would acquire more relevance as functional nanosatellite missions and other small platforms gradually populate orbital altitudes below 400 km.

$$\ddot{\vec{r}}_{drag} = -\frac{1}{2} \frac{C_{DA_{dcs}}}{m} \rho v_{rel}^2 \frac{\vec{v}_{rel}}{|\vec{v}_{rel}|} \quad (19)$$

It is possible to include thermosphere wind variations in model in Eq. (19) by adding it into the relative atmosphere velocity vector as shown in Eq. (20). In this equation  $v_w$  is the wind speed, with  $\beta_w$ ,  $\alpha$ , and  $\delta$  as the satellite's azimuth, right ascension, and declination respectively. The Horizontal Wind Model (HWM) is commonly used in computational orbit propagators to incorporate wind variations to atmospheric drag estimations.

$$\vec{v}_{rel} = \begin{bmatrix} \dot{r}_x + \omega_{\oplus} r_y + v_w (-\cos \alpha \sin \delta \cos \beta_w - \sin \alpha \cos \beta_w) \\ \dot{r}_y - \omega_{\oplus} r_x + v_w (-\sin \alpha \sin \delta \cos \beta_w + \cos \alpha \sin \beta_w) \\ \dot{r}_z + v_w (\cos \delta \cos \beta_w) \end{bmatrix} \quad (20)$$

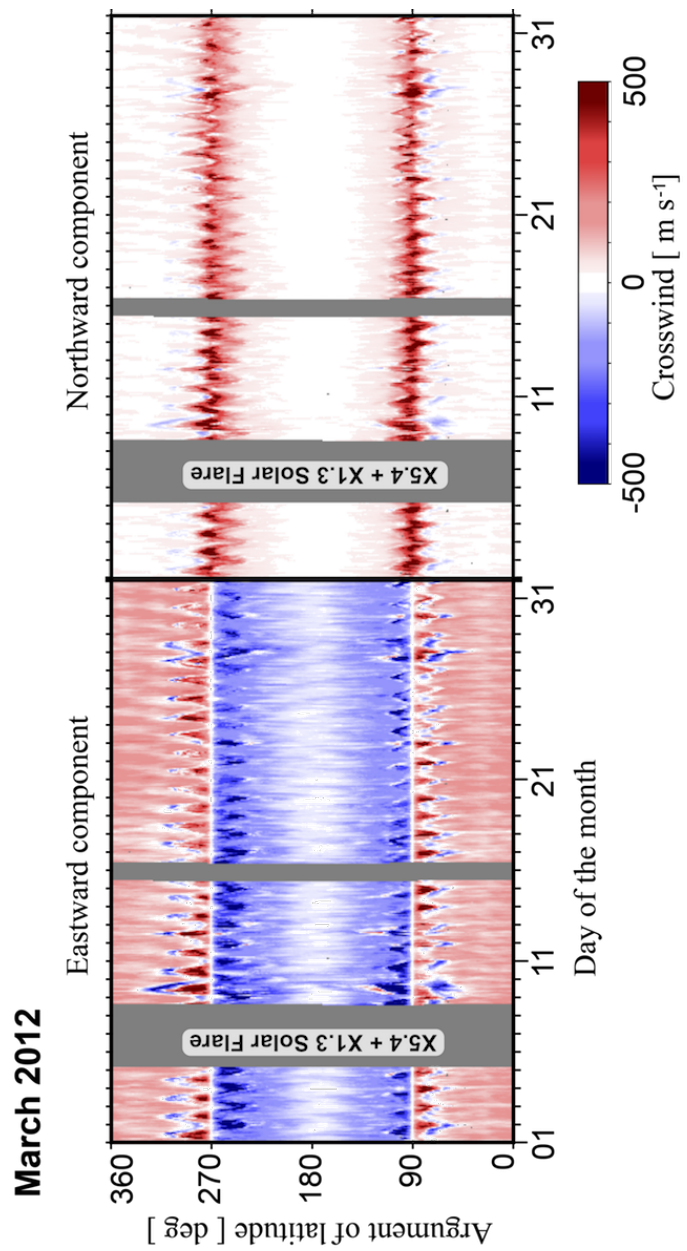


Fig. 4 Crosswind speed along GOCE orbit. Two solar flares on 6 March, and corresponding Coronal Mass Ejections directly impacting Earth on 8 March, caused drastic atmospheric density and dynamics variations reducing the orbit altitude about 1 km in one day. Subsequently the propulsion system cancelled the orbital offset to the nominal orbital altitude of 270 km. Image composed with data from ESA [113].

Blank page

## E: Ideal photovoltaic solar cell efficiency

This appendix expands on photovoltaic solar cell efficiency discussed in Chapter 2. Photovoltaic conversion efficiency is limited by many factors. Radiation angle of incidence, temperature gradients, and technology are some of them. In thermodynamic arguments, the conversion can be simplified to a general case in order to establish the maximum theoretical attainable efficiency. Although unreachable, it is worthwhile introducing this concept as the efficiency limit offers a reference point to assess current technologies and helps delimiting technology expectancies. Ultimately, photovoltaic cells support current general operations in nanosatellites and enable the use of high performant propulsion systems.

Assume the hypothetical system shown in Fig. 5, where the incoming heat energy flux from the Sun and its corresponding entropy flux are defined by  $\dot{E}_\odot$  and  $\dot{S}_\odot$  respectively. This hypothetical converter produces useful work  $\dot{W}_\square$ , and rejects heat  $\dot{Q}_\square$  [273]. In order to impose the physical restrictions found in a real device, it is necessary to include additional entropy terms.  $\dot{S}_G$  is the entropy resulted from the generation process itself, and the entropies generated during black-body absorption and emission of radiation are  $\dot{S}_\alpha$  and  $\dot{S}_e$  respectively. The energy and entropy flux re-radiated by the converter are denoted by  $\dot{E}_R$  and  $\dot{S}_R$ . Expressions for these hypothetical converter parameters are given by Eq. (21)–(26)

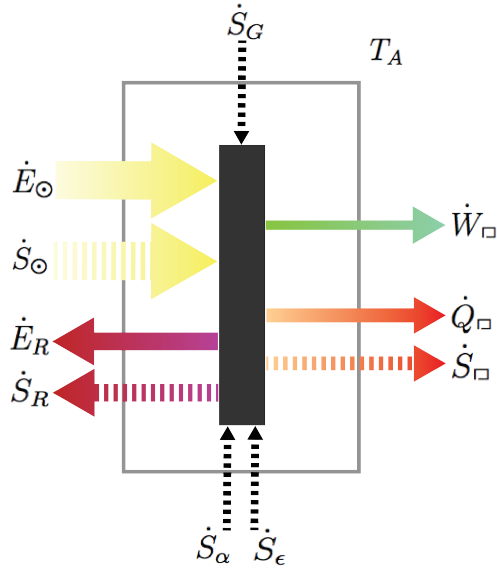


Fig. 5 The hypothetical solar converter for calculating efficiency limit.

$$\dot{E}_\odot = \sigma T_\odot^4 \quad (21)$$

$$\dot{S}_\odot = \frac{4\dot{E}_\odot}{3T_\odot} \quad (22)$$

$$\dot{S}_\alpha = \dot{E}_\odot \left( \frac{1}{T_R} - \frac{4}{3T_\odot} \right) \quad (23)$$

$$\dot{S}_\epsilon = \frac{\dot{E}_R}{3T_R} \quad (24)$$

$$\dot{E}_R = \sigma T_R^4 \quad (25)$$

$$\dot{S}_R = \frac{4}{3}\sigma T_R^3 \quad (26)$$

From energy balance it is possible to define Eq. (27)

$$\dot{W}_\square = \dot{E}_\odot - \dot{E}_R - \dot{Q}_\square \quad (27)$$

Similarly, entropy balance yields Eq. (28)

$$\dot{S}_\square = \dot{S}_\odot + \dot{S}_G + \dot{S}_\alpha + \dot{S}_\epsilon - \dot{S}_R \quad (28)$$

---

The system's energy and entropy are related through the term  $\dot{S}_{\square} = \frac{\dot{Q}_{\square}}{T_A}$ , and the hypothetical converter efficiency is given by Eq. (29)

$$\eta_{\square} = \frac{\dot{W}_{\square}}{\dot{E}_{\odot}} \quad (29)$$

By substituting Eq. (21)–(26) in Eq. (29) and after algebraic simplification, the conversion efficiency can be written in the form of Eq. (30)

$$\eta_{\square} = \frac{(T_A - T_R)(T_R^4 - T_{\odot}^4)}{T_R T_{\odot}^4} - \frac{\dot{S}_G T_A}{\sigma T_{\odot}^4} \quad (30)$$

The maximum conversion efficiency is only possible in the absence of irreversibilities associated to the generation process, in other words  $\dot{S}_G$  must be zero. Assuming that the solar photosphere temperature ( $T_{\odot}$ ) is known as well as the local ambient temperature ( $T_A$ ), then the value of  $T_R$  is obtained by maximising for efficiency. For instance, in a terrestrial converter wherein  $T_{\odot} = 6000\text{ K}$  and  $T_A = 300\text{ K}$ , the optimum value is  $T_R = 2544\text{ K}$  corresponding to a maximum attainable efficiency of 85.36%.

Blank page

## F: Propulsion systems in CubeSats

Table 5 Reported historical and planned CubeSat missions equipped with propulsion systems.

CubeSat Name	Launch Date	Size Factor	Propellant	Details
AeroCube 7B&C (AC 7B&C, OCSD B&C)	2016	1.5U	Water	$T_{max} = 5\text{ mN}$ and $I_{sp} = 75\text{ s}$ [40]
AeroCube 8A&B (AC 8A&B, IMPACT A&B)*	20/05/2015	1.5U	Polyether ether ketone	$T = 12.5\text{ }\mu\text{N}$ ca. <sup>†</sup> and $I_{sp} = 1200\text{ s}$ [66]. Scalable ion-Electrospray Propulsion system SiEPro
BRICSat-P (NO 83, OSCAR 83)	20/05/2015	1.5U	Titanium cathode	$T = 1\text{ }\mu\text{N}$ and $I_{sp} = 3000\text{ s}$ [39]. Micro-Cathode Arc Thruster $\mu$ CAT <sup>‡</sup>
BRICSat-2	2017	1.5U	Titanium cathode	$T = 1\text{ }\mu\text{N}$ and $I_{sp} = 3000\text{ s}$ [39]. Micro-Cathode Arc Thruster $\mu$ CAT <sup>‡</sup>
NJUST-2	25/09/2015	2U	–	Cold gas? [47]
RAMPART*	2013	2U	DuPont Dymel-134a	$T = 0.5\text{ N}$ and $I_{sp} = 67 - 90\text{ s}$ [68]. Warm-gas Resistojet
Shankeda-2	25/09/2015	2U	–	Cold gas? [47]
Pegasus (QB50 AT03)	2017	2U	–	PPT [274]
TW-1 (A/B/C Constellation)	25/09/2015	2 – 3U	Butane	$T = 1\text{ mN}$ , $I = 40\text{ N s}$ [275], Nanospace
Bianri-Squad 1&2&3	2016	3U	–	Microthrusters [276]
URSA MAIOR (QB50 LT02)	2017	3U	Nitrogen	$T = 1\text{ mN}$ [277]
CanX-2*	28/04/2008	3U	$SF_6$	$T = 50\text{ mN}$ and $I_{sp} = 35 - 40\text{ s}$ [69], NanoPS
CPOD A&B	01/01/2016	3U	R-134a	$T = 25\text{ mN}$ and $I_{sp} = 40\text{ s}$ [71], VACCO
Delfi-n3Xt*	21/11/2013	3U	Nitrogen	$T = 6 - 150\text{ mN}$ [72] and $I_{sp} > 30\text{ s}$ [73]
BEVO-2*	29/01/2016	3U	DuPont 236-fa	$T = 110 - 150\text{ mN}$ and $I_{sp} = 65.7 - 89.5\text{ s}$ [70]
LituaniaSAT 2 (QB50 LT01)	2016	3U	LMPI03S	$T = 0.3\text{ N}$ and $\Delta v = 200\text{ m s}^{-1}$ [278]
NJPA-1	25/09/2015	3U	–	Cold gas? [47]
PATRIOT	–	3U	–	$T = 2\text{ mN}$ and $I_{sp} = 2000\text{ s}$ at an input power of 10W [74]. Ambipolar Thruster (CAT)
POPSAT-HIP 1	19/06/2014	3U	Argon	$T = 0.1 - 10\text{ mN}$ and $I_{sp} = 50\text{ s}$ , Cold Gas Thruster [30]
ALL-STAR PropSat	–	3U	R-134a	Cold Gas Thruster [279]
SERPENS*	19/08/2015	3U	Teflon	$T = 40\text{ }\mu\text{N}$ and $I_{sp} = 600\text{ s}$ at an input power of 2 W [75], PPTCUP <sup>§</sup>
StraND-1*	25/02/2013	3U	Elkonite	$T = 0.9\text{ }\mu\text{N}$ and $I_{sp} = 1340\text{ s}$ [31], PPT
SAMSON	2017	6U	Water-isopropanol	Resistojet <sup>**</sup> [280]
ARAPAIMA	–	6U	Teflon	$T = 40\text{ }\mu\text{N}$ and $I_{sp} = 600\text{ s}$ at an input power of 2 W [281], PPTCUP <sup>§</sup>
Lunar-IceCube	2018	6U	Hexafluoropropene	$T = 100\text{ mN}$ and $I_{sp} = 47\text{ s}$ [76]
MarcO 1 & 2	2018	6U	Solid iodine	$T = 1.4\text{ mN}$ and $I_{sp} = 3500\text{ s}$ [77], Miniature electric RF ion engine BIT-3 <sup>§</sup>
			R-236fa	$T = 25\text{ mN}$ [282], VACCO

\* Propulsion technology demonstration mission

<sup>†</sup> Values for the reported original S-iEPS module

<sup>‡</sup> Operates at 1 – 50Hz generating 1mNs/pulse and  $I_{sp} = 2000 - 3000\text{ s}$  [283]

<sup>§</sup> Commercial propulsion unit

<sup>\*\*</sup> A butane resistojet was originally proposed with  $C_4H_{10}$   $T = 502\text{ mN}$  and  $I_{sp} = 75\text{ s}$  [31]

Data collected from stated main references, and miscellaneous data from eoPortal Directory [47]

Blank page

# G: Fitted momentum accommodation coefficients

This appendix expands on fitted drag parameters discussed in Chapter 5. It is explored the possibility to look into weaker characteristics of atmospheric drag such as the average quality of reflections of atmospheric particles on satellite surfaces. To this objective, computed models<sup>1</sup> of  $\bar{\phi}_{ic,w}$  and the instantaneous weighted average of the exposed area,  $\bar{A}_{s,w}$  are assumed sufficiently detailed practical geometry abstractions of RAX-2. That geometry abstraction is intended to replace the actual cuboidal geometry of RAX-2, enabling the derivation of a simple closed-form GSI model. In addition, geometry simplification is intended to reduce the computational burden generated by the high number of orbit and attitude propagations required by the fitting method.

In order to represent the geometry abstraction of RAX-2, this study uses a dynamic cone model with zero angle of attack and variable angle of aperture  $\Delta$ , as shown in Fig. 6. The characteristics of the cone are defined by the temporal-spacial variations of  $\bar{\phi}_{ic,w}$  and  $\bar{A}_{s,w}$ . The purpose of this approach is to enrich the atmospheric-spacecraft interaction analysis (fitting process) by adding a dimension to the typical 2-D cross-sectional approach. For example, a typical static average cross-sectional area can be represented as a discoid vector area parallel to a reference vector, i.e. velocity or Sun vector. In the study of  $C_{DF}$  in this investigation, the discoid vector area varies according to temporal-spatial features of the orbit, CubeSat attitude, and reference vector in

---

<sup>1</sup>Detailed attitude and orbit simulations, covering a great variety of scenarios such as attitude steady state response, eclipse conditions, etc., furnish information about likely cross-sectional area variations and angles of incidence (of atmospheric particles and photons).

## G: Fitted momentum accommodation coefficients

---

the so-called dynamic cross-sectional areas. Intuitively, the 2D disc abstraction of a cross-sectional area can be extrapolated to a 3D shape to enclose a richer representation of the actual CubeSat geometry. In this last case, the disk is transformed into a cone to embed information about the angle of incidence as well as the exposed surface area. It is important to bear in mind that the use of a cone is intended to replace the actual geometry of RAX-2 to enable the fitting of variables only, and not as a trivial substitution to estimate the physical drag coefficient of RAX-2.

### Cone geometry in free-molecular flow

The general analysis of the aerodynamic force on a cone in free-molecular flow is only possible though numerical simulations, i.e. for the complete spectrum of angles of attack. However for a cone with zero angle of attack, like the one proposed for this investigation, a closed form solution exists. Thus, the following procedure considers a cone with transversal circular cross section and null angle of attack as shown in Fig. 6.

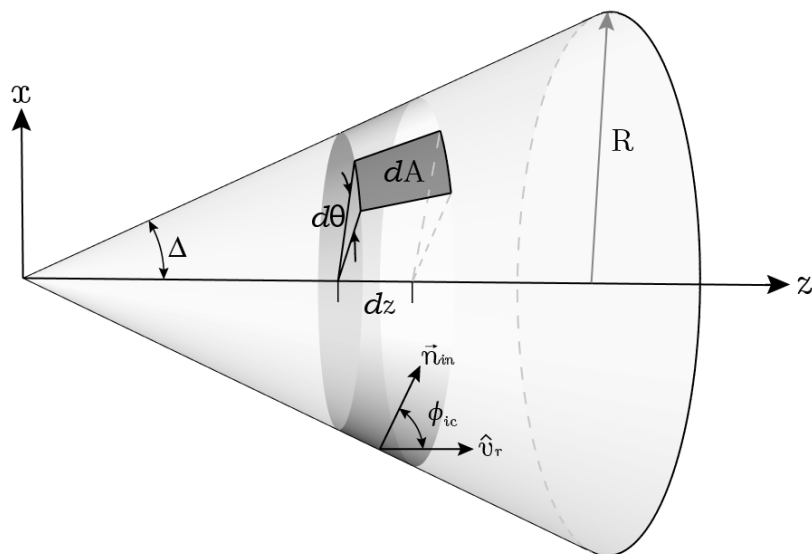


Fig. 6 Cone geometry used to derive an aerodynamic force closed form solution.

In cylindrical coordinates the surface of the cone is described by  $0 \leq \theta \leq 2\pi$ ,  $0 \leq r \leq R$ , and  $r = \tan \Delta z$ . A surface area element located at an arbitrary point is given by  $dA = \sin \Delta / \cos^2 \Delta z dz d\theta$  with inward normal vector  $\vec{n}_{in} = -\cos \Delta \cos \theta \hat{i} - \cos \Delta \sin \theta \hat{j} +$

---

$\sin \Delta \hat{k}$ . The scalar product of  $\vec{n}_{in}$  and  $\hat{v}_r$  is used to relate the cone's angle of aperture to the particles' angle of incidence, yielding  $\sin \Delta = \cos \phi_{ic}$ .

The drag force acting on a body moving in a Maxwellian flow is defined by Eq. (31), where the auxiliary functions  $\mathcal{F}$  are given by Eq. (32) – (35). In this respect, the work of Storch [239] provides detailed derivation of these formulae.

$$\vec{F}_D = \rho v_r^2 \left( \frac{\sigma_t}{s} \mathcal{F}_1 \hat{v}_r + \frac{2 - \sigma_n}{s^2} \vec{\mathcal{F}}_2 - \frac{\sigma_t}{s} \vec{\mathcal{F}}_3 + \frac{\sigma_n}{s} \frac{v_w}{v_r} \vec{\mathcal{F}}_4 \right) \quad (31)$$

$$\mathcal{F}_1 = \iint \Gamma_1 (s \cos \phi_{ic}) dA \quad (32)$$

$$\vec{\mathcal{F}}_2 = \iint \Gamma_2 (s \cos \phi_{ic}) \vec{n}_{in} dA \quad (33)$$

$$\vec{\mathcal{F}}_3 = \iint \Gamma_1 (s \cos \phi_{ic}) \cos \phi_{ic} \vec{n}_{in} dA \quad (34)$$

$$\vec{\mathcal{F}}_4 = \iint \Gamma_1 (s \cos \phi_{ic}) \vec{n}_{in} dA \quad (35)$$

In these equations,  $\Gamma_{1,2}$  (Eq. (36) and Eq. (37)) are universal functions used to ease the symbolic integration process.

$$\Gamma_1(x) = \frac{1}{2\sqrt{\pi}} \left[ e^{-x^2} + \sqrt{\pi}x(1 + \operatorname{erf} x) \right] \quad (36)$$

$$\Gamma_2(x) = \frac{1}{2\sqrt{\pi}} \left[ xe^{-x^2} + \frac{\sqrt{\pi}}{2} (1 + 2x^2)(1 + \operatorname{erf} x) \right] \quad (37)$$

Note that the terms in parentheses in Eq. (31) should be equivalent to  $A_{ref} C_D / 2$ . This is deduced by comparison to the standard drag force equation. Using this comparison and the surface integration over the given limiting conditions, enable the identification of a function for the drag coefficient of the cone in Eq. (38).

$$C_{D\triangle} = \frac{1}{2\sqrt{\pi}s^2} (\mathcal{G}_1 + \mathcal{G}_2 + \mathcal{G}_3) \quad (38)$$

The substitution variables,  $\mathcal{G}_1, \mathcal{G}_2, \mathcal{G}_3$ , are given by

$$p = s \cos \phi_{ic} \quad (39)$$

$$\mathcal{G}_1 = \frac{2\sigma_t}{p} s^2 e^{-p^2} \quad (40)$$

$$\mathcal{G}_2 = \sqrt{\pi} \left[ (2 - \sigma_{n1} + 2s^2\sigma_t) (1 + \operatorname{erf} p) + \sigma_{n2} \sqrt{\frac{T_w}{T_\infty}} e^{-p^2} \right] \quad (41)$$

$$\mathcal{G}_3 = p \left[ 2\sqrt{\pi}p(2 - \sigma_{n1} - \sigma_t)(1 + \operatorname{erf} p) + 2(2 - \sigma_{n1} - \sigma_t)e^{-p^2} + \pi\sigma_{n2}\sqrt{\frac{T_w}{T_\infty}}(1 + \operatorname{erf} p) \right] \quad (42)$$

By rearranging factors into the familiar drag acceleration equation form, the drag acceleration of a cone is given by Eq. (43).

$$\ddot{\vec{r}}_{drag} = \frac{1}{2} \frac{C_{D\triangle} A_s \cos \phi_{ic}}{m_{sc}} \rho v_r^2 \frac{\vec{v}_r}{|\vec{v}_r|} \quad (43)$$

Note that Eq. (41) and Eq. (42) are functions of  $\sigma_{n1}$  and  $\sigma_{n2}$ ,  $T_w$ , and  $T_\infty$  instead of  $\sigma_n$ ,  $v_r$  and  $v_w$  in Eq. (31). This new equation form allows the adaptation of the CLL kernel functions (44) and (45) proposed in the work of Walker et al. [223]. In a necessary assumption, the values of the best-fit parameters for a flat plate are used in the cone geometry.

$$\sigma_{n1} = 1 - \sqrt{1 - \alpha_n} \quad (44)$$

$$\sigma_{n2} = \frac{\zeta}{s} \left( \frac{T_w}{T_\infty} \right)^\delta e^{-\beta(1-\alpha_n)^\gamma} \quad (45)$$

As final remark in this section, note that the limit of the expression in Eq. (38), for  $\Delta \rightarrow \pi/2$  or  $\phi_{ic} \rightarrow 0$ , recovers the flat plate function given by Eq. (5.10) in Chapter 5.

### Fitted tangential accommodation coefficient

Eq. (38) requires the knowledge of the tangential and normal momentum accommodation coefficients. A sensitivity analysis on Eq. (46) shows that change on  $\sigma_t$  prompts approximately three times more variation on  $C_{D\triangle}$  than  $\sigma_n$  for the characteristic average values of  $s = 6.75$ ,  $\Delta = 31.70^\circ$ ,  $T_w = 307.10\text{K}$ , and  $T_\infty = 1055.50\text{K}$  during the time

---

arc under analysis for RAX-2.

$$\left| \frac{\partial C_{D\triangleleft}}{\partial \sigma_t} \right| \approx 2.9 \left| \frac{\partial C_{D\triangleleft}}{\partial \sigma_n} \right| \quad (46)$$

It is known that the value of  $\sigma_t$  largely describes the quality of the reflections of the GSI process as explained in subsection 5.1.1 in Chapter 5. In addition, the higher variability of  $C_{D\triangleleft}$  on  $\sigma_t$  changes, defines  $\sigma_t$  as the adequate variable to fit. Hence, the use of a function to estimate  $\sigma_n$  is necessary. In this respect, laboratory experiments carried out by Knechtel and Pitts [284] show that the momentum accommodation coefficients in GSIs are functions of  $\phi_{ic}$  and the collision activation energy,  $\mathcal{E}$ , according to Eq. (47) and Eq. (48). Further, the value of  $\mathcal{E}$  is equivalent to the total kinetic energy,  $E$ , of an impinging neutral gas molecule. The three curve fit parameters,  $C_{xa}$ ,  $C_{xb}$ ,  $C_{xc}$ , account for other miscellaneous factors such as gas and surface molecular sizes.

$$\sigma_n = C_{na} - C_{nb} e^{-C_{nc} \mathcal{E} \cos^2 \phi_{ic}} \quad (47)$$

$$\sigma_t = C_{ta} - C_{tb} e^{-C_{tc} \mathcal{E} \sin^{\frac{3}{4}} \phi_{ic}} \quad (48)$$

Laboratory bombardment of a molecularly contaminated aluminium surface (atomic oxygen surface contamination is expected in low LEO objects) with molecular nitrogen can be approximated by Eq. (49) and Eq. (50) [285]. In this investigation Eq. (49) is used to define the value of  $\sigma_n$  to fulfil the requirement in Eq. (38).

$$\sigma_n = 0.93 - 1.48 \times 10^{-3} \phi_{ic} - 7.00 \times 10^{-5} \phi_{ic}^2 \quad (49)$$

$$\sigma_t = 0.63 - 0.63 e^{-3.38 \times 10^{-2} \phi_{ic}} \quad (50)$$

## Simulations and results

In general, the simulation approach is similar to that presented in Chapter 5. That is, RAX-2 orbit and attitude propagation required by the fitting method is performed in consecutive pairs of TLE sets. A starting TLE set data is used to define the initial state

## G: Fitted momentum accommodation coefficients

---

vector and epoch for simulation. In addition, this information establishes space weather conditions and initial attitude of the RAX-2. The propagation time arc is defined by the difference between an initial TLE set and the successive TLE available. To compute the instantaneous solar radiation pressure, the spherical harmonic functions approach presented in Chapter 5 is used. The Stokes coefficients have been computed as functions of geocentric latitude and longitude differences between the Sun vector and RAX-2 position. The estimation of  $\bar{\phi}_{ic,w}$  is carried out with the Stokes coefficients function of the geocentric position of RAX-2 as in Chapter 5. Finally, the values of  $\bar{\phi}_{ic,w}$  are used in  $C_{D\triangleleft}$  (Eq. (38)) to evaluate the instantaneous drag coefficient.

As a first analysis of the fitting results, the cross-correlation map amongst  $\phi_{ic}$ , AO,  $\sigma_t$ ,  $s$ , and  $E$  is reported in Fig. 7. In general, weak cross-correlation amongst the values is observed. However, cross-correlation coefficients still show the relationships foreseen by theory. For instance,  $\sigma_t$  is to some extent dependent on AO,  $E$ ,  $s$ , and  $\phi_{ic}$  as shown by the figure; an increment in  $\phi_{ic}$  produces increment in  $\sigma_t$  (positive cross-correlation coefficient) as shown by Eq. (50); and high atmospheric energy  $E$  conditions increase AO and  $s$  values.

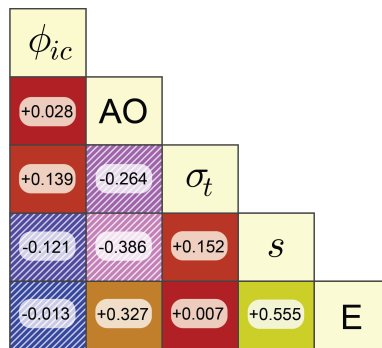


Fig. 7 Cross-correlation map of  $\sigma_t$ , AO,  $E$ ,  $s$ , and  $\phi_{ic}$ .

It is discussed in Chapter 5 that AO is positively related to the accommodation coefficients  $\alpha$  and  $\sigma$ . This means that an increment in AO, for fixed values of other parameters, causes increment in  $\alpha$  and  $\sigma$ . The correlation map in Fig. 7 fails to show this positive relationship in  $\sigma_t$ . In order to explain this, note that the condition of fixed variables for a variation in AO is not satisfied. What is shown by the cross-correlation

---

map is that under high atmospheric energy conditions, the  $\sigma_t$  fitting procedure to reduce differences between observed-simulated semi-major axis for RAX-2, fails to capture the relationship between  $\sigma_t$  and AO. In addition it underestimates the relationship between  $\sigma_t$  and  $E$ .

The plot in Fig. 8 shows the averaged fitted  $\sigma_t$  values versus  $\bar{\phi}_{ic}$ , according to their respective time intervals of propagation. Analytic  $\sigma_t$  values estimated with Eq. (50) are superimposed for comparison purposes. The figure shows that the averaged  $\bar{\phi}_{ic}$  covers the range  $58 - 59^\circ$ . This range corresponds to the  $\bar{\phi}_{ic}$  characterising the average intervals of propagation. Expanding on this, from Fig. 5.8 is observed that most filtered TLE sets cover epoch time differences of more than one Julian day implying reduced variability on the averaged  $\bar{\phi}_{ic}$ . That is, if the TLE sets epoch time difference were shorter, then a richer range of  $\bar{\phi}_{ic}$  values would be collected. Applying a statistical kernel distribution on the fitted  $\sigma_t$  yields an estimated value of  $\tilde{\sigma}_t = 0.5854$  with standard deviation of 0.2154. On the other hand, the evaluation of Eq. (50) at the average value  $\bar{\phi}_{ic} = 58.28^\circ$  covering the range under analysis, yields a  $\sigma_t$  value of 0.5421. This represents a variation of +7.99% of  $\tilde{\sigma}_t$  with respect to the analytic value  $\sigma_t$ .

The information collected in this investigation about the fitted value of  $\sigma_t$ , suggests that it is likely to use this method to estimate its value. However, data dispersion in Fig. 8 also suggests that the fitting method based on observed noisy data (TLE sets) for the analysed orbital and environmental conditions of the RAX-2, may be in the limit of sensitivity. Additional investigation of a wider variety of space weather conditions and orbital altitudes is required to further clarify the source of high fitted data dispersion and abnormal cross-correlation amongst variables.

## G: Fitted momentum accommodation coefficients

---

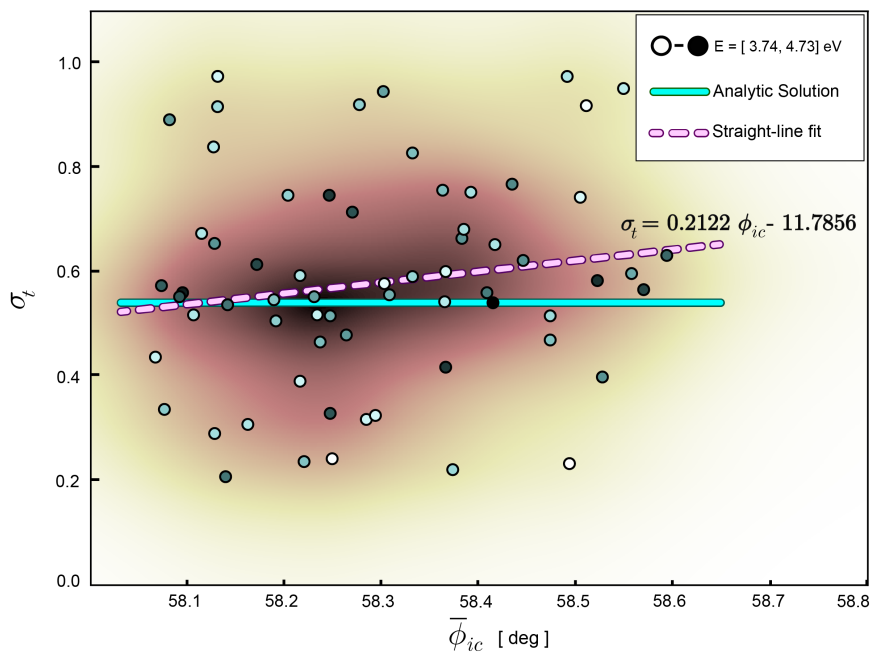


Fig. 8 Fitted  $\sigma_t$  for RAX-2. The straight line fit shows a weak positive linear relationship with Spearman's correlation coefficient of 0.159. The results are confined to a small range of  $\bar{\phi}_{ic}$  as imposed by large TLE time intervals.

# H: Spiral coning algorithm example

A Matlab R2014a script example for low thrust estimation using the proposed spiral coning manoeuvre.

```
% ****
% * SPIRAL CONING MANOEUVRE FOR IN-ORBIT LOW THRUST CHARACTERISATION IN *
% * CUBESATS: ALGORITHM EXAMPLE
% ****
%
% Author : Alejandro Macario Rojas
% e-mail : alexmacario.rojas@gmail.com
% Created : 09/04/16
% Last Modified: 10/04/16
%
% Description: Implementation of the spiral coning manoeuvre for in-orbit *
% low thrust characterisation in CubeSats.
%
% Inputs : Noisy 3-axis Gyroscope readings and misc data
% Outputs : Estimated thrust level and relative error percentage
% References:
% - Macario-Rojas,A., & Smith, K. L. (2017). Spiral coning
%   manoeuvre for in-orbit low thrust characterisation in CubeSats.*  

%   Aerospace Science and Technology, 71, 337-346.
% - MATLAB Signal Processing Toolbox
%
%
function [] = f_ThrustFromXYZ()
% Constants and conversion factors
d2r = pi/180;
%
% * RETRIEVE DATA FROM FILE * -----
%
% Load data
load('SampleFile');
% Retrieve vectors
tgyro = Sample.Data_Sample(:,1); % Time [s]
dataXd = Sample.Data_Sample(:,2); % X rate in [deg/s]
dataYd = Sample.Data_Sample(:,3); % Y rate in [deg/s]
dataZd = Sample.Data_Sample(:,4); % Z rate in [deg/s]
% Retrieve experiment schedule (manoeuvre 1, coast, manoeuvre 2)
man1 = Sample.Schedule(1); % First rotation about X or Y [min]
cst = Sample.Schedule(2); % Coasting after man1 [min]
man2 = Sample.Schedule(3); % Second rotation about Z [min]
% Retrieve satellite information
It = Sample.SatInfo(1); % Transversal moment of inertia [kg m**2]
IZ = Sample.SatInfo(2); % Moment of inertia in Z [kg m**2]
MZ = Sample.SatInfo(3); % Known total thrust angular momentum [N m]
armm = Sample.SatInfo(4); % Effective moment arm in the CubeSat model [m]
odr = Sample.SatInfo(5); % Digital output data rate [Hz]
% Input data from [deg/s] to [rad/s]
dataXr = d2r.*dataXd;
dataYr = d2r.*dataYd;
dataZr = d2r.*dataZd;
%
% * TIME VECTOR DIVISION * -----
```

## H: Spiral coning algorithm example

---

```
% ****
% Coast 1 (Pre-characterising manoeuvre)
coast1 = tgyro >= 60*(man1) & tgyro <= 60*(man1 + cst);
t_coast1 = tgyro(coast1); % Absolute time vector
rt_coast1 = t_coast1 - t_coast1(1); % Relative time vector
% Characterising Manoeuvre
mano2 = tgyro >= 60*(man1 + cst) & tgyro <= 60*(man1 + cst + man2);
t_mano2 = tgyro(mano2); % Absolute time vector
rt_mano2 = t_mano2 - t_mano2(1); % Relative time vector
% Coast 2 (Post-characterising manoeuvre)
coast2 = tgyro >= 60*(man1 + cst + man2);
t_coast2 = tgyro(coast2); % Absolute time vector
rt_coast2 = t_coast2 - t_coast2(1); % Relative time vector
% ****
% * SIGNAL CONDITIONING * -----
% ****
% SMOOTHED CURVES IN X AND Y
% Data range of interest (e.g. From man1 up to the end)
range = tgyro >= 60*(man1);
% Filtering (e.g. Applying a linear Savitzky-Golay filter)
% filter to data frames of length 1001
% Matlab Signal Processing Toolbox required
frm = 1001;
fit_X = sgolayfilt(dataXr(range),1,frm);
fit_Y = sgolayfilt(dataYr(range),1,frm);
fit_Z = sgolayfilt(dataZr(mano2),1,frm);
% Final smoothed curves
coast1_SC_X = fit_X(1:size(t_coast1,1));
coast1_SC_Y = fit_Y(1:size(t_coast1,1));
coast2_SC_X = fit_X(size(t_coast1,1) + size(t_mano2,1) - 1:end);
coast2_SC_Y = fit_Y(size(t_coast1,1) + size(t_mano2,1) - 1:end);
% ****
% * FREQUENCY ANALYSIS * -----
% ****
% Obtain main frequency from the transversal periodic signals in [rad/s]
[w_fit_coast1] = freqFmXYsignal(rt_coast1,coast1_SC_X,coast1_SC_Y,odr);
[w_fit_coast2] = freqFmXYsignal(rt_coast2,coast2_SC_X,coast2_SC_Y,odr);
% ****
% * THRUST ESTIMATION * -----
% ****
%
% Traditional _/ \
% Directly from angular acceleration in Z (Spin/Despin)
lcf_Z = polyfit(t_mano2,fit_Z,1); % Lienar curve fitting
angacc2 = lcf_Z(1);
% Thrust Torque Magnitude
MZ_mano2_dir = abs(angacc2*IZ);
% Reference actual thrust level
MZ_actual_ea = MZ/2; % From each one of the two active patch thrusters
Thrust_actual = abs(MZ_actual_ea)/armm; % [N]
fprintf('\n\nActual thrust level: %2.2e [N]',Thrust_actual)
MZ_est_mano2_ea = MZ_mano2_dir/2; % From each one of the two thrusters
thrust_est_1 = abs(MZ_est_mano2_ea/armm);
error_1 = 100*(Thrust_actual - thrust_est_1)/Thrust_actual;
fprintf('\nEstimated Thrust from Spin/Despin: %2.2e [N] (Deviation %2.2f %%)',...
, ...
thrust_est_1,error_1)

% ::::::::::::::::::::: ::::::::::::::::::::: ::::::::::::::::::::: ::::::::::::::::::::: ::::::::::::
%
% From transversal components /~~~~~/
% Estimated effective thrust moment from equation (6.42)
MZ_fraq_mano2 = (It*IZ)/((It - IZ)*rt_mano2(end))*...
abs(w_fit_coast2 - w_fit_coast1);
MZ_fit_mano2_ea = MZ_fraq_mano2/2; % From each one of the two thrusters
thrust_est_s = (abs(MZ_fit_mano2_ea)/armm);
error_s = 100*(Thrust_actual - thrust_est_s)/Thrust_actual;
fprintf('\nEstimated Thrust from frequencies: %2.2e [N] (Deviation %2.2f %%)',...
, ...
thrust_est_s,error_s)
% ::::::::::::::::::::: ::::::::::::::::::::: ::::::::::::::::::::: ::::::::::::::::::::: ::::::::::::
end
```

---

```

function [w_fit_coast] = freqFmXYsignal(rt_coast,coast_SC_X,coast_SC_Y,smpf)
% This function estimates the pre/post transversal natural frequencies
% Input transversal angular velocities
wXo_coast1 = coast_SC_X(1);
wYo_coast1 = coast_SC_Y(1);
% Identify the characteristic main frequency of input signal
coastingfreq = coast_SC_Y';
Y = fft(coastingfreq); % Fast Fourier transform
f = smpf*(0:(size(coastingfreq,2)/2))/size(coastingfreq,2);
P2 = abs(Y/size(coastingfreq,2));
P1 = P2(1:round(size(coastingfreq,2)/2+1));
P1(2:end-1) = 2*P1(2:end-1);
[~,idx] = max(P1);
% Signal frequency of maximum energy (Initial guess for fitting)
w_seed = abs(f(idx))*2*pi; % [Hz] -> [rad/s]
% *****
% * Frequency refinement * -----
% *****
% e.g. by residuals reduction
j_test = 1;
w_ac = zeros(1,2);
for i_test = 1:1:500
    % Generate anchor points
    if i_test == 1
        w_test = w_seed; % Initial guess
    elseif ((i_test < 20) && (i_test > 1))
        nrn = -1 + (2)*rand;
        w_test = w_test + nrn*w_test/2;
    elseif i_test >= 20 % END anchor points
        [~,I_test] = min(w_ac(:,1));
        ref1 = abs(w_ac(I_test,2));
        xmx = ref1 + rand*ref1/(j_test^2);
        x1 = 0:xmx/10000:xmx;
        y1 = spline(w_ac(:,2),w_ac(:,1),x1);
        [~,I_test] = min(y1);
        w_test = x1(I_test);
        j_test = j_test + 1;
    end
    % Evaluate transversal angular rate equations
    % in X
    wX_coast1 = wXo_coast1*cos(w_test.*rt_coast) + ...
                wYo_coast1*sin(w_test.*rt_coast);
    diffXs = abs(coast_SC_X - wX_coast1);
    residX = sqrt(sum(diffXs.*diffXs)/size(diffXs,1));
    % in Y
    wY_coast1 = wYo_coast1*cos(w_test.*rt_coast) - ...
                wXo_coast1*sin(w_test.*rt_coast);
    diffYs = abs(coast_SC_Y - wY_coast1);
    residY = sqrt(sum(diffYs.*diffYs)/size(diffYs,1));
    resid = residX*residY;
    % Store results in array
    w_ac(i_test,:) = [resid,w_test];
end
[~,I_test] = min(w_ac(:,1));
% Best fit transversal natural frequency
w_fit_coast = w_ac(I_test,2);
end

```

Blank page